State University of Londrina
Center of Technology and Urbanism
Department of Electrical Engineering
Doctorate Program in Electrical Engineering
UEL/UTFPR-CP Association

David William Marques Guerra

Advanced Techniques for Channel Modeling, Estimation, and Resource Allocation Optimization in 5G/6G Wireless Communication Systems

Londrina,
July 12, 2024

David William Marques Guerra

Advanced Techniques for Channel Modeling, Estimation, and Resource Allocation Optimization in 5G/6G Wireless Communication Systems

Técnicas Avançadas para Modelagem, Estimativa e Recursos de Canais Otimização de alocação em sistemas de comunicação sem fio 5G/6G

Doctoral Thesis submitted to the Electrical Engineering Doctorate Program at the State University of Londrina in fulfillment of the requirements to acquire the degree of Doctor of Philosophy in Electrical Engineering.

Area: Telecommunications Systems

Supervisor: Taufik Abrão

Londrina,
July 12, 2024

David William Marques Guerra

Advanced Techniques for Channel Modeling, Estimation, and Resource Allocation Optimization in 5G/6G Wireless Communication Systems

Doctoral Thesis submitted to the Electrical Engineering Doctorate Program at the State University of Londrina in fulfillment of the requirements to acquire the degree of Doctor of Philosophy in Electrical Engineering.

Area: Telecommunications Systems

Examining Committee

Dr. Cássio Gonçalves do Rego
Department of Electronic Engineering
Federal University of Minas Gerais
External member

Dr. Cristiano Magalhães Panazio
Department of Telecommunications and Control
University of São Paulo
External member

Dr. José Cândido Silveira Santos Filho
School of Electrical and Computer Engineering
University of Campinas
External member

Dr. Marcello Luiz Rodrigues de Campos
Electrical Engineering Program
Federal University of Rio de Janeiro
External member

Dr. Taufik Abrão
Department of Electrical Engineering
State University of Londrina
Supervisor

Londrina,
July 12, 2024

I dedicate this thesis to God, to my parents, to my beloved wife, and to all my colleagues and friends, whose collaboration and encouragement were essential for this achievement.

Acknowledgements

Completion of this doctoral thesis marks a significant milestone in my academic and personal life, and none of this would have been possible without the support and dedication of many people to whom I am immensely grateful.

First and foremost, I thank God, the source of wisdom and strength, for guiding and sustaining me throughout this journey. Without His grace and blessings, I would not have been able to overcome the challenges and achieve this goal.

To my parents, Idelcio Ferreira Guerra and Marilda Cézar Marques Guerra, my eternal gratitude for their unconditional love, unwavering support, and countless sacrifices made throughout my life. You have always believed in me, even in the most difficult moments, and provided me with the necessary tools to reach this point. Your words of encouragement and examples of perseverance were fundamental for me to keep moving forward.

To my dear wife, Camila Maria Galo da Silva, my constant companion, my eternal gratitude for your patience, understanding, and support. You stood by my side in moments of joy and difficulty, always offering a friendly shoulder and words of encouragement. Your love and support were essential for me to fully dedicate myself to this research.

To my advisor, Professor Dr. Taufik Abrão, I am deeply grateful for your guidance, valuable advice, and constant encouragement. Your expertise and dedication were crucial to the development of this work. Your constructive criticism and support were fundamental for my growth as a researcher, academic, and individual.

I also thank Professor Dr. Ekram Hossain, who welcomed me and significantly contributed to my work during my time in Canada. The collaboration with the UofM research group was undoubtedly fundamental in the final phase of my research.

To my laboratory colleagues, both those who directly participated in this project and those who contributed indirectly, my sincere thanks. The collaboration, enriching discussions, and mutual support were vital for the realization of this thesis. The exchange of ideas and camaraderie we shared were, without a doubt, one of the highlights of this journey.

To all of you, my deepest and sincerest thanks. This achievement is largely the result of the support and encouragement I received from each one of you. May this thesis be just the beginning of many other accomplishments to come.

"The Lord is my shepherd, I lack nothing.
He makes me lie down in green pastures,
he leads me beside quiet waters,
he refreshes my soul.
He guides me along the right paths
for his name's sake."
(Psalm 23:1-3 Holy Bible (NIV))

Abstract

Several emerging technologies have being proposed to meet the growing demand for high-speed, reliable, and high-quality communications for the next-generation (6G) mobile systems. The Extra-Large Multiple-Input Multiple-Output (XL-MIMO) system, a MIMO communication system with a very large number of antennas, is presented as a promising solution, as well as Reconfigurable Intelligent Surfaces (RIS), which are structures composed of reflecting elements capable of altering the phase and amplitude of the reflected signal, thus improving communication performance. Building on the potential of these techniques, this thesis explores the characteristics, challenges, and solutions associated with implementing these schemes in mobile communication systems. The first part proposes a double-scattering XL-MIMO channel modeling, considering specific concepts of this scenario and evaluating the impact of the spatial and temporal evolution of the dynamic environment. We observe that the birth and death processes of scatterers and clusters considerably impact system performance. In the second part, a channel estimator is proposed for RIS-assisted systems using signal compression techniques. More specifically, an efficient estimation of sparse channel gains using a modified redundant dictionary to reconstruct the BS-RIS/UE-RIS links in RIS-aided communication is proposed. This is achieved through a compressed sensing (CS) based method called Matching Pursuit with Phase Rotation (MP-PR), which uses a few active elements on the RIS panel. This procedure aims to optimize the efficiency and accuracy of channel estimation, representing one of the main challenges for effectively integrating RIS in beyond 5G (B5G) wireless networks. The third part of this work proposes an energy-efficient uplink power control for RIS-aided IoT systems. To address the battery limitations of IoT devices, the approach employs Riemannian manifolds and a convex power allocation solution to improve energy efficiency (EE) by reducing IoT transmit power in RIS-aided uplink Massive MIMO (M-MIMO) systems. Numerical results indicate significant improvements in the total power consumption of the devices compared to existing techniques. Additionally, an alternative approach using statistical channel state information (CSI) demonstrates comparable performance with reduced complexity.

Keywords: 1. M-MIMO, 2. XL-MIMO, 3. Channel Modeling, 4. RIS, 5. Channel Estimation, 5. QoS, 6. IoT, 7. Manifolds, 8. Multiple Access, 9. Energy Efficiency, 10. Spectral Efficiency.

Resumo

Várias tecnologias emergentes estão sendo propostas para atender à crescente demanda por comunicações de alta velocidade, confiáveis e de alta qualidade para os sistemas móveis de próxima geração (6G – *sixth generation*). O sistema de extra larga escala de múltiplas entradas e múltiplas saídas (XL-MIMO – *Extra-Large Multiple-Input Multiple-Output*), um sistema de comunicação MIMO com um número muito grande de antenas, é apresentado como uma solução promissora, bem como as superfícies inteligentes reconfiguráveis (RIS – *Reconfigurable Intelligent Surfaces*), que são estruturas compostas de elementos refletores capazes de alterar a fase e a amplitude do sinal refletido, melhorando assim o desempenho da comunicação. Aproveitando o potencial dessas técnicas, esta tese explora as características, os desafios e as soluções associadas à implementação desses esquemas em sistemas de comunicação móvel. A primeira parte deste trabalho apresenta e analisa um modelo de canal XL-MIMO de duplo espalhamento, considerando conceitos específicos desse cenário e avaliando o impacto da evolução espacial e temporal do ambiente dinâmico. Observa-se que os processos de nascimento e morte dos espalhadores afetam consideravelmente o desempenho do sistema. Na segunda parte, é proposto um estimador de canal para sistemas assistidos por RIS usando técnicas de compressão de sinal. Mais especificamente, propõe-se uma estimativa eficiente dos ganhos de canal esparsos usando um dicionário redundante modificado para reconstruir os links BS-RIS/UE-RIS em comunicações assistidas por RIS. Isso é alcançado por meio de um método baseado em amostragem compressiva (CS – *Compressed Sensing*) chamado busca correspondente com rotação de fase (MP-PR – *Matching Pursuit with Phase Rotation*), que utiliza poucos elementos ativos no painel RIS. Este procedimento visa otimizar a eficiência e a precisão da estimativa de canal, representando um dos principais desafios para integrar efetivamente a RIS nas redes sem fio além do 5G (B5G – *Beyond 5G*). A terceira parte deste trabalho propõe um controle de potência de uplink eficiente em termos de energia para sistemas IoT assistidos por RIS. Para abordar as limitações de bateria dos dispositivos IoT, a abordagem emprega variedades Riemannianas e uma solução de alocação de potência CVX para melhorar a eficiência energética (EE) ao reduzir a potência de transmissão dos dispositivos IoT em sistemas de uplink MIMO massivo (M-MIMO – *Massive MIMO*) assistidos por RIS. Resultados numéricos indicam melhorias significativas no consumo total de potência dos dispositivos em comparação com as técnicas existentes. Além disso, uma abordagem alternativa usando conhecimento estatítico da informação do canal estatístico demonstra um desempenho comparável com complexidade reduzida.

Palavras-chave: 1. M-MIMO, 2. XL-MIMO, 3. Modelagem de Canal, 4. RIS, 5. Estimação de Canal, 5. QoS, 6. IoT, 7. Manifolds, 8. Acesso Múltiplo, 9. Eficiência Energética, 10. Eficiência Espectral.

List of abbreviations and acronyms

3D	Three-Dimensional
3GPP	Third Generation Partnership Project
1G	First generation
2G	Second generation
3G	Third generation
4G	Fourth generation
5G	Fifth generation
6G	Sixth generation
ADMM	Alternating Direction Method of Multipliers
AI	Artificial Intelligence
AMP	Approximate Message Passing
AMPS	Advanced Mobile Phone System
ANM	Atomic Norm Minimization
AoAs	Angle-of-Arrivals
AoDs	Angle-of-Departures
AO	Alternating Optimization
AP	Access Point
AWGN	Additive White Gaussian Noise
B5G	Beyond fifth generation of mobile communications networks
BDMA	Beam Division Multiple Access
BS	Base Station
BW	BandWidth
CBSM	Correlation-Based Stochastic Models
CCDF	Complementary Cumulative Distribution Function

CDMA Code Division Multiple Access

CE Channel Estimation

CG Conjugate Gradient

CS Compressed Sensing

CSI Channel State Information

CN Condition Number

CV-DnCNN Complex-Valued Denoising Convolution Neural Network

DOA Direction-Of-Arrival

DL Downlink

DRL Deep Reinforcement Learning

DS Double-Scattering

EDGE Enhanced Data Rates for Global Evolution

EE Energy Efficiency

EGPRS Enhanced General Packet Radio Service

eMBB Enhanced Mobile Broadband

EPA Equal Power Allocation

ESPRIT Estimation of Signal Parameters via Rotational Invariance Technique

FBMC-MA Filter Bank Multi-Carrier Multiple Access

FDMA Frequency Division Multiple Access

FLOPs Floating Point OPerations

GAMP Generalized Approximate Message Passing

GBSM Geometry-Based Stochastic Models

GmAMP Gaussian-mixture Approximate Message Passing

GPRS General Packet Radio Service

GSM Global System for Mobile communications

IMT2000 International Mobile Telecommunications 2000

HBF Hybrid BeamForming

HMIMOS Holographic MIMO Surface

HSPA High-Speed Packet Access

IoT Internet of Things

LoS Line-of-Sight

LS Least Squares

LTE Long-Term Evolution

M-MIMO Massive Multiple-Input Multiple-Output

MIMO Multiple-Input Multiple-Output

MISO Multiple-Input Single-Output

ML Machine Learning

MSE Mean-Squared Error

MMSE Minimum Mean-Squared Error

mMTC massive Machine-Type Communications

mmWave Millimeter Wave

MRC Maximum-Ratio Combining

MU Multi-User

MuI Multi-user Interference

MPCs MultiPath Components

MUSIC MUltiple SIgnal Classification

NB-IoT Narrow-Band IoT

NLoS Non-Line-of-Sight

NMSE Normalized Mean-Squared Error

NMT Nordic Mobile Telephone

OFDM Orthogonal Frequency Division Multiplexing

OFDMA Orthogonal Frequency Division Multiple Access

OMP-PR Orthogonal Matching Pursuit with Phase Rotation

OMP Orthogonal Matching Pursuit

PCP Poisson Clustering Process

PDC Personal Digital Cellular

PSO Particle Swarm Optimization

PPP Poisson Point Process

QoS Quality of Service

RAN Radio Access Network

RE Resource Efficiency

RIS Reconfigurable Intelligent Surface

RF Radio Frequency

RM Riemannian Manifold

SD Steepest-Descent

SDP SemiDefinite Programming

SDR SemiDefinite Relaxation

SE Spectral Efficiency

SINR Signal-to-Interference-plus-Noise Ratio

SMS Short Message Service

SNR Signal-to-Noise Ratio

SOMP Simultaneously Orthogonal Matching Pursuit

STV Space-Time-Variant

SVD Singular Value Decomposition

SAE/EPC System Architecture Evolution/Evolved Packet Core

TACS Total Access Communications System

TDMA Time Division Multiple Access

TLS Total Least Square

TR Trust-Region

UAV Unmanned Aerial Vehicle

UE User Equipment

UHD Ultra High Definition

ULA Uniform Linear Array

UMTS Universal Mobile Telecommunication System

UPA Uniform Planar Array

uRLLC Ultra Reliable Low Latency Communication

UT User Terminal

V2V Vehicle-to-Vehicle

VR Visibility Region

XL-MIMO Extra Large Multiple-Input Multiple-Output

ZF Zero-Forcing

List of Notations

j	$\sqrt{-1}$;
$\mathbf{a}$	bold lowercase letters represent column vectors;
$\mathbf{A}$	capital letters in bold represent matrices;
$\mathcal{A}$	capital calligraphic letters denote finite sets;
$\lvert\mathcal{A}\rvert$	Cardinality of the set $\mathcal{A}$;
$\mathbf{A}_{i,j}$	element present in the ith row and jth column of $\mathbf{A}$;
$\mathbf{A}^{-1}$	matrix inversion;
$\mathbf{I}_N$	$N \times N$ identity matrix;
$(\cdot)^T$	transpose operator;
$(\cdot)^H$	Hermitian operator;
$\odot$	Hadamard product;
$\otimes$	Kronecker product;
$\langle a, b \rangle$	inner product between a and b;
$\mathrm{Tr}(\cdot)$	trace of a matrix;
$\det(\cdot)$	determinant of a matrix;
$\mathrm{diag}(\cdot)$	diagonal operator;
$\lVert \cdot \rVert$	Frobenius norm;
$\lvert \cdot \rvert$	modulus operator;
$\mathbb{E}\{\cdot\}$	expectation operator;
$\mathbb{V}\mathrm{ar}\{\cdot\}$	variance operator;
$\mathrm{vec}\{\cdot\}$	vectorization operator;
$\mathrm{Cov}\{\cdot\}$	covariance operator;
$\lceil x \rceil$	nearest integer greater than or equal to x;
$\Re\{x\}$	real part of x;
$\Im\{x\}$	imaginary part of x;

$\mathcal{O}\{\cdot\}$ Big-O notation;

List of Symbols

Chapter 2

M	number of antennas at the BS
K	number of users
C	number of clusters at the BS side
S_i	number of scatterers at the i-th BS-cluster
S_k	number of scatterers at the k-th U-cluster
r_i	number of visible antennas for the i-th BS-cluster
$\mathbf{y}$	received baseband signal $\mathbf{y} \in \mathbb{C}^{M\times 1}$
$\mathbf{H}$	complex channel matrix $\mathbf{H} \in \mathbb{C}^{M\times K}$
$\mathbf{x}$	vector of complex input symbols $\mathbf{x} \in \mathbb{C}^{K\times 1}$
$\mathbf{h}_k$	channel between the k-th user and the BS $\mathbf{h}_k \in \mathbb{C}^{K\times 1}$
$\mathbf{n}$	AWG noise modeled by a complex Gaussian distribution $\mathbf{n} \sim \mathcal{CN}(0, \sigma_n^2 \mathbf{I}_M)$
$\tilde{\mathbf{H}}$	sub-channel between the i-th BS-cluster and the k-th user $\tilde{\mathbf{H}} \in \mathbb{C}^{M\times K}$
$\boldsymbol{\Upsilon}_i$	cluster VR matrix for the i-th BS-cluster
$\boldsymbol{\rho}_i$	power distribution vector
$\mathbf{R}_i$	correlation matrix between the BS and the i-th BS-cluster
$\tilde{\mathbf{R}}_{i,k}$	correlation matrix between the i-th BS-cluster and the U-cluster for the k-th user
$\mathbf{D}_k$	visibility matrix for the$k$-th user
d_s	spacing between scatterers
d_r	spacing between antenna elements
$\mathrm{Pr}_{\mathrm{srv}}^{\mathrm{scat}}$	survival probability of the scatterers
λ_r	recombination rate of the scatterers

λ_g rate of regeneration of scatterers

D coherence factor related to the environment for the scatterers

μ average number of newly generated scatterers

$\Pr_{\text{clus}}^{\text{scat}}$ survival probability of the clusters

λ_r^c recombination rate of the clusters

λ_g^c rate of regeneration of clusters

D_c coherence factor related to the environment for the clusters

μ^c average number of newly generated clusters

Chapter 3

N_{BS} number of antennas at the BS

N_{UE} number of antennas at the UEs

N_{SC} number of subcarriers

K number of users

N_{RIS} number of passive reflecting elements at the RIS

N_{act} number of active channel sensors at the RIS

$N_{\text{BS}}^{\text{RF}}$ number of RF chains at the BS side

$N_{\text{UE}}^{\text{RF}}$ number of RF chains at the k-th UE

$N_{\text{RIS}}^{\text{RF}}$ number of RF chains at the RIS

N_s^{UE} data stream length at the UE

N_s^{BS} data stream length received at the BS

L number of multi-path components

$\mathbf{y}_k$ received signal from the k-th user at BS

$\mathbf{y}_k \in \mathbb{C}^{N_{\text{BS}} \times 1}$

$\mathbf{H}$ complex channel matrix

$\mathbf{H} \in \mathbb{C}^{M \times K}$

$\mathbf{H}_k$ channel between the k-th user and the BS

$\mathbf{H}_k \in \mathbb{C}^{N_{\text{BS}} \times N_{\text{UE}}}$

$\mathbf{H}_{\text{D},k}$ direct channel between the k-th user and the BS

$\mathbf{H}_{\text{D},k} \in \mathbb{C}^{N_{\text{BS}} \times N_{\text{UE}}}$

$\mathbf{H}_{\text{R},k}$ channel between the k-th user and the RIS

$\mathbf{H}_{\text{R},k} \in \mathbb{C}^{N_{\text{RIS}} \times N_{\text{UE}}}$

$\mathbf{G}$ RIS-BS channel matrix

$\mathbf{G} \in \mathbb{C}^{N_{\text{BS}} \times N_{\text{RIS}}}$

$\mathbf{\Theta}$ diagonal matrix representing the phase-shift matrix of the RIS

$\mathbf{h}_{k,n}$ channel between the k-th UE and the BS at the n-th subcarrier

$\mathbf{H}_{\text{R},k} \in \mathbb{C}^{N_{\text{RIS}} \times 1}$

$\mathbf{G}_n$ channel between the RIS and the BS at the n-th subcarrier

$\mathbf{G}_n \in \mathbb{C}^{N_{\text{BS}} \times N_{\text{RIS}}}$

$\mathbf{W}_{S,t}$ selection matrix at the t-th time slot

$\mathbf{W}_{S,t} \in \mathbb{Z}^{N_{S_{\text{RIS}}} \times N_{\text{RIS}}}$

$\mathbf{\Phi}_{k,t}$ measurement matrix in the t-th time slot for the k-th UE

$\mathbf{W}_{\text{RF}}$ BS analog beamforming

$\mathbf{W}_{\text{RF}} \in \mathbb{C}^{N_{\text{BS}} \times N_{\text{BS}}^{\text{RF}}}$

$\mathbf{W}_{\text{BB},k}$ BS digital beamforming

$\mathbf{W}_{\text{BB},k} \in \mathbb{C}^{N_{\text{BS}}^{\text{RF}}}$

$\mathbf{F}_{\text{RF}}$ UE analog precoder

$\mathbf{F}_{\text{RF},k} \in \mathbb{C}^{N_{\text{UE}} \times N_{\text{UE}}^{\text{RF}}}$

$\mathbf{F}_{\text{BB},k}$ UE digital precoder

$\mathbf{F}_{\text{BB},k} \in \mathbb{C}^{N_{\text{UE}}^{\text{RF}} \times N_s^{\text{UE}}}$

$\mathbf{a}_R$ spatial steering vector at the receiver side

$\mathbf{a}_R \in \mathbb{C}^{N_r \times 1}$

$\mathbf{a}_T$ spatial steering vector at the transmitter side

$\mathbf{a}_T \in \mathbb{C}^{N_t \times 1}$

$\mathbf{s}_k$ the transmit signal of the k-th user

$\mathbf{s}_k \in \mathbb{C}^{N_s^{\text{UE}} \times 1}$

$\mathbf{n}$ AWG noise modeled by a complex Gaussian distribution

$\mathbf{n} \sim \mathcal{CN}(\mathbf{0}_{N_{\text{BS}}}, \sigma^2 \mathbf{I}_{N_{\text{BS}}})$

β_k^{LoS} path loss for the *line-of-sight* (LoS) link between the UEs and the RIS

β_k^{NLoS} the path loss for the *non-line-of-sight* (NLoS) component between the UEs and the RIS

κ_k Rician factor for the k-th UE

β_G the path loss between the BS and the RIS

κ_G Rician factor for the BS-RIS link

γ oversampling factor

M total number of measurements

$N_{S_{\text{RIS}}}$ number of measurements in each time slot

$N_{\text{RIS}}^{\text{RF}}$ number of RF chains

τ_p length of the pilot sequence

T_S sampling period

T training overhead

Chapter 4

N_{BS} number of antennas at the BS

K number of UTs

N_{RIS} number of passive reflecting elements at the RIS

$\mathbf{H}$ aggregated channel from UTs to the BS

$\mathbf{H} = \mathbf{G} + \mathbf{D} \in \mathbb{C}^{N_{\text{BS}} \times K}$

$\hat{\mathbf{H}}$ channel between the UTs and the RIS

$\hat{\mathbf{H}} \in \mathbb{C}^{N_{\text{RIS}} \times K}$

$\mathbf{F}$ channel between the RIS and the BS

$\mathbf{F} \in \mathbb{C}^{N_{\text{BS}} \times N_{\text{RIS}}}$

$\mathbf{D}$ direct channel between the UTs and the BS

$\mathbf{D} = [\mathbf{d}_1, \ldots, \mathbf{d}_K] \in \mathbb{C}^{N_{\text{BS}} \times K}$

$\mathbf{G}$ cascaded user-RIS-BS channel

$\mathbf{G} = \mathbf{F}\mathbf{\Phi}\hat{\mathbf{H}} \in \mathbb{C}^{N_{\text{BS}} \times K}$

$\mathbf{\Phi}$ phase shift matrix of the RIS

$\mathbf{\Phi} = \text{diag}\left(e^{j\theta_1}, \ldots, e^{j\theta_{N_{\text{RIS}}}}\right) \in \mathbb{C}^{N_{\text{RIS}} \times N_{\text{RIS}}}$

$\mathbf{r}$ received signal

$\mathbf{r} \in \mathbb{C}^{N_{\text{BS}} \times 1}$

θ_n phase shift of the n-th RIS element

γ_k distance-dependent path-loss factor for the k-th UT

β path loss

κ Rician factor

$\mathcal{K}$ set of IoT devices

p_k k-th link power consumption

$P_{k,\max}$	maximum available power (power budget) for each UT
P_{UT}	total uplink average power transmission
PL	path loss
C_0	path-loss value at the reference distance D_0
α	path-loss exponent
D_0	reference distance
d	distance between transmitter and receiver
α_{lr}	step size (or learning rate)
$\mathscr{M}$	generic Riemannian manifold
$\mathscr{P}$	complex circle manifold
$\text{Proj}\{\mathcal{T}_p\mathcal{M}\}$	projection operator onto the tangent space $\mathcal{T}_p\mathcal{M}$
$\nabla f(p)$	Euclidean gradient of f at p
$\nabla_{\mathcal{M}} f(p)$	Riemannian gradient
$\text{Retr}_p(v)$	retraction operator
β_k	Fletcher-Reeves conjugate gradient parameter
α_k^{ss}	step size at the k-th iteration

List of Figures

List of Tables

Contents

1 Introduction

The implementation of the fifth generation (5G) of wireless communication systems began in the year of 2019, initially in developed countries, and has since spread throughout the world. This process involved upgrading existing infrastructure, including installing new base stations (BSs) and replacing older hardware to support the higher bandwidth and lower latency requirements of 5G networks (LIU; JIANG, 2016). In addition, new technologies such as Massive Multiple-Input Multiple-Output (M-MIMO) and millimeter wave (mmWave) frequencies have been developed to improve the performance of 5G networks (VANNITHAMBY; TALWAR, 2017). As mobile traffic continues to increase and reliance on connections with stringent requirements for massive usage modes increases, technical restrictions related to massive connectivity and data rates are expected to arise in 5G technology while fulfilling strict demands for low latency, high reliability, and energy efficiency.

1.1 Mobile Communications Generations: From 1G to 4G

The advent of commercial analog mobile communication systems traces back to the 1950s and 1960s (OSSEIRAN et al., 2016; MARSCH et al., 2018), albeit with limited market penetration. In 1981, the emergence of the First Generation (1G) mobile cellular standards marked a pivotal moment with the launch of commercial deployments such as the Nordic Mobile Telephone (NMT) in Nordic countries, C-Netz in Germany, Portugal, and South Africa, Total Access Communications System (TACS) in the United Kingdom, and Advanced Mobile Phone System (AMPS) in the Americas. These 1G standards, characterized by analog technology, utilized frequency modulated radio signals with a digital signaling channel.

The subsequent era witnessed the inception of the Global System for Mobile communications (GSM) in Europe, as a pan-European 2G mobile communication system initiated by the European Conference of Postal and Telecommunications Administrations (CEPT) in 1982. GSM, the dominant 2G standard, ushered in digital transmission and switching technology, heralding improvements in voice quality, network capacity, and the introduction of supplementary services like the Short Message Service (SMS).

GSM, operating on a hybrid Time Division Multiple Access (TDMA)/Frequency Division Multiple Access (FDMA) method, aimed to establish a unified digital voice telephony network enabling international roaming across Europe. Concurrently, other digital 2G systems emerged globally, including TIA/EIA-136 (North American TDMA),

TIA/EIA IS-95A (CDMAOne), and Personal Digital Cellular (PDC) in Japan. The evolution to 2.5G introduced packet-switched data services alongside voice and circuit-switched data, with standards like General Packet Radio Service (GPRS) and TIA/EIA-951 extending the capabilities of GSM and TIA/EIA IS-95A, respectively.

Further advancements led to the evolution of GSM into Enhanced Data Rates for Global Evolution (EDGE) and Enhanced General Packet Radio Service (EGPRS), featuring higher order modulation and coding schemes. Concurrently, discussions and preparations for the next wireless generation standards were already underway, culminating in the development of Universal Mobile Telecommunication System (UMTS), a major 3G mobile communication system adopted by the European Telecommunications Standards Institute (ETSI) in 1998.

UMTS, qualifying for the International Mobile Telecommunications 2000 (IMT-2000) classification, represented a significant leap in cellular technology. The subsequent phases, witnessed the development of Radio Access Network (RAN) approaches like 1xEV-DO, 1xEV-DV, and High-Speed Packet Access (HSPA), enhancing packet data rates and paving the way for higher data rates with the introduction of Multiple Input Multiple Output (MIMO) technology.

The advent of Long Term Evolution (LTE) marked the transition to the commercially accepted 4G standard, featuring Orthogonal Frequency Division Multiple Access (OFDMA) and a new architecture known as System Architecture Evolution/Evolved Packet Core (SAE/EPC). LTE, designed for higher spectrum block allocations and flexible carrier arrangements, offered significant improvements in capacity and operational cost reductions compared to previous generations.

As LTE continued to evolve, subsequent releases refined capabilities such as carrier aggregation, relaying, and interference cancellation. Notably, LTE Release 12 introduced features to support heterogeneous networks and offloading of backhaul and core networks. Furthermore, LTE-M and Narrow-Band IoT (NB-IoT) solutions were introduced to facilitate massive Machine Type Communication (mMTC) devices, enhancing coverage, battery life, and cost-effectiveness (ZAIDI et al., 2018).

In the evolving landscape of cellular technology, GSM/EDGE, UMTS/HSPA, and LTE have played significant roles, with LTE emerging as the dominant mobile technology. Projections indicate a continued rise in LTE subscriptions, solidifying its position as the largest mobile technology in the foreseeable future.

1.2 5G: Overview, Features, and Applications

The 21st century is marked by rapid advancements in wireless communication, with 5G emerging as the next-generation technology. Built on the foundation of 4G, 5G aims to address key needs such as increased data rates, enhanced capacity, reduced latency, and

improved Quality of Service (QoS) (AL-DULAIMI; WANG, 2018).

Characterized by faster speeds, lower latency, and the ability to connect multiple devices simultaneously, 5G represents a significant leap forward in wireless technology. It leverages technologies like Beam Division Multiple Access (BDMA) and Filter Bank Multi-Carrier Multiple Access (FBMC-MA) to surpass the capabilities of 4G (OSSEIRAN et al., 2016).

Key to 5G's functionality is its use of mmWave technology, enabling unprecedented data transmission speeds exceeding 1 Gbps. 5G promised to revolutionize various sectors including manufacturing, automotive, healthcare, and energy, facilitating the transition from wired to wireless connectivity in industrial settings. Although 5G has been operational since 2019, many of these initial promises are still far from being realized.

In addition to its technical advancements, 5G introduces new network design paradigms, such as M-MIMO and dense networks, to maximize spectrum utilization and enhance user experience (OSSEIRAN et al., 2016). It also embraces machine learning (ML) and artificial intelligence (AI) for automation and efficient resource management (MARSCH et al., 2018).

Various technologies underpin the 5G ecosystem, including millimeter wave communications, advanced waveforms, multiple access schemes, M-MIMO with beamforming, and dense networks (DAHLMAN et al., 2018). These technologies enable diverse applications across three main categories: Enhanced Mobile Broadband (eMBB), mMTC, and Ultra-Reliable Low-Latency Communication (URLLC).

eMBB focuses on providing high-speed data services for applications like ultra high definition (UHD) video streaming, cloud gaming, and virtual reality. mMTC supports a large number of connected devices with low-cost and energy-efficient communication, benefiting smart home and smart city initiatives. URLLC ensures ultra-reliable and low-latency communication for critical applications such as industrial automation and autonomous vehicles.

Overall, the initial idea of the 5G was to be a transformative technology poised to reshape how we communicate, connect, and interact with the world around us.

1.3 What is Next?

Thinking about how to surpass the current 5G limitations, researchers and industry leaders are already looking ahead to the future of wireless technology. The development of beyond fifth generation (B5G) and sixth generation (6G) is expected to revolutionize various activities, including healthcare, transportation, and manufacturing, and enable the deployment of new applications such as autonomous vehicles, smart cities, and virtual reality (VANELLI-CORALLI et al., 2020).

B5G and 6G refer to developing and implementing wireless communication technologies that offer faster speeds, lower latency, higher capacity, and more reliability than 5G (HONG et al., 2022). These technologies will likely be based on new approaches such as Extra-Large MIMO (XL-MIMO), Reconfigurable Intelligent Surface (RIS), terahertz frequency-based systems, advanced signal processing, and artificial intelligence. The research and development of beyond 5G and 6G technologies are still in their early stages, and it may take many years before they become widely available. However, the potential benefits of these technologies are significant, particularly for applications such as autonomous vehicles, virtual and augmented reality, and the internet of things (IoT).

The XL-MIMO, a novel concept of radio BSs for areas with high-density user traffic, such as stadiums or shopping centers, proposes the installation of a large number of antennas in the form of extensive panels that can be integrated into building facades. Nevertheless, with the proximity of the transceiver to the significant population of mobile users, a new electromagnetic wave propagation scenario arises, requiring adaptations of typical 5G technologies to unreliable models. In a similar setting, passive reflecting elements in the form of RIS can be employed to achieve remarkable performance enhancements at an exceptionally low energy consumption cost.

This thesis aims to investigate the application and implementation of promising solutions, specifically focusing on the XL-MIMO and RIS-assisted M-MIMO systems, which have gained much interest of the academic community in recent years.

1.4 Objectives

The objectives of this doctoral thesis are the following:

1. **General:** Systematically investigate the application of M-MIMO, XL-MIMO, and RIS-assisted communication systems in the context of B5G and 6G technology, aiming to demonstrate the effectiveness and efficiency of such topologies and propose relevant scientific contributions regarding the connectivity optimization and energy efficiency of the investigated systems.

2. **Specifics:**

   a) Carry out a comprehensive literature review on M-MIMO/XL-MIMO, as well as the integration of RIS panels with these technologies, exploiting application scenarios and open issues;

   b) Develop algorithms and numerical simulations to demonstrate the effectiveness of the proposed solutions, comparing them with the most advanced and recent techniques in the literature;

   c) Generate innovative scientific contributions to publish in specialized and recognized journals – Electrical Engineering area (Eng. IV in QUALIS-CAPES).

1.5 Outline of the Work

The remainder of this work is organized as follows:

Chapter 2: ***Channel Modeling for XL-MIMO with Uniform Arrays.*** This chapter discusses the potential of XL-MIMO systems for use in 6G wireless communication systems. Accurately modeling XL-MIMO channels is crucial as the urban environment is full of obstacles and reflectors, leading to spatial non-stationarities in the signal received at the BS. Then, this chapter proposes and analyzes a double-scattering XL-MIMO channel model, considering two types of scattering clusters and two distinct antenna array configurations.

Chapter 3: ***Channel Estimation on RIS-Aided Communication Systems.*** This chapter discusses the challenges faced by RIS in integrating efficiently into wireless networks, which include reflection optimization, channel estimation, and optimization of deployment locations. Then, a solution for channel estimation in RIS-assisted systems using compressive sensing techniques is proposed.

Chapter 4: ***Spectral and Energy Efficiency in RIS-Aided Systems.*** This chapter focuses on an energy-efficient uplink (UL) power control strategy for RIS-aided IoT systems. To tackle the battery limitations of IoT devices, the approach utilizes Riemannian manifolds and a convex power allocation solution to enhance energy efficiency (EE) by reducing IoT transmit power in RIS-aided uplink M-MIMO systems. Numerical results reveal significant improvements in the total power consumption of the devices compared to existing techniques. Additionally, an alternative approach using statistical channel state information (CSI) demonstrates comparable performance with reduced complexity.

Chapter 5: ***Conclusions and Perspectives*** This chapter presents the main conclusions of the thesis work and provides some research directions for future works. In other words, it discusses the main findings and contributions achieved so far, highlighting the strengths and limitations of the proposed solutions. Furthermore, it identifies the open research issues and challenges that need to be addressed in future work.

1.6 Contributions

So far, this scientific and technological research work has resulted in the following publications and submissions in indexed journals or relevant international conferences for the field of telecommunication systems:

[A] **David William Marques Guerra** e Taufik Abrão. ***Clustered Double-Scattering Channel Modeling for XL-MIMO with Uniform Arrays***. *IEEE Access*, IEEE (`IF=3.9`), Vol. 10, 2022, DOI: ⟨10.1109/ACCESS.2022.3152704⟩.

[B] **David William Marques Guerra**, Taufik Abrão, Ekram Houssain. ***Channel Estimation in RIS-Aided mmWave Wireless Systems Using Matching Pursuit With Phase Rotation***. Published on 17-May-2024 (Early Access) on *IEEE Transactions on Wireless Communications* (`IF=10.4`), DOI: ⟨10.1109/TWC.2024.3399450⟩.

Additionally, another important result is the book chapter described below:

[C] **David William Marques Guerra**, José Carlos Marinello, Taufik Abrão, Ekram Hossain. ***Energy-Efficient Uplink Transmission in RIS-Aided M-MIMO IoT Systems***. Book Chapter accepted on 20-Jan-2024 on *Wiley-IEEE Press*. To appears as Chapter 6 of the book *Massive MIMO for Future Wireless Communication Systems: Technology and Applications*. Wiley-IEEE Press, 2024.

It is also important to mention two conference papers, one of them is already published and the other one was submitted recently, which is a short version of the paper in [B]. The description of this works is as follows:

[D] **David William Marques Guerra**, Taufik Abrão. ***RIS-aided System Channel Estimation using NN***. 2022 Symposium on Internet of Things (SIoT), São Paulo, Brazil, 2022, pp. 1-4, DOI: ⟨10.1109/SIoT56383.2022.10070280⟩.

[E] **David William Marques Guerra**, Taufik Abrão, Ekram Hossain. ***Matching Pursuit With Phase Rotation for RIS-Aided mmWave Channel Estimation***. Accepted on 27-May-2024 on *ISWCS' 24*.

Finally, it is also worth noting the co-authorship in the following publication:

[F] Lígia May Taniguchi, João Henrique Inacio de Souza, **David William Marques Guerra**, Taufik Abrão. ***Resource efficiency and pilot decontamination in XL-MIMO double-scattering correlated channels***. Transactions on Emerging Telecommunications Technologies, Wiley (`IF=3.6`), Vol. 32, *Issue* 12, 2021, DOI: ⟨https://doi.org/10.1002/ett.4365⟩.

2 Channel Modeling for XL-MIMO with Uniform Arrays

Due to their features, XL-MIMO systems are a potential candidate for the 6G wireless communication systems. As XL-MIMO has a large antenna array, and, typically, the urban environment is plenty of obstacles and reflectors, the spatial non-stationarities are introduced in the signal received at the BS, which means that only a portion of the antenna array is visible to users.Accurately modeling XL-MIMO channels is paramount in this case. Previous works on XL-MIMO channel modeling have adopted the non-stationarities only in a spatial sense and do not consider spatial-time evolution scenarios. Moreover, simplified models with only one set of clusters between the BS and the user equipment (UE) are usually adopted; hence, there needs to be more understanding regarding such channel modeling in the literature. This chapter presents and extensively analyzes a double-scattering (DS) XL-MIMO channel model by admitting two types of scattering clusters, one placed at the BS side and another near the UEs. In addition, two distinct antenna array configurations are included in the analysis, the uniform linear and planar arrays (ULA and UPA, respectively). Hence, a new DS channel model under UPA arrangements is proposed, suitable for modeling spatial non-stationarities scenarios in XL-MIMO dynamic environments subject to BS-cluster and UE-cluster correlation and birth-death channel clusters and scatterers. Numerical results for signal-to-interference-plus-noise ratio (SINR), condition number (CN), and spectral efficiency (SE) performance metrics considering different XL-MIMO channels, and system configurations are analyzed via Monte-Carlo simulations under linear combiners maximum-ratio combining (MRC), zero-forcing (ZF), and minimum mean-squared error (MMSE). Also, we characterize the impact of the number of visible clusters per user, the birth-death rate growth effect on the channel clusters and scatterers, and the favorable propagation effect according to the size of the visibility region (VR) overlap. It can be observed that the birth and death processes have a significant impact on the system's performance. Under the proposed clustered DS channel modeling, the analyzed XL-MIMO linear receivers presented an SINR degradation of around 3 to 4 dB for the MMSE when the number of UEs substantially increased. At the same time, the ZF and MRC receivers present a decrease of 1 to 2 dB, approximately, in SINR for the considered dynamic configuration compared with static scenarios.

2.1 XL-MIMO in 6G Wireless Communication Systems

The XL-MIMO is a promising research direction of multi-antenna technology for the 6G wireless communication networks (BJÖRNSON et al., 2019; ALWIS et al., 2021; LU; ZENG, 2021b). In the following section, we will discuss the primary characteristics of the XL-MIMO channel.

2.1.1 XL-MIMO channel characteristics

It is well-known in the literature that when the number of antennas increases, the array becomes physically large and takes advantage of some benefits, including channel hardening, asymptotic favorable propagation, and area throughput (GUNNARSSON et al., 2020; BJöRNSON et al., 2017). These features promised by M-MIMO can be fully harnessed from a theoretical point of view and extended to the XL-MIMO context with some adaptations.

M-MIMO and XL-MIMO are advanced wireless communication technologies that primarily differ in the number of antennas they employ. M-MIMO typically involves tens to hundreds of antennas, while the main idea of XL-MIMO is to employ a significant number of antennas (10^3 or more) at the BS, which can be widely spread, *e.g.*, on the walls of dense buildings in the city, the roof of airports, public open spaces, walls of stadiums, among others. This increase in antennas in XL-MIMO allows for extremely high spatial resolution, enabling finer beamforming and spatial multiplexing compared to M-MIMO (CARVALHO et al., 2019).

When the number of antennas becomes very large, spatial non-stationarities emerge. In other words, when the dimension of the antenna array becomes very large, the far-field propagation assumption is no longer valid since the distance between the BS and the scatterers/clusters or users is smaller than the Rayleigh distance (LU; ZENG, 2021a). This fact implies that users can see only a physical portion of the BS antenna array due to the limited energy dispersion of the propagation paths and the array dimensions. The portion of the antenna array in the BS users see is the VR (ALI et al., 2019). As there is still a lack of understanding of the XL-MIMO propagation environment, further research on channel modeling and system-level performance evaluation is highly required. Indeed, such knowledge is paramount in the design of efficient signal-processing techniques for communications aided by extra-large arrays (CHEN et al., 2020; HAN et al., 2020b). In the XL-MIMO context, we have particular physical characteristics that the wireless channel model should cover adopted, *e.g.*, non-stationarities and near-field propagation, which directly impact the wireless channel modeling and other important channel metrics (YANG et al., 2020; RODRIGUES et al., 2020). An essential factor for modeling the channel

propagation in XL-MIMO is the effects caused by obstacles, such as buildings and trees, which scattering points can represent. In general, there are two classic types of statistical channel models, the correlation-based stochastic models (CBSM), in which a correlation factor only models the correlation degree, and the geometry-based stochastic models (GBSM) that take into account the effects of specific propagation geometry parameters, such as the distribution of the scatterers and their locations around the transmitters and receivers; such distribution results in a correlation degree between the antennas. Therefore, although CBSM models are less complex than the GBSM ones, some environmental features are only partially captured with the CBSM models. Consequently, the GBSM is more accurate for describing specific scenarios, such as M-MIMO and XL-MIMO (TANIGUCHI; ABRãO, 2020).

Deployment scenarios further highlight their differences (CARVALHO et al., 2020). M-MIMO is commonly found in cellular BS across various environments, including urban, suburban, and rural areas. In contrast, XL-MIMO is targeted for ultra-dense urban environments, smart buildings, and advanced industrial applications where extremely high data rates and low latency are essential. This system can thus serve multiple UEs simultaneously, substantially increasing SE thanks to the high spatial multiplexing gain.

2.1.2 Literature overview

Recent researches on wireless channel modeling have included non-stationary properties (TANIGUCHI; ABRãO, 2020; JIANG et al., 2019; AMIRI et al., 2021). The work (TANIGUCHI; ABRãO, 2020) describes, evaluates, and compares stochastic channel models for M-MIMO and XL-MIMO systems. More specifically, in the case of the XL-MIMO channel, the authors analyze the one-ring model using metrics such as capacity and SINR. Additionally, the correlation effect due to the location of the clusters is evaluated in the performance of linear precoding schemes. In (JIANG et al., 2019), a three-dimensional (3D) wireless channel model for vehicle-to-vehicle (V2V) communication environments is presented adopting the spherical wavefront assumption, while the non-stationarity property is only considered in a temporal sense. In (AMIRI et al., 2021), a DS channel model is presented for a linear array in the XL-MIMO context, also considering the near-field propagation with the spherical wavefront, including the spatial non-stationarity properties for the system with the VR concept. However, the work is restricted to the uniform linear array (ULA), and the space-time evolution of scatterers/clusters is neglected, considering only a static perspective.

In addition, some research works have adopted *birth and death processes* to model the channel non-stationarities (CHEN et al., 2017; WU et al., 2018; LóPEZ; WANG, 2020; LóPEZ et al., 2021; MA et al., 2021). Both (CHEN et al., 2017; WU et al., 2018) propose a one-ring M-MIMO channel model with only one set of clusters near the BS. A birth and death process of channel clusters is incorporated to reproduce the non-stationary

properties of clusters on both the array and time axes. While in (CHEN et al., 2017), the VR of each cluster is obtained from the ray visibility gain to the receive antennas, in (WU et al., 2018), the mean power updates of rays are embedded in the small-scale fading channel model with the assumption of the inverse square law, not considering the VR effect. Authors in (LóPEZ; WANG, 2020) propose a transformation method to model space-time-variant (STV) two-dimensional non-stationary wideband M-MIMO channels considering the disappearance of multipath components (MPCs) and the drift and spread of the time of arrival over the array. In this case, only a set of scatterers are implemented with a specific distribution governed by a birth and death process. López *et al.* (LóPEZ et al., 2021) update (LóPEZ; WANG, 2020) to a 3D wideband M-MIMO channel model, where statistical properties are derived. In this work, the scatterers are clustered, and now a Poisson process determines the appearance/disappearance of these clusters to capture array-variant characteristics, such as the VR effect. Lastly, in (MA et al., 2021), a GBSM non-stationary channel model operating at mmWave is proposed for an unmanned aerial vehicle (UAV) MIMO communications, where is considered both local and far clusters, in which a continuous-time Markov model is adopted to model the dynamic properties of the clusters, *i.e.*, the appearance/disappearance of clusters over time.

Channel measurements provided in (CARVALHO et al., 2020) highlight the complexity of modeling XL-MIMO channels. This work observed a considerable variation in power that reaches the array (more than 10 dB) and different patterns for signals coming from each device. Therefore, the non-stationary properties of XL arrays indicate that a substantial modification of the widely used correlated channel model is needed to consider the variation in the average channel gain along with the array. A clustered DS channel model can reflect more appropriately the effects of the non-stationarity phenomenon in XL arrays since it depends on both spatial correlations at the communication endpoints and the scattering structure along the propagation environment.

Against this background, we emphasize that previous literature does not present a specific and accurate channel model that accurately describes the XL-MIMO scenario and effects, including non-stationarities, correlation, and near-field effects. Therefore, the descriptions and models on the XL-MIMO channel found in the literature are incipient yet require further discussion since it is crucial to understand the XL-MIMO channel and system better. To our knowledge, non-stationary properties of clusters and scatterers in XL-MIMO correlated channel modeling with distributed scattering have yet to be comprehensively analyzed in the literature.

The *contribution* of this chapter is threefold.

- The primary *contribution* of this chapter is to propose a dedicated channel modeling for XL-MIMO systems, where the BS has XL uniform linear or planar arrays (ULA and UPA). For that, a DS channel model is reasonable. There are two scattering

clusters; one emerges stochastically near the BS side, while the second cluster appears near the user side. Such a specific channel model has been conceived for XL-MIMO structures based on current appealing application scenarios in 5G, including crowded system and channel configurations subject to many obstacles, typically found in urbanized environments.

- We have modeled the birth and death of the correlated BS-cluster and UE-cluster, as well as the scatterers, via Poisson processes, generating a space-time evolutionary process of scatterers/clusters that results in quasi-static and dynamic spatial correlated XL-MIMO channels.

- Extensive numerical results corroborate the validity of the proposed XL-MIMO channel modeling methodology by comprehensively evaluating the effect of birth and death Poisson point processes (PPP) and Poisson clustering process (PCP), the effect of interference, channel correlation, and the SE of an XL-MIMO system equipped with UPA or ULA and linear combiners at the receiver. Besides, we analyze the impact of parameters choice of DS correlated quasi-static or dynamic channels under XL-UPA and XL-ULA arrays via condition number (CN) of channel matrix and attainable average SINR, also considering different linear combiners.

The remainder of this chapter is organized as follows. Section 2.2 describes the adopted multi-user (MU) XL-MIMO system model. The XL-MIMO channel modeling considering linear and planar arrays are also discussed in section 2.2. Numerical results corroborating the validity of the proposed channel models are explored in section 2.4. Section 2.5 concludes the chapter.

2.2 XL-MIMO Channel Modeling

In the XL-MIMO system, different channel conditions are obtained due to the close distance between the array and the user and the use of extremely large arrays. Thus, the far-field propagation of the electromagnetic wave is no longer valid. In this case, the array will experience spherical wavefronts instead of planar wavefronts, which characterizes the near-field propagation. Hence, spatial non-stationarity is introduced with VR, DS clusters, and near-field wave propagation aiming to describe the XL-MIMO channel suitably (HAN et al., 2020a).

Assuming narrow-band transmissions, the received baseband signal $\mathbf{y} \in \mathbb{C}^{M\times 1}$ across the whole array is defined as:

$$\mathbf{y} = \mathbf{H}\mathbf{x} + \mathbf{n}, \tag{2.1}$$

in which $\mathbf{x} \in \mathbb{C}^{K\times 1}$ denotes the vector of complex input symbols with normalized power $\mathbb{E}[\mathbf{x}^2] = 1$; besides, the complex channel matrix can be defined as

$$\mathbf{H} = [\mathbf{h}_1, \ldots, \mathbf{h}_K] \in \mathbb{C}^{M\times K}, \tag{2.2}$$

where $\mathbf{h}_k$ is the channel between the k-th user and the BS, defined in the following section, eq. (2.3); finally, the AWG noise is a random variable modeled by a complex Gaussian distribution $\mathbf{n} \sim \mathcal{CN}(0, \sigma_n^2\mathbf{I}_M)$.

The following subsections explore two different antenna arrangements of interest in practical application scenarios for multi-user XL-MIMO wireless communications *i.e.*, ULA, and UPA. Also, we have presented the XL-MIMO a single-scattering (SS) XL-MIMO channel model, which can be seen as a simplification of the DS for an ULA arrangement.

2.2.1 DS XL-MIMO correlated channel model with ULA

Let $\mathbf{h}_k \in \mathbb{C}^{M\times 1}$ denote the k-th column of $\mathbf{H}$, corresponding to user k. Additionally, let K denote the number of simultaneously active users that are single-antenna equipped. Fig. 2.1 illustrates the scenario for the XL-MIMO with the ULA arrangement. Blue points represent the scatterers, while a set of near-scatterers forms a cluster. Furthermore, the shading elements (scatterers and clusters) represent the evolution of the scenario based on the birth and death Poisson process described in more detail in section 2.2.4.

To model the channel generically, the DS model is considered (AMIRI et al., 2021). The DS concept defines two types of scattering clusters placed at the BS side called BS-cluster and another located near the user side called U-cluster. In this channel, the spatial correlation between the transmitter and receiver is separable. Additionally, we assume that there are C clusters at the BS side and only one cluster for each user. Additionally, $\tilde{\alpha}_{i,k}$ is the azimuth angle, $\tilde{\theta}_{i,k}$ denotes the corresponding angular spread between the i-th BS-cluster and the U-cluster of user k, α_i represents the azimuth angle, while θ_i is the angular spread between the BS and the i-th BS-cluster.

One can assume that each cluster's VR equals or exceeds 50 antennas (NGO, 2015). Therefore, all users in front of the BS uniform array attain the M-MIMO condition; hence, both massive antenna reception properties, namely *channel hardening* and *favorable propagation*, are satisfied. Under such a channel condition, small-scale fading disappears within each VR, while large-scale effects dominate. As a result, the small-scale fading can be disregarded at the BS for processing purposes. However, in the adopted typical XL-MIMO geometric scenarios, the geographic distribution of UEs occurs in front of and close to the extension of the ULA or UPA panel, with similar distances and much smaller than the length of the uniform array. Therefore, in this case, the large-scale coefficients of each user do not differ significantly.

In this context, the channel model between the k-th user and the BS is as follows:

$$\mathbf{h}_k = [\tilde{\mathbf{H}}_{1,k}, \cdots, \tilde{\mathbf{H}}_{C,k}]\mathbf{D}_k\mathbf{g}_k, \quad \forall \quad k \in \{1, \ldots, K\}, \tag{2.3}$$

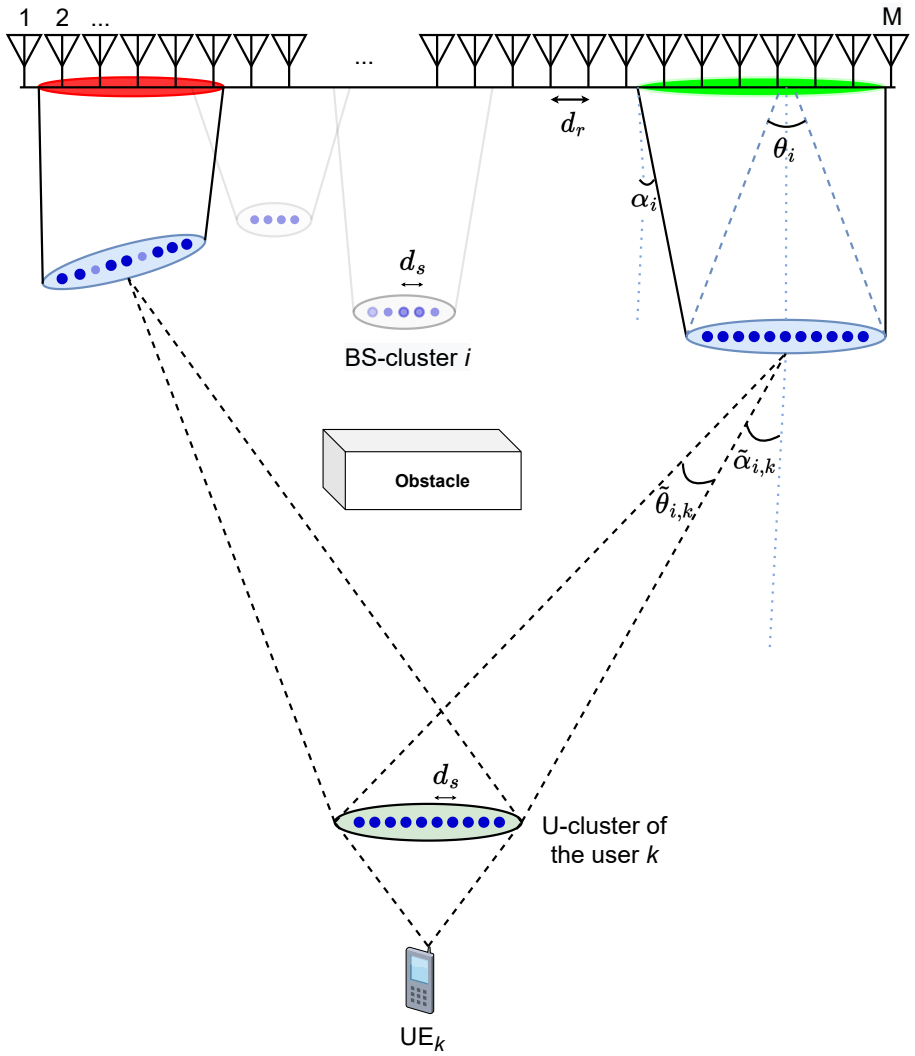

Figure 2.1 – XL-MIMO array with spatial non-stationary regions along the ULA with DS channel modeling: i-th BS-cluster, with $i = 1, 2, \ldots C$, and k-th U-cluster.

where $\tilde{\mathbf{H}}_{i,k} \in \mathbb{C}^{M \times S_i}$ represents the sub-channel between the i-th BS-cluster with S_i scatterers for the k-th user, $\mathbf{D}_k \in \mathbb{C}^{S^{'} \times S_k}$ is responsible for defining which BS-clusters are visible to the U-cluster of the k-th user, and $\mathbf{g}_k \sim \mathcal{CN}(0,1) \in \mathbb{C}^{S_k \times 1}$ denotes the small-scale fading between the k-th user and the S_k scatterers in its U-cluster. Furthermore, we assume that $S^{'}$ constitutes the visible scatterers at the BS side w.r.t. the U-cluster, *i.e.*, $S^{'} = \sum_{i=1}^{C} S_i$.

Then, the formulation of the sub-channel between the i-th BS-cluster and the U-cluster related to the k-th user is

$$\tilde{\mathbf{H}}_{i,k} = \boldsymbol{\Upsilon}_i \boldsymbol{\rho}_i^{\frac{1}{2}} \mathbf{R}_i^{\frac{1}{2}} \mathbf{G}_i \tilde{\mathbf{R}}_{i,k}^{\frac{1}{2}}, \tag{2.4}$$

where $\boldsymbol{\Upsilon}_i \in \{0,1\}^{M \times r_i}$ indicates which BS antennas are visible to the i-th BS-cluster, since r_i is the number of visible antennas, $\boldsymbol{\rho}_i \in \mathbb{C}^{r_i \times r_i}$ represents the visibility power (energy) gain, $\mathbf{R}_i \in \mathbb{C}^{r_i \times r_i}$ the correlation matrix between the BS and the i-th BS-cluster, $\mathbf{G}_i \in \mathbb{C}^{r_i \times S_i}$ is the complex scattering amplitudes between the BS and the i-th BS-cluster

and $\tilde{\mathbf{R}}_{i,k} \in \mathbb{C}^{S_i \times S_i}$ is the correlation matrix between the i-th BS-cluster and the U-cluster for the k-th user. Next, each channel component presented in equations (2.3) and (2.4) will be explained in more detail based on (Gesbert et al., 2002; AMIRI et al., 2021).

Cluster VR ($\boldsymbol{\Upsilon}_i$): The set of BS antennas visible to a given BS-cluster defines the cluster VR concept in this channel propagation model. Therefore, this set contains the indexes of the antennas that are visible to each BS-cluster channel, which is denoted by $\mathcal{R}_i = \{a_1^i, \cdots, a_{r_i}^i\}$, where a_l^i is the index of the l-th antenna element inside the i-th BS-cluster VR.

$$\boldsymbol{\Upsilon}_i = \begin{bmatrix} \mathbf{0}_{m_i^{'} \times r_i} \\ \mathbf{I}_{r_i} \\ \mathbf{0}_{m_i^{''} \times r_i} \end{bmatrix}, \tag{2.5}$$

where $\mathbf{0}_{m_i \times r_i}$ are zero matrices with $m_i^{'} = a_1^i - 1$ and $m_i^{''} = M - a_{r_i}^i$ and $\mathbf{I}_{r_i}$ is the identity matrix of dimensions $r_i \times r_i$. If we have, *e.g.*, a system with $M = 7$ antennas and a BS-cluster ($i = 1$) that has a VR defined by the set $\mathcal{R}_1 = \{3, 4, 5\}$, the matrix $\boldsymbol{\Upsilon}_1 \in \{0, 1\}^{7 \times 3}$ can be written as follows:

$$\boldsymbol{\Upsilon}_1 = \begin{bmatrix} 0 & 0 & 0 \\ 0 & 0 & 0 \\ 1 & 0 & 0 \\ 0 & 1 & 0 \\ 0 & 0 & 1 \\ 0 & 0 & 0 \\ 0 & 0 & 0 \end{bmatrix}.$$

Power distribution ($\boldsymbol{\rho}_i$): Due to the spherical wavefront propagation inherent to the XL-MIMO system, the amount of power that arrives in each antenna of the sub-array which forms the i-th cluster VR is not equally distributed, as shown from practical measurements performed on (GAO et al., 2013). As a result of this physical effect, the power peak occurs at the center of the visibility region. Then it is attenuated linearly with a constant rate ψ_i (dB/m) inside the VR. To better describe this phenomenon, the power distribution matrix for the i-th cluster VR can be represented by $\boldsymbol{\rho}_i = \text{diag}(\rho_i[1], \ldots, \rho_i[r_i]) \in \mathbb{C}^{r_i \times r_i}$. Additionally, this visibility gain matrix of the n-th antenna included in the VR can be evaluated using a discrete function such as:

$$\rho_i[n] = 10^{-\psi_i |a_{c_i}^i - a_n^i| d_r}, \quad \forall \quad n \in \{1, \ldots, r_i\}, \tag{2.6}$$

where $a_{c_i}^i = \lceil \frac{a_1^i + a_{r_i}^i}{2} \rceil$ denotes the index of the antenna located in the center of the i-th cluster VR, a_n^i is the index of the n-th antenna included in this VR, while d_r represents the BS antenna spacing in multiples of the signal wavelength.

Correlation between the BS and the i-th BS-cluster ($\mathbf{R}_i$): The correlation between the receiver side (BS antennas) and the i-th BS-cluster is defined by the correlation matrix

$\mathbf{R}_i \in \mathbb{C}^{r_i \times r_i}$, which its $(m,\ n)$ element can be evaluated as follows:

$$[\mathbf{R}_i]_{(m,n)} = \frac{1}{S_i} \sum_{\ell=\frac{1-S_i}{2}}^{\frac{S_i-1}{2}} e^{-2\pi j d_r (m-n) sin\left(\alpha_i + \frac{\ell\theta_i}{S_i-1}\right)}. \tag{2.7}$$

Correlation between the i-th BS-cluster and the U-cluster for the k-th user ($\tilde{\mathbf{R}}_{i,k}$): Assuming we have S_k scatterers at the k-th U-cluster, these scatterers can be represented as a virtual antenna array with S_k elements and an average spacing d_s in multiples of the wavelength. Therefore, the $(m,\ n)$ element of the correlation matrix between the i-th BS-cluster and the U-cluster can be obtained as:

$$[\tilde{\mathbf{R}}_{i,k}]_{(m,n)} = \frac{1}{S_i} \sum_{\ell=\frac{1-S_i}{2}}^{\frac{S_i-1}{2}} e^{-2\pi j d_s (m-n) sin\left(-\tilde{\alpha}_{i,k} + \frac{\ell\tilde{\theta}_{i,k}}{S_i-1}\right)}. \tag{2.8}$$

The above expressions capture how the spatial arrangement and angular characteristics of the scatterers affect the correlation between different antennas in the BS-cluster and U-cluster. They essentially model the phase shifts and signal variations caused by the different paths the signal takes from the BS antennas to the scatterers (Gesbert et al., 2002).

Visibility matrix ($\mathbf{D}_k$): Another type of VR considered in this propagation environment is the U-cluster VR for each k user. This user VR is represented by a set of clusters that are visible for the k-th user, denoted by $\mathcal{V}_k$. The practical mean of the user VR is that only part of the C BS-clusters is visible to each k U-cluster. Moreover, we need to define the scatterer visibility set $\mathcal{C}_k$, which can be seen as a set containing all the indexes representing the visible scatterers of the BS-clusters in $\mathcal{V}_k$ related to the k-th user. Thus, the mth row of the visibility matrix $\mathbf{D}_k \in \mathbb{C}^{S' \times S_k}$ is obtained as:

$$[\mathbf{D}_k]_{(m,:)} = \begin{cases} \mathbf{1}, & \text{if } m \in \mathcal{C}_k \\ \mathbf{0} & \text{otherwise} \end{cases}. \tag{2.9}$$

For example, consider 4 BS-clusters with three scatterers each, a U-cluster ($k = 1$) with six scatterers, and the user VR set given by $\mathcal{V}_1 = \{2, 4\}$. Therefore, the set representing

the scatterer visibility is written as $\mathcal{C}_1 = \{4, 5, 6, 10, 11, 12\}$, and the visibility matrix is

$$\mathbf{D}_1 = \begin{bmatrix} 0 & 0 & 0 & 0 & 0 & 0 \\ 0 & 0 & 0 & 0 & 0 & 0 \\ 0 & 0 & 0 & 0 & 0 & 0 \\ 1 & 1 & 1 & 1 & 1 & 1 \\ 1 & 1 & 1 & 1 & 1 & 1 \\ 1 & 1 & 1 & 1 & 1 & 1 \\ 0 & 0 & 0 & 0 & 0 & 0 \\ 0 & 0 & 0 & 0 & 0 & 0 \\ 0 & 0 & 0 & 0 & 0 & 0 \\ 1 & 1 & 1 & 1 & 1 & 1 \\ 1 & 1 & 1 & 1 & 1 & 1 \\ 1 & 1 & 1 & 1 & 1 & 1 \end{bmatrix}.$$

Note that this matrix shows which scatterers contribute to the received signal at the user, considering the obstacles and reflectors in the environment (AMIRI et al., 2021). It highlights that in a complex ultra-dense urban environment, only a subset of scatterers might be relevant for signal reception.

2.2.2 DS XL-MIMO correlated channel model with UPA

Consider a planar antenna array in the y-z-plane with $M = M_z \times M_y$ antennas, where M_z represents the horizontal rows, each with M_y antennas. In this case, the antennas are uniformly spaced with vertical and horizontal spacing d_z and d_y (given in multiples of the wavelength), respectively, as shown in Fig. 2.2. Moreover, the antennas are indexed row-by-row so that $\mathbf{u}_m \in R^3$ is the location of the m-th antenna $(m = 1, ..., M)$on the x, y, and z axis for the planar arrangement, which can be described as:

$$\mathbf{u}_m = \begin{bmatrix} 0 \\ p_y(m) \\ p_z(m) \end{bmatrix}, \tag{2.10}$$

where $p_y(m) =$ mod $(m-1, M_h)d_h$ and $p_z(m) = \lfloor (m-1)/M_h \rfloor d_v$ are the horizontal and vertical position of antenna m, respectively.

In this context, we can model the channel between the k-th user and the BS similarly to eq. (2.3) rewriting some terms to adapt the formulation to the new geometry of the scenario considered. So we need to reformulate the matrices presented in eq. (2.4), which denotes the sub-channel between the i-th BS-cluster and the U-cluster.

Cluster VR ($\boldsymbol{\Upsilon}_i$): Similarly to the ULA case, the matrix $\boldsymbol{\Upsilon}_i \in \{0, 1\}^{M \times r_i}$ denotes the set of BS antennas that are visible to a given BS-cluster, by introducing the VR cluster concept in this channel model. The set containing the indexes of the antennas that are

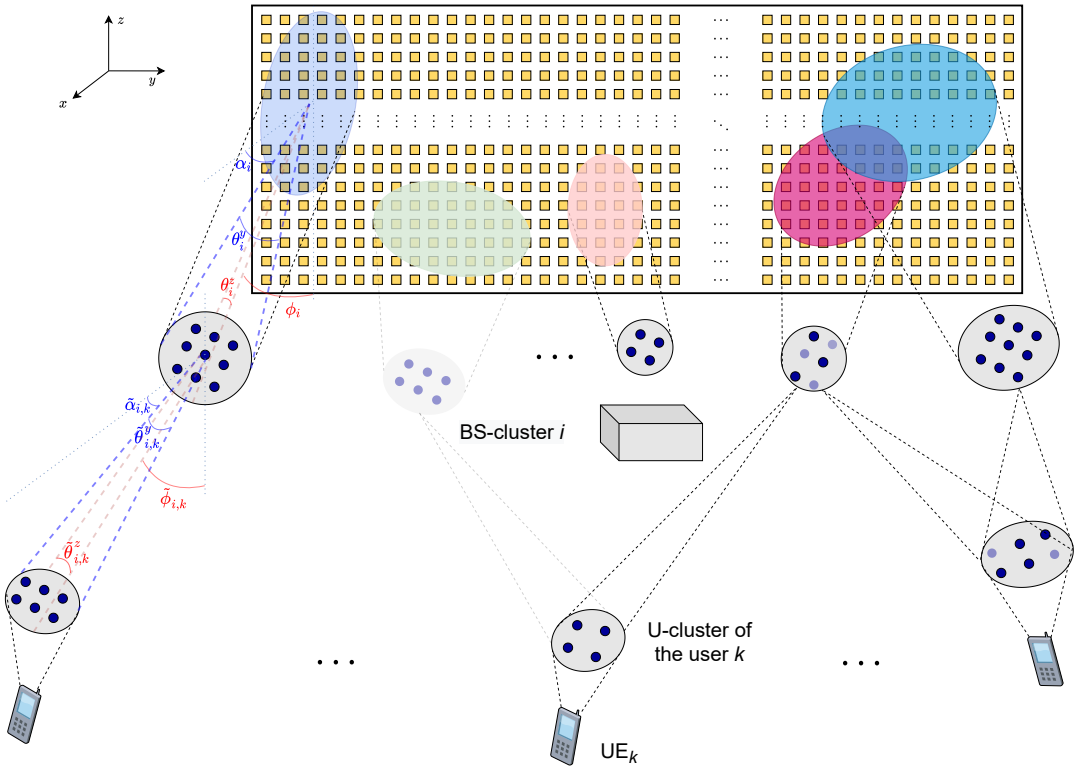

Figure 2.2 – XL-MIMO configuration highlights the spatial non-stationary regions along with the UPA, and the DS entities, where for each UE-BS link, one cluster appears near each UE and the other rises near the BS. Shading elements (scatterers and clusters) represent the death in the Poisson process.

visible to each BS-cluster is denoted by $\mathcal{R}_i = \{a_1^i, \cdots, a_{r_i}^i\}$, where a_n^i is the index of the nth antenna element inside the i-th BS-cluster VR. However, as antennas are now indexed row-by-row, the cluster VR for the planar array is written as:

$$[\boldsymbol{\Upsilon}_i]_{(a_n^i,n)} = \begin{cases} 1, & \forall \quad n \in \{1,\ldots,r_i\} \\ 0 & \text{otherwise} \end{cases} . \tag{2.11}$$

Power distribution ($\boldsymbol{\rho}_i$): The power distribution for the UPA scenario differs from the ULA case due to the geometry of the problem since now we have to consider both y and z coordinates. From this, the power distribution matrix for the i-th cluster VR can also be represented by $\boldsymbol{\rho}_i = \text{diag}(\rho_i[1],\ldots,\rho_i[r_i]) \in \mathbb{C}^{r_i \times r_i}$, and the power received by the n-th antenna inside the VR is obtained as follows:

$$\rho_i[n] = 10^{-\psi_i \sqrt{\left[p_y(a_{c_i}^i) - p_y(a_n^i)\right]^2 + \left[p_z(a_{c_i}^i) - p_z(a_n^i)\right]^2}}, \tag{2.12}$$

$\forall\, n \in \{1,\ldots,r_i\}$, where ψ_i is the attenuation factor (dB/m) for the i-th BS-cluster, p_y and p_z are the coordinates in the y and z axes, respectively, as represented in eq. (2.10).

Correlation between UPA and i-th BS-cluster ($\mathbf{R}_i$): This correlation matrix can be obtained by the Kronecker product between two ULA correlation matrices (GUERRA et

al., 2018). From the UPA antenna configuration, having M_z antenna elements along the Z coordinate and M_y along the Y coordinate results in an with $M = M_z \times M_y$ antennas. Hence, considering that the correlation between the elements along the Z coordinate given by matrix $\mathbf{R}_i^z$ does not depend on Y and, similarly, the correlation along the Y coordinate ($\mathbf{R}_i^y$) does not depend on Z, the Kronecker model approximation for the UPA correlation matrix can be written as:

$$\mathbf{R}_i = \mathbf{R}_i^y \otimes \mathbf{R}_i^z, \tag{2.13}$$

where $\otimes$ is the Kronecker product.

Notice that $\mathbf{R}_i^{\mathrm{y}}$ and $\mathbf{R}_i^{\mathrm{z}}$ refer to a subset of the BS antenna array (concerning the Y and Z coordinates, respectively), forming ULA visible region arrangements in both directions. In this case, one can consider the number of scatterers in each direction, independently, for the corresponding ULA arrangements, *i.e.*, S_i^{y} and S_i^{z} scatterers along Y and Z coordinates, respectively, for the i-th BS-cluster. In other words, these matrices can be calculated similarly to in eq. (2.7), resulting in:

$$[\mathbf{R}_i^{\mathrm{y}}]_{(m,n)} = \frac{1}{S_i^{\mathrm{y}}} \sum_{\ell=\frac{1-S_i^{\mathrm{y}}}{2}}^{\frac{S_i^{\mathrm{y}}-1}{2}} e^{-2\pi j d_y (m-n) \sin\left(\alpha_i + \frac{\ell\theta_i^{\mathrm{y}}}{S_i^{\mathrm{y}}-1}\right)}, \tag{2.14}$$

where α_i represents the azimuth angle, while θ_i^{y} is the angular spread along Y coordinate between the BS and the i-th BS-cluster.

$$[\mathbf{R}_i^{\mathrm{z}}]_{(m,n)} = \frac{1}{S_i^{\mathrm{z}}} \sum_{\ell=\frac{1-S_i^{\mathrm{z}}}{2}}^{\frac{S_i^{\mathrm{z}}-1}{2}} e^{-2\pi j d_z (m-n) \sin\left(\phi_i + \frac{\ell\theta_i^{\mathrm{z}}}{S_i^{\mathrm{z}}-1}\right)}, \tag{2.15}$$

where ϕ_i is the elevation angle and θ_i^{z} denotes the angular spread in the Z coordinate between the BS and the i-th BS-cluster.

Correlation between the i-th BS-cluster and the U-cluster for the k-th user ($\tilde{\mathbf{R}}_{i,k}$): In order to model this correlation matrix, the same principle as the ULA scenario was adopted, for simplicity. Considering that each U-cluster has S_k scatterers can be seen as a virtual antenna array, but now with a UPA arrangement of S_k antenna elements. Therefore, the (m,n)-th element of the correlation matrix between the i-th BS-cluster and the k-th U-cluster can be obtained as:

$$\tilde{\mathbf{R}}_{i,k} = \tilde{\mathbf{R}}_{i,k}^{\mathrm{y}} \otimes \tilde{\mathbf{R}}_{i,k}^{\mathrm{z}}, \tag{2.16}$$

where $\tilde{\mathbf{R}}_{i,k}^{\mathrm{y}}$ and $\tilde{\mathbf{R}}_{i,k}^{\mathrm{z}}$ are the correlation matrices corresponding to the virtual ULA arrangements considered separately, *i.e.*, w.r.t. the Y and Z coordinates, respectively. Now, these correlation matrices can be evaluated as follows:

$$[\tilde{\mathbf{R}}_{i,k}^{\mathrm{y}}]_{(m,n)} = \frac{1}{S_i^{\mathrm{y}}} \sum_{\ell=\frac{1-S_i^{\mathrm{y}}}{2}}^{\frac{S_i^{\mathrm{y}}-1}{2}} e^{-2\pi j d_s (m-n) \sin\left(\tilde{\alpha}_{i,k} + \frac{\ell\tilde{\theta}_{i,k}^{\mathrm{y}}}{S_i^{\mathrm{y}}-1}\right)}, \tag{2.17}$$

in which $\tilde{\alpha}_{i,k}$ represents the azimuth angle, while $\tilde{\theta}^{\mathrm{y}}_{i,k}$ is the angular spread between the i-th BS-cluster and the k-th U-cluster in Y coordinate, and

$$[\tilde{\mathbf{R}}^{\mathrm{z}}_{i,k}]_{(m,n)} = \frac{1}{S^{\mathrm{z}}_i} \sum_{\ell=\frac{1-S^{\mathrm{z}}_i}{2}}^{\frac{S^{\mathrm{z}}_i-1}{2}} e^{-2\pi j d_s (m-n)\sin\left(\tilde{\phi}_{i,k}+\frac{\ell\tilde{\theta}^{\mathrm{z}}_{i,k}}{S^{\mathrm{z}}_i-1}\right)}, \tag{2.18}$$

where $\tilde{\phi}_{i,k}$ is the elevation angle between the i-th BS-cluster and the U-cluster of user k and $\tilde{\theta}^{\mathrm{z}}_{i,k}$ denotes the angular spread between them in the Z coordinate.

2.2.3 SS XL-MIMO correlated channel model with ULA

In the SS correlated channel model, there is only one type of linear scatterer cluster between the BS and the UE, as depicted in Fig. 2.3.

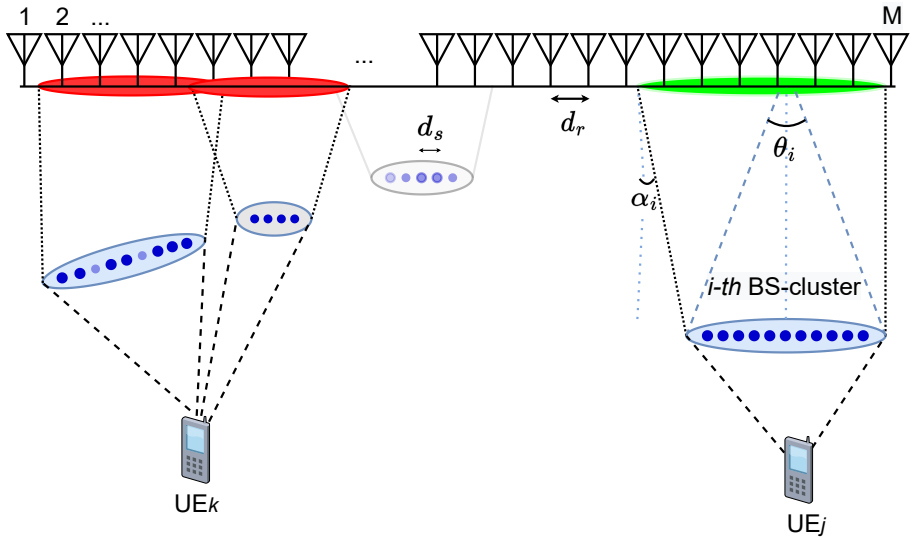

Figure 2.3 – XL-MIMO array with spatial non-stationary regions along the ULA with SS channel modeling.

Unlike the DS model, the SS model includes only a single cluster between the BS and the UE. Consequently, the C clusters receive the signal from the UE, and each cluster creates a VR at the BS. In the SS model, the cluster is composed of S_i linear scatterers, with the formulation between the k-th UE and the i-th cluster given by:

$$\mathbf{h}_{i,k} = \boldsymbol{\Upsilon}_i \boldsymbol{\rho}_i^{\frac{1}{2}} \mathbf{R}_i^{\frac{1}{2}} \bar{\mathbf{g}}_k \tag{2.19}$$

where $\bar{\mathbf{g}}_k \in \mathbb{C}^{r_i \times 1}$ is the small-scale fading, while $\boldsymbol{\Upsilon}_i$, $\boldsymbol{\rho}_i$, and $\mathbf{R}_i$ are calculated in the same way as in eq. (2.7).

Thus, the k-th UE channel can be described combining all C clusters for the UE k, such that (TANIGUCHI et al., 2021):

$$\mathbf{h}_k = \sum_{i \in \mathcal{C}_k} \tilde{\mathbf{h}}_{i,k}, \tag{2.20}$$

where $\mathcal{C}_k$ denotes the subset of active clusters visible to each UE k.

In summary, the choice between a DS or an SS channel model depends on the specific characteristics of the MIMO system and the propagation environment. For XL-MIMO scenarios with rich scattering and spatial variability, the DS model is preferred due to its detailed and accurate representation of the channel (AMIRI et al., 2021). However, in simpler environments or for less dense scenarios, the SS model can be a practical and less complex alternative.

2.2.4 Birth-death processes of clusters and scatterers

Since both UEs and clusters are moving, the appearance and disappearance of clusters and scatterers on the array axis must be included in the channel model. This work considers a birth-death approach from a spatial evolution model to insert this dynamic property of clusters and scatterers. Let us consider only one cluster for each user and C clusters with S_i scatterers, $i = 1, 2, \ldots, C$, for the i-th BS-cluster, initially. Therefore, intending to implement the birth and death process, we propose to adopt two different strategies: *a*) PPP to model the birth and death of the scatterers for the kth U-cluster, and *b*) PCP on the BS side when new clusters with S_i scatterers are generated following the clustered Poisson process.

Scatterers Birth-Death at the UE side: The scatterers can be modeled and assumed to be PPP distributed in the XL-MIMO channel (WU et al., 2018). According to the birth and death Markovian process, the appearance and disappearance of scatterers are exponentially distributed. The *survival probability of the scatterers* between different U-clusters can be expressed as:

$$\Pr_{\text{srv}}^{\text{scat}} = e^{-\frac{\lambda_r d_s}{D}}, \tag{2.21}$$

where λ_r is the recombination rate of the scatterers, D is the coherence factor related to the environment, and d_s represents the spacing between the adjacent scatterers.
Then the *average number of newly generated scatterers* can be expressed as (CHEN et al., 2017):

$$\mu = \frac{\lambda_g}{\lambda_r}\left(1 - e^{-\frac{\lambda_r d_s}{D}}\right), \tag{2.22}$$

where λ_g represents the *rate of regeneration of scatterers*. A pseudo-code for scatterers' birth and death process generation is depicted in Algorithm 1.

Algorithm 1 Birth and Death Process of Scatterers

Input: $\lambda_r, \lambda_g, d_s, D, \mathcal{S}_k$
for $\ell = 1 : S_k$ **do**
  Determine if the scatterer survived
  if $\mathcal{S}_k\{\ell\}$ survived **then**
    $\mathcal{S}_k\{\ell\} = 1$
  else
    $\mathcal{S}_k\{\ell\} = 0$
  end if
  New scatterers are generated according to the Poisson process
  Update the number of scatterers ($\mathcal{S}_k$)
  Update the set of scatterers for k-th UE ($\mathcal{S}_k$)
end for
Output: $\mathcal{S}_k$

Clusters Birth-Death at the BS side: Similarly, the clusters at the BS side can be modeled assumed to be PCP distributed. The *survival probability of the clusters* can be expressed as:

$$\mathrm{Pr}_{\mathrm{srv}}^{\mathrm{clus}} = e^{-\frac{\lambda_r^{\mathrm{c}} d_r}{D_c}}, \tag{2.23}$$

where λ_r^{c} is the recombination rate of the clusters, D_c is the coherence factor related to the environment on the array axis, and d_r represents the spacing between different antenna elements.

Therefore, the average number of newly generated clusters can be expressed as (CHEN et al., 2017):

$$\mu^{\mathrm{c}} = \frac{\lambda_g^{\mathrm{c}}}{\lambda_r^{\mathrm{c}}} \left(1 - e^{-\frac{\lambda_r^{\mathrm{c}} d_r}{D_c}}\right), \tag{2.24}$$

where λ_g^{c} represents the rate of regeneration of clusters.

The pseudo-code for clusters' birth and death generation is similar to that described in Algorithm 1, simply substituting the entity "scatterer" by "cluster" and setting suitable parameter values for the recombination and regeneration rates, coherence factor, and spacing between antennas.

We summarize the whole procedure for generating the proposed XL-MIMO channel model in Algorithm 2. Lines 4 and 6 generate the birth and death process of clusters and scatterers, respectively. After this, the VR size related to each cluster is determined in line 8. The correlation matrices are obtained as presented above according to the antenna adopted arrangement (ULA or UPA).

Algorithm 2 Generation of XL-MIMO channel with birth and death process

Input: $M,\ K,\ d_r,\ d_s$
Define $\mathbf{H} = \mathbf{0}_{M\times K}$
for $k = 1 : K$ **do**
  Update C (similar procedure to Algorithm 1)
  for $i = 1 : C$ **do**
    Update S_i (Algorithm 1)
    Define $\tilde{\mathbf{H}}_{i,k} = \mathbf{0}_{M\times S_i\times C}$
    Obtain $\mathcal{R}_i$
    Compute $\boldsymbol{\Upsilon}_i$ in eq. (2.5) for ULA or (2.11) for UPA
    Compute $\boldsymbol{\rho}_i$ in eq. (2.6) for ULA or (2.12) for UPA
    Obtain azimuth and elevation angles
    Compute the correlation matrices
    Obtain $\mathbf{G}_i$
    Update $\tilde{\mathbf{H}}_{i,k}$ in (2.4)
  end for
  Compute visibility matrix $\mathbf{D}_k$ in (2.9)
  Obtain $\mathbf{g}_k$
  Update $\mathbf{H}(:,k)$ in (2.3)
end for
Output: H

2.3 Figures of Merit: SINR, SE, CN, and Favorable Propagation

2.3.1 Spectral efficiency (SE): linear combiners

Rewriting the expression in (2.1) as:

$$\mathbf{y} = \sum_{k=1}^{K} \mathbf{h}_k x_k + \mathbf{n}, \tag{2.25}$$

and adopting linear receiver schemes at the BS, denoted by matrix $\mathbf{V} \in \mathbb{C}^{M\times K}$, the received signal is separated into K streams by multiplying $\mathbf{y}$ with the linear combining matrix:

$$\tilde{\mathbf{y}} = \mathbf{V}^H\mathbf{y} = \mathbf{V}^H\mathbf{H}\mathbf{x} + \mathbf{V}^H\mathbf{n}. \tag{2.26}$$

Therefore, from (2.26), the received signal for the k-th user is given by:

$$\tilde{\mathbf{y}} = \mathbf{v}_k^H\mathbf{y} = \underbrace{\mathbf{v}_k^H\mathbf{h}_k x_k}_{\text{desired signal}} + \underbrace{\sum_{j=1,j\neq k}^{K} \mathbf{v}_k^H\mathbf{h}_j x_j}_{\text{inter-user interference}} + \underbrace{\mathbf{v}_k^H\mathbf{n}}_{\text{noise}}, \tag{2.27}$$

where $\mathbf{v}_k$ is the k-th column of $\mathbf{V}$.

The SINR can be defined by:

$$\gamma_k = \frac{|\mathbf{v}_k^H\mathbf{h}_k|^2}{\sum_{j\neq k}|\mathbf{v}_k^H\mathbf{h}_j|^2 + \sigma_n^2\|\mathbf{v}_k\|^2}. \tag{2.28}$$

Hence, the *overall SE* is defined according to:

$$SE = \left(1 - \frac{\tau}{T_{\mathrm{C}}}\right) \cdot \sum_{k=1}^{K} \log_2(1+\gamma_k) \quad \left[\frac{\text{bits}}{\text{s} \cdot \text{Hz}}\right], \tag{2.29}$$

where T_{C} is the channel coherence time, and τ is the period dedicated to training and channel estimation (CE) tasks.

In the sequel, we revisit some classical linear receivers deployed for the XL-MIMO channel analysis.

Maximum-Ratio Combining (MRC). This receiver neglects the effect of multi-user interference (MuI), aiming to maximize the received signal-to-noise ratio (SNR) of each user at the BS (BJöRNSON et al., 2017). Following this policy, the MRC receiver is obtained by assigning $\mathbf{v}_k^{\mathrm{MRC}} = \mathbf{h}_k$ in eq. (2.28), while the attained SINR for the k-th user is:

$$\gamma_k^{\mathrm{MRC}} = \frac{\|\mathbf{h}_k\|^4}{\sum_{j\neq k} |\mathbf{h}_k^H \mathbf{h}_j|^2 + \sigma_n^2 \|\mathbf{h}_k\|^2}. \tag{2.30}$$

Notice that the signal processing is straightforward; however, as previously commented, this receiver performs poorly in the channel scenarios limited by interference since MRC does not consider the effect of MuI.

Zero-Forcing (ZF) Combiner. Unlike MRC, zero-forcing receivers take into account inter-user interference but do not consider the effect of noise. The ZF combiner can eliminate MuI interference by projecting each user vector onto the orthogonal complement of the inter-user interference but assuming perfect CSI knowledge. The ZF combiner matrix is given by:

$$\mathbf{V}^{\mathrm{ZF}} = \mathbf{H}(\mathbf{H}^H\mathbf{H})^{-1}, \tag{2.31}$$

and the received SINR for the k-th user deploying ZF combiner at BS is defined as (NGO et al., 2013):

$$\gamma_k^{\mathrm{ZF}} = \frac{1}{\sigma_n^2 \left[(\mathbf{H}^H\mathbf{H})^{-1}\right]_{kk}}, \tag{2.32}$$

where $[\cdot]_{kk}$ is the element of the k-th row and k-th column of the matrix.

Minimum Mean-Squared Error (MMSE) Receiver. The linear minimum mean-square error (MMSE) receiver aims to minimize the mean-square error between the estimate $\mathbf{v}_k^H\mathbf{y}$ and the transmitted signal $\mathbf{x}$. Therefore, the MMSE combiner matrix is:

$$\mathbf{V}^{\mathrm{MMSE}} = (\mathbf{H}\mathbf{H}^H + \sigma_n^2\mathbf{I}_M)^{-1}\mathbf{H}. \tag{2.33}$$

Therefore, the received SINR of the k-th user for the MMSE combiner results:

$$\gamma_k^{\mathrm{MMSE}} = \mathbf{h}_k^H \left(\sum_{i\neq k}^{K} \mathbf{h}_i\mathbf{h}_i^H + \sigma_n^2\mathbf{I}_M\right)^{-1} \mathbf{h}_k. \tag{2.34}$$

2.3.2 Condition number (CN)

The *condition number* (CN) of the channel matrix $\mathbf{H}$ is given by:

$$\kappa(\mathbf{H}) = \frac{\sigma_{\max}(\mathbf{H})}{\sigma_{\min}(\mathbf{H})} = \frac{|\lambda_{\max}(\mathbf{H})|}{|\lambda_{\min}(\mathbf{H})|}, \tag{2.35}$$

where $\sigma_{\max}(\mathbf{H})$ and $\sigma_{\min}(\mathbf{H})$ are maximal and minimal singular values of $\mathbf{H}$ respectively. If $\mathbf{H}$ is normal[1], then the second equally holds, where $\lambda_{\max}(\mathbf{H})$ and $\lambda_{\min}(\mathbf{H})$ are maximal and minimal eigenvalues of $\mathbf{H}$ respectively.

In XL-MIMO, the CN is obtained considering the channel matrix formed by the VRs. The cluster visibility regions for the channel link are established by evaluating the received signal at each antenna of the array. Only the subset of antennas that receive significant energy is selected to compose the cluster VR. For simplicity in our analysis, we have assumed that all antennas receiving any level of energy (> 0) are included in the VR.

2.3.3 Favorable propagation

Favorable propagation is an M-MIMO channel characteristic that can be deployed to determine the level of interference the UEs cause to each other in the massive antenna configuration. Hence, one can define a metric to evaluate how near to the orthogonal the channels are. In addition, we also have the VR concept for the XL-MIMO system, in which only a part of the array receives the signal transmitted by the users. In fact, the MuI for XL-MIMO tends to be less aggressive than the M-MIMO case since the VR overlap among users does not necessarily occur in all VR antennas.

To analyze the interference caused by UEs to each other when considering the DS channel model, the inner product of the normalized channels $\mathbf{h}_k$ and $\mathbf{h}_j$ is given by:

$$\frac{\mathbf{h}_k^H \mathbf{h}_j}{\sqrt{\mathbb{E}\{||\mathbf{h}_k||^2\}\mathbb{E}\{||\mathbf{h}_j||^2\}}}, \tag{2.36}$$

that can be evaluated by simulation or experimentally. The inter-user interference can be obtained by using the correlation matrix of each user. For the DS correlated channel model, the correlation matrix for the k-th user ($\mathbf{\Phi}_k$) can be calculated as (NADEEM et al., 2019):

$$\mathbf{\Phi}_k = \mathrm{Tr}(\tilde{\mathbf{R}}_{i,k})\mathbf{R}_i. \tag{2.37}$$

Therefore, the variance of the normalized *favorable propagation* in (2.36) can be determined as (BJöRNSON et al., 2017):

$$\mathbb{V}\mathrm{ar}\left\{\frac{\mathbf{h}_k^H \mathbf{h}_j}{\sqrt{\mathbb{E}\{||\mathbf{h}_k||^2\}\mathbb{E}\{||\mathbf{h}_j||^2\}}}\right\} = \frac{\mathrm{Tr}(\mathbf{\Phi}_k\mathbf{\Phi}_j)}{\mathrm{Tr}(\mathbf{\Phi}_k)\,\mathrm{Tr}(\mathbf{\Phi}_j)}, \tag{2.38}$$

[1] A complex square matrix $\mathbf{A}$ is normal if it commutes with its conjugate transpose: $\mathbf{A}^*\mathbf{A} = \mathbf{A}\mathbf{A}^*$

which expresses the variability of the k-th and j-th user channel realization regarding the perfect favorable propagation condition in eq. (2.36) (orthogonality), *i.e,* $\mathbf{h}_k^H \mathbf{h}_j = 0$ when $M \to \infty$.

This metric can determine how close the spatial correlation matrices are between the user k and j; ideally, the variance in eq. (2.38) should be close to zero, which implies that the channels are practically orthogonal. Thus the inter-user interference is negligible.

2.4 Numerical Results

In this section, we evaluate and validate the proposed XL-MIMO channel models considering a) the effects of the number of visible clusters on the post-combining SINR; b) favorable propagation effect and VR overlap; c) The attainable SE in XL-MIMO system equipped with ULA and UPA received antennas, and d) the effect of birth and death PPP and PCP over the XL-MIMO performance.

2.4.1 Impact of the number of visible clusters on the SINR

This analysis evaluates the average, minimum, and maximum SINR for the XL-MIMO channel by increasing the number of users (K) under three linear receiver schemes (MRC, ZF, and MMSE) at the BS equipped with massive ULA antennas. The number of visible BS-clusters (n_b) for the k-th user is changed to measure how this parameter affects the SINR for different combiners. Table 2.1 shows the simulation parameters considered in this scenario. Moreover, the numerical results are obtained via Monte-Carlo simulation (MCS) with 5000 realizations for each number of users.

Table 2.1 – Simulation parameters used to evaluate the impact of the number of visible clusters on the SINR.

Parameter	**Value**	**Parameter**	**Value**
M	256	K	[4; 16; 32; 64; 128; 256]
d_r	0.5λ	d_s	5λ
S_i	31	S_k	5
C	20	ψ_i	$\mathcal{LN}(\mu = 0.7, \sigma = 0.8)$ [dB/m]
θ_i	$7\pi/8$	$\tilde{\theta}_{i,k}$	$3\pi/4$
SNR	30 dB	$\alpha_i, \tilde{\alpha}_{i,k}$	$\mathcal{U}(-\pi/2, \pi/2)$
$\mathbb{E}[\mathbf{x}^2]$	1	n_b	[4; 8; 16]
f_c	2.6 GHz	Combiners	[MRC; ZF; MMSE]

Although the number of visible clusters varies, *i.e.*, $n_b \in \{4, 8, 16\}$, the total power received was fixed. Therefore, this means that the user's VR is more spread out across the array but with less power reaching each antenna element of the VR. As a result, as users' VR is higher in this case, the trend is for MuI to grow as well. Fig. 2.4 shows the numerical results obtained. As the MRC receiver does not consider MuI, seeking to maximize only

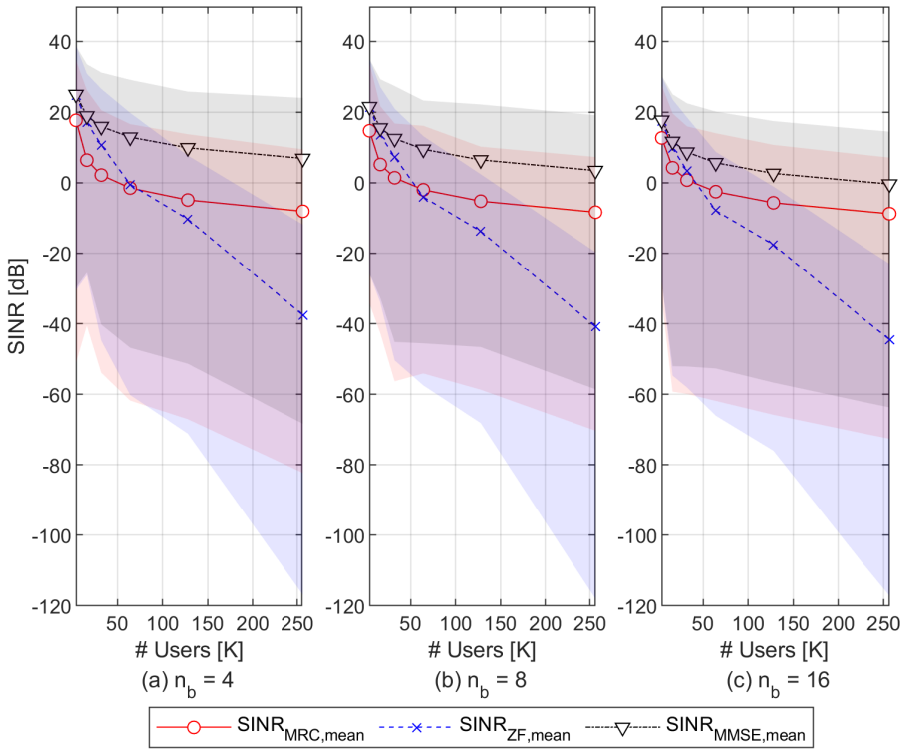

Figure 2.4 – Minimum, maximum, and average SINR for the XL-MIMO system with $M = 256$ ULA antennas and MRC, ZF, and MMSE receivers. Number of visible clusters per user: a) $n_b = 4$; b) $n_b = 8$; c) $n_b = 16$.

the SNR of the received signal, the SINR (minimum, maximum, and average) remains practically the same in the three scenarios analyzed. As for the ZF and MMSE combiners, there is a slight decrease in the SINR as the number of visible clusters increases, which indicates that the MuI also increases, but this increase is not very significant. Then, the SE remains almost the same.

2.4.2 Favorable propagation and VR overlap

In this section, the favorable propagation effect is obtained by evaluating eq. (2.38). For this analysis, three cases were considered in the numerical results: a) low VR overlap (20%); b) medium VR overlap (50%); c) high VR overlap (90%). For instance, considering $M_{\text{VR}} = 50$ antennas as the number of antennas in the VR for the users w.r.t. their respective clusters, a 20% of VR overlap means that only 10 antenna elements receive power from both users.

To determine the impact of the XL-MIMO channel and the effect of the spatial correlation matrices between the user k and j in the numerical simulations, we have adopted the parameter values of Table 2.2. In the analyzed scenario of Fig. 2.5, the azimuth angle of one of the users is fixed in $\pi/6$ [rad], while for the other interfering user, it is varied from $-\pi$ to π. Moreover, both users keep spreading angles constant, $\theta_i = 7\pi/8$ and $\tilde{\theta}_{i,k} = 3\pi/4$. In addition, the energy is exponentially attenuated from the

center to the frontier of the VR, dictated by the factor ψ_i with a log-normal distribution as $\psi_i \sim \mathcal{LN}(\mu = 0.7, \sigma = 0.8)$ [dB/m].

Table 2.2 – Simulation parameters for favorable propagation analysis and VR overlap in XL-MIMO with ULA arrangement.

Parameter	**Value**	**Parameter**	**Value**
M	256	K	2
d_r	0.5λ	d_s	5λ
S_i	31	S_k	5
C	2	ψ_i	$\mathcal{LN}(0.7; 0.8)$ [dB/m]
θ_i	$7\pi/8$	$\tilde{\theta}_{i,k}$	$3\pi/4$
α_1	$\pi/6$	α_2	$[-\pi : \pi/180 : \pi]$
$\tilde{\alpha}_{i,k}$	$\pi/6$	n_b	1
M_{VR}	50	VR overlap	[20%; 50%; 90%]

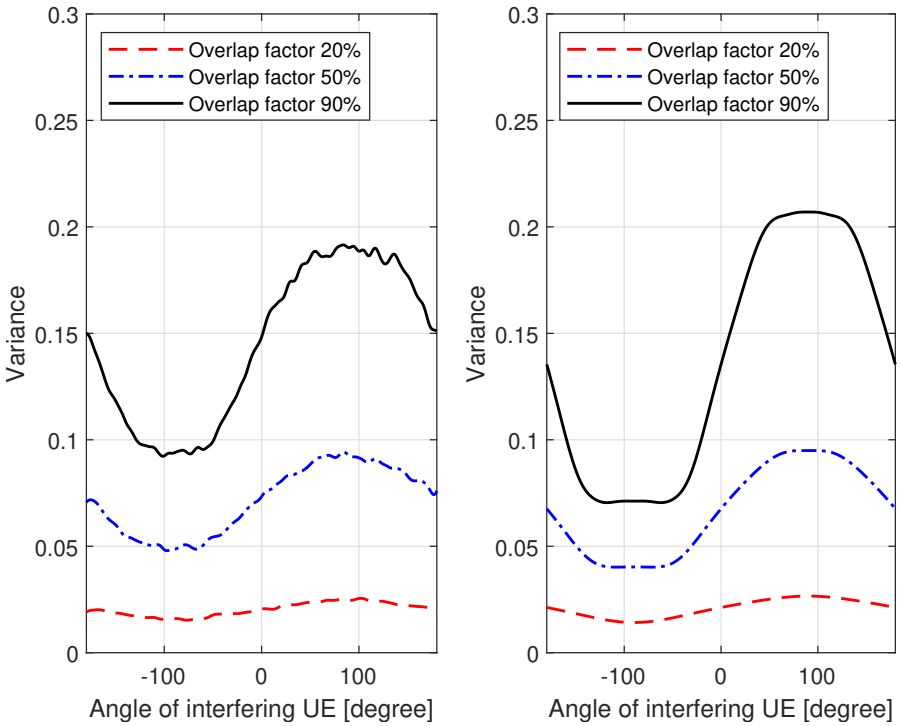

Figure 2.5 – Interference evaluation for the XL-MIMO system with ULA arrangement and different VR overlap factors: (a) MCS obtained from the left side of eq. (2.38) with $\mathcal{T} = 1000$ channel realizations; (b) Analytical expression provided by the right side of eq. (2.38).

From Fig. 2.5, the well-defined angles of interest related to the interfering UE can be identified. The interference (variance) generated by one user over the desired UE, given by eq. (2.38), is significantly larger when the interfering user is angularly located around the angle of the desired UE or closed to the mirror reflection angle $180° - 30° = 150°$. Furthermore, note that $\theta_i = 7\pi/8$ $(157,5°)$ and $\tilde{\theta}_{i,k} = 3\pi/4$ $(135°)$ introduce a high angular standard deviation (ASD) σ_φ. So, the most significant variance occurs when the

UEs have different angles across the range between the angle of the desired UE and the mirror reflection angle. In addition, the VR overlap factor also significantly influences the variance, as expected, since this parameter directly impacts inter-user interference.

2.4.3 SE of XL-MIMO system with ULA versus UPA arrangements

In this subsection, for simplicity, a purely static approach to describe the XL-MIMO channel was adopted, *i.e.*, assuming a fixed number of scatterers and clusters. The aim is to evaluate the overall SE as a function of the number of users. Furthermore, we are considering a fixed SNR $= \frac{P}{\sigma_n^2}$, where P is the expected transmitting power of the users. Simulation parameters for the adopted scenario are shown in Table 2.3. Moreover, for the SE analysis, the numerical results were obtained via MCS averaged over $\mathcal{T} = 10^4$ realizations.

Table 2.3 – Simulation parameters adopted in the SE Analysis for XL-MIMO System with ULA and UPA Arrangement.

Parameter	**Value**	**Parameter**	**Value**
M	256	K	[4; 16; 32; 64; 128; 256]
d_r	0.5λ	d_s	5λ
C	20	ψ_i	$\mathcal{LN}(0.7, 0.8)$ [dB/m]
SNR	30 dB	$\alpha_i, \tilde{\alpha}_{i,k}$	$\mathcal{U}(-\pi/2, \pi/2)$
$\mathbb{E}[\mathbf{x}^2]$	1	τ/T_c	0.2
f_c	2.6 GHz	Combiners	[MRC; ZF; MMSE]
		ULA	
S_i	31	S_k	5
θ_i	$7\pi/8$	$\tilde{\theta}_{i,k}$	$3\pi/4$
		UPA	
S_i^y, S_i^z	31	S_k	5
θ_i^{y}, θ_i^{z}	$7\pi/8$	$\tilde{\theta}_{i,k}^{\mathrm{y}}$, $\tilde{\theta}_{i,k}^{\mathrm{z}}$	$3\pi/4$
α_i, $\tilde{\alpha}_{i,k}$	$\mathcal{U}(-\pi/2, \pi/2)$	ϕ_i, $\tilde{\phi}_{i,k}$	$\mathcal{U}(-\pi/2, \pi/2)$

It is considered an XL-MIMO system with 256 antennas at the BS distributed in a ULA arrangement. Fig. 2.6 depicts results for the overall SE evaluated from eq. (2.29) by varying the number of users and deploying three different linear combiners: the MRC, ZF, and MMSE. The parameter $\frac{\tau}{T_c} = 0.2$ denotes that the CE task requires 20% of the channel coherence time.

From Fig. 2.6, one can observe that the MRC receiver presents a poor performance in terms of SE. This behavior is expected since MRC considers only the SNR, neglecting the multi-user interference, which grows significantly with increased users. Moreover, the ZF combiner performs better than MRC up to $K = 32$ users ($M/K = 8$). However, from that point on, the ZF can no longer separate the interference from the desired signal and

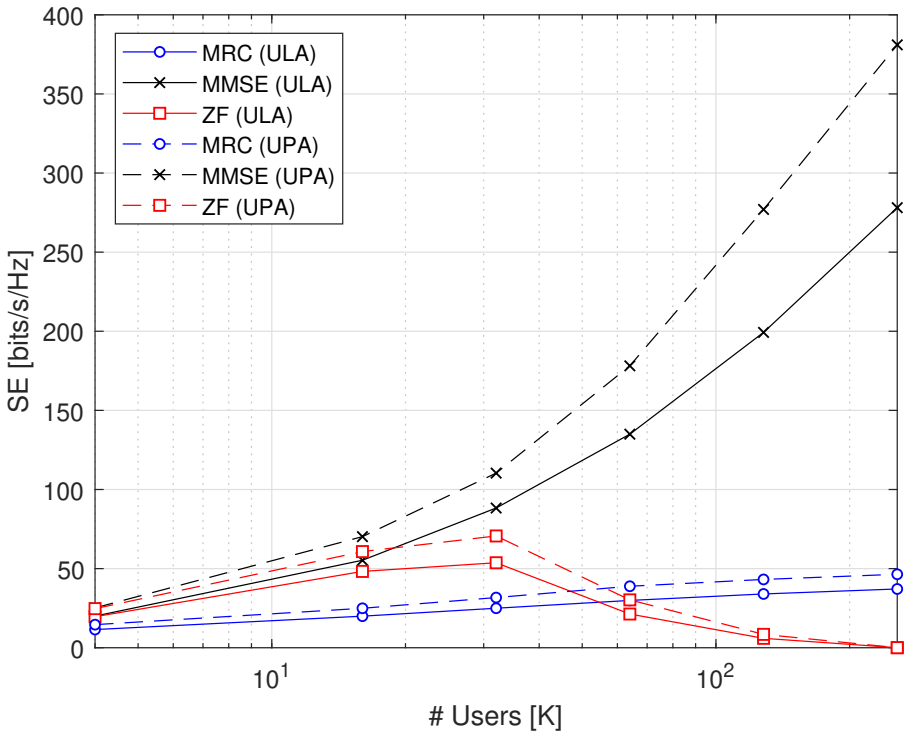

Figure 2.6 – SE for XL-MIMO system with UPA *vs.* ULA antenna arrangements.

then ends up suppressing the signal of interest when trying to eliminate MuI. As a result, the SE curve for the ZF combiner shows a trend reversal, decreasing until a value close to zero when the number of users reaches 128 or 256. Also, note that for $K = 64$ users, the MRC already exceeds the SE attained by the ZF since the performance degradation of the ZF occurs quickly with the number of users increasing. Unlike MRC and ZF, the MMSE combiner performs greatly, even with increased users, as expected. Observe that the MMSE receiver appears to have unlimited capacity w.r.t. the increase in the number of users, a feature previously observed in M-MIMO systems (BJÖRNSON et al., 2018).

The XL-MIMO system with UPA arrangement described in subsection 2.2.2, a more effective array arrangement than ULA, is also analyzed in this section. However, unlike the ULA model, we now also have the elevation angles (ϕ_i, $\tilde{\phi}_{i,k}$) in addition to azimuth angles (α_i, $\tilde{\alpha}_{i,k}$); the adopted range of values can be seen in Table 2.3. Beyond that, we have scatterers in both z and y coordinates in the i-th BS-cluster. Thus, the channel model with UPA antenna arrangement has an extra degree of freedom compared to the ULA model.

Considering Fig. 2.6, the performance curves in terms of SE for the three combiners analyzed operating under the UPA arrangement present a very similar behavior to that observed with the ULA. However, there are improvements in the SE performance of all combiners, with a gain of approximately 25 to 35%, compared with the ULA scenario; such SE improvement is more prominent with MMSE combiner under a higher user loading regime. Moreover, the MRC and ZF receivers performed worse compared to the MMSE in the scenario with a planar array arrangement; indeed, the ZF receiver encounters

issues similar to those seen previously. Again, the MMSE combiner presented the best performance, revealing an unlimited capacity trend concerning the number of users.

Fig. 2.7 depicts the channel matrix $\mathbf{H}$'s CN, as calculated by eq. (2.35), when the number of users increases, considering both linear and planar arrays. It is an interesting metric to explain the ZF receiver behavior since the CN measures how well-conditioned is the analyzed matrix, which implies that the matrix is invertible or not. As the ZF needs to calculate the pseudoinverse of the channel matrix, this matrix must present a low CN value. Therefore, its inverse can be computed with reasonable accuracy. On the other hand, if the CN is huge, the channel matrix is ill-conditioned. Additionally, three levels of channel correlation are considered for ULA and UPA arrangements: *i*) lowly correlated channel, *i.e.*, $\theta_i = 7\pi/8$, yielding $\mathbf{R}_i$ very close to the identity matrix; *ii*) moderately correlated channel with $\theta_i = \pi/3$, and *iii*) highly correlated channels under $\theta_i = \pi/8$. It is possible to notice that under moderately and highly correlated channel scenarios, the *CN* κ for both ULA and UPA arrangement is slightly higher than attainable under lowly correlated channels. However, there is not a very significant difference, so it can be concluded that the effect of spatial correlation does not represent an impacting parameter in the CN analysis of the XL-MIMO channel matrix $\mathbf{H}$. In this situation, the matrix is almost singular, and the computation of its inverse tends to present large numerical errors. Notice that in Fig. 2.7 for $K \geq 64$, the CN κ reveals significant values increasing compared to the moderated or reduced system loading values, *i.e.*, $\mathcal{L} = \frac{K}{M} \geq \frac{64}{256} \approx 0.25$. Comparing the ULA array and the UPA, it is noticed that it presents similar κ values for $\mathcal{L} \leq \frac{32}{256} = 0.125$. However, from then on, the ULA scenario's condition number grows much faster than UPA, tending to close values for many users or $\mathcal{L} \geq 1$. Thus, for $K > 32$, the channel matrix becomes poorly conditioned, and consequently, the performance with the ZF combiner is directly and heavily degraded.

Finally, in Fig. 2.8, a comparative analysis is conducted between the SS and DS models in terms of SE performance. It is observed that both the SS and DS channel models exhibit the same behavior for all combiners considered. However, it is noted that the SE achieved for linear receivers using the SS channel model is significantly higher compared to the DS XL-MIMO channel model. This is mainly because the DS channel model considers a much more aggressive (rich scattering) scenario, where the level of correlation is much more significant. For this reason, the SS channel model is not appropriate for ultra-urbanized and ultra-dense scenarios since it cannot capture some of this important channel characteristics.

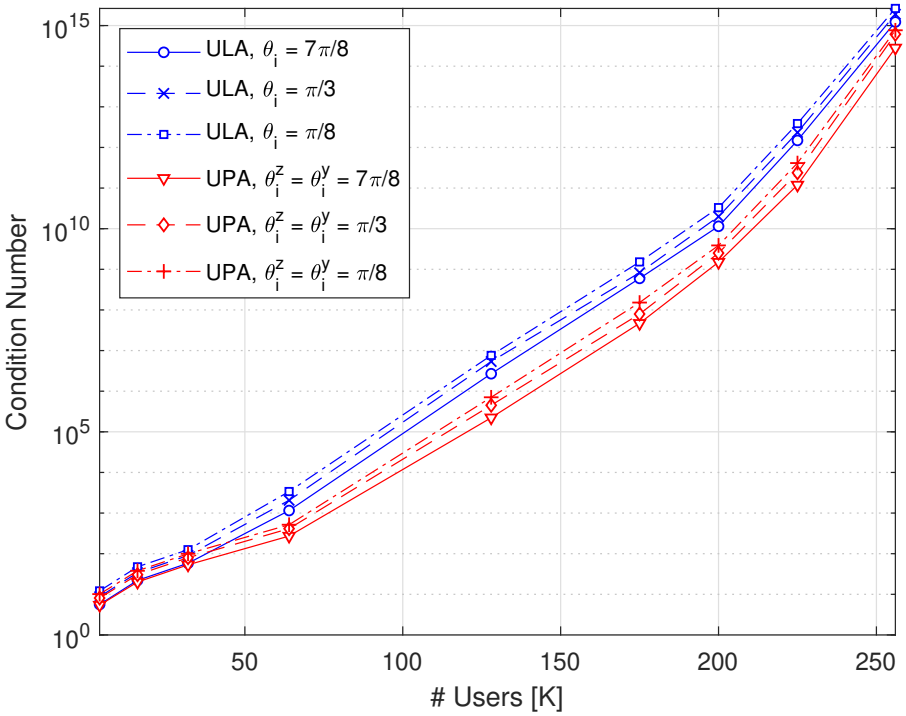

Figure 2.7 – Averaged CN of the $\mathbf{H}$ channel matrix with ULA and UPA arrangement over $\mathcal{T} = 1000$ channel realizations under low, moderate and high correlated channels.

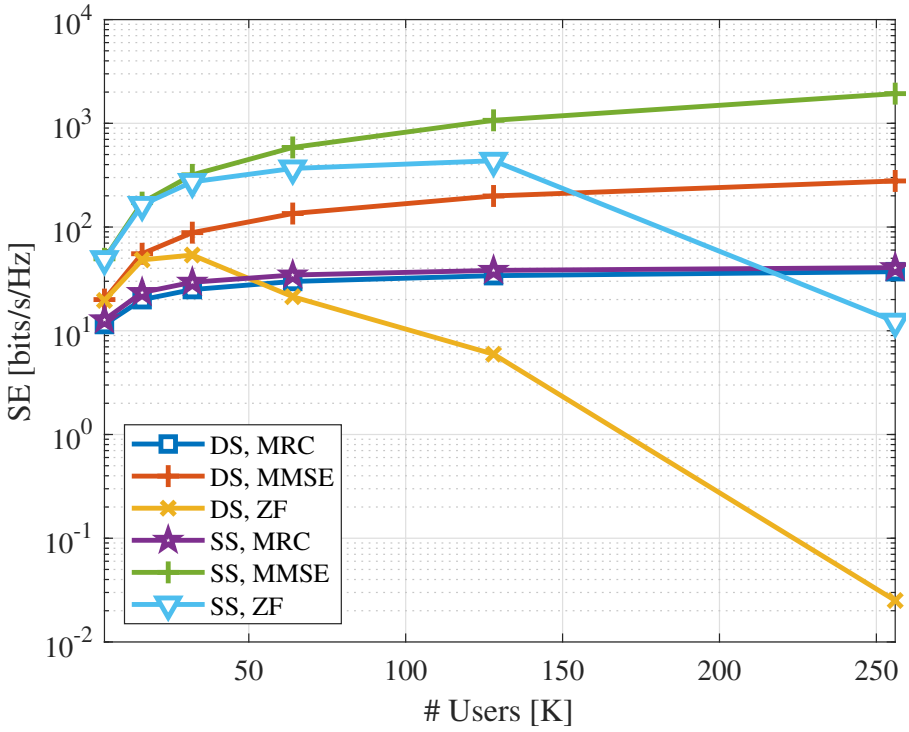

Figure 2.8 – SE for XL-MIMO system with ULA antenna arrangements and SS *vs.* DS models.

2.4.4 Birth and death PPP and PCP effect over the XL-MIMO channel

This subsection considers dynamic *vs.* quasi-static channel scenarios to analyze the effect of birth and death PPP and PCP modeling over the XL-MIMO performance. Table 2.4 summarizes the main parameter values considered in such analysis. Additionally, numerical results obtained via MCS were averaged over $\mathcal{T} = 10^4$ realizations for each number of users K, while ULA arrangement is adopted. Since the non-line-of-sight (NLoS) case is considered, the adopted parameter values follow the XL-MIMO channel measurements provided in (PAYAMI; TUFVESSON, 2012) and (GAO et al., 2012).

Table 2.4 – Simulation parameters used to evaluate the impact of birth and death PPP and PCP over the XL-MIMO SINR.

Parameter	**Value**	**Parameter**	**Value**
M	256	K	[4; 16; 32; 64; 128; 175; 200; 225; 256]
d_r	0.5λ	d_s	5λ
$S_{i,\text{ initial}}$	31	$S_{k,\text{ initial}}$	5
C_{initial}	20	ψ_i	$\mathcal{LN}(0.7,\ 0.8)$ [dB/m]
θ_i	$7\pi/8$	$\tilde{\theta}_{i,k}$	$3\pi/4$
SNR	30 dB	$\alpha_i, \tilde{\alpha}_{i,k}$	$\mathcal{U}(-\pi/2, \pi/2)$
f_c	2.6 GHz	Combiners	[MRC; ZF; MMSE]
Quasi-static scenario			
D	100 m	λ_R	2 m^{-1}
λ_G	20 m^{-1}	D_c	100 m
λ_R^{c}	8 m^{-1}	λ_G^{c}	80 m^{-1}
$\text{Pr}_{\text{srv}}^{\text{scat}}$	0.9885	$\text{Pr}_{\text{srv}}^{\text{clus}}$	0.9954
μ	0.1147	μ^{c}	0.0460
Dynamic scenario			
D	80 m	λ_R	4 m^{-1}
λ_G	20 m^{-1}	D_c	50 m
λ_R^{c}	16 m^{-1}	λ_G^{c}	200 m^{-1}
$\text{Pr}_{\text{srv}}^{\text{scat}}$	0.9716	$\text{Pr}_{\text{srv}}^{\text{clus}}$	0.9817
μ	0.1422	μ^{c}	0.2287

In order to evaluate the effects and features of the parameters that define the PPP and PCP processes on the average SINR of the system, two scenarios have been considered for comparison purposes: *i*) *quasi-static* scenario, *i.e.*, the birth and death process for scatterers and clusters occurs much more slowly than the second case; and *ii*) *dynamic* scenario, in which the birth and death process happens more quickly, with a higher average number of newly generated and disappeared scatterers and clusters as well. For scenario *i*), $D = D_c = 100$ m represents the scenario-dependent correlation factor for the scatterers and clusters. Moreover, $\lambda_R = 2\text{m}^{-1}$ and λ_R^{c} are set as 8m^{-1}, and the values of λ_G and λ_G^{c} are chosen as 20m^{-1} and 80m^{-1}, respectively. Using these values implies

that the *survival probabilities* are 0.9885 for the scatterers and 0.9954 for the clusters. However, the *average number of newly generated scatterers* is $\mu = 0.1147$. In contrast, for the clusters, such number $\mu^{c} = 0.0460$, which results in a slow variation of the number of scatterers and clusters dictated by birth and death Poisson processes, denoted herein as a *quasi-static* setting. On the other hand, scenario *ii*) considers a more aggressive setup in terms of birth and death since the *survival probabilities* are minor, *i.e.*, $\Pr_{\text{srv}}^{\text{scat}} = 0.9716$ and $\Pr_{\text{srv}}^{\text{clus}} = 0.9817$, but the average number of newly generated scatterers and clusters are also increased. Analyzing such channel modeling aims to characterize a real dynamic scenario with different levels of mobility of both the user and the surrounding objects.

Fig. 2.9 illustrates the birth and death Poisson process with 20 realizations, for simplicity, in both analyzed scenarios. The dots in Fig. 2.9 represent the active scatterers, while the circles are the clusters. Note that their disappearance demonstrates that they have been inactivated/dead. From that, it is possible to observe that the quasi-static scenario's birth and death rate is much lower than the dynamic scenario adopted in this work.

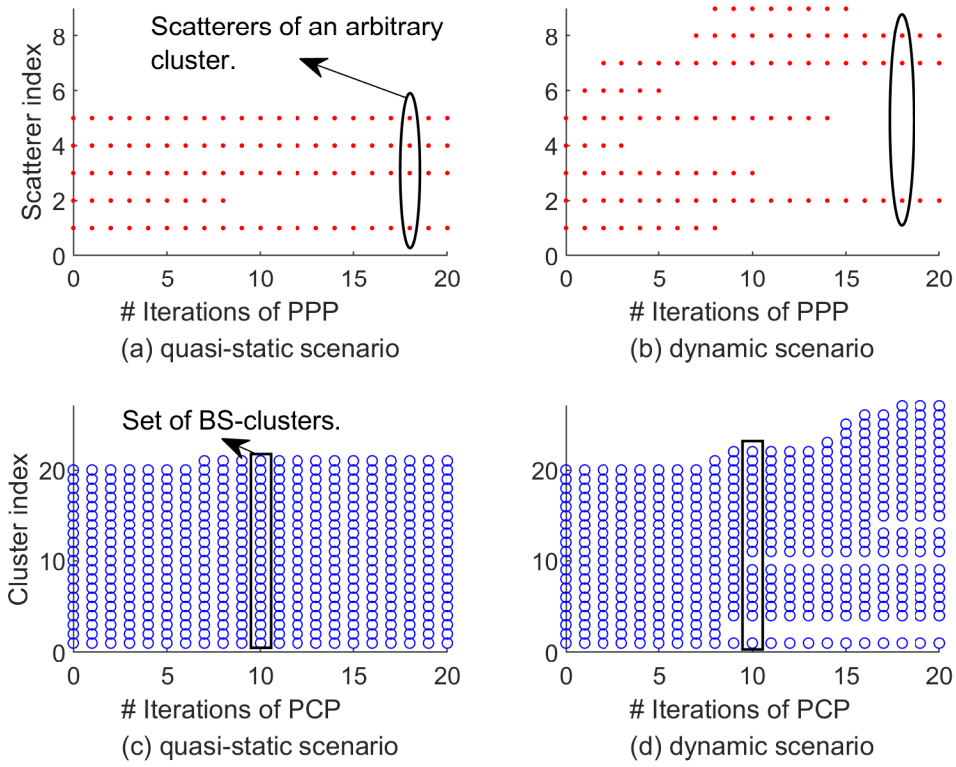

Figure 2.9 – Birth and death PPP and PCP over the XL-MIMO ULA arrangement. $\mathcal{T} = 20$ realizations.

Comparing the average SINR depicted in Fig. 2.4 with the *quasi-static* channel scenario shown in Fig. 2.10, one can notice that the three reception schemes present a similar performance obtained in the static scenario. However, under the *dynamic* birth and death process setup, there is an intrinsic degradation of the SINR. While the MRC and ZF receivers show a 1 to 2 dB decrease in SINR, the MMSE was even more affected, presenting

a 3 to 4 dB degradation in SINR. Notice the same performance pattern observed in the SE of Fig. 2.6 regarding ZF and MRC when $K \geq 64$ also occurs in Fig. 2.10 in terms of average SINR of the XL-MIMO system equipped with the ZF and MRC combiners.

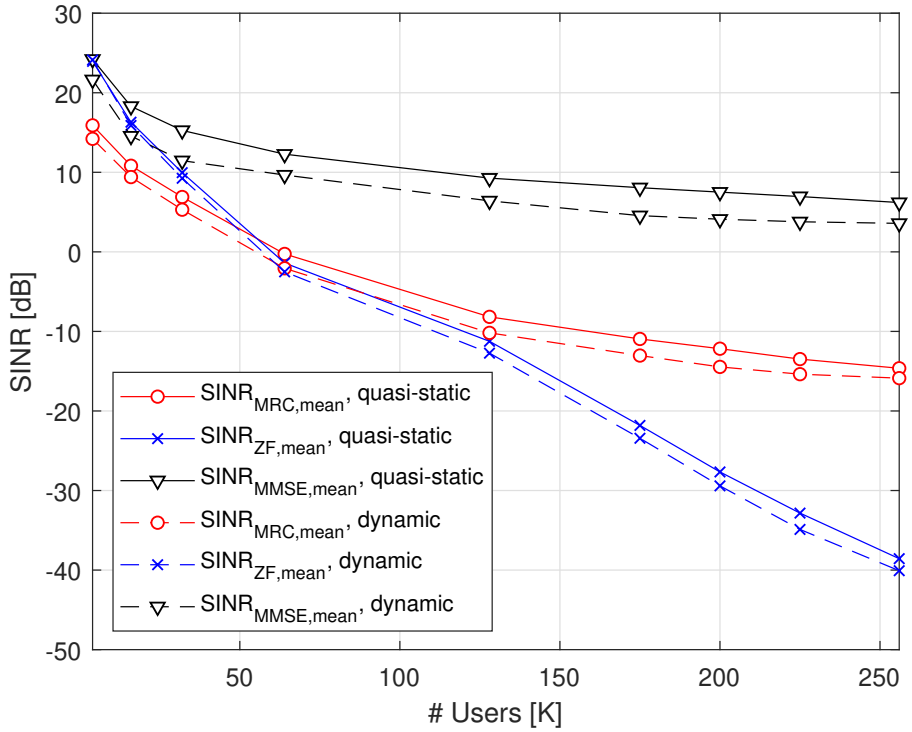

Figure 2.10 – Average SINR with birth and death PPP and PCP over the XL-MIMO ULA arrangement. $\mathcal{T} = 10^4$ channel realizations.

The impact of the birth and death process on the channel correlations is evaluated in Fig. 2.11 employing eq. (2.38). For this, a MCS is carried out varying the angle of interfering UE in three different scenarios: *static*, with a fixed number of scatterers and clusters (without the birth and death process); *quasi-static* and *dynamic*, in which we adopt the same parameters depicted in Table 2.4. From Fig. 2.11, the static and quasi-static scenarios reveal similar behavior. However, it is noted that there is a slight increase in the level of interference. In the dynamic scenario, yet, there is a more significant increase ($\approx 30\%$) in the interference level when compared to the static channel scenario due to the higher birth and death rate of scatterers and clusters, indicating that this phenomenon directly affects the level of interference in the MU XL-MIMO channels.

Next, we analyze the effect of the birth and death process on the VR size and its power distribution. For this, we consider the parameters presented in Table 2.4, except that $K = 128$ and $\mathcal{T} = 10^5$ channel realizations. The number of antennas in users' VR (M_{VR}) is evaluated in the same scenarios adopted above (static, quasi-static, and dynamic). Note that while the birth and death rate increases, M_{VR} also shows an increasing trend. This behavior also directly impacts the power distribution within the VR antennas, as seen in the figures 2.12(b), 2.12(c), and 2.12(d), representing static, quasi-static, and dynamic scenarios, respectively. We also have selected three M_{VR} values (low, medium, and high) for

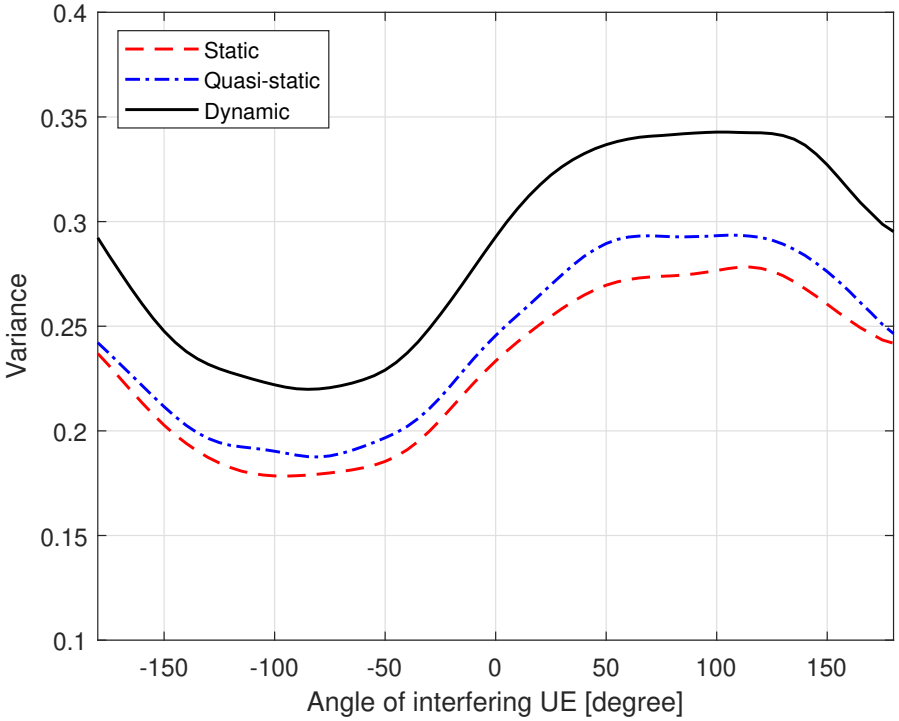

Figure 2.11 – Interference for the XL-MIMO system with ULA arrangement at the static (without birth and death process), quasi-static and dynamic scenarios.

each scenario according to the CCDF curves (CCDF $\approx [0.2; 0.5; 0.9]$). As the normalized power is considered, it can be observed that when the VR size increases, the energy peak in the center of the VR is smaller, and the energy received in the rest of the VR also tends to be smaller.

2.5 Conclusions

In this chapter, we propose a DS channel model for XL-MIMO systems equipped with UPA and ULA antennas arrangements, aiming to provide analysis tools for evaluating features and performance of such M-MIMO system configurations, also taking into account linear receiver schemes for realistic system application scenarios.

The XL-MIMO with UPA arrangement reveals a SE performance gain of $\approx 35\%$ compared to the ULA counterpart. This gain can be explained by the fact that the XL-MIMO equipped with UPA presents an extra spatial degree of freedom compared to the ULA, which leads to a lower level of correlation between users, reducing inter-user interference accordingly. Moreover, numerical results unveil the performance of the ZF combiner is greatly affected in the medium to high-loaded and crowded M-MIMO scenarios, *i.e.*, $\mathcal{L} = \frac{K}{M} \geq \frac{64}{256} \approx 0.25$, leading to remarkable performance degradation in such a context. Even though the MRC does not present the same problems as the ZF receiver, the MRC combiner also ends up with a minimal SE performance, which is expected in crowded scenarios since inter-user interference is not considered in such a receiver. Unlike ZF and

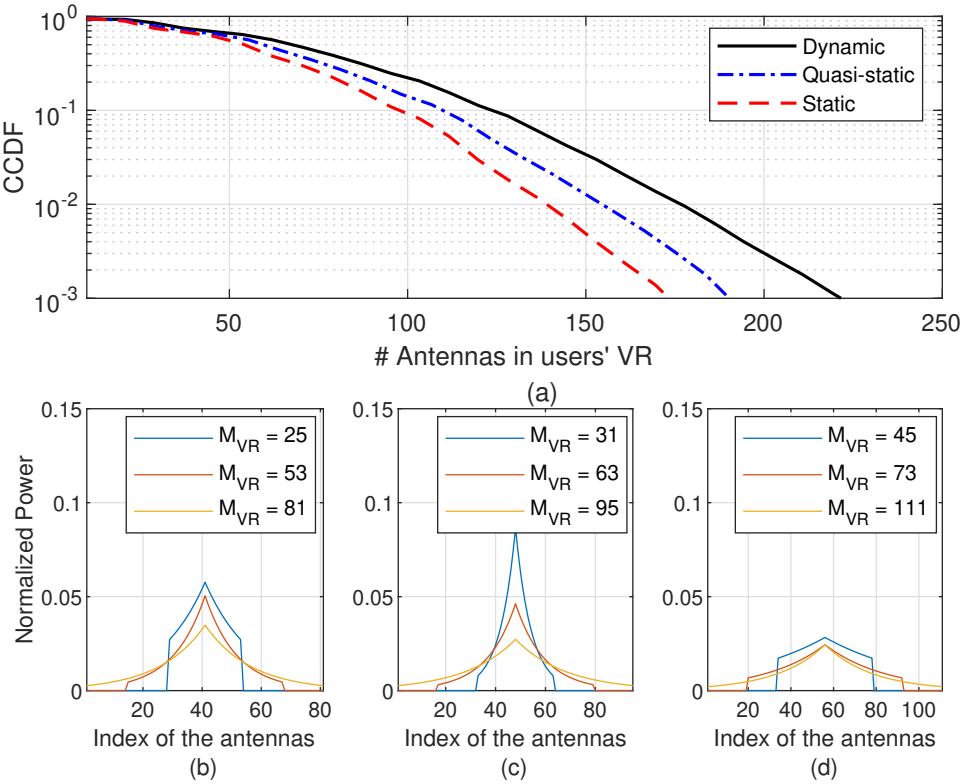

Figure 2.12 – User's VR size for the XL-MIMO system with ULA arrangement. a) CCDF of the number of antennas in users' VR; power profile of user's VR in three different scenarios: b) static; c) quasi-static; d) dynamic.

MRC combiners, the MMSE combiner presents an optimal performance in both analyzed types of massive arrays, resulting in unlimited capacity regarding the number of users, even under crowded configurations, *i.e.* $\mathcal{L} \approx 1$.

The proposed birth and death Poisson processes modeling the rising and the disappearance appearance and vanishing of scatterers and clusters in the XL-MIMO channels with ULA and UPA arrangements were analyzed to emulate a dynamic system scenario, where both user and the surrounding objects present a certain level of mobility. Hence, the analyzed linear receivers reveal an SINR performance degradation with the increase of the birth and death rate of scatterers and clusters, a clear indication that the mobility directly affects the level of interference in the doubly scattered MU XL-MIMO channels. This effect is 3 to 4 dB for the MMSE, while the ZF and MRC receivers present a decrease of around 1 to 2 dB in SINR for the considered dynamic configuration.

In this chapter, we focus on the analysis of near-field propagation condition, *i.e.*, the spatial non-stationarities, including the VR effects, and also consider the *birth* and *death processes* to accordingly model DS XL-MIMO channels with uniform distributions of antennas and scatterers, for simplicity. Future works include investigating irregular distributions of scatterers to represent more realistic scenarios and proposing appropriate models that consider hardware constraints, such as radio frequency impairment and hardware response, and all-digital or hybrid structures.

3 Channel Estimation on RIS-Aided Communication Systems

RIS is considered one of the most promising technologies for the next generation of wireless communication networks. Despite its great potential, RIS faces new challenges to integrate efficiently into wireless networks, which include reflection optimization, CE, and optimization of deployment locations. This chapter presents and analyzes a solution for CE in RIS-assisted systems using compressive sensing techniques. The steering vector and the complex channel gains of the BS-RIS/UE-RIS links are estimated separately by using the *orthogonal matching pursuit* with phase rotation (OMP-PR) by deploying a few active elements at the RIS panel. The performance and complexity of the proposed method are analyzed comprehensively under different scenarios and compared against those of several other related methods in the literature. Numerical results show the effectiveness of the proposed method, which achieves better (or at least very similar) performance compared to other relevant techniques but with a significant decrease in computational complexity.

3.1 Implementation of RIS in Wireless Communication Systems

5G wireless networks are already being used in many parts of the world. However, the combination of massive multiple-inputs and multiple-outputs (M-MIMO) operating on mmWaves, which was initially seen as one of the essential technologies for 5G networks, has not yet been widely adopted. The major impediments to mmWave communications include its sensitivity to blockages, limited coverage, and significant signal path loss operating in such frequency bands. However, some innovative applications will require high data rates, high reliability, ultra-low latency, and high QoS requirements, which existing systems cannot readily meet (TARIQ et al., 2020). Given the abundant bandwidth availability in the millimeter wave bands, future-generation wireless networks must use these bands. Techniques used in M-MIMO systems at BSs cannot solve the signal-blocking problem in these high-frequency bands (ALEXANDROPOULOS et al., 2021; GUERRA; ABRãO, 2022).

Due to recent advances in metamaterials, RIS has emerged as an enabling technology to overcome the abovementioned problem. An RIS can reconfigure signal propagation in a wireless network environment by adjusting the phase shifts of many low-cost passive reflective elements (PAN et al., 2021). In some situations, active, reflective elements also bring superior performance (ZHI et al., 2022a). For example, Holographic MIMO Surface

(HMIMOS) (HUANG et al., 2020; WEI et al., 2022), which can be active or passive, harnesses the power of RIS. The electronically-controlled active and passive RIS elements can dynamically manipulate the impinging electromagnetic waves, and this dynamic reconfigurability is the foundation of HMIMOS and sets it apart from traditional MIMO systems (HUANG et al., 2020).

One of the main challenges to reaping the full benefits of RIS and HMIMOS-aided wireless systems is to acquire the CSI accurately to design the phase shifts of the reflecting elements. Since the number of reflecting elements in an RIS is usually large, the estimated channel contains many coefficients. This implies that the conventional channel estimation (CE) process would incur a considerable training overhead proportional to the number of reflective elements in the RIS, the number of antennas at the base stations, and the user devices.

Related work: To deal with the above challenge, *semi-passive* RIS architectures have recently been proposed in the literature (ALEXANDROPOULOS; VLACHOS, 2020; HU et al., 2021; LIU et al., 2020; TAHA et al., 2019; TAHA et al., 2020; TAHA et al., 2021; JIN et al., 2021; HU et al., 2022; WU et al., 2022). Specifically, an RIS architecture composed of semi-passive elements connected to a single radio frequency (RF) chain using random spatial sampling and analog combining techniques was proposed in (ALEXANDROPOULOS; VLACHOS, 2020). For CE, its normalized mean-squared error (NMSE) performance was evaluated w.r.t. the number of training symbols. It was observed that, to achieve low NMSE values, a large number of training symbols are required when the number of passive elements increases, leading to a high training overhead. The authors in (HU et al., 2021) proposed a two-step RIS-based CE approach. An alternating direction multipliers (ADMM) method is initially implemented to recover training signals at the passive RIS elements. After that, the global channel is obtained by combining a channel sparsification step with a generalized approximate message passing (GAMP) algorithm. In (LIU et al., 2021), a similar approach based on ADMM as in (HU et al., 2021) was proposed but now applied to a fully passive RIS-aided system. In (TAHA et al., 2019; TAHA et al., 2020; TAHA et al., 2021; LIU et al., 2020), for *semi-passive* RIS-aided *single-input single-output* (SISO) systems, CE algorithms based on compressive sensing (CS) and deep learning (DL) techniques were proposed. While in (TAHA et al., 2019; TAHA et al., 2020; TAHA et al., 2021), the impact of both the number of RIS sensors and the channel sensing time on the achievable SE was numerically evaluated, in (LIU et al., 2020), a complex-valued denoising convolution neural network (CV-DnCNN) was proposed to improve the NMSE performance of CE in *semi-passive* RIS systems.

The authors in (HU et al., 2022) proposed a two-stage CE method for separately estimating the channels between BS-RIS and user-RIS in a *semi-passive* RIS-aided system. First, the BS-RIS channel is estimated using the classic *estimation of signal parameters via rotational invariance technique* (ESPRIT) (TREES, 2002), representing an extremely low

training overhead and complexity. In the second stage, the user-RIS channels are obtained by combining *total least square* (TLS) ESPRIT and *multiple signal classification* (MUSIC) techniques (TREES, 2002). The method proposed in (HU et al., 2022) has the advantage that the training overhead does not scale with the number of RIS reflecting elements, resulting in much lower training overhead than the conventional cascaded channel-based estimation schemes[1]. The authors in (CHEN et al., 2021b) employed a *semi-passive* RIS-aided system composed of N_{RF} active reflecting elements with an L-shaped array, each linked with a sensor and an RF chain. A low-complexity CE method based on direction-of-arrival (DOA) estimation was proposed. Both (CHEN et al., 2021b; HU et al., 2022) proposed an RIS-aided structure in which each of the semi-passive elements is equipped with a receiving RF chain, and hence, the hardware complexity is significantly increased.

An RIS-aided system with only passive elements was analyzed in (WANG et al., 2020a), considering the inherent *sparsity property* of mmWave channels aiming to obtain a cascaded CE description. From this, the authors proposed a sparse representation of the cascade channel applied to CS-based methods. More specifically, the classical *least square* (LS) estimator was compared with the orthogonal matching pursuit (OMP) and the Gaussian-mixture approximate message passing (GAMP) approach by using the proposed sparsity representation. The proposed solutions can significantly reduce training overhead under the analyzed scenarios. In (ZHANG et al., 2020), the uplink (UL) CE for the RIS-aided M-MIMO system was investigated; also, this system deploys an *all-passive* RIS structure, equipped with many reflecting elements, which can only passively reflect the incident signal (instead of intentionally transmitting signal).

CE performance and achieved SE of the purely passive *versus* hybrid RIS architectures were analyzed in (SCHROEDER et al., 2022). The CE task is done via *atomic norm minimization* (ANM). A two-stage procedure was used for the purely passive RIS (HE et al., 2021) to estimate the channel parameters sequentially. For hybrid RIS, the individual channels were estimated at the RIS based on the observations from active RIS elements, assuming alternating UL and downlink (DL) training. Hybrid RIS attains better CE and SE performance than full passive RIS under the same training overhead. Unfortunately, these methods exhibit high computational complexity, especially for a large number of RIS elements or with a large number of antennas at the BS, which is an essential assumption for real applications.

Another challenge inherent to the RIS-aided communication systems involves jointly designing/optimizing the RIS phase shifts and the CE of both UE-RIS and BS-RIS links. Recent works dealing with these common tasks include (AN et al., 2022; SCHROEDER et al., 2022; MILLER et al., 2021). Indeed, in practical RIS-assisted communication systems, the acquisition of CSI and RIS reflection optimization constitute a pair of challenges.

[1]In conventional cascaded channel-based estimation schemes, the training overhead generally increases linearly with the number of RIS elements (WANG et al., 2020b).

Low-complexity CE and passive beamforming designs for RIS-aided systems have been proposed (AN et al., 2022). Also, a two-stage CE procedure for a multi-antenna BS assisted by an RIS was proposed in (MILLER et al., 2021). In Stage 1, the BS estimates the direct link from the UE-BS and the UE-RIS link using partial knowledge of the RIS-BS channel. The UE-RIS CSI is interpolated from channel estimates for a subset of active RIS elements to reduce pilot overhead. CSI obtained in Stage 1 is then used to inform the RIS phase design and form an initial estimate of the global channel, which is refined with more pilot symbols in Stage 2 and subsequently used to perform UL processing during data transmission. Besides, the authors studied the impact of *ray angular spread*, RIS size, and inter-element spacing on the global CE accuracy.

However, the CE methods mentioned above have limitations for RIS-aided mmWave systems. The CE of (WANG et al., 2020b) requires low pilot overhead in a rich scattering communication scenario (full rank channel). Still, it is not applicable in mmWave MISO communication systems due to spatial sparsity. In Wang 2020, the cascade CE problem does not consider the typical parameters of the cascade channel, leading to high power leakage. As demonstrated in (WEI et al., 2021), OMP-based solutions can bring good CE results when the spatial angles are on the quantized grid. However, in practical scenarios, this assumption may not hold, and consequently, a larger dictionary matrix should be employed, resulting in high computational complexity. In (ANJINAPPA et al., 2020), the authors introduce channel and covariance estimation algorithms in MIMO mmWave networks for a ULA setup, specifically addressing off-grid effects. The algorithms, such as parameter perturbed simultaneous orthogonal matching pursuit (PPSOMP) and Parameter Perturbed Covariance OMP (PPCOMP), utilize controlled perturbations and modified frameworks to improve efficiency and reconstruction accuracy compared to existing methods. This is achieved through a gradient-based optimization process that jointly updates the perturbation parameters and weights iteratively within their respective grid regions, ensuring they do not cross the upper and lower bounds of the grid points. By finding the optimal perturbations, the solver aims to minimize the residual term and improve the accuracy of CE in MIMO mmWave networks. However, one of the main weaknesses of the method in (ANJINAPPA et al., 2020) is that it may have higher computational complexity than existing methods due to the iterative optimization process involved in solving for perturbation parameters and weights, which need to be recalculated on every iteration. Moreover, the paper in (RODRíGUEZ-FERNáNDEZ et al., 2017) introduces a mixed compressive sensing-maximum likelihood (ML) algorithm for off-grid wideband CE at millimeter wave frequencies. This algorithm utilizes continuous dictionaries to estimate the channel, thereby reducing quantization errors and enhancing estimation performance. Simulation results demonstrate that the proposed algorithm surpasses previous methods based on finite-resolution dictionaries. The work in Bayraktar (2022) introduces a novel joint CE and localization strategy for mmWave MIMO systems enhanced by RIS. The

technique utilizes a multidimensional OMP algorithm for compressive CE, employing separate dictionaries for angular and delay domains. This approach aims to improve localization accuracy in realistic three-dimensional (3D) indoor environments. However, using different dictionaries for every angle of arrival/angle of departure (AoA/AoD) in the algorithm may lead to error propagation issues, as the complexity of the model increases with separate dictionaries for each path, increasing the risk of inaccuracies propagating through the estimation process. These problems motivate the development of a new and efficient CE strategy.

Novelty: We consider that the AoAs and AoDs in an RIS-aided mmWave wireless system are randomly generated and do not necessarily lie in a discretized grid. Power leakage will weaken the sparsity if there is a grid mismatch when the channel is represented on the virtual sparse angular domain by the redundant dictionary. Moreover, conventional on-grid CS methods for CE, such as OMP, present high power leakage, resulting in high CE error. Differently from (ANJINAPPA et al., 2020), we proposed a *phase rotation* (PR) based on a discretized controlled perturbation combined with a matching pursuit (MP)-based method aiming to mitigate the power leakage issue. In our case, the controlled perturbation is achieved through a one-shot method, eliminating the need for an iterative optimization process that requires recalculating all parameters at each iteration, as in (ANJINAPPA et al., 2020). We also extend our solution to wideband scenarios (frequency-selective channels) using a SOMP-PR/SMP-PR technique, which is missing in (ANJINAPPA et al., 2020). Moreover, our proposed approach does not require knowledge of the sparsity level for CE, differently from (RODRíGUEZ-FERNáNDEZ et al., 2017; BAYRAKTAR et al., 2022). Instead, only the noise variance must be estimated, which is straightforward. Overall, the proposed CE strategy (MP-PR) has several attractive features such as: a) low computational complexity; b) low training overhead; c) low power consumption; and d) differently of some sparse recovery CE techniques, such as *compressive sampling matching pursuit* (CoSaMP) and *subspace pursuit* (SP), the proposed technique does not need the knowledge of the sparsity level (number of spatial paths) in the RIS-aided mmWave wireless system.

To corroborate the effectiveness of the proposed CE method for RIS-aided systems, in the numerical results section, we also compare our technique with two recent methods of the literature, namely: **a**) the *nuclear norm minimization* (NNM)-based CE for RIS-aided MIMO systems with active and passive RIS elements of (WU et al., 2022); **b**) ANM-based CE for RIS-aided mmWave MIMO systems with hybrid (active and passive RIS elements) architecture from (SCHROEDER et al., 2022). Both (WU et al., 2022; SCHROEDER et al., 2022) implemented an off-grid CE method to overcome the mismatch problem in on-grid algorithms, such as OMP, improving the CE performance. Moreover, in (SCHROEDER et al., 2022), it was shown that the proposed CE method could bring better performance than the passive RIS with the help of a small number of active elements. In this paper,

we adopt an extended configuration and more scenarios and metrics w.r.t. (WU et al., 2022; SCHROEDER et al., 2022), including ULA at the UE instead of single-antenna devices and UPA at the RIS instead of ULA. Besides the NMSE, the effective average SE is deployed as a figure of merit when comparing the system performance of these three methods.

Contributions: The contribution of this chapter is fourfold.

i. From the virtual angular-domain channel representation, we propose to efficiently estimate the sparse channel gains over a modified redundant dictionary to reconstruct the BS-RIS/UE-RIS links in an RIS-aided communication by deploying a CS-based method, namely, *matching pursuit with phase rotation* (MP-PR).

ii. The performance and complexity of the proposed MP-PR CE method are characterized for different channel and system scenarios, including flat and frequency-selective channels, single- and multi-carrier configurations, single- and multiple-user scenarios with pilot contamination, different ratios of active/passive antenna elements, and MP stopping criteria.

iii. Extensive numerical results corroborating the superiority of the proposed MP-PR method for CE in an RIS-aided communication system in terms of the performance-complexity trade-off are explored and compared with the state-of-the-art deep CNN-based method in (LIU et al., 2020).

iv. To corroborate the effectiveness of the proposed method, we deploy the MP-PR CE method in the design of discrete RIS phases. The RIS phase shift optimization is carried out aiming at maximizing the sum capacity (or SINR) subject to the transmit power constraint for the k-th user.

The remainder of this chapter is organized as follows. The system model is presented in Section 3.2. The communication protocol for a semi-passive RIS-aided MIMO system is presented in Section 3.3. The CE process in a semi-passive RIS-aided wireless system is described in Section 3.3.1. The proposed MP with Phase Rotation (MP-PR)-based CE method in a *semi-passive* RIS-aided system is described in Section 3.4. Extensive numerical results are provided in Section 3.5. Section 3.6 concludes the chapter.

3.2 System Model and Assumptions

3.2.1 RIS-Aided communication model

We consider an RIS-aided UL communication system with K users, as illustrated in Fig. 3.1. Herein, we assume N_{BS} antennas at the BS side while UEs are equipped with N_{UE} antenna elements, where both are deployed with ULA arrays. We consider a semi-passive

RIS structure composed of N_{act} active channel sensors and N_{RIS} passive reflecting elements as in (LIU et al., 2020; WU et al., 2022). We also consider that there are direct links between the UEs and the BS, as illustrated in Fig. 3.1. Hence, the effective UL channel between the k-th UE and the BS is given by

$$\mathbf{H}_k = \mathbf{H}_{\text{D},k} + \mathbf{G}\boldsymbol{\Theta}\mathbf{H}_{\text{R},k}, \tag{3.1}$$

where $\mathbf{H}_{\text{D},k} \in \mathbb{C}^{N_{\text{BS}} \times N_{\text{UE}}}$ represents the channel matrix from the k-th user to BS, $\mathbf{G} \in \mathbb{C}^{N_{\text{BS}} \times N_{\text{RIS}}}$ represents the RIS-BS channel, and matrix $\mathbf{H}_{\text{R},k} \in \mathbb{C}^{N_{\text{RIS}} \times N_{\text{UE}}}$ denoting the channel between the k-th user and the RIS for $k = 1, \ldots, K$. In addition, the RIS phase shift matrix is defined as $\boldsymbol{\Theta} = \text{diag}\{\theta_1, \ldots, \theta_m, \ldots, \theta_{N_{\text{RIS}}}\} \in \mathbb{C}^{N_{\text{RIS}} \times N_{\text{RIS}}}$, where the diagonal matrix representing the phase-shift matrix of the RIS composed of $N_{\text{RIS}} = N_{\text{RIS},v} N_{\text{RIS},h}$ reflecting elements in total (note that the amplitude of each reflection element is set to one, for simplicity); $N_{\text{RIS},v}$ and $N_{\text{RIS},h}$ are the number of elements in vertical and horizontal directions, respectively, where $\theta_m = e^{j\phi_m}$, $\forall\, m = 1, 2, \ldots, N_{\text{RIS}}$.

In this work, a hybrid beamforming (HBF) architecture is adopted. Therefore, the received UL signal from the k-th user $\mathbf{y}_k \in \mathbb{C}^{N_s^{\text{BS}} \times 1}$ at BS is modeled as

$$\mathbf{y}_k = (\mathbf{W}_{\text{RF}}\mathbf{W}_{\text{BB},k})^H \sum_{k=1}^{K} \mathbf{H}_k \mathbf{F}_{\text{RF},k}\mathbf{F}_{\text{BB},k}\mathbf{s}_k + \mathbf{n}, \tag{3.2}$$

where the BS analog beamforming and the BS digital beamforming for the k-th user are denoted by $\mathbf{W}_{\text{RF}} \in \mathbb{C}^{N_{\text{BS}} \times N_{\text{BS}}^{\text{RF}}}$ and $\mathbf{W}_{\text{BB},k} \in \mathbb{C}^{N_{\text{BS}}^{\text{RF}} \times N_s}$, respectively, with $N_{\text{BS}}^{\text{RF}}$ being the number of RF chains at the BS side, and N_s^{BS} is the data stream at the BS. Similarly, $\mathbf{F}_{\text{RF},k} \in \mathbb{C}^{N_{\text{UE}} \times N_{\text{UE}}^{\text{RF}}}$ and $\mathbf{F}_{\text{BB},k} \in \mathbb{C}^{N_{\text{UE}}^{\text{RF}} \times N_s^{\text{UE}}}$ represents the UE analog precoder and the UE digital precoder of user k, respectively, where $N_{\text{UE}}^{\text{RF}}$ is the number of RF chains at the k-th UE and N_s^{UE} is the data stream at the UE. In addition, $\mathbf{n} \sim \mathcal{CN}(\mathbf{0}_{N_{\text{BS}}}, \sigma^2 \mathbf{I}_{N_{\text{BS}}})$ represents the thermal noise with $\mathbf{I}_{N_{\text{BS}}}$ representing a $N_{\text{BS}} \times N_{\text{BS}}$ identity matrix, and $\mathbf{s}_k \in \mathbb{C}^{N_s^{\text{UE}} \times 1}$ denotes the transmitted signal from the k-th user, with $\mathbb{E}\{\mathbf{s}_k \mathbf{s}_k^H\} = \mathbf{I}_{N_s^{\text{UE}}}, k = 1, \ldots, K$.

3.2.2 Narrowband channel model

We consider a Rician fading channel model for either $\mathbf{G}$, $\mathbf{H}_{\text{R},,k}$, or $\mathbf{H}_{\text{D},k}$ channels. Moreover, we have assumed that the k-th UE is equipped with a ULA with N_{UE} antennas. Therefore, the channel matrix between the k-th user and the RIS can be expressed as:

$$\mathbf{H}_{\text{R},k} = \sqrt{\frac{\beta_k^{\text{LoS}} \kappa_k}{\kappa_k + 1}} \mathbf{H}_{\text{R},k}^{\text{LoS}} + \sqrt{\frac{\beta_k^{\text{NLoS}}}{\kappa_k + 1}} \mathbf{H}_{\text{R},k}^{\text{NLoS}}, \tag{3.3}$$

where β_k^{LoS} is the path loss for the *line-of-sight* (LoS) link between the UEs and the RIS, β_k^{NLoS} is the path loss for the *non-line-of-sight* (NLoS) component between the UEs and the RIS, while κ_k is the Rician factor. $\mathbf{H}_{\text{R},k}^{\text{LoS}}$ and $\mathbf{H}_{\text{R},k}^{\text{NLoS}}$ are the LoS and NLoS components,

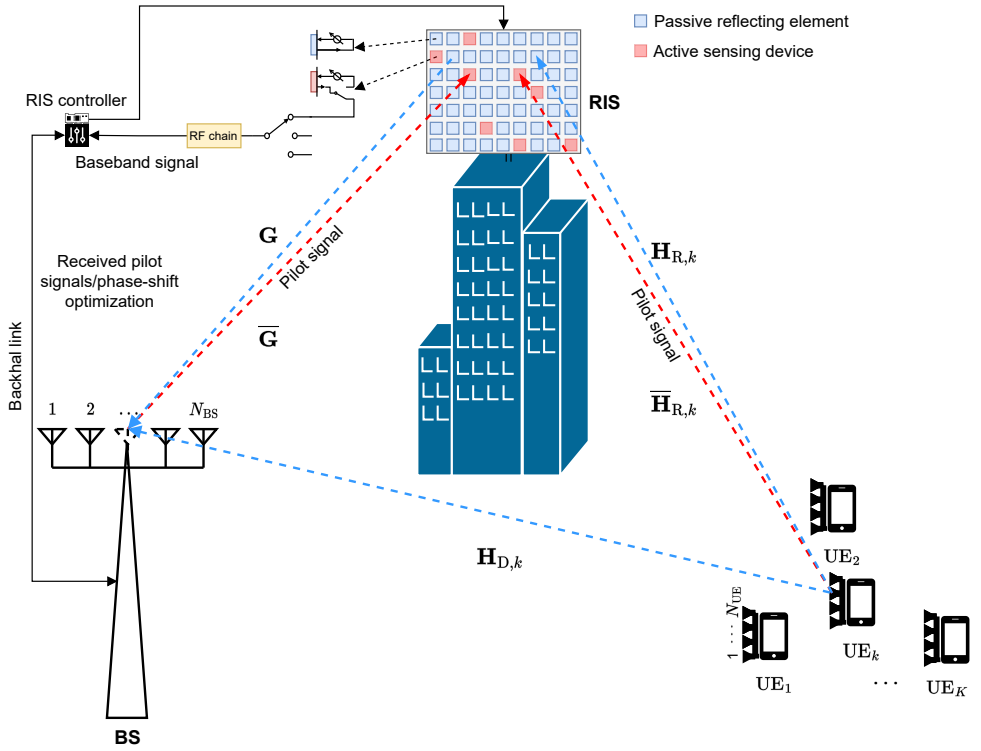

Figure 3.1 – RIS-aided MIMO system with semi-passive RIS elements; The UE$_k$ is equipped with a ULA, following eq. (3.5) and (3.4).

respectively, which are given by

$$\mathbf{H}_{\text{R},k}^{\text{LoS}} = \mathbf{a}_R(\vartheta_{R,k}^{\text{RIS}}, \varphi_{R,k}^{\text{RIS}})\mathbf{a}_T^H(\vartheta_{T,k}^{\text{UE}_k}), \tag{3.4}$$

$$\mathbf{H}_{\text{R},k}^{\text{NLoS}} = \sqrt{\frac{1}{L}}\sum_{l=1}^{L}\alpha_{l,k}\mathbf{a}_R(\vartheta_{R,l,k}^{\text{RIS}}, \varphi_{R,l,k}^{\text{RIS}})\mathbf{a}_T^H(\vartheta_{T,l,k}^{\text{UE}_k}), \tag{3.5}$$

with $\vartheta_{R,k}^{\text{RIS}}$ and $\varphi_{R,k}^{\text{RIS}}$ being the azimuth and elevation angles of arrival (AoA) at the RIS, while $\vartheta_{T,k}^{\text{UE}_k}$ is the azimuth angle of departure (AoD) for the k-th user of the LoS component. In addition, $\alpha_{k,l} \in \mathbb{C}$ being the equivalent complex channel gain of the l-th path for the k-th user, with L being the number of resolvable paths, $\vartheta_{R,l,k}^{\text{RIS}}$ and $\varphi_{R,l,k}^{\text{RIS}}$ are the azimuth and elevation AoA at the RIS, and $\vartheta_{T,l,k}^{\text{UE}_k}$ is the azimuth AoD for the k-th user of the NLoS component. $\mathbf{a}_R(\vartheta_{R,k}^{\text{RIS}}, \varphi_{R,k}^{\text{RIS}}) \in \mathbb{C}^{N_{\text{RIS}}\times 1}$ denotes the RIS *spatial steering vector* (receiver side), and $\mathbf{a}_T^H(\vartheta_{T,k}^{\text{UE}_k}) \in \mathbb{C}^{N_{\text{UE}}\times 1}$ is the k-th UE *spatial steering vector* (transmitter side). These spatial steering vectors can be defined as:

$$\mathbf{a}_R(\vartheta_{R,k}^{\text{RIS}}, \varphi_{R,k}^{\text{RIS}}) = \left[1,\ e^{j\frac{2\pi d_s}{\lambda}\sin(\vartheta_{R,k}^{\text{RIS}})\sin(\varphi_{R,k}^{\text{RIS}})},\ \ldots, e^{j\frac{2\pi d_s}{\lambda}(M_h-1)\sin(\vartheta_{R,k}^{\text{RIS}})\sin(\varphi_{R,k}^{\text{RIS}})}\right]^\top \otimes \left[1,\ e^{j\frac{2\pi d_s}{\lambda}\cos(\varphi_{R,k}^{\text{RIS}})}, \ldots,\ e^{j\frac{2\pi d_s}{\lambda}(M_v-1)\cos(\varphi_{R,k}^{\text{RIS}})}\right]^\top, \tag{3.6}$$

$$\mathbf{a}_T^H(\vartheta_{T,k}^{\text{UE}_k}) = [1,\ e^{j\frac{2\pi d_s}{\lambda}\sin(\vartheta_{T,k}^{\text{UE}_k})},\ \ldots,\ e^{j\frac{2\pi d_s}{\lambda}(N_{\text{UE}}-1)\sin(\vartheta_{T,k}^{\text{UE}_k})}]^\top \tag{3.7}$$

where λ denotes the signal wavelength, and d_s is the antenna spacing. Note that the array steering vectors $\mathbf{a}_R(\vartheta_{R,l,k}^{\text{RIS}}, \varphi_{R,l,k}^{\text{RIS}})$ and $\mathbf{a}_T^H(\vartheta_{T,l,k}^{\text{UE}_k})$ related to the NLoS components have the

same shape of the LoS signal, as in eqs. (3.6) and (3.7). The channel matrix from the k-th UE to BS ($\mathbf{H}_{\mathrm{D},k}$) is modeled similarly to $\mathbf{H}_{\mathrm{R},k}$.

On the other hand, the $N_{\mathrm{RIS}} \times N_{\mathrm{BS}}$ UL channel matrix $\mathbf{G}$ from RIS to BS is obtained similar to (3.3) as:

$$\mathbf{G} = \sqrt{\beta_G}\left(\sqrt{\frac{\kappa_G}{\kappa_G+1}}\mathbf{G}^{\mathrm{LoS}} + \sqrt{\frac{1}{\kappa_G+1}}\mathbf{G}^{\mathrm{NLoS}}\right) \tag{3.8}$$

where β_G is the path loss between the BS and the RIS, while κ_G is the Rician factor. Here, $\mathbf{G}^{\mathrm{LoS}}$ and $\mathbf{G}^{\mathrm{NLoS}}$ refer to the LoS and NLoS components, which can be obtained similarly to $\mathbf{H}_{\mathrm{R},k}^{\mathrm{LoS}}$ and $\mathbf{H}_{\mathrm{R},k}^{\mathrm{NLoS}}$, as described previously. In this case, it is reasonable to assume $\kappa_G \to \infty$, since we can consider a pure (AWGN – Additive White Gaussian Noise) LoS channel between BS and RIS.

3.2.3 RIS-aided M-MIMO OFDM communication model

Consider a wideband RIS-aided UL communication system with K users. We assume N_{BS} antennas at the BS side, while UEs are single-antenna devices ($N_{\mathrm{UE}} = 1$). We consider a semi-passive RIS structure composed of N_{act} active elements and N_{RIS} passive reflecting elements as in (LIU et al., 2020; WU et al., 2022). Additionally, an Orthogonal Frequency Division Multiplexing Access (OFDM) system with N_{SC} subcarriers is employed to combat channel frequency selectivity. Also, in this case we consider that the channel between the RIS and the BS is strongly dominated by the LoS component, which is deterministic as the BS and RIS are located in a fixed position, then only the BS-UEs RIS-UEs links need to be estimated in this scenario.

The effective UL channel between the k-th UE and the BS at the n-th subcarrier is:

$$\mathbf{h}_{k,n} = \mathbf{G}_n \boldsymbol{\Theta} \mathbf{h}_{\mathrm{R},k,n} = \mathbf{G}_n \mathbf{H}_{\mathrm{R},k,n} \boldsymbol{\theta}, \tag{3.9}$$

where $\mathbf{G}_n \in \mathbb{C}^{N_{\mathrm{BS}} \times N_{\mathrm{RIS}}}$ represents the RIS-BS channel at the n-th subcarrier, and $\mathbf{h}_{\mathrm{R},k,n} \in \mathbb{C}^{N_{\mathrm{RIS}} \times 1}$, with $k = 1, \ldots, K$ denotes the channel between the k-th user and the RIS at the n-th subcarrier. In addition, $\mathbf{H}_{\mathrm{R},k,n} = \mathrm{diag}(\mathbf{h}_{\mathrm{R},k,n})$, and the phase shift vector is defined at the same way we have done in section 3.2.1.

3.2.4 Wideband channel Model

We consider a wideband geometric channel model for both communication links. Adopting a *frequency selective fading channel*, an OFDM-based scheme with N_{sc} subcarriers can be appropriately employed to turn the channel flat in each sub-channel. Therefore, the channel vector of the n-th subcarrier between the k-th user and the RIS can be expressed, in the frequency domain, as (LIU et al., 2020):

$$\mathbf{h}_{\mathrm{R},k,n} = \sqrt{\frac{1}{L}} \sum_{d=0}^{D-1} \sum_{l=1}^{L} \alpha_{k,l} p(dT_s - \tau_l) \mathbf{a}(\vartheta_{k,l}, \varphi_{k,l}) e^{-j\frac{2\pi n}{N_{\mathrm{SC}}} d}, \tag{3.10}$$

where $\alpha_{k,l} \in \mathbb{C}$ is the equivalent complex channel gain of the lth path for the k-th user, with L being the number of resolvable paths, D is the channel tap length, $p(\tau)$ represents the pulse shaping function for T_S-spaced signaling evaluated at τ seconds, and τ_l is the time delay. $\mathbf{a}(\vartheta_{k,l}, \varphi_{k,l}) \in \mathbb{C}^{N_{\text{RIS}} \times 1}$ denotes the *spatial steering vector* at the receiver side, with $\vartheta_{k,l}$ and $\varphi_{k,l}$ representing the azimuth and elevation angles of arrival (AoA) of the lth path of the k-th user at the RIS. The spatial steering vector can be defined as in 3.6.

3.3 Communication Protocol for Semi-Passive RIS-Aided MIMO System

In the analyzed semi-passive RIS-aided wireless communication system, the CE task consists of obtaining reliable estimates for the BS-RIS channel coefficients and the RIS-UE channel coefficients. Hence, the CSI of the BS-RIS link is applied for all UEs in the system. Moreover, observe that both BS and RIS structures are in a fixed position (*i.e.*, no mobility). Thus, the BS-RIS link is characterized as a quasi-static channel, varying much more slowly than the UEs-RIS channels. This implies that the BS-RIS does not need to be estimated on every channel coherence block. Consequently, only the UEs-RIS communication links need to be re-estimated on every channel coherence time, which can significantly reduce the CE complexity compared with the existing cascaded CE. In the sequel, we will describe the CE protocol for the semi-passive RIS-aided MIMO system adopted in this work and the proposed CS-based CE algorithm.

The communication steps (or phases) for the assumed system are shown in Fig. 3.2. In the following, we describe how the proposed communication protocol works.

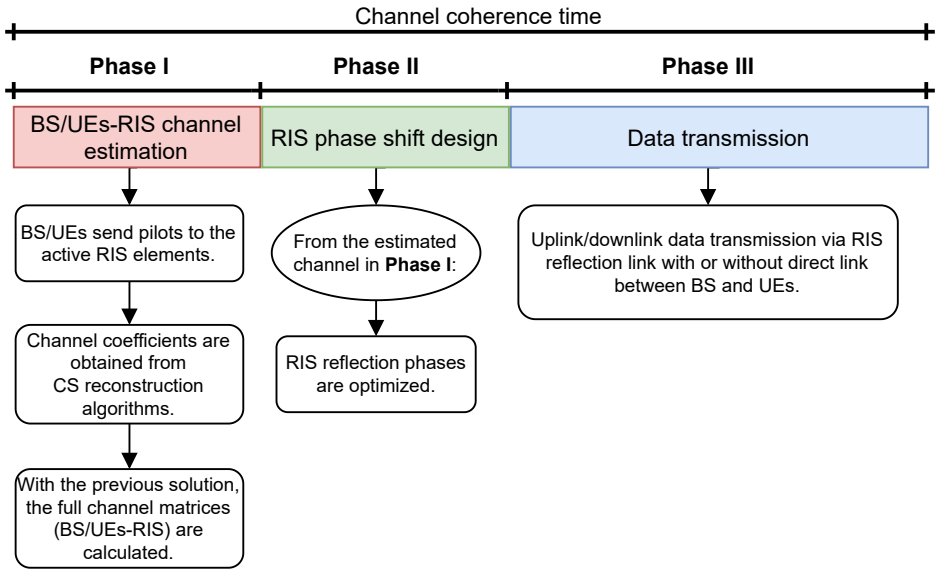

Figure 3.2 – Communication steps for a semi-passive RIS-aided system.

3.3.1 CE Task in narrowband semi-passive RIS-aided systems

As the direct link can be seen as a conventional MIMO system, CE for this link can be implemented by using traditional CE algorithms. Nevertheless, the proposed CS-based CE approach can also be applied in the direct link case.

In **Phase I**, we aim to obtain the CSI estimates for the BS-RIS and UE-RIS links separately. Then, the active sensors are sequentially activated by connecting them to the $N_{\text{RIS}}^{\text{RF}}$ receive RF chains via a switching network to receive the pilot signals from the BS or UEs. At the same time, all of the passive reflecting elements are turned off. In the pilot training phase, we activate every $N_{\text{RIS}}^{\text{RF}}$ active elements to obtain $N_{\text{RIS}}^{\text{RF}}$ measurements in each time slot. Subsequently, during the data transmission phase, these active elements operate as passive element. By exploiting the channel from the k-th user to the active elements, which are selected by the matrix $\mathbf{W}_{S,t} \in \mathbb{Z}^{N_{S_{\text{RIS}}} \times N_{\text{RIS}}}$, the received UL training signal of the k-th transmitter consists of T time slots; therefore, the received signal $\mathbf{y}_{k,t} \in \mathbb{C}^{N_{S_{\text{RIS}}}}$ for the link between the RIS and the k-th user at the t-th time slot can be expressed as follows:

$$\mathbf{y}_{k,t} = \mathbf{W}_{S,t}\mathbf{H}_{\text{R},k}\mathbf{F}_{\text{RF},k,t}\mathbf{F}_{\text{BB},k,t}\mathbf{s}_{k,t} + \mathbf{n}_{k,t}. \tag{3.11}$$

Here, matrices $\mathbf{F}$ have the same meaning as in eq. (2), but $\mathbf{W}_{S,t}$ refers to the selection matrix at the t-th time slot, which will select the active elements at the RIS, while in eq. (2) $\mathbf{W}_{\text{RF}}$ and $\mathbf{W}_{\text{BB},k}$ are the BS analog and digital beamforming matrices for the k-th, respectively. Moreover, in eq. (3.11), each row of the selection matrix $\mathbf{W}_{S,t}$ contains $N_{\text{RIS}} - 1$ zeros and a single one entry, $\mathbf{s}_{k,t} \in \mathbb{C}^{\tau_p \times 1}$ is the vector containing the pilot signal of the k-th user and t-th time slot with length τ_p, and $\mathbf{n}_{k,t} \in \mathbb{C}^{N_{S_{\text{RIS}}} \times 1}$ is the AWGN vector at the active elements of the RIS. The pilot sequences used have the following cross-correlation properties:

$$\mathbf{s}_k\mathbf{s}_j^H = \begin{cases} \rho, & \forall k \neq j \\ 1, & \forall\, k = j \end{cases},$$

where for *orthogonal* pilot sequences, $\rho = 0$.

In the context of sparse channel estimation, the channel matrix $\mathbf{H}_{\text{R},k}$ can be represented in a sparse form. Vectorizing this matrix, $\mathbf{h}_{\text{R},k} = \text{vec}(\mathbf{H}_{\text{R},k})$, allows us to utilize sparse signal recovery techniques more effectively. Sparse vectors are easier to handle computationally and can be processed using algorithms designed for sparse signals. Further, through the vectorization operation applied to (3.11), we achieve

$$\begin{aligned} \mathbf{y}_{k,t} = \text{vec}(\mathbf{y}_{k,t}) &= (\mathbf{F}_{k,t}\mathbf{s}_{k,t})^T \otimes (\mathbf{W}_{S,t})\text{vec}(\mathbf{H}_{\text{R},k}) + \mathbf{n}_{k,t} \\ &= \mathbf{\Phi}_t\mathbf{h}_{\text{R},k} + \mathbf{n}_{k,t}, \end{aligned} \tag{3.12}$$

where $\mathbf{\Phi}_{k,t} = (\mathbf{F}_{k,t}\mathbf{s}_{k,t})^T \otimes (\mathbf{W}_{S,t})$ is the measurement matrix in the t-th time slot for the k-th UE, $\mathbf{F}_{k,t} = \mathbf{F}_{\text{RF},k,t}\mathbf{F}_{\text{BB},k,t}$, and $\mathbf{h}_{\text{R},k}$ denotes the vectorized channel of the k-th user.

Measurement matrix: Note that the number of measurements in each time slot is equal to the number of RF chains, *i.e.*, $N_{S_{\text{RIS}}} = N_{\text{RIS}}^{\text{RF}}$. This means that with a total number of measurements $M = TN_{\text{RIS}}^{\text{RF}}$, we can reduce the training overhead T by increasing $N_{\text{RIS}}^{\text{RF}}$, although this comes at the expense of higher power consumption and hardware requirements. Consequently, we can opt for just 1 RF chain to conserve energy and reduce costs. Then, there is a trade-off between training overhead and hardware complexity that we can manage. It is important to note that, generally, the training overhead in the full passive structures available in the literature is proportional to the number of RIS elements N_{RIS}, which is much higher than in our proposed semi-passive structure.

Once $M = TN_{\text{RIS}}^{\text{RF}}$, we have $N_{\text{RIS}}^{\text{RF}}$ active elements being successively turned on over T time slots, resulting in the following full observation vector

$$\begin{aligned}\mathbf{y}_k &= \left[(\mathbf{y}_{k,1})^T, (\mathbf{y}_{k,2})^T, \ \ldots, \ (\mathbf{y}_{k,T})^T\right]^T \\ &= \left[(\mathbf{\Phi}_{k,1})^T, (\mathbf{\Phi}_{k,2})^T, \ \ldots, \ (\mathbf{\Phi}_{k,T})^T\right]^T \mathbf{h}_{\text{R},k} + \mathbf{n}_k \\ &= \mathbf{\Phi}_k \mathbf{h}_{\text{R},k} + \mathbf{n}_k, \end{aligned} \tag{3.13}$$

$\mathbf{\Phi}_k = \left[(\mathbf{\Phi}_{k,1})^T, (\mathbf{\Phi}_{k,2})^T, \ \ldots, \ (\mathbf{\Phi}_{k,T})^T\right]^T \in \mathbb{C}^{M \times N_{\text{RIS}} N_{\text{UE}}}$ representing the full measurement matrix for the k-th UE, and $\mathbf{n}_k = [(\mathbf{n}_{k,1})^T, \ (\mathbf{n}_{k,2})^T, \ \ldots, \ (\mathbf{n}_{k,T})^T]^T$ is the stacked noise vector.

3.3.2 CE Task in wideband semi-passive RIS-aided systems

We aim to obtain the CSI estimates for the BS-RIS and UE-RIS links separately. Then, in each training period, only one active sensor is turned on to receive the pilot signals from the BS or UEs, while all passive reflecting elements are turned off. By exploiting the channels from the k-th user to the active elements, the received training signal of the k-th transmitter at the t-th time slot is written as:

$$y_{k,n,t} = \mathbf{w}_{s,t} \mathbf{h}_{\text{R},k,n} s_{k,t} + n_{n,t}, \tag{3.14}$$

where $\mathbf{w}_{s,t} \in \mathbb{Z}^{1 \times N_{\text{RIS}}}$ is the selection vector at the t-th time slot, containing $N_{\text{RIS}} - 1$ zeros and a single one entry. Here, we consider *orthogonal* pilot sequences. Rewriting eq. (3.14) as:

$$\begin{aligned} y_{k,n,t} &= (s_{k,t} \mathbf{w}_{s,t}) \mathbf{h}_{\text{R},k,n} + n_{n,t} \\ &= \boldsymbol{\psi}_{k,t} \mathbf{h}_{\text{R},k,n} + n_{n,t}, \end{aligned} \tag{3.15}$$

where $\boldsymbol{\psi}_{k,t} = s_{k,t} \mathbf{w}_{s,t}$ is the measurement vector in the t-th time slot for the k-th UE, while $\overline{\mathbf{h}}_{\text{R},k,n} = \boldsymbol{\psi}_{k,t} \mathbf{h}_{\text{R},k,n}$ is the the sampled channel vector from the active RIS elements used to estimate the full channel vector $\mathbf{h}_{\text{R},k,n}$.

Note that the number of measurements in each time slot equals the number of RF chains. As we are proposing a low-hardware complexity structure, only 1 RF chain

is adopted to conserve energy and reduce costs. Hence, the number of measurements is equal to the number of active elements ($T = N_{\text{act}}$) being successively turned on over T time slots, resulting in the following full observation vector in each subcarrier n

$$\begin{aligned} \mathbf{y}_{k,n} &= [y_{k,n,1}, y_{k,n,2}, \ \ldots, \ y_{k,n,T}]^T \\ &= \boldsymbol{\Psi}_k \mathbf{h}_{\mathrm{R},k,n} + \mathbf{n}_k, \end{aligned} \tag{3.16}$$

$\boldsymbol{\Psi}_k = \left[(\boldsymbol{\psi}_{k,1})^T, (\boldsymbol{\psi}_{k,2})^T, \ \ldots, \ (\boldsymbol{\psi}_{k,T})^T\right]^T \in \mathbb{C}^{M \times N_{\text{RIS}}}$ representing the full measurement matrix for the k-th UE, and $\mathbf{n}_n = [n_{n,1}, \ n_{n,2}, \ \ldots, \ n_{n,T}]^T$ is the stacked noise vector.

3.3.3 Compressive Sensing-Based Channel Estimation Approach

3.3.3.1 Narrowband scenario

In mmWave systems, the number of paths L is usually small (around 3-5), resulting in sparse scattering. We consider that the N_{act} active channel sensors are randomly selected from the passive RIS panel and $N_{\text{act}} \ll N_{\text{RIS}}$. Adopting the angular-domain representation of the MIMO channels, it is possible to estimate the full channel vector $\mathbf{H}_k$ from the aggregate observation vector $\mathbf{y}_k$ by employing the CS-based theory to solve this CE problem. First, we design a redundant dictionary and rewrite the channel $\mathbf{H}_{\mathrm{R},k}$ in (3.3) in the angular-domain, represented by:

$$\mathbf{H}_{\mathrm{R},k} = \mathbf{A}_{\mathrm{R}} \overline{\mathbf{H}}_{\mathrm{R},k} \mathbf{A}_{\mathrm{T}}^H + \mathbf{Q}_e, \tag{3.17}$$

where $\mathbf{Q}_e$ represents the quantization error matrix, $\overline{\mathbf{H}}_{\mathrm{R},k}$ is an approximate $\overline{L}$-sparse angular-domain representation of the channel in the redundant dictionary, where $\mathbf{A}_{\mathrm{R}}$ and $\mathbf{A}_{\mathrm{T}}$ are the receiver and transmitter dictionaries, respectively. Then, considering a UPA structure in the RIS, and ULA arrays for mobile users, in the UL, the receiver and transmitter dictionaries matrices can be described, respectively, as:

$$\begin{aligned} \mathbf{A}_{\mathrm{R}} &= [\mathbf{a}(\vartheta_{R,1}, \varphi_{R,1}), \ldots, \mathbf{a}(\vartheta_{R,1}, \varphi_{R,N_{R,\text{el}}}), \ldots, \\ &\quad \mathbf{a}(\vartheta_{R,N_{R,\text{az}}}, \varphi_{R,N_{R,\text{el}}})], \end{aligned} \tag{3.18}$$

$$\mathbf{A}_{\mathrm{T}} = [\mathbf{a}(\vartheta_{T,1}), \ldots, \mathbf{a}(\vartheta_{T,N_{T,\text{az}}})], \tag{3.19}$$

with $\vartheta_{R,\ell}$, $\varphi_{R,\ell}$, and $\vartheta_{T,\ell}$ being selected from uniformly distributed angle grids in the range of $[-\pi/2, \pi/2]$, given by:

$$\begin{cases} \vartheta_{R,\ell} &= -\frac{\pi}{2} + \ell \frac{\pi}{N_{R,\text{az}}}, \quad \ell = 1, 2, \ldots, N_{R,\text{az}}, \\ \varphi_{R,\ell} &= -\frac{\pi}{2} + \ell \frac{\pi}{N_{R,\text{el}}}, \quad \ell = 1, 2, \ldots, N_{R,\text{el}}, \\ \vartheta_{T,\ell} &= -\frac{\pi}{2} + \ell \frac{\pi}{N_{T,\text{az}}}, \quad \ell = 1, 2, \ldots, N_{T,\text{az}}. \end{cases}$$

The number of grid points in the azimuth and elevation dictionaries is $N_{R,\text{az}} = \gamma N_{\text{RIS},h}$, $N_{R,\text{ele}} = \gamma N_{\text{RIS},v}$ and $N_{T,\text{az}} = \gamma N_{\text{UE}}$, respectively, in which γ is the *oversampling*

factor. If the grid sizes are large enough, the azimuth and elevation angles ($\vartheta_{R,l}$, $\varphi_{R,l}$, $\vartheta_{T,l}$, $\forall l$) match exactly L points in the redundant dictionary, which is a common assumption in the formulations considering sparse CE approaches. Substituting (3.17) into (3.13), we obtain

$$\begin{aligned}\mathbf{y}_k &= \mathbf{\Phi}_k \text{vec}\left(\mathbf{A}_\text{R}\overline{\mathbf{H}}_{\text{R},k}\mathbf{A}_\text{T}^H + \mathbf{Q}_e\right) + \mathbf{n}_k \\ &= \mathbf{\Phi}_k\mathbf{\Psi}\overline{\mathbf{h}}_{\text{R},k} + \mathbf{n}_{\text{E},k} \\ &= \mathbf{\Upsilon}_k\overline{\mathbf{h}}_{\text{R},k} + \mathbf{n}_{\text{E},k}, \end{aligned} \tag{3.20}$$

where $\mathbf{\Psi} = (\mathbf{A}_\text{T})^* \otimes \mathbf{A}_\text{R}$ denotes the redundant dictionary matrix, $\mathbf{\Upsilon}_k = \mathbf{\Phi}_k\mathbf{\Psi}$ is the sensing matrix of the k-th user, $\overline{\mathbf{h}}_{\text{R},k} = \text{vec}(\overline{\mathbf{H}}_{\text{R},k})$ denotes the vectorized sparse formulation under the basis of redundant dictionary, and $\mathbf{n}_{\text{E},k} = \mathbf{\Phi}\text{vec}(\mathbf{Q}_e) + \mathbf{n}_k$ denotes the effective noise.

The objective is to estimate the sparse vector $\overline{\mathbf{h}}_{\text{R},k}$ that solves the non-convex combinatorial problem

$$\begin{aligned} \underset{\overline{\mathbf{h}}_{\text{R},k}}{\text{minimize}} \quad & \|\overline{\mathbf{h}}_{\text{R},k}\|_0 \\ \text{s.t.} \quad & \|\mathbf{\Phi}_k\mathbf{\Psi}\overline{\mathbf{h}}_{\text{R},k} - \mathbf{y}_k\|_2 \leq \sigma. \end{aligned} \tag{3.21}$$

Previous solutions: Several works in the literature propose to solve this problem by applying CS-based approaches. For instance, in (TAHA et al., 2021) an MP-based approach and a grid of size $N_{R,\text{az}} = 2N_{\text{RIS},h}$; $N_{R,\text{el}} = 2N_{\text{RIS},v}$ are used to find an approximate solution for $\overline{\mathbf{h}}_{\text{R},k}$. However, this solution presents a poor performance even for a SISO setup. Increasing the oversampling of the discretized grids (γ) to deal with the power leakage problem leads to high computational complexity, especially in MIMO configurations, making the problem almost intractable and resulting in poor CE performance. Additionally, the authors in (WU et al., 2022) propose a low-rank matrix completion (LRMC) solution based on the *nuclear norm minimization* (NNM) to solve this CE problem. However, this algorithm requires the knowledge of a significant number of measurements to work satisfactorily; otherwise, the CE performance is inferior.

3.3.3.2 Wideband scenario

For a wideband solution we have a similar problem as stated previously, but now multiple measurements. Them, adopting the angular-domain representation of the channels, it is possible to obtain an estimation of the entire channel vector $\mathbf{h}_{\text{R},k,n}$ from the aggregate observation vector $\mathbf{y}_{k,n}$ by employing the CS-based theory to solve this CE problem. First, we design a redundant dictionary and rewrite the channel $\mathbf{h}_{\text{R},k,n}$ in (3.10) in the angular-domain:

$$\mathbf{h}_{\text{R},k,n} = \mathbf{A}_\text{R}\widehat{\mathbf{h}}_{\text{R},k,n} + \mathbf{q}_e, \tag{3.22}$$

where $\mathbf{q}_e$ represents the quantization error vector, $\widehat{\mathbf{h}}_{\text{R},k,n}$ is an approximate $\overline{L}$-sparse angular-domain representation of the channel in the redundant dictionary, where $\mathbf{A}_\text{R}$ is the receiver dictionary as in (3.18).

Substituting (3.22) into (3.16), we obtain

$$\begin{aligned} \mathbf{y}_{k,n} &= \boldsymbol{\Psi}_k \left(\mathbf{A}_{\mathrm{R}} \widehat{\mathbf{h}}_{\mathrm{R},k,n} + \mathbf{q}_e \right) + \mathbf{n}_k \\ &= \boldsymbol{\Upsilon}_k \widehat{\mathbf{h}}_{\mathrm{R},k,n} + \mathbf{n}_{\mathrm{E},k}, \end{aligned} \tag{3.23}$$

where $\boldsymbol{\Upsilon}_k = \boldsymbol{\Psi}_k \mathbf{A}_{\mathrm{R}}$ is the sensing matrix of the k-th user, and $\mathbf{n}_{\mathrm{E},k} = \boldsymbol{\Psi}_k \mathbf{q}_e + \mathbf{n}_k$ denotes the effective noise.

The objective is to estimate the sparse matrix $\widehat{\mathbf{H}}_{\mathrm{R},k}$ that solves the non-convex combinatorial problem:

$$\begin{aligned} \underset{\widehat{\mathbf{H}}_{\mathrm{R},k}}{\text{minimize}} \quad & \left(\sum_{n=1}^{N_{\mathrm{SC}}} \| \widehat{\mathbf{H}}_{\mathrm{R},k}(:,n) \|_0^2 \right)^{\frac{1}{2}} \\ \text{s.t.} \quad & \| \boldsymbol{\Upsilon}_k \widehat{\mathbf{H}}_{\mathrm{R},k} - \mathbf{Y}_k \|_2 \leq \epsilon. \end{aligned} \tag{3.24}$$

where $\{\widehat{\mathbf{H}}_{\mathrm{R},k}(:,n)\}_{n=1}^{N_{\mathrm{SC}}}$ share the common sparse support set, $\|\widehat{\mathbf{H}}_{\mathrm{R},k}(:,n)\|_0$ is the number of non-zero elements of $\widehat{\mathbf{H}}_{\mathrm{R},k}(:,n)$, $\widehat{\mathbf{H}}_{\mathrm{R},k} = [\widehat{\mathbf{h}}_{\mathrm{R},k,0},\ \widehat{\mathbf{h}}_{\mathrm{R},k,1},\ \ldots,\ \widehat{\mathbf{h}}_{\mathrm{R},k,N_{\mathrm{SC}}}]$, $\mathbf{Y}_k = [\mathbf{y}_{k,1},\ \mathbf{y}_{k,2},\ \ldots,\ \mathbf{y}_{k,N_{\mathrm{SC}}}] \in \mathbb{C}^{N_{\mathrm{act}} \times N_{\mathrm{SC}}}$ is the sampled received signal of the k-th user from all over the subcarriers.

3.4 Proposed Channel Estimation Method for RIS-Aided mmWave Communication

3.4.1 MP with phase rotation (MP-PR) method

To improve the estimates of the BS-RIS and UE-RIS channels while keeping such estimation process as simple as possible, an MP-based method, namely, MP with phase rotation (MP-PR), is proposed herein to obtain the virtual channel gains in the angular-domain represented by a redundant dictionary. Basically, we exploit the sparsity structure of the problem in mmWave channels, in which we have at most $L+1$ channel paths (LoS and L NLoS paths). First of all, let us consider a simplified one-dimension dictionary, for simplicity of exposition, $\mathbf{A} = [\mathbf{a}(\vartheta_1),\ \ldots,\ \mathbf{a}(\vartheta_L)] \in \mathbb{C}^{N \times L}$, similar to that as in eq. (3.19). The asymptotic properties of $\mathbf{A}$ are presented in the following lemmas, and the proofs of them are available in (ZHOU et al., 2022) (Appendices A and B).

Lemma 1: For $N \to \infty$, the following property holds

$$\lim_{N \to \infty} \frac{1}{N} \mathbf{a}^H(\vartheta_i) \mathbf{a}(\vartheta_j) = \begin{cases} 1, & \vartheta_i = \vartheta_j \\ 0, & \text{otherwise} \end{cases}, \tag{3.25}$$

also implying that $\mathbf{A}^H \mathbf{A} = N \mathbf{I}_L$.

Lemma 2: For $N \to \infty$, and considering that $\frac{d_s}{\lambda} \leq \frac{1}{2}$ to avoid angle ambiguity, the DFT of $\mathbf{A}$, *i.e.*, $\mathbf{U}^H \mathbf{A}$, exhibits a tall sparse matrix, containing only one nonzero element in each column

$$\lim_{N \to \infty} [\mathbf{U}^H \mathbf{A}]_{n_\ell, \ell} \neq 0, \forall \ell, \tag{3.26}$$

where $\mathbf{U} \in \mathbb{C}^{N\times N}$ is the normalized DFT matrix, and $n_\ell = N\vartheta_\ell + 1$ for $\vartheta_\ell \in [0, \frac{d_s}{\lambda})$.

It can be noticed that since $\vartheta_\ell \in [0, \frac{d_s}{\lambda})$, the range of n_ℓ is $n_\ell \in [1, N\frac{d_s}{\lambda} + 1)$. In addition, based on eq. (3.26) matrix $\mathbf{U}^H\mathbf{A}$ can be regarded as a row sparse matrix with full column rank. As N is finite in practice, and thus $N\vartheta_\ell$ is usually not an integer, most of the power of $\mathbf{U}^H\mathbf{A}$ will be concentrated in the $(\lceil N\vartheta_\ell \rfloor + 1)$th row, where $\lceil\cdot\rfloor$ rounds to the closest integer, while the remaining power leaks to nearby rows. This effect is known as the *power leakage*. Since the DFT resolution is $1/N$, a mismatch exists between the estimated discrete and real continuous angles. Note that this analysis can be easily extended to the redundant dictionary $\mathbf{\Psi}$ in eq. (3.20). To improve the CE of the RIS-aided system, we propose the MP-PR to deal with the power leakage problem caused by the mismatch of the redundant dictionary. The functionality of the proposed technique is described as follows, while Fig. 3.3 gives us an overview of the proposed CE method.

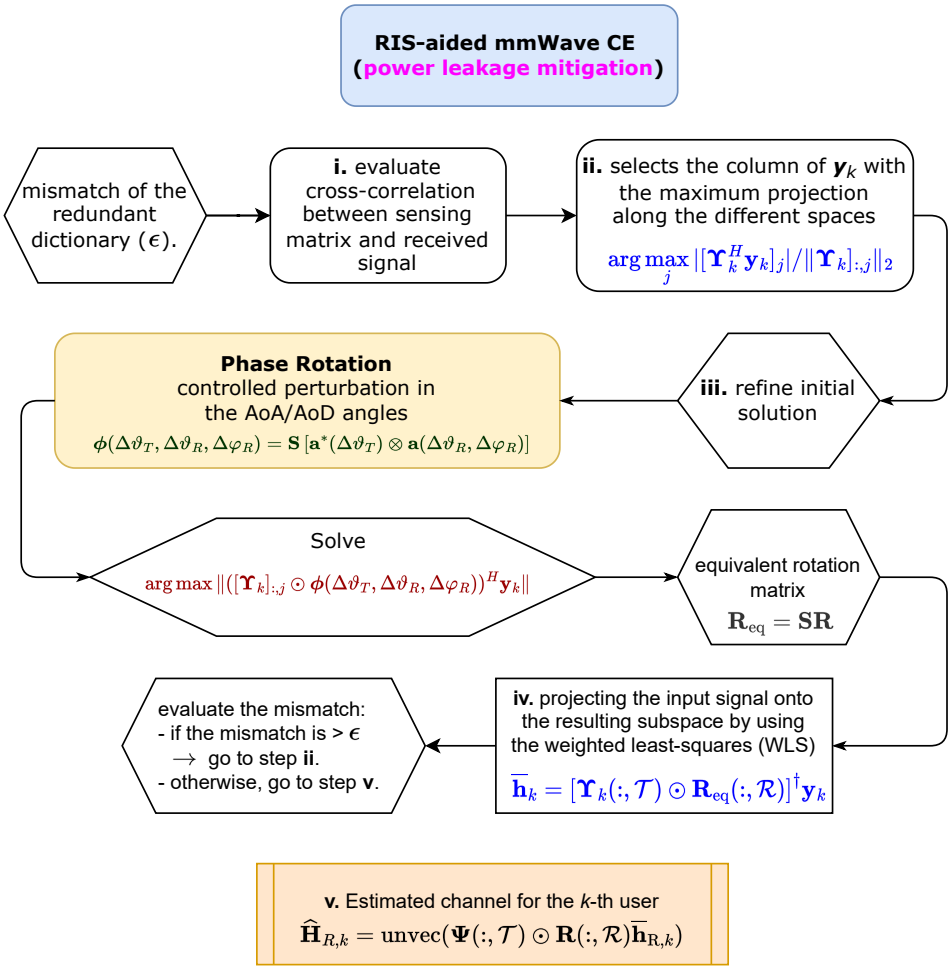

Figure 3.3 – An overview for the proposed channel estimation method for RIS-aided mmWave communications.

For each iteration, the proposed algorithm proceeds with five steps: ***i***) it evaluates the correlation between the sensing matrix ($\boldsymbol{\Upsilon}_k$) and the received signal ($\mathbf{y}_k$); ***ii***) selects the column of $\boldsymbol{\Upsilon}_k$ with the maximum projection along the different spaces. Each column index the algorithm selects is stored in the $\mathcal{T}$ set. As different scatterers have different

angles, we can conclude that all indexes of $\mathcal{T}$ are different, *i.e.*, they are not in the same row. This operation is summarized as

$$\arg\max_{j} |[\boldsymbol{\Upsilon}_k^H \mathbf{y}_k]_j| / \|\boldsymbol{\Upsilon}_k]_{:,j}\|_2. \tag{3.27}$$

iii) Refine the initial solution: to mitigate the power leakage of this initial estimation, we apply a phase rotation (controlled perturbation in AoA/AoD) to refine this preliminary solution. This phase rotation is defined as

$$\boldsymbol{\phi}(\Delta\vartheta_T, \Delta\vartheta_R, \Delta\varphi_R) = \mathbf{S}\left[\mathbf{a}^*(\Delta\vartheta_T) \otimes \mathbf{a}(\Delta\vartheta_R, \Delta\varphi_R)\right] \tag{3.28}$$

where $\Delta\vartheta_T$, $\Delta\vartheta_R$, and $\Delta\varphi_R$ are the azimuth AoD, azimuth AoA, and elevation AoA phase rotations, and $\mathbf{S} = \mathbf{1}_{N_{\text{UE}}} \otimes \mathbf{W}_S$ is the equivalent selection matrix, with $\mathbf{1}_{N_{\text{UE}}}$ being a vector of ones of dimension $1 \times N_{\text{UE}}$, and $\mathbf{W}_S = [\mathbf{W}_{S,1},\ \ldots,\ \mathbf{W}_{S,T}] \in \mathbb{Z}^{M \times N_{\text{RIS}}}$ the stacked selection matrices.

In this case, the optimal phase rotation parameters $\Delta\vartheta_T$, $\Delta\vartheta_R$, and $\Delta\varphi_R$ can be found based on a three-dimensional search by solving the following problem

$$\begin{aligned}[\Delta\vartheta_T,\ \Delta\vartheta_R,\ \Delta\varphi_R] = \\ \arg\max \|([\boldsymbol{\Upsilon}_k]_{:,j} \odot \boldsymbol{\phi}(\Delta\vartheta_T, \Delta\vartheta_R, \Delta\varphi_R))^H \mathbf{y}_k\|,\end{aligned} \tag{3.29}$$

where phase rotation parameter values are confined in the following ranges: $\Delta\vartheta_T \in \left[-\frac{\pi}{N_{T,\text{az}}}, \frac{\pi}{N_{T,\text{az}}}\right]$, $\Delta\vartheta_R \in \left[-\frac{\pi}{N_{R,\text{az}}}; \frac{\pi}{N_{R,\text{az}}}\right]$, and $\Delta\varphi_R \in \left[-\frac{\pi}{N_{R,\text{ele}}}, \frac{\pi}{N_{R,\text{ele}}}\right]$,

One option to solve the problem in eq. (3.29) is to perform a targeted search based on a predefined phase rotation matrix. Hence, the angle rotation matrix can be defined as

$$\begin{aligned}\mathbf{R} = [\mathbf{a}^*(\Delta\vartheta_{T,1}), \ldots, \mathbf{a}^*(\Delta\vartheta_{T,N_{\text{UE}}})] \otimes [\mathbf{a}(\Delta\vartheta_{R,1}, \Delta\varphi_{R,1}), \ldots, \\ \mathbf{a}(\Delta\vartheta_{R,1}, \Delta\varphi_{R,N_{\text{RIS},v}}), \ldots, \mathbf{a}(\Delta\vartheta_{R,N_{\text{RIS},h}}, \Delta\varphi_{R,N_{\text{RIS},v}})],\end{aligned} \tag{3.30}$$

where $\Delta\vartheta_{T,l}$, $\Delta\vartheta_{R,l}$, and $\Delta\varphi_l$ are uniformly phase shifts selected in the range described above. Hence, the uniform phase shifts result in:

$$\begin{aligned}\Delta\vartheta_{T,l} &= -\frac{\pi}{N_{T,\text{az}}} + \frac{2l\pi}{N_{T,\text{az}} N_{\text{UE}}},\ l = 1, 2, \ldots, N_{\text{UE}}, \\ \Delta\vartheta_{R,l} &= -\frac{\pi}{N_{R,\text{az}}} + \frac{2l\pi}{N_{R,\text{az}} N_{\text{RIS},h}},\ l = 1, 2, \ldots, N_{\text{RIS},h}, \\ \Delta\varphi_l &= -\frac{\pi}{N_{R,\text{ele}}} + \frac{2l\pi}{N_{R,\text{ele}} N_{\text{RIS},v}},\ l = 1, 2, \ldots, N_{\text{RIS},v}.\end{aligned} \tag{3.31}$$

Note that $\mathbf{R}$ is an $N_{\text{UE}}N_{\text{RIS}} \times N_{\text{UE}}N_{\text{RIS}}$ matrix, however, as the received signal corresponds to the active elements of the RIS, the phase rotation may consider only these elements, and so the equivalent rotation matrix is obtained multiplying the phase rotation matrix by the equivalent selection matrix $\mathbf{R}_{\text{eq}}$ as

$$\mathbf{R}_{\text{eq}} = \mathbf{S}\mathbf{R} \quad \in \mathbb{C}^{M \times N_{\text{UE}}N_{\text{RIS}}} \tag{3.32}$$

Algorithm 3 Phase Rotation (PR) Evaluation

Input $\mathbf{r}^{[i-1]},\ \boldsymbol{\Upsilon}_k,\ \mathbf{R}_{\text{eq}},\ j^{[i]}$
$\boldsymbol{\Upsilon}_R = \boldsymbol{\Upsilon}_k(:, j^{[i]}) \odot \mathbf{R}_{\text{eq}}$
$\mathbf{r}_{\text{PR}}^{[i]} = \boldsymbol{\Upsilon}_R^H \mathbf{r}^{[i-1]}$
$\varrho^{[i]} = \arg\max_\ell |[\mathbf{r}_{\text{PR}}^{[i]}]_\ell| / \|[\boldsymbol{\Upsilon}_R]_{:,\ell}\|_2$
Output $\varrho^{[i]}$

Moreover, the set $\mathcal{R}$ contains the selected phase rotation indexes from matrix $\mathbf{R}_{\text{eq}}$. Algorithm 3 presents the problem's solution in eq. (3.30).

iv) After obtaining the sensing support columns and the phase rotation angles, we can evaluate the virtual channel gains $\overline{\mathbf{h}}_{\text{R},k}$ by projecting the input signal onto the resulting subspace using the *weighted least-squares* (WLS) method given as

$$\overline{\mathbf{h}}_k = [\boldsymbol{\Upsilon}_k(:, \mathcal{T}) \odot \mathbf{R}_{\text{eq}}(:, \mathcal{R})]^\dagger \mathbf{y}_k. \tag{3.33}$$

v) Finally, the *estimated channel* for the k-th user is obtained:

$$\widehat{\mathbf{H}}_{\text{R},k} = \text{unvec}(\boldsymbol{\Psi}(:, \mathcal{T}) \odot \mathbf{R}(:, \mathcal{R}) \overline{\mathbf{h}}_{\text{R},k}). \tag{3.34}$$

Algorithm 4 MP with Phase Rotation (MP-PR)

Input $\mathbf{y}_k,\ \boldsymbol{\Psi},\ \boldsymbol{\Phi}_k,\ \mathbf{R},\ \mathbf{R}_{\text{eq}},\ \epsilon,\ \mathcal{I}_{\max}$
Initialize $\mathbf{r}^{[0]} = \mathbf{y}_k$, $\overline{\mathbf{h}}_k^{[0]} = \mathbf{0}$, $\boldsymbol{\Upsilon}_k = \boldsymbol{\Phi}_k \boldsymbol{\Psi}$, $\mathcal{T}^{[0]} = \emptyset$, $\mathcal{R}^{[0]} = \emptyset$, $i = 1$, MSE $= 2\epsilon$
while MSE $> \epsilon$ or $i > \mathcal{I}_{\max}$ **do**
  $\mathbf{g}^{[i]} = \boldsymbol{\Upsilon}_k^H \mathbf{r}^{[i-1]}$
  $\mathcal{J}^{[i]} = \arg\max_j |[\mathbf{g}^{[i]}]_j| / \|[\boldsymbol{\Upsilon}_k]_{:,j}\|_2$, with $j^{[i]} \neq j^{[i-1]}$
  $\mathcal{T}^{[i]} = \mathcal{T}^{[i-1]} \cup \mathcal{J}^{[i]}$
  Obtain support column index $\varrho^{[i]}$ of $\mathbf{R}_{\text{eq}}$, Algorithm 3
  $\mathcal{R}^{[i]} = \mathcal{R}^{[i-1]} \cup \varrho^{[i]}$
  $\overline{\mathbf{h}}_k^{[i]} = \left[\boldsymbol{\Upsilon}_k(:, \mathcal{T}^{[i]}) \odot \mathbf{R}_{\text{eq}}(:, \mathcal{R}^{[i]})\right]^\dagger \mathbf{y}_k$
  $\mathbf{r}^{[i]} = \mathbf{y}_k - \boldsymbol{\Upsilon}_k(:, \mathcal{T}^{[i]}) \odot \mathbf{R}_{\text{eq}}(:, \mathcal{R}^{[i]}) \overline{\mathbf{h}}_k^{[i]}$
  MSE $= \frac{1}{N_{\text{UE}}} \text{Tr}\left[(\mathbf{r}^{[i]})^H \mathbf{r}^{[i]}\right]$
  $i := i + 1$
end while
Output $\widehat{\mathbf{H}}_{\text{R},k} = \text{unvec}(\boldsymbol{\Psi}(:, \mathcal{T}) \odot \mathbf{R}(:, \mathcal{R}) \overline{\mathbf{h}}_{\text{R},k})$

3.4.2 SMP with phase rotation (SMP-PR) method

For each iteration, the proposed algorithm proceeds with five steps: ***i***) it evaluates the correlation between the sensing matrix ($\boldsymbol{\Upsilon}_k$) and the received signal ($\mathbf{y}_k$); ***ii***) selects the column of $\boldsymbol{\Upsilon}_k$ with the maximum projection along the different spaces. Each column index the algorithm selects is stored in the $\mathcal{T}$ set. As different scatterers have different

angles, we can conclude that all indices of $\mathcal{T}$ are different, *i.e.*, they are not in the same row. This operation is summarized as

$$\arg\max_{j} |[\boldsymbol{\Upsilon}_k^H \mathbf{Y}_k]_j| / \|\boldsymbol{\Upsilon}_k]_{:,j}\|_2, \tag{3.35}$$

where $\mathbf{Y}_k = [\mathbf{y}_{k,1},\ \mathbf{y}_{k,2},\ \ldots,\ \mathbf{y}_{k,N_{\text{SC}}}] \in \mathbb{C}^{N_{\text{act}} \times N_{\text{SC}}}$ is the sampled received signal of the k-th user from all over the subcarriers.

iii) Refine the initial solution: to mitigate the power leakage of this initial estimation, we apply a phase rotation (controlled perturbation in AoA) to refine this preliminary solution. This phase rotation is defined as

$$\boldsymbol{\phi}(\Delta\vartheta_R, \Delta\varphi_R) = \mathbf{W}_S \mathbf{a}(\Delta\vartheta_R, \Delta\varphi_R), \tag{3.36}$$

where $\Delta\vartheta_R$, and $\Delta\varphi_R$ are azimuth AoA, and elevation AoA phase rotations, and $\mathbf{W}_S = [(\mathbf{w}_{s,1})^T,\ (\mathbf{w}_{s,2})^T,\ \ldots,\ (\mathbf{w}_{s,T})^T]^T \in \mathbb{Z}^{N_{\text{act}} \times M}$ the stacked selection matrices.

In this case, the optimal phase rotation parameters $\Delta\vartheta_T$, $\Delta\vartheta_R$, and $\Delta\varphi_R$ can be found based on a three-dimensional search by solving the following problem

$$\begin{aligned} &[\Delta\vartheta_R,\ \Delta\varphi_R] = \\ &\arg\max \|([\boldsymbol{\Upsilon}_k]_{:,j} \odot \boldsymbol{\phi}(\Delta\vartheta_R, \Delta\varphi_R))^H \mathbf{Y}_k\|, \end{aligned} \tag{3.37}$$

where phase rotation parameter values are confined to the following ranges: $\Delta\vartheta_R \in \left[-\frac{\pi}{N_{\text{az}}}; \frac{\pi}{N_{\text{az}}}\right]$, and $\Delta\varphi_R \in \left[-\frac{\pi}{N_{\text{ele}}}, \frac{\pi}{N_{\text{ele}}}\right]$. One option to solve the problem in eq. (3.37) is to perform a targeted search based on a predefined phase rotation matrix. Hence, the angle rotation matrix can be defined systematically as

$$\begin{aligned} \mathbf{R} \ &= \mathbf{a}(\Delta\vartheta_{R,1}, \Delta\varphi_{R,1}), \ldots, \mathbf{a}(\Delta\vartheta_{R,1}, \Delta\varphi_{R,M_v}), \\ &\quad \ldots, \mathbf{a}(\Delta\vartheta_{R,M_h}, \Delta\varphi_{R,M_v}), \end{aligned} \tag{3.38}$$

where $\Delta\vartheta_{R,l}$ and $\Delta\varphi_l$ are uniformly phase shifts selected in the range described above. Hence, the uniform phase shifts result in:

$$\begin{aligned} \Delta\vartheta_{R,l} &= -\frac{\pi}{N_{\text{az}}} + \frac{2l\pi}{N_{\text{az}} M_h},\ l = 1, 2, \ldots, M_h, \\ \Delta\varphi_l &= -\frac{\pi}{N_{\text{ele}}} + \frac{2l\pi}{N_{\text{ele}} M_v},\ l = 1, 2, \ldots, M_v. \end{aligned}$$

Note that $\mathbf{R}$ is an $M \times M$ matrix. However, as the received signal corresponds to the active elements of the RIS, the phase rotation may consider only these elements, and so the equivalent rotation matrix is obtained by multiplying the phase rotation matrix by the equivalent selection matrix $\mathbf{R}_{\text{eq}} \in \mathbb{C}^{N_{\text{act}} \times M}$ as

$$\mathbf{R}_{\text{eq}} = \mathbf{W}_S \mathbf{R}. \tag{3.39}$$

Moreover, the set $\mathcal{R}$ contains the selected phase rotation indices from matrix $\mathbf{R}_{\text{eq}}$. Lines 8-10 of Algorithm 5 demonstrates how to obtain the problem's solution in eq. (3.38).

iv) After obtaining the sensing support columns and the phase rotation angles, we can evaluate the virtual channel gains $\widehat{\mathbf{H}}_{\mathrm{R},k}$ by projecting the input signal onto the resulting subspace using the *weighted least-squares* (WLS) method given as

$$\widehat{\mathbf{H}}_{\mathrm{R},k} = \left[\boldsymbol{\Upsilon}_k(:,\mathcal{T}) \odot \mathbf{R}_{\mathrm{eq}}(:,\mathcal{R})\right]^{\dagger} \mathbf{Y}_k. \tag{3.40}$$

v) Finally, the *estimated channel* for the k-th user is obtained as

$$\widetilde{\mathbf{H}}_{\mathrm{R},k} = \mathbf{A}_{\mathrm{R}}(:,\mathcal{T}) \odot \mathbf{R}(:,\mathcal{R})\widehat{\mathbf{H}}_{\mathrm{R},k}. \tag{3.41}$$

Algorithm 5 describes the steps of the proposed solution. The proof of convergence for the algorithm 5 is available in Appendix A.

Algorithm 5 SMP with Phase Rotation (SMP-PR)

Input $\mathbf{Y}_k$, $\mathbf{A}_{\mathrm{R}}$, $\boldsymbol{\Psi}_k$, $\mathbf{W}_S$, $\mathbf{R}$, $\mathbf{R}_{\mathrm{eq}}$, ϵ, $\mathcal{I}_{\max}$
Initialize $\mathbf{R}_{\mathrm{res}}^{[0]} = \mathbf{Y}_k$, $\widehat{\mathbf{H}}_{\mathrm{R},k}^{[0]} = \mathbf{0}$, $\boldsymbol{\Upsilon}_k = \boldsymbol{\Psi}_k\mathbf{A}_{\mathrm{R}}$, $\mathcal{T}^{[0]} = \emptyset$, $\mathcal{R}^{[0]} = \emptyset$, $i = 1$, $\mathrm{MSE} = 2\epsilon$
while $\mathrm{MSE} > \epsilon$ or $i > \mathcal{I}_{\max}$ **do**
  $\mathbf{P}^{[i]} = \boldsymbol{\Upsilon}_k^H \mathbf{R}_{\mathrm{res}}^{[i-1]}$
  $\mathcal{J}^{[i]} = \arg\max_j |[\mathbf{P}^{[i]}]_j| / \|[\boldsymbol{\Upsilon}_k]_{:,j}\|_2$, with $j^{[i]} \neq j^{[i-1]}$
  $\mathcal{T}^{[i]} = T^{[i-1]} \cup \mathcal{J}^{[i]}$
  $\boldsymbol{\Upsilon}_R = \boldsymbol{\Upsilon}_k(:, j^{[i]}) \odot \mathbf{R}_{\mathrm{eq}}$
  $\mathbf{R}_{\mathrm{PR}}^{[i]} = \boldsymbol{\Upsilon}_R^H \mathbf{R}_{\mathrm{res}}^{[i-1]}$
  $\varrho^{[i]} = \arg\max_\ell |[\mathbf{R}_{\mathrm{PR}}^{[i]}]_\ell| / \|[\boldsymbol{\Upsilon}_R]_{:,\ell}\|_2$
  $\mathcal{R}^{[i]} = \mathcal{R}^{[i-1]} \cup \varrho^{[i]}$
  $\widehat{\mathbf{H}}_{\mathrm{R},k}^{[i]} = \left[\boldsymbol{\Upsilon}_k(:,\mathcal{T}) \odot \mathbf{R}_{\mathrm{eq}}(:,\mathcal{R})\right]^{\dagger} \mathbf{Y}_k$
  $\mathbf{R}_{\mathrm{res}}^{[i]} = \mathbf{Y}_k - \boldsymbol{\Upsilon}_k(:,\mathcal{T}^{[i]}) \odot \mathbf{R}_{\mathrm{eq}}(:,\mathcal{R}^{[i]})\widehat{\mathbf{H}}_{\mathrm{R},k}^{[i]}$
  $\mathrm{MSE} = \frac{1}{N_{\mathrm{act}} N_{\mathrm{SC}}} \mathrm{Tr}\left[(\mathbf{R}_{\mathrm{res}}^{[i]})^H \mathbf{R}_{\mathrm{res}}^{[i]}\right]$
  $i := i + 1$
end while
Output $\widetilde{\mathbf{H}}_{\mathrm{R},k} = \mathbf{A}_{\mathrm{R}}(:,\mathcal{T}) \odot \mathbf{R}(:,\mathcal{R})\widehat{\mathbf{H}}_{\mathrm{R},k}$

With the estimated CSI between the RIS-BS and UEs/RIS in hand, the RIS reflection coefficients are optimized via RIS controller link. Finally, the RIS-aided system operates in *reflection mode* to assist data transmission between the BS and mobile users.

3.4.3 Complexity analysis

The computational complexity of a CE method can be analyzed in terms of the number of *floating point operations* (FLOPs). One FLOP is computed as a complex/real multiplication or a complex/real summation. We assume that real and complex operations have the exact computational cost for simplicity and compactness of analysis, although complex operations generally have more computational cost. Herein, we consider that transposition, Hermitian, conjugate, and real-part operators require no FLOP and, therefore, are not considered in our analysis.

The number of FLOPs required for the main operations of the analyzed algorithms is depicted in Table 3.1, which summarizes the computational cost in terms of the number

of FLOPs for each operation (GOLUB; LOAN, 2013). In addition, the full complexity expressions denoted by Υ are shown in Table 3.2.

Table 3.1 – Number of FLOPs for vector and matrices operations: $\mathbf{w} \in \mathbb{R}^{q\times 1}, \mathbf{A} \in \mathbb{R}^{m\times q}, \mathbf{B} \in \mathbb{R}^{q\times p}, \mathbf{C} \in \mathbb{R}^{m\times q}, \mathbf{D} \in \mathbb{R}^{q\times q}$

Operation	# FLOPs (GOLUB; LOAN, 2013)
Matrix-matrix multiply $\mathbf{AB}$	$mp(2q-1)$
Scalar-matrix multiply $\beta\mathbf{A}$	mq
Matrix-vector multiplication $\mathbf{Aw}$	$m(2q-1)$
Matrix-matrix add $\mathbf{A}+\mathbf{C}$	mq
Matrix inversion: LU factorization of $\mathbf{D}$ (GOLUB; LOAN, 2013)	$2/3q^3+2q^2$

Table 3.2 – Number of FLOPs per iteration for the CE algorithms

Algorithm	**Number of Operations**
Υ_{OMP}	$N_{\text{RIS}}(N_{\text{act}}+1)+\frac{2}{3}L^3+2L^2+N_{\text{act}}(L^2+4L+1)-L-2$
Υ_{MP}	$\gamma^2 N_{\text{RIS}}(N_{\text{act}}+1)+\frac{2}{3}L^3+2L^2+N_{\text{act}}(L^2+4L+1)-L-2$
$\Upsilon_{\text{OMP-PR}}$	$N_{\text{RIS}}(N_{\text{act}}+1)+\frac{2}{3}L^3+2L^2+N_{\text{act}}[L^2+4(N_{\text{RIS}}+L)+1]-L-2$
$\Upsilon_{\text{MP-PR}}$	$\gamma^2 N_{\text{RIS}}(N_{\text{act}}+1)+\frac{2}{3}L^3+2L^2+N_{\text{act}}[L^2+4(N_{\text{RIS}}+L)+1]-L-2$

γ: *oversampling factor*

Note that both analyzed algorithms have a variable number of operations in each iteration since the sizes of some matrices and vectors change with the execution step of their respective `for` loops. Therefore, for comparison purposes only, we extrapolate the complexity value considering the worst case, *i.e.*, the last iteration of the algorithms, where the maximum number of mathematical operations occurs. Therefore, in practice, the complexity of both algorithms should be even lower.

From Table 3.2, one can infer that the proposed MP-PR algorithm is very competitive in terms of complexity, presenting a substantial complexity reduction compared with the conventional MP, presenting a reduction of the order of 50% or more in terms of FLOPs, without loss of NMSE performance as will be confirmed in Section 3.5. Fig. 3.4 presents the *relative complexity factor*

$$\text{RCF}(\gamma, L) = \frac{\Upsilon_{\text{MP-PR}}}{\Upsilon_{\text{MP}}}, \tag{3.42}$$

which is a function of $N_{\text{RIS}} \times N_{\text{act}}$, and is parameterized in γ and L. For instance, assuming $N_{\text{RIS}} = 256$, $N_{\text{act}} = 64$, $L = 6$, $\gamma = 4$ (MP), and $\gamma = 2$ (MP-PR), one can infer an $\text{RCF} = \frac{\Upsilon_{\text{MP-PR}}(\gamma=2)}{\Upsilon_{\text{MP}}(\gamma=4)} = \frac{136208}{270352} = 0.5038$. In Fig. 3.4, all RCF values are generated assuming $\gamma = 2$ for the MP-PR and varying γ for the conventional MP. The conventional MP is less complex than our proposed MP-PR only when $\gamma_{\text{MP}} = \gamma_{\text{MP-PR}} = 2$, but at the same time the performance of the conventional MP is very poor under $\gamma = 2$. Besides, notice

that the best performance-complexity trade-off occurs for the MP-PR for $\gamma = 2$. On the other hand, the conventional MP performs poorly for $\gamma = 2$, with some improvement for $\gamma = 4$, while there is a marginal performance gain when $\gamma = 8$. However, even for $\gamma = 8$, conventional MP does not achieve the NMSE performance attained by the MP-PR with $\gamma = 2$. In fact, the RCF differences w.r.t. L, N_{RIS}, and N_{act} across the $\frac{N_{\text{act}}}{N_{\text{RIS}}}$ practical, feasible configurations are marginal. It is also observed that the parameters N_{RIS}, N_{act}, and L have little impact on the relative complexity factor. The most impactful parameter is the *oversampling factor* γ when the differences are quite significant.

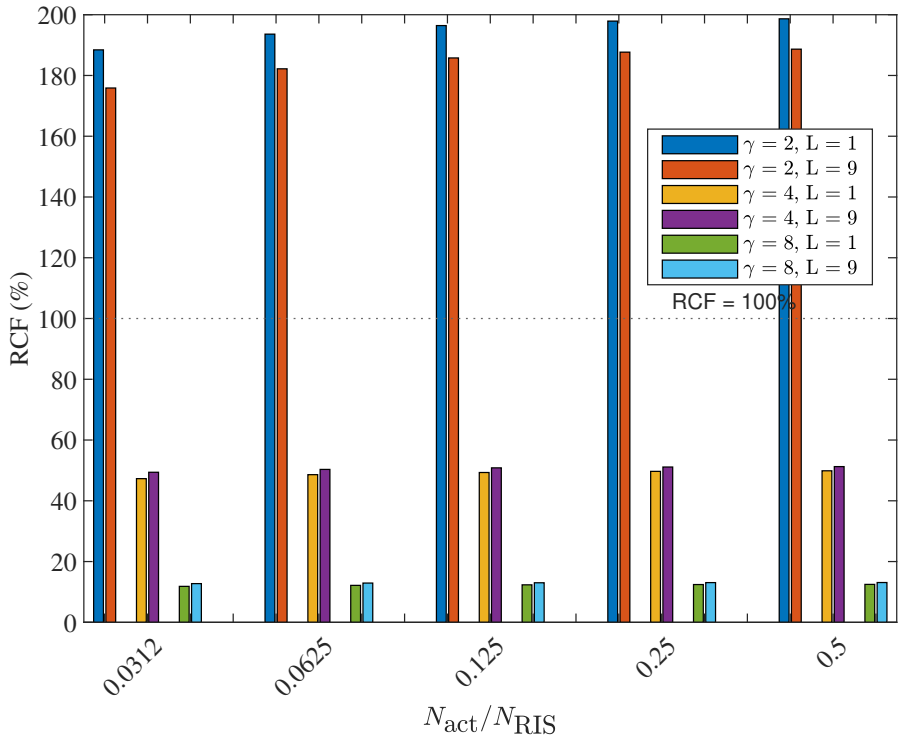

Figure 3.4 – RCF (%) *vs.* L *vs.* γ_{MP} with $\gamma_{\text{MP-PR}} = 2$ for different $\frac{N_{\text{act}}}{N_{\text{RIS}}}$ ratios, $\gamma = [2; 4; 8]$ for the conventional MP, considering $N_{\text{RIS}} = 256$ and varying $N_{\text{act}} \in [8; 16; 32; 64; 128]$.

3.5 Numerical Results

3.5.1 Simulation parameters and performance metrics

We evaluate different RIS-aided MIMO (and MISO) communication scenarios to assess the accuracy of the proposed OMP-PR and MP-PR methods in terms of NMSE:

$$\text{NMSE}_{\widehat{\mathbf{H}}_{\text{R},k}} = \frac{\|\widehat{\mathbf{H}}_{\text{R},k} - \mathbf{H}_{\text{R},k}\|^2}{\|\mathbf{H}_{\text{R},k}\|^2}. \tag{3.43}$$

We also implement the following algorithms as benchmarks: OMP (ALEXANDROPOULOS; VLACHOS, 2020), MP (TAHA et al., 2019; LIU et al., 2020), CoSaMP

(MUZAVAZI; OYERINDE, 2022), l_1 minimization (BRUNTON; KUTZ, 2019), SP (BRUNTON; KUTZ, 2019), multidimensional OMP (MOMP) in (BAYRAKTAR et al., 2022), and the NNM proposed in (WU et al., 2022). Further, we compare these solutions with our proposed ones, the OMP and MP-based with phase rotation (OMP-PR and MP-PR), to corroborate the superiority of our approach. The well-known OMP method is an iterative algorithm for sparse signal recovery, aiming to select orthogonal atoms from a dictionary to approximate the signal. MP is similar but does not enforce strict orthogonality. CoSaMP is tailored for compressive sensing and efficiently recovers sparse signals from limited measurements. SP identifies the support of sparse signals and is particularly effective for low-dimensional subspace recovery, while l_1 minimization promotes sparsity in optimization problems by penalizing the absolute values of coefficients, commonly used for feature selection and regression. On the other hand, NNM encourages low-rank solutions in matrix problems, replacing rank with the sum of singular values, and is valuable for tasks like matrix completion and denoising. The MOMP tries to minimize the complexity and mitigate memory overflow issues in high-dimensional systems. It achieves this by employing a separate dictionary for each dimension of the problem. However, this method may introduce an error propagation phenomenon in scenarios where the channel gain is not precisely known beforehand.

Unless otherwise mentioned, the simulation parameter values adopted here are shown in Table 3.3. The path-loss (PL) is modeled as in (RAPPAPORT et al., 2017) by using the mmMAGIC UMi-Street Canyon model as follows:

$$\mathrm{PL}_{\mathrm{LoS}} = 19.2\log(d_{\mathrm{3D}}) + 32.9 + 20.8\log(f_c) \quad [\mathrm{dB}];$$

and

$$\mathrm{PL}_{\mathrm{NLoS}} = 45.0\log(d_{\mathrm{3D}}) + 31.0 + 20.0\log(f_c) \quad [\mathrm{dB}]$$

where d_{3D} is the 3D distance, and f_c is the carrier frequency.

In addition, we have considered two stopping criteria for the OMP, MP, OMP-PR, and MP-PR, a maximum number of iterations $\mathcal{I}_{\max} = 10$ and $\epsilon \leq \sigma^2$, where ϵ represents the *mean squared error* (MSE) of the residue (such as line 11 of Algorithm 4), and σ^2 is the variance of the noise power at the RIS. The numerical results are obtained via Monte-Carlo simulation (MCS) averaged over 10^4 channel realizations for all the CE methods.

3.5.2 Scenario 1: quantization error evaluation

In Fig. 3.5 we examine a noise-free scenario. Consequently, the exclusive source of error in the CE task arises from the quantization resolution intrinsic to the redundant dictionary, as detailed in eq. (3.17). The investigation encompasses two distinct configurations: (a) NLoS ($\kappa_k = 0,\ \forall\ k = 1,\ \ldots, K$, and $L = 3$ resolvable paths); and (b) Dominant LoS ($\kappa_k = 100,\ \forall\ k = 1,\ \ldots, K$). Moreover, as only one RF chain is adopted at the RIS, the number of measurements (M) equals the number of active elements at the RIS (N_{act}).

Table 3.3 – Simulation Parameters

Parameter	**Value**
UE-BS distance	$d_{\text{3D,UE-BS}} = 57$ [m]
RIS-BS distance	$d_{\text{3D,RIS-BS}} = 65$ [m]
UE-RIS distance	$d_{\text{3D,UE-BS}} = 10$ [m]
κ_G	100
κ_k	$\{0; 10; 100\}$
f_c and BW	28 GHz and 100 MHz
d_s	0.5λ
N_{BS} and N_{UE}	16 and $\{1; 4\}$
N_{RIS} and N_{act}	256 and 64 elements
$\vartheta_T, \vartheta_R, \varphi_R$	$\mathcal{U}(-\pi/2, \pi/2)$
$[N_{\text{BS}}^{\text{RF}}; N_{\text{UE}}^{\text{RF}}; N_{\text{RIS}}^{\text{RF}}]$	$[4; 1; 1]$
T_{C}	500 symbol periods
τ_p	64 symbol periods
# mobile users, K	8
Oversampling factor, γ	$\{1, 2, 4\}$
Monte-Carlo simulation (MCS)	10^4 realizations

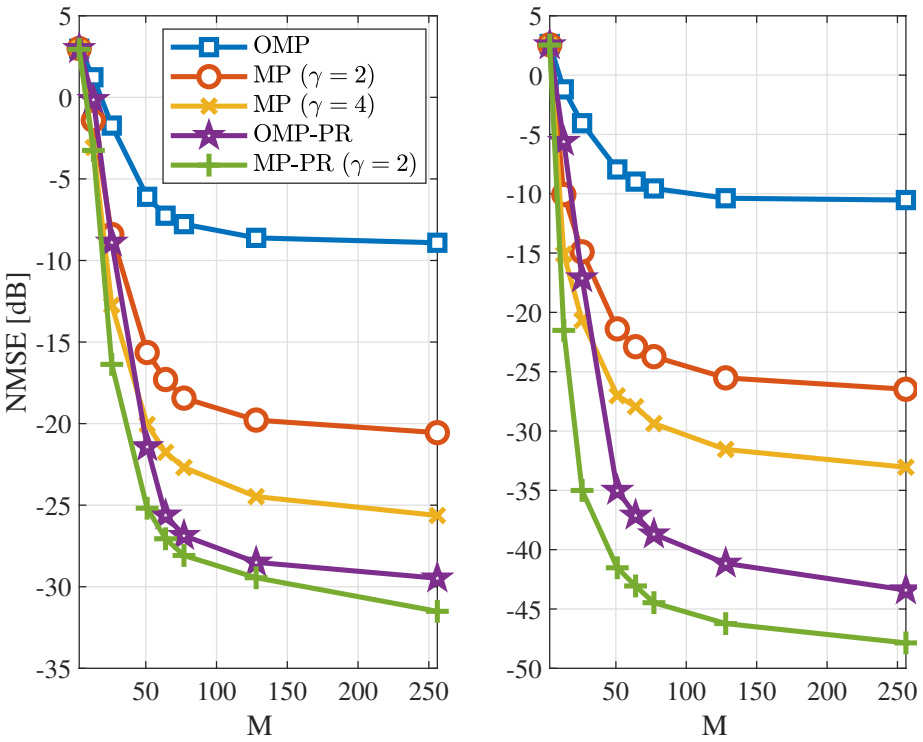

Figure 3.5 – NMSE *vs.* the number of measurements (M) with $N_{\text{UE}} = 1$, and $\epsilon = 10^{-9}$ for: (a) NLoS ($\kappa_k = 0$, and $L = 3$); and (b) Dominant LoS ($\kappa_k = 100$). $K = 8$ users equipped with a single antenna.

Fig. 3.5 presents the average performance obtained by MCS realizations for various techniques: OMP, MP ($\gamma = 2$), and MP ($\gamma = 4$) - all established benchmarks, along with our proposed methodologies: OMP-PR, and the MP-PR ($\gamma = 2$). Notably, OMP-PR employs an orthogonal dictionary ($\gamma = 1$), similar to the conventional OMP. However, this innovative approach incorporates an additional phase rotation step, elaborated in Algorithm 3. Analyzing Fig. 3.5, a significant insight emerges across both scenarios (NLoS and dominant LoS). Specifically, as the number of measurements (M) increases, the quantization error demonstrates a linear decline until the point of $M = 64$, regardless of the chosen solution. However, as M surpasses 64, the quantization error's reduction persists with increasing M, although all solvers begin to present a performance floor at this point. Thus, considering practical implications, we can consider that $M = 64$ is a reasonable value for the number of measurements since $M = N_{\text{act}}$, and, consequently, $N_{\text{act}}/N_{\text{RIS}} = 25\%$ of active elements w.r.t. the total number of RIS elements.

The comparative examination reveals a consistent trend, with the conventional OMP exhibiting the least favorable outcome, while our MP-PR ($\gamma = 2$) consistently emerges as the best solution across all scenarios. The performance differential between these two algorithms is notably substantial. This is particularly evident when scrutinizing Figs. 3.5(a) and 3.5(b) for the NLoS and dominant LoS cases, respectively. For instance, with $M = 64$ measurements (equal to the number of active elements at the RIS, N_{act}), a pronounced enhancement of approximately 20 dB is observed for MP-PR ($\gamma = 2$) in the NLoS scenario, while an even more substantial gain of around 35 dB is realized in the dominant LoS scenario. When comparing the proposed MP-PR ($\gamma = 2$) with MP ($\gamma = 4$), a noteworthy performance advancement is evident, with improvements amounting to 5 dB and 15 dB in the NLoS and dominant LoS scenarios, respectively. Also, it is vital to highlight the substantial complexity reduction achieved by the proposed method, which demonstrates a nearly 50% decrease compared to MP ($\gamma = 4$), as visually depicted in Fig. 3.4. Lastly, it is pertinent to note that the proposed OMP-PR exhibits a performance profile similar to MP-PR with $\gamma = 2$, particularly in the context of the NLoS scenario. However, in the dominant LoS scenario, a discernible distinction becomes evident, with MP-PR ($\gamma = 2$) revealing a gain of ≈ 5 dB in NMSE performance when contrasted with OMP-PR. Also, it is interesting to note that the MOMP solution is slightly better than the MP ($\gamma = 4$) for all scenarios considered in this case.

3.5.3 Scenario 2: multi-user, flat-fading channel

In Fig. 3.6 we compare the achievable NMSE performance for $N_{\text{UE}} = 1$ of our proposed OMP-PR and MP-PR ($\gamma = 2$) solutions against several CS-based algorithms, such as: OMP, MP, CoSaMP, SP, and l_1 minimization. Also, we have implemented an LRMC-based algorithm proposed in (WU et al., 2022) for the CE with active elements at the RIS, called NNM. For all these solutions adopted as benchmarks, except for the OMP,

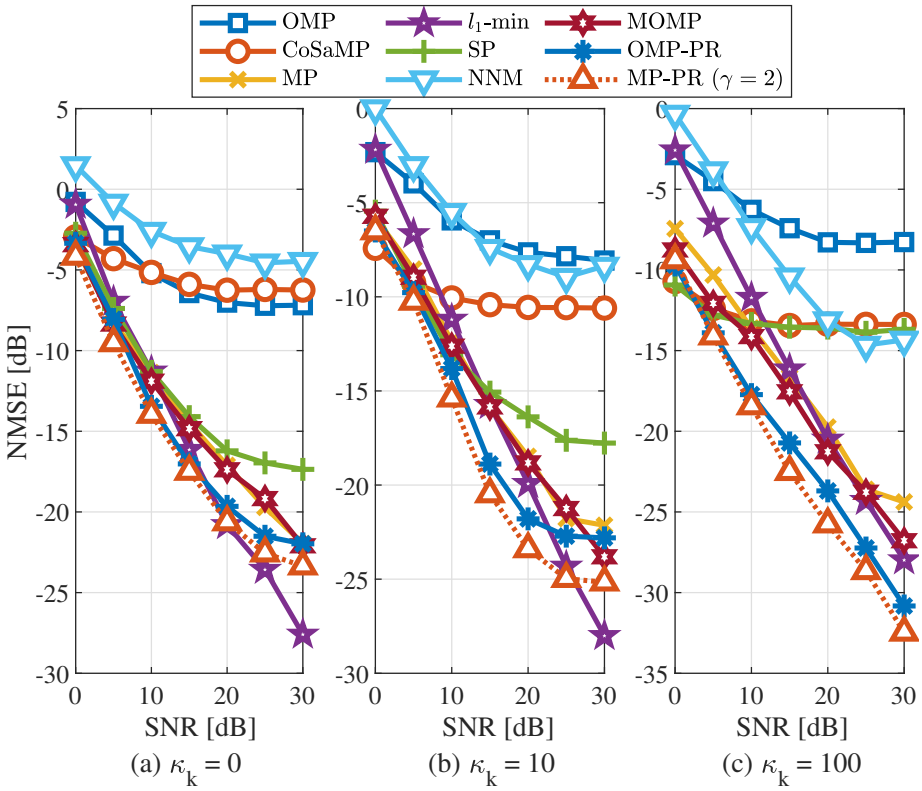

Figure 3.6 – NMSE *vs.* SNR with $N_{\text{UE}} = 1$ for: (a) NLoS ($\kappa_k = 0$, and $L = 3$); (b) LoS and NLoS ($\kappa_k = 10$, and $L = 3$); and (c) Dominant LoS ($\kappa_k = 100$).

we consider $\gamma = 4$ oversampling factor, which increases the computational complexity since the dictionary is bigger in this case. In addition, we have considered $K_{\text{res}} = 128$ for the MOMP algorithm, which represents the resolution of each dictionary. In this analysis, we have considered three different scenarios: (a) NLoS ($\kappa_k = 0$, and $L = 3$); (b) LoS and NLoS ($\kappa_k = 10$, and $L = 3$); and (c) Dominant LoS ($\kappa_k = 100$).

Observing the results in Fig. 3.6, a recurring pattern emerges, reaffirming the superior performance exhibited by our proposed methodologies in terms of NMSE across all investigated scenarios. This trend, however, undergoes a nuanced shift in the context of LoS and dominant LoS scenarios at high SNR values (≥ 25 dB), as shown in Figs. 5(a) and 5(b) respectively. Here, the l_1 minimization solution demonstrates a performance that is either close or slightly superior compared to the proposed ones, however, at a high complexity cost.

Fig. 3.7 presents the CE performance for a MIMO setup with $N_{\text{UE}} = 4$ antennas, in which two different scenarios are adopted: (a) LoS and NLoS ($\kappa_k = 10$, and $L = 3$); and (b) Dominant LoS ($\kappa_k = 100$). Here, it can be noticed in both scenarios that the l_1 minimization-based solution presents the best NMSE performance at high SNR range, *e.g.*, for SNR > 15 dB in the dominant LoS case, and SNR > 25 dB in the LoS setup. Despite that, the proposed MP-PR ($\gamma = 2$) is the best solution considering the performance-complexity trade-off. Also, it can be observed that for the dominant LoS case, the CoSaMP and SP algorithms with $\gamma = 4$ have almost the same performance for all SNR ranges and

are superior to all the others for low SNR (< 10 dB), presenting a gain of almost 3 dB compared with our proposed method MP-PR ($\gamma = 2$). However, when the SNR increases, they begin to show an NMSE floor, and it is worth mentioning that as the CoSaMP and SP solvers need a higher oversampling factor for the redundant dictionary, implying high computational complexity.

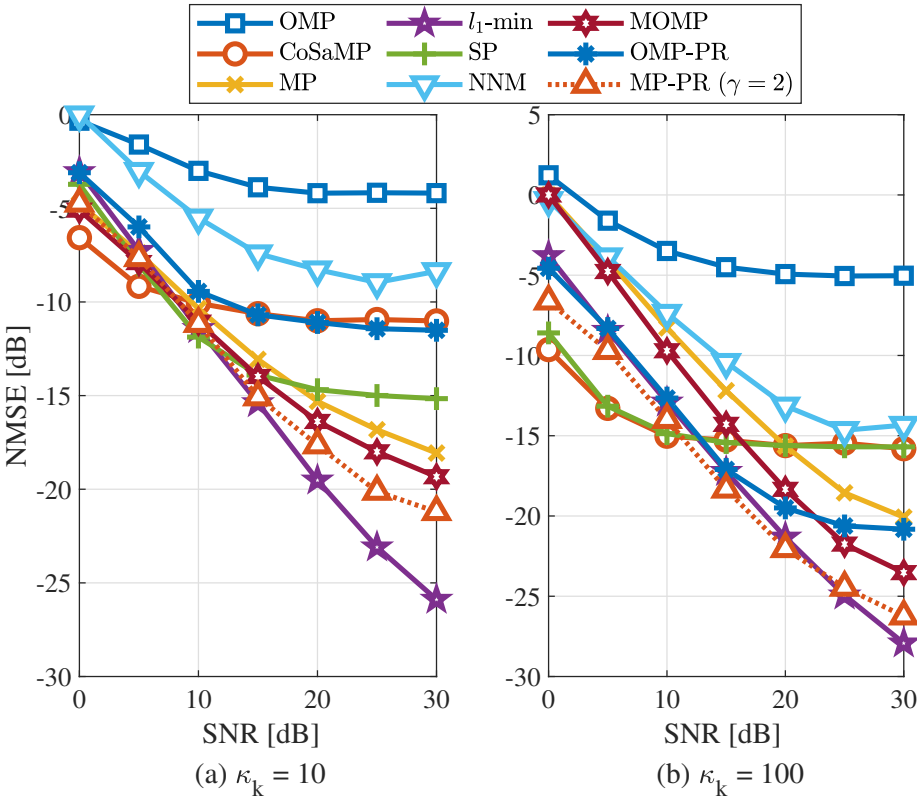

Figure 3.7 – NMSE *vs.* SNR with $N_{\text{UE}} = 4$ for: (a) LoS and NLoS ($\kappa_k = 10$, and $L = 3$); and (b) Dominant LoS ($\kappa_k = 100$).

In Fig. 3.8 we analyze the NMSE performance at the BS side. For that, it is considered $N_{\text{BS}} = 16$ antennas and a dominant LoS ($\kappa_k = 100$) scenario, which is reasonable in this case. Here, we assume an oversampling factor $\gamma = 2$ for all the benchmarks (CoSaMP, SP, MP, l_1 minimization, MOMP, and NNM) since a higher γ in this case is unfeasible. From the obtained results depicted in Fig. 3.8, one can notice that, similarly to the obtained results in Fig. 3.7(b), again, for low SNR (< 5 dB), the CoSaMP and SP algorithms present slightly better NMSE performance than the proposed MP-PR ($\gamma = 2$); for medium and high SNR, there is an inversion trend, and the proposed one becomes the algorithm with the best CE performance, presenting an NMSE performance gain of almost 4 dB compared with the l_1 minimization.

3.5.4 Scenario 3: frequency-selective channel

The performance of the proposed CE schemes are compared with the conventional OMP and MP-based algorithms in multipath channel scenarios with frequency selectivity,

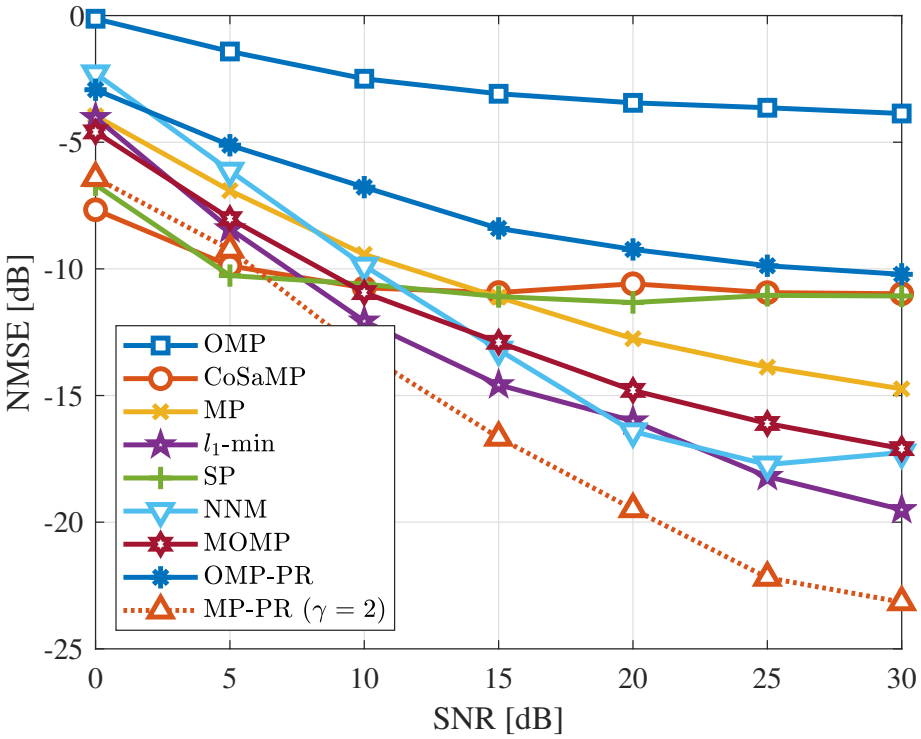

Figure 3.8 – NMSE *vs.* SNR with $N_{\text{BS}} = 16$ for a dominant LoS scenario ($\kappa_G = 100$).

i.e., $L > 1$ and $\Delta B_c \ll \text{BW}$, where ΔB_c is the coherence bandwidth. In order to turn the frequency-selective channel into a flat fading channel, an OFDM system is deployed. The adopted carrier frequency is 28 GHz, with a bandwidth of $\text{BW} = 100$ MHz, and $N_{\text{sc}} = 64$ subcarriers in the pilot training phase. In this case, the average NMSE for the k-th user is defined as:

$$\text{NMSE}_{\widehat{\mathbf{H}}_{\text{R},k}} = \frac{1}{N_{\text{sc}}} \sum_{n=1}^{N_{\text{sc}}} \frac{\|\widehat{\mathbf{H}}_{\text{R},k,n} - \mathbf{H}_{\text{R},k,n}\|^2}{\|\mathbf{H}_{\text{R},k,n}\|^2}. \tag{3.44}$$

As we now have a system with N_{sc} subchannels, the CE task should be done for each subchannel, so we must apply the solutions to each subcarrier. Hence, the *simultaneous orthogonal matching pursuit* (SOMP) in (LIU et al., 2020) is used to solve the optimization problem. Also, notice that if we consider $\gamma > 1$, we will have a *simultaneous matching pursuit* (SMP) approach. In this context, our proposed solutions are the SOMP-PR (when $\gamma = 1$) and SMP-PR (for $\gamma > 1$), which have a similar structure to the OMP-PR and MP-PR, respectively. The only difference between these methods is that the $\mathbf{y}_k$ is now a matrix $\mathbf{Y}_k$ of dimension $N_{\text{act}} \times N_{\text{sc}}$, and hence, some operations become matrix-matrix multiplications instead of matrix-vector multiplications. In fact, the proposed solution (MP-PR) was extended via *multiple measurement vectors* (MMV) approach, in a similar way of (LIU et al., 2020) but also combined with the PR technique, and then Algorithm 2 becomes the SMP-PR, described in Algorithm 5. Basically, such an algorithm is an extended version of the proposed solution (MP-PR) but in the frequency-selective context, in which an OFDM system is employed. Then, as in Fig. 3.9 and 3.10 we have a multicarrier system, the proposed solution needs to be adapted using the MMV approach.

Figs. 3.9 and 3.10 are generated to compare the scenario explored in (LIU et al., 2020). Comparing such results with our proposed SOMP-PR and SMP-PR CE methods against the CNN-based RIS channel estimator of (LIU et al., 2020), it is noted that both proposed methods achieve results very close to or even better than the reference technique, depending on the SNR and L ranges. Furthermore, the computational complexity of the proposed method is also significantly lower since the method in (LIU et al., 2020) uses the SMP (with $\gamma = 4$) as an initial estimation, refining this estimation from a CV-DnCNN approach. The channel estimator proposed by (LIU et al., 2020) considers a preliminary estimation obtained from the SOMP as the input of the CV-DnCNN model. This CV-DnCNN consists of 15 repeated convolutional layers, an input convolutional layer, and an output convolutional layer. Thus, the real and imaginary parts of the estimated channel are processed by the CV-DnCNN, and the residual noise is output after pilot training. As discussed previously, the SMP-PR ($\gamma = 2$) CE is less complex than the conventional SMP ($\gamma = 4$). Moreover, the proposed SMP-PR ($\gamma = 2$) results in a much less complex solution than the SOMP aided by CV-DnCNN of (LIU et al., 2020), as discussed in subsection 3.5.5. Here, it is worth mentioning that the proposed SOMP-PR also achieves a very similar performance w.r.t. the SMP-PR ($\gamma = 2$) while attains a reduced computational complexity. Additionally, it can be noted that the MOMP of (BAYRAKTAR et al., 2022), which presents a low-complexity solution, easily outperforms the SMP with $\gamma = 2$; however, it is still significantly inferior compared with our proposed technique.

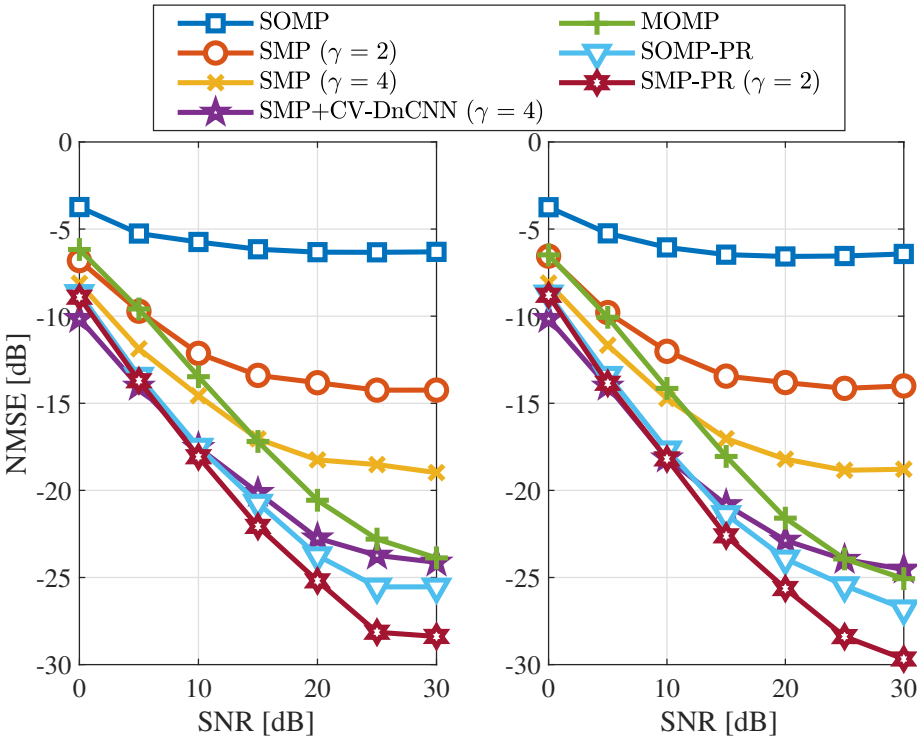

(a) Uniform PDP (b) Exponential PDP

Figure 3.9 – NMSE *vs.* SNR with $N_{\text{RIS}} = 256$, $K = 8$, $N_{\text{act}} = 64$, $L = 6$, $N_{\text{sc}} = 64$ under uniform and exponential PDP.

Elaborating further, Figs. 3.9(a) and 3.9(b) reveal the superiority of the modified SOMP and SMP algorithms against both the conventional ones, and also compared with the SMP ($\gamma = 4$) + CV-DnCNN (LIU et al., 2020), with CE over $N_{sc} = 64$ subcarriers, and assuming uniform and exponential *power-delay profile* (PDP) with $L = 6$ paths. All CE methods are analyzed in a wide SNR regime, *i.e.,* [0; 30] dB. The results demonstrate consistent robustness of the SOMP-PR and SMP-PR ($\gamma = 2$) methods. It can be noted that the conventional SOMP and SMP with $\gamma = 2$ offer a poor NMSE performance. Additionally, in both uniform and exponential PDP scenarios, our proposed SMP-PR with $\gamma = 2$ has a considerable performance gain ($2 \sim 4$ dB) over the conventional SMP with $\gamma = 4$, which is the best configuration for this approach in this case. Another interesting behavior is, as can be seen in 3.9(b), under an exponential PDP, our proposed CE method has an improvement of around 2 to 3 dB at medium SNR (20 to 30 dB) when compared with the uniform PDP scenario.

In Fig. 3.10, we compare the behavior of the analyzed algorithms considering a fixed SNR = 10 dB and varying the number of paths L from 1 to 9. In such a scenario, the conventional SOMP with $\gamma = 1$ reveals an inferior NMSE performance for all values of L. Comparing the conventional SMP with $\gamma = 2$ and the same one with $\gamma = 4$, it is possible to conclude that this technique has a considerable gain with the highest γ value (≈ 2 to 3 dB). Again, the MOMP solution (BAYRAKTAR et al., 2022) presents an improvement of around ≈ 2 dB compared with the SMP with $\gamma = 4$. Moreover, it can be seen that our proposed SMP-PR method shows the best NMSE performance for all L values, presenting an improvement of at least 3.5 dB w.r.t. the best conventional SOMP setup. Compared with the SMP + CV-DnCNN ($\gamma = 4$) (LIU et al., 2020), our proposed SMP-PR method ($\gamma = 2$) offers a very similar NMSE performance, being slightly worse only for $L > 6$.

3.5.5 Complexity analysis

Table 3.4 summarizes the overall computational complexity of all RIS-aided mmWave CE methods compared in this work. It can be observed that the OMP and OMP-PR methods have the least computational complexity among the CE methods analyzed, while both of the ANM approaches have the highest ones. In addition, it can be inferred that SMP+CV-DnNN has a higher computational complexity than the SOMP and SMP-PR techniques since this technique employs the SMP along with a convolutional neural network of N_{layers}, as previously mentioned. NMSE performance in Figs. 3.5 to 3.10 combining with complexity in Table 3.4 confirm that the proposed PR-based CE techniques present the best performance-complexity trade-off.

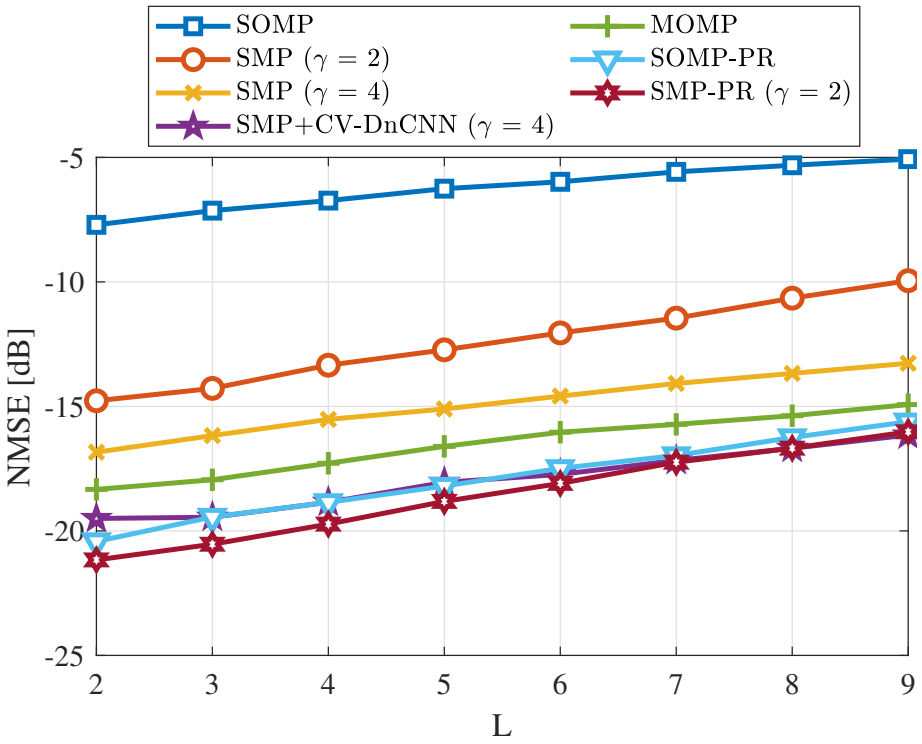

Figure 3.10 – NMSE *vs.* number of paths L considering $N_{\text{RIS}} = 256$, $K = 8$, $N_{\text{act}} = 64$, $N_{\text{sc}} = 64$, uniform PDP, and SNR = 10 dB.

Table 3.4 – Computational complexity order for the seven CE algorithms.

Algorithm	**Complexity**
OMP	$\mathcal{O}(\mathcal{I}_{\max} M N_{\text{act}} K)$
MP	$\mathcal{O}(\mathcal{I}_{\max} \gamma^2 M N_{\text{act}} K)$
MP-PR	$\mathcal{O}(\gamma^2 M N_{\text{act}} L K)$
SOMP	$\mathcal{O}(\mathcal{I}_{\max} M N_{\text{act}} N_{\text{sc}} K)$
SMP	$\mathcal{O}(\mathcal{I}_{\max} \gamma^2 M N_{\text{act}} N_{\text{sc}} K)$
SMP-PR	$\mathcal{O}(\gamma^2 M N_{\text{act}} L N_{\text{sc}} K)$
SMP+CV-DnNN	$\mathcal{O}(N_{\text{act}} K(\gamma^2 N_{\text{RIS}} \mathcal{I}_{\max} + 9 N_{\text{layers}}))$
Hybrid ANM	$\max\{\mathcal{O}(K(N_{\text{RIS}} + N_{\text{BS}})^{3.5}), \mathcal{O}(K(N_{\text{UE}} + N_{\text{RIS}})^{3.5})\}$
MOMP	$\mathcal{O}(K((N_{\text{act}} N_{\text{UE}} L)^2 + (1 + N_{\text{act}} N_{\text{UE}} L)((N_{\text{act},h})^2 + (N_{\text{act},v})^2 + L^2) K_{\text{res}}))$

3.6 Conclusion

We have analyzed the CE problem in semi-passive RIS-aided mmWave communication systems, and a very low-complexity effective CS-based CE method has been proposed for mmWave MIMO wireless communication systems. The proposed CE method presents low training overhead and can operate satisfactorily in different channel and system scenarios. Our proposed MP-PR/SMP-PR method has demonstrated NMSE performance robustness with a relatively small number of active elements ($\leq 25\%$). In addition, MP-PR has proved to be much superior in performance-complexity trade-off compared with the OMP, CoSaMP, SP, l_1 minimization, MOMP, NNM, and ANM methods, achieving reduced

NMSE with a significant decrease in computational complexity in certain cases. On the other hand, in multicarrier scenarios, our SMP-PR method offers performance similar to the SMP + CV-DnNN with $\gamma = 4$ but with a significantly reduced computational complexity. Notice that the analyzed CE methods are not very reasonable for low-order systems (*i.e.*, $N_{\text{RIS}} \leq 64$ RIS reflecting elements), as they depend on channel sparsity properties. Due to its lower computational complexity, the MP-PR/SMP-PR methods achieve a significant performance-complexity tradeoff for medium and high-order RIS elements.

4 Energy-Efficient Uplink Transmission in RIS-Aided M-MIMO IoT Systems

IoT applications are widespread and recently empowered by the dissemination of technologies like smart cities, autonomous vehicles, smart grids, industry 4.0, home automation, wearable, etc. On the other hand, global warming and climate crises demand urgent, bold actions toward EE technologies for telecommunication systems, which are responsible for a significant part of global energy consumption. To this end, RISs appear as an essential technology to improve the propagation channel gain at the expense of very little power expenditures, recognized as a key element in achieving green telecommunication systems.

In this Chapter, we focus on the EE UL transmission of M-MIMO IoT systems aided by an RIS. We propose and evaluate different schemes to minimize the total UL transmit power by optimizing the transmit power of IoT devices, the RIS phase-shift element, and the combining receiver at the BS. Notably, we give special attention to manifold optimization techniques, which are well suited to the RIS phase-shifts optimization problem. Herein, we jointly treat the three optimization variables via an alternating optimization (AO) approach: RIS phase-shift elements vector, BS combining matrix, and unit terminal (UT) power allocation vector. Extensive numerical results are provided and discussed, revealing that the proposed conjugate gradient (CG) method based on the Riemannian manifold (RM) with the MMSE combining achieves the highest power savings, being able to reduce the UL transmit power by up to 89% under typical operation conditions scenarios in comparison with conventional systems without RIS.

4.1 RIS-Aided Multi-User MIMO System

This introductory section discusses the relevance of SE and EE optimization in M-MIMO IoT wireless communication systems aided by the RIS enabling structures. Currently, The use of IoT applications in different fields is intensifying, such in scenarios as smart cities, smart grids, industry 4.0, autonomous vehicles, and others. To allow IoT devices to connect, interact, and exchange data anywhere and anytime, they have to be interconnected wirelessly. Hence, wireless access technology providing reliable communications is essential for IoT applications (CHEN et al., 2021a). Besides, while some IoT applications are characterized by a huge amount of simple devices demanding sporadic and low-speed connections, like in monitoring and tracking applications, other scenarios are characterized

by the demand for high-speed and reliable coverage, like in driverless vehicles, factory automation, remote surgery, and others.

Concomitantly, it becomes each time more important the need for sustainable development and better usage of energy in many fields, including telecommunications. Climate change has achieved alarming levels, imposing the necessity of restricting global warming at the limit of 1.5° above the pre-industrial marks, as well as reducing the gas emissions by half until 2030 (ERICSSON, 2022). In this context, it is worth developing the next-generation telecommunication standard, the so-called B5G or 6G, as a highly energy-efficient system able to fulfill the expected requirements, as peak throughputs of 1Tbps and latencies in the order of μs (HUANG et al., 2019).

RIS has been recognized as a promising candidate technology to be integrated into the 6G standard (LIU et al., 2021; WU et al., 2021). Such surfaces are composed of reflecting elements whose reflection coefficients can be individually adjusted, aiming to improve the propagation features of the environment. The most appealing RIS application scenario is the passive operation, *i.e.*, when the reflecting RIS elements cannot amplify the reflected signal, alleviating the need to be equipped with power-hungry RF chains (BJöRNSON et al., 2020). In (CHIEN et al., 2022), authors have shown that implementing RISs in conjunction with M-MIMO technology can circumvent several problems, such as channel rank deficiency in propagation environments with few scatterers. Besides, the passive implementation enables such benefits at the cost of very little energy consumption, being thus an excellent approach under the perspective of EE (LIU et al., 2021; WU et al., 2021). A remarkable challenge in the operation of RISs is how to suitably find the phase shifts of the reflection elements while enabling an effective operation according to certain performance metrics. An obstacle toward this goal is the reduced amount of available information in such contexts. For example, under the passive operation regime, it is very likely that the RISs do not have estimates for the isolated channels, *i.e.*, between their reflecting elements and the BS and between them and the users (WU et al., 2021). This is justified since usually RF chains would be required at the RIS to acquire such isolated estimates, increasing the energy consumption and the overhead associated with the training stage, which is proportional to the number of reflecting elements at the RIS (BJöRNSON et al., 2020; WANG et al., 2023), which is usually very high.

Given the above scenario, we focus in this Chapter on employing an RIS to reduce the uplink transmit power of an energetically-efficient M-MIMO IoT network. For this purpose, we propose and investigate several schemes optimizing the devices' transmit powers, the RIS phase shifts, and the combiner matrix at the BS. Besides, we give particular attention to the manifold optimization schemes since the unit-modulus constraint of the RIS reflection optimization makes applying such a framework very convenient.

4.1.1 SE and EE general formulation in M-MIMO

In this subsection, we introduce two critical performance metrics crucial for analyzing efficient communication systems. We initiated the discussion with the concept of SE and expanded into EE.

To assess the system performance of a communication system, it is crucial to evaluate the capacity for transmitting bits per second per Hertz (SE) – a fundamental metric that measures the efficiency of information transmission through a channel. The SE reflects the average number of bits transmitted per channel use across varying fading conditions, serving as a typical metric for evaluating communication system capabilities. Since for the RIS-assisted systems, the channel is a generalization of the conventional M-MIMO systems, the SE can be equally represented as the following.

$$\text{SE} = \log_2(1 + \text{SINR}). \qquad \left[\frac{\text{bit}}{\text{s} \cdot \text{Hz}}\right] \tag{4.1}$$

The metric designed to evaluate the sustainable capacity of a system is referred to as EE. This metric essentially quantifies the number of bits that can be reliably transmitted per unit of energy, expressed as the following

$$\text{EE} = \frac{\text{Thoughput [bit/s]}}{\text{System Power Consumption [W]}} = \frac{B \cdot \log_2(1 + \text{SINR})}{P_{\text{T}}}, \qquad \left[\frac{\text{bit}}{\text{Joule}}\right] \tag{4.2}$$

where B is the system bandwidth and P_{T} is the total power required for the communication system to operate. Notice that the power consumption for RIS-assisted M-MIMO systems requires more detailed consideration than traditional M-MIMO systems since although the RIS technology achieves low power consumption, its consumption is not entirely negligible and should be thoroughly examined.

4.1.2 RIS and metasurfaces

An RIS is a programmable surface structure that can be used to control the reflection of electromagnetic (EM) waves by changing the electric and magnetic properties of the surface. RIS is a planar *metasurface* with many low-cost reflecting elements. RISs have been envisioned to reduce energy consumption and improve the spectral efficiency of wireless networks by artificially reconfiguring the wireless propagation environment of EM waves.

Metasurfaces represent a novel class of artificial materials known as metamaterials, with a microstructure designed to display special electromagnetic properties not seen in nature and previously thought to be physically impossible (JEVREMOVIC, 2023). Atoms make up the periodic structure of any material found in nature. An artificial periodic structure is made and grafted onto a host material to form metamaterials. The constituent elements of this manufactured periodic structure are larger than the atoms of the host

material. This size difference effectively overrides the host material's natural reaction to the incoming electromagnetic radiation. As a result, the penetration, reflection loss, and reflection angle are unique to the artificial structure rather than the host material's atomic structure.

RIS-based transmission is supported by a large number of small, low-cost, and passive elements (metamaterial) on the RIS panel that only reflect the incident signal with an adjustable reflection amplitude and phase shift without requiring a dedicated energy source for radio frequency processing, decoding, or encoding, being completely different from existing active relays.

RIS is an enabling technology for 5G-advanced and 6G systems composed of voltage-controlled metamaterial elements that allow manipulation of the wireless channel state response; as a result, the primary characteristics of RIS are wireless system coverage enhancement, channel rank enhancement, interference suppression, and Doppler spread reduction. There are many possible applications, but terahertz (THz) signal enhancement is the most promising. Implementation issues are paramount, where the most crucial issue is creating workable protocols for real-time reconfigurability. Models and methods to deal with EM signal propagation in the presence of RIS should include large-scale path loss near-field and far-field approximation and a hybrid ray tracing method.

4.1.3 Manifolds optimization in RIS-aided M-MIMO

RMs are mathematical objects that generalize the notion of Euclidean space to more complex and curved geometries. They are widely used in optimization (ABSIL et al., 2007). A RM is a space that locally looks like Euclidean space, but a Riemannian metric tensor defines the distances and angles between points. This tensor assigns a positive definite inner product to each tangent space of the manifold, which allows us to explain concepts such as length, angle, and curvature. A couple of key definitions and concepts in Riemannian geometry, including *Riemannian gradient* $\nabla_{\mathcal{M}} f(p)$ and *retraction operation* $\mathrm{Retr}_p(v)$ are provided in Section C.

Manifold optimization is concerned with the following optimization problem:

$$\min_{x \in \mathcal{M}} f(x), \tag{4.3}$$

where $\mathcal{M}$ is a RM and the objective function (OF) f is a real-valued function on $\mathcal{M}$, which can be non-smooth.

If additional constraints other than the manifold constraint are applied, one can add in the OF an indicator function of the feasible set of such additional constraints. Hence, the optimization in (4.3) covers a general formulation for manifold optimization. The existence of the manifold constraint is one of the main difficulties in algorithmic design and theoretical analysis.

One of the main challenges in Manifold optimization usually is the non-convexity of the manifold constraints. By utilizing the geometry of the manifold, a large class of constrained optimization problems can be viewed as unconstrained optimization problems on the manifold (HU et al., 2020).

RISs are typically employed to improve the channel gain between the BS and the UTs, which obstacles of the environment can obstruct. The most appealing operation scenario for the RISs is the passive configuration, in which the device is not equipped with active RF elements for EE purposes. Therefore, the RIS cannot amplify the incoming signal, nor even perform further elaborated processing on it. Besides, since the signal departing from the RIS is not originated by it, but indeed coming from a transmitter in a different position, the channel intermediated by the RIS suffers from the so-called double attenuation effect, or multiplicative path-loss, since the signal attenuates in both transmitter-RIS and RIS-receiver links. Aiming to mitigate this effect, it is convenient to have RISs with the largest aperture possible, as well as to make the reflection coefficients magnitude as high as possible, which is one under the passive operation. Therefore, most of the RIS literature constrains the reflection coefficients to be of unit modulus.

One of the most common manifolds is the complex circle one, in which all the elements of the optimization variable should have a unit modulus. This is the case for the problems involving the RIS phase-shift optimization under passive operation mode. Therefore, one can see that the manifold optimization framework is well-suited for the RIS problems in general, which justifies the particular attention we devote to such techniques in this chapter.

4.1.4 Contributions of the chapter

In this chapter, we focus on the UL of a multiple access M-MIMO system, where K IoT single-antenna devices transmit simultaneously to a BS equipped with M antennas, representing a typical M-MIMO scenario, Fig. 4.1. Strategically positioning an RIS can improve the system reliability, facilitating the communication link between users and the BS. The RIS contains N reconfigurable reflecting elements. The RIS delivers a phase-shifted version of the transmitted signal, maximizing the composite channel gain. Besides that, it can be noticed that the downlink (DL) dual problem can be considered similarly; hence, for the sake of compactness, we do not introduce the DL dual problem in this chapter.

The primary *Contribution* of this Chapter is formulating the EE power minimization problem in the UL RIS-aided M-MIMO IoT network and establishing a solution methodology based on the **Riemannian manifold optimization** approach. Specifically, the contributions of this Chapter are fourfold, and they can be summarized as follows:

1. Develop an optimization methodology for EE power minimization problem in different RIS-aided M-MIMO system configurations by deploying specific manifold

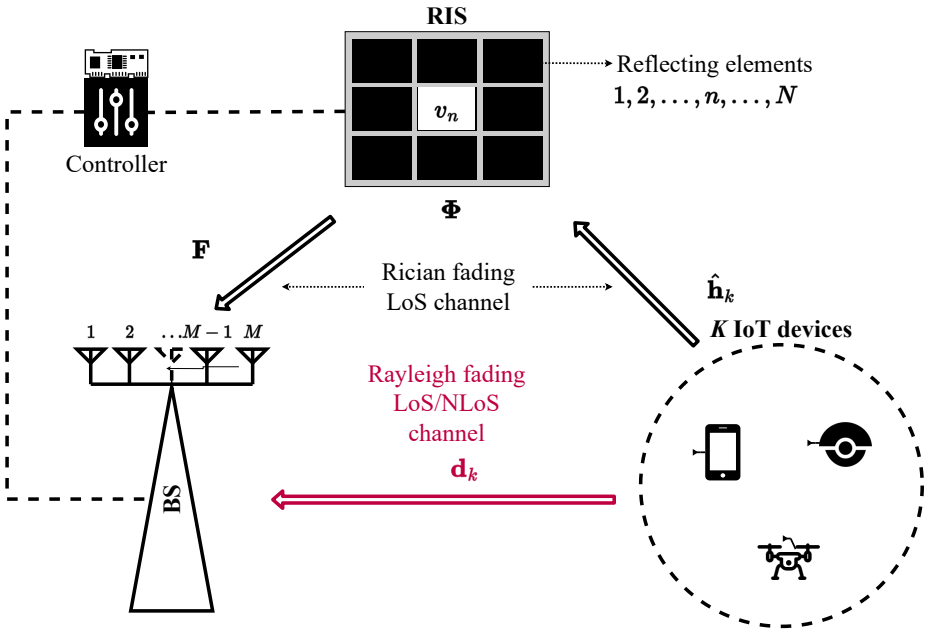

Figure 4.1 – Passive RIS-aided MU M-MIMO system model with LoS/NLoS BS-IoT device links.

optimization formulations and tools.

2. Conduct comprehensive analyses, encompassing key performance indicators, for the optimization problems related to RIS-aided M-MIMO systems. These problems include maximization of system SE and EE, design of precoding/combining techniques, as well as effective power allocation strategies for M-MIMO systems.

3. Investigate channel modeling for RIS-aided M-MIMO wireless communication systems.

4. Thorough analysis of numerical data that support the analytical formulations and provide fresh insights and hypotheses on the progress of these technical subjects.

4.1.5 Organization

The remainder of this Chapter is organized as follows. We commence our discourse by formulating a general multi-purpose system model for RIS-aided M-MIMO systems in **Section 4.3**. In the subsequent sections, we aggregate specific considerations and particularities in the system model, presenting the formulation and development of new strategies and algorithms for the energy-efficient power control optimization problem in RIS-aided M-MIMO system configuration scenarios.

In this Chapter, the focus of analysis is the maximization of the energy efficiency in M-MIMO systems aided by RIS; we deploy specific optimization tools based on **manifold** optimization procedures and methodologies, confirming the promising results attainable by applying Manifold's optimization tools. **Appendix D** shows some of the considered RM

solutions, while **Appendix C** discusses the concepts and definitions of RMs optimization. **Section 4.3.2** discusses an optimization technique for optimizing the RIS phase shifts and the BS combining vectors when the instantaneous CSI is available at the BS. This technique is designed to minimize the UL transmit power of the UTs in the context of an IoT network supported by RIS. Initially, we formulate the joint optimization for the RIS phase-shift and BS combining vectors to improve the overall system EE by minimizing the UL transmit power while guaranteeing a minimum QoS for the devices. To tackle the non-convexity of the problem, **RM**-based iterative AO (i-AO) technique was deployed. Numerical results reveal that the Riemannian Manifold iterative alternating optimization (RM-AO) algorithm is able to maintain a minimum QoS requirement for the devices, while reduce the total transmit power compared with the non-RIS M-MIMO system. In **Section 4.3.3** we address the same problem, but now we make some assumptions that leads us to optimize the system by using only the statistical knowledge of the channel. Section 4.3.4 presents a method for optimizing RIS phase shifts with imperfect CSI by employing the CE proposed in Chapter 3. Finally, **Section 4.5** brings the main conclusions and findings associated with this research work.

4.2 Related Works

In the following, we scan the literature on the RIS-aided M-MIMO. Particularly, we discuss two optimization problems in multiuser M-MIMO systems: a) the design of precoding in the BS transmitter (combiner at the UT receiver) and b) the SE and/or EE in RIS-aided M-MIMO systems.

Several parameters in RIS-aided M-MIMO systems can be optimized, such as power consumption, spectrum deployment, and latency. These parameters generate specific quantitative figures of merit, such as spectral efficiency, energy efficiency, and resource efficiency (RE). Subsection 4.1.1 discusses the general definitions of the SE and EE.

The authors in (ZHOU et al., 2020) present a downlink beamforming method for transmit power minimization in RIS-aided MIMO systems under imperfect CSI. In (GOUDA et al., 2020), for downlink transmission in cell-free M-MIMO systems, the authors design a distributed precoding scheme that eliminates the need for CSI exchange via backhaul signaling. The authors in (WU; ZHANG, 2019a) and (XIE et al., 2020) consider active and passive beamforming subject to users' average transmit power limitations. Besides, (XIE et al., 2020) focuses on optimizing UL beamforming at the BS and passive beamforming at the RIS, employing a low-complexity max-min strategy. A joint beamforming optimization design for a multi-cell system aiming to maximize SE and minimize the MSE of the users' received symbols is developed in (REHMAN et al., 2021). The above works do not consider UT side beamforming for multi-antenna devices. We consider a scenario where mobile users maintain quasi-stationary positions to benefit from

user-side precoding. They establish connections to the BS aided by an outdoor or indoor RIS.

A scheme for enhancing wireless networks using RIS in conjunction with joint active and passive beamforming is proposed in (WU; ZHANG, 2019b). The scheme is applied to a single-cell system with multiple single-antenna users in a downlink scenario, where direct and reflected links between AP and user are considered. An AO approach combined with semi-definite programming (SDP) formulation is used to minimize the total power at the access point (AP) subject to user SINR and phase shift constraints at the RIS. The proposed solution achieves an interesting performance improvement over conventional approaches.

In a downlink RIS-aided MU multiple-input single-output (MISO) system, where the BS serves single-antenna users, the authors in (HUANG2019 et al., 2019) present an energy-efficient solution for the transmit power distribution and the phase shifts. To do so, (HUANG2019 et al., 2019) proposes two computationally feasible solutions that make use of alternating maximization, gradient descent search, and sequential fractional programming. In addition, perfect CSI knowledge is available at the BS, which makes it possible to perform interference cancellation among users by employing ZF precoding. However, in practical scenarios, this assumption is not realistic.

In (PAN et al., 2020), the authors suggest that by attempting to reduce inter-cell interference, the weighted sum rate (WSR) in RIS-aided downlink multicell can be maximized. In order to achieve this aim, (PAN et al., 2020) jointly optimizes the active precoding matrices at BSs and the phase shifts at the RIS subject to each BS's power constraint and unit modulus constraint, respectively. In this case, the optimization problem does not consider any QoS restriction, *e.g.*, a minimum rate requirement for the users. Hence, this solution tends to maximize the rate of users with better channel conditions.

The EE of RIS-aided communications has been investigated recently in (ZENG et al., 2021). The EE maximization problem is addressed by considering uplink MU single-antenna devices and MISO RIS-aided systems. The joint optimization involves the transmit power at users, phase shift at the RIS, and combining matrix at BS. The proposed block coordinate descent (BCD) iterative procedure can handle one variable during each iteration while the others are held fixed. Numerical results indicate that the proposed scheme outperforms baselines that optimize only two of the three variables. Differently from (ZENG et al., 2021), in (YOU et al., 2021), an RIS-aided MU MIMO uplink system is considered. The authors assume that there is no multi-user interference (MuI) and then propose an optimization framework for RE maximization, which aims to find a balance between EE and SE by maximizing the bi-objective function $\text{EE}/\text{BW} + \beta\text{SE}/P_{\text{tot}}$ in [bits/Joule/Hz], with $\beta > 0$, while BW is the system bandwidth, and P_{tot} is the overall available power budget. To tackle this problem, an AO-based technique for maximizing the RE is proposed. This technique obtains the covariance matrices and the RIS phase shift

matrix. Numerical results demonstrate the effectiveness of this technique when compared to baselines that adopt equal power allocation (EPA) or a fixed phase shift matrix.

More recently, (MA et al., 2022) investigated a cooperative beamforming design for downlink multi-RIS-assisted MU MISO systems. An optimization problem is proposed to maximize the sum rate of users in this multi-reflection link system. Due to the non-convexity and coupling of variables, the problem is first decoupled into three sub-problems, and closed-form expressions for decision variables are derived. A low-complexity cooperative beamforming algorithm is proposed, and simulation results corroborate its effectiveness against two baselines: the semidefinite relaxation (SDR)-based and the alternating direction method of multipliers (ADMM)-based algorithms.

In (WU et al., 2022), an RIS-aided MU MISO uplink system is considered by applying the Riemannian conjugate gradient-based joint optimization (RCG-JO) technique, which jointly optimizes the RIS phase shifts and the BS beamforming vectors to minimize uplink transmit power in an RIS-aided IoT network. The technique uses the Riemannian conjugate gradient method to exploit the product RM structure of the sets of unit-modulus phase shifts and unit-norm beamforming vectors. The non-convex uplink power minimization problem is converted into an unconstrained problem, allowing for an optimal solution over the product of Riemannian manifolds. From that, it is shown that the proposed RCG-JO algorithm is more efficient in reducing the uplink transmit power of RIS-assisted IoT networks compared to the SDR-based and deep reinforcement learning (DRL)-based schemes.

The work in (LI et al., 2023) deals with the EE problem in RIS-assisted communication systems within the context of green wireless communications. In this study, the authors investigate EE maximization through the joint optimization of power consumption for both the BS and the RIS. Notably, the research addresses a gap in the existing literature by considering the disparate power consumption characteristics of the ON and OFF states of RIS elements, aligning more closely with the real-world behavior of physical components. The authors introduce a novel ON-OFF aware power dissipation model for RIS elements, and subsequently they reformulate the EE optimization problem. The paper proposes low-complexity algorithms grounded in the mathematical structures of the problem. Simulation results underscore the effectiveness of the proposed algorithms across a diverse array of scenarios, contributing valuable insights to the ongoing discourse on optimizing EE in RIS-aided systems. In (REN et al., 2023), the enhancement of EE in unmanned aerial vehicle (UAV)-enabled wireless power transfer (WPT) systems incorporating multiple ground sensors is explored. It introduces the use of RIS to minimize the total energy consumption of the UAV while fulfilling the energy requirements of each sensor. The study presents two scenarios: one employing a fly-hover-broadcast (FHB) protocol and the other allowing RF signals during flight. The proposed algorithms, based on successive convex approximation (SCA) and path discretization (PD) protocols, effectively optimize UAV trajectory, hover-

ing time, and RIS reflection coefficients, demonstrating by simulation results a substantial energy savings. Additionally, (HUO et al., 2023) focuses on the emergence of 6G wireless communication following the widespread commercialization of 5G networks. Emphasizing the importance of precise modeling in the THz spectrum, the research employs 3-D ray tracing to analyze realistic indoor THz propagation with human blockers. Introducing a distributed RISs framework (DRF), the study addresses the EE problem formulation in THz wireless communication. The simulation results demonstrate the efficacy of DRF in overcoming mobile human blockage, enhancing THz signal coverage, and improving SNRs and QoS. The work envisions practical deployment, considering hardware constraints, highlighting the potential application of DRF in efficient THz communications for IoT networks.

Differently from (WU et al., 2022), in this Chapter we consider several RM-based approaches to solve the EE uplink transmission, where we consider heuristic solutions, as well as solutions based on gradient descent and trust region methods. Additionally, a mixed solution employing RM-based techniques to optimize the RIS phase-shifts while adopting a ZF combining scheme also proved to be a promising solution for the RIS-aided M-MIMO scenario considered in this Chapter.

4.3 System Model, Assumptions, and Problem Formulation

4.3.1 Signal model

The analyzed scenario consists of a M-MIMO RIS-aided UL communication system with K devices, as illustrated in Fig. 4.1. Herein, we assume N_{BS} antennas at the BS side while UTs are equipped with *single-antenna*, where $N_{\text{BS}} > K$, and the number of RIS elements is denoted as N_{RIS}. We also consider that there is a direct link between the UTs and the BS, as illustrated in Fig. 4.1. Let $\hat{\mathbf{H}} \in \mathbb{C}^{N_{\text{RIS}} \times K}$ represent the channel between the UTs and the RIS, $\mathbf{F} \in \mathbb{C}^{N_{\text{BS}} \times N_{\text{RIS}}}$ denote the channel between the RIS and the BS, and $\mathbf{D} = [\mathbf{d}_1, \ldots, \mathbf{d}_K] \in \mathbb{C}^{N_{\text{BS}} \times K}$ describe the direct channel between the user devices and the BS.

Also, we have the phase shift matrix of the RIS as $\mathbf{\Phi} = \text{diag}\left(e^{j\theta_1}, \ldots, e^{j\theta_{N_{\text{RIS}}}}\right)$, where θ_n represents the phase shift of the n-th RIS element. Subsequently, the cascaded user-RIS-BS channel can be expressed as $\mathbf{G} = \mathbf{F}\mathbf{\Phi}\hat{\mathbf{H}} \in \mathbb{C}^{N_{\text{BS}} \times K}$, and the aggregated channel from UTs to the BS can be expressed as $\mathbf{H} = \mathbf{G} + \mathbf{D} \in \mathbb{C}^{N_{\text{BS}} \times K}$. Notably, this aggregated channel $\mathbf{H}$ shares the same dimension as the conventional M-MIMO system.

Based on the provided definitions, we will elaborate on the $\mathbf{H}$ channel model in detail. To address the potential blockage of direct links, we opt for the Rayleigh channel

model for $\mathbf{D}$, expressed as follows:

$$\mathbf{D} = \overline{\mathbf{D}}\boldsymbol{\Omega}_d^{1/2}, \tag{4.4}$$

where $\boldsymbol{\Omega}_d = \text{diag}\,(\gamma_1, \ldots, \gamma_K)$, with γ_k denoting the distance-dependent path-loss factor. Each element of the matrix $\overline{\mathbf{D}} \in \mathbb{C}^{N_{\text{BS}} \times K}$ is an independent and identically distributed (i.i.d.) complex Gaussian random variable, having a zero mean and a unit variance.

Considering that the RIS is situated near the users and often installed above ground, we assume line-of-sight (LoS) paths for the user-RIS channels. We represent this as:

$$\hat{\mathbf{H}} = \left[\sqrt{\alpha_1}\bar{\mathbf{h}}_1, \ldots, \sqrt{\alpha_K}\bar{\mathbf{h}}_K\right], \tag{4.5}$$

where α_k represents the path loss, and $\mathbf{h}_k$ is specified using the two-dimensional uniform planar array (UPA) model. The spatial steering vector for a $N_h \times N_v$ RIS can be defined as in (3.6) Consequently, $\bar{\mathbf{h}}_k = \mathbf{a}(\vartheta_k, \varphi_k)$, and $\hat{\mathbf{h}}_k = \sqrt{\alpha_k}\bar{\mathbf{h}}_k$.

Since the RIS may be located at a considerable distance from the BS, and both the RIS and the BS have certain heights, the RIS-BS channel is not guaranteed to be purely LoS. Therefore, we adopt the Rician model for the RIS-BS channel, allowing us to study the impact of scatterers in RIS-aided systems. In this case, the Rician model is defined as:

$$\mathbf{F} = \sqrt{\frac{\beta\kappa}{\kappa+1}}\overline{\mathbf{F}} + \sqrt{\frac{\beta}{\kappa+1}}\tilde{\mathbf{F}}. \tag{4.6}$$

Here, β represents the path loss, and κ denotes the Rician factor, varying from 0 to ∞, which characterizes the strength ratio between LoS and non-LoS (NLoS) paths.

The NLoS path $\tilde{\mathbf{F}}$ consists of i.i.d. complex Gaussian random variables with a zero mean and unit variance. While the LoS path, $\overline{\mathbf{F}}$, is expressed as:

$$\overline{\mathbf{F}} = \mathbf{a}_M(\vartheta_R, \varphi_R)\mathbf{a}_N^H(\vartheta_T, \varphi_T), \tag{4.7}$$

where ϑ_T and φ_T represent the azimuth and elevation AoDs from the RIS, while ϑ_R and φ_R are the azimuth and elevation AoAs at the BS. Hence, $\mathbf{a}_M$ and $\mathbf{a}_N$ represent the spatial steering vector at the receiver and transmitter sides, respectively. Note that if the BS has a ULA arrangement, the corresponding steering vector simplifies to

$$\mathbf{a}(\vartheta) = [1,\ \ldots, e^{j\frac{2\pi d_s}{\lambda}(N_{\text{BS}}-1)\sin(\vartheta)}]^{\text{T}} \tag{4.8}$$

Therefore, the cascaded channel link UTs-RIS-BS can be written in the function of the amplitude/phase-shift imposed by the RIS as the following

$$\mathbf{h}_k = \mathbf{d}_k + \mathbf{F}\boldsymbol{\Phi}\hat{\mathbf{h}}_k, \tag{4.9}$$

and, hence, we have $\mathbf{H} = [\mathbf{h}_1, \ldots, \mathbf{h}_K]$.

The $N_{\text{BS}} \times 1$ received signal vector at the BS can be expressed as

$$\mathbf{y} = \mathbf{H}\mathbf{x} + \mathbf{n} = (\mathbf{F}\boldsymbol{\Phi}\hat{\mathbf{H}} + \mathbf{D})\mathbf{x} + \mathbf{n}, \tag{4.10}$$

where $\mathbf{\Phi} = \text{diag}(\boldsymbol{\phi}^H) \in \mathbb{C}^{N_{\text{RIS}} \times N_{\text{RIS}}}$, with $\boldsymbol{\phi} = [\phi_1, \ldots, \phi_{N_{\text{RIS}}}]^H \in \mathbb{C}^{N_{\text{RIS}} \times 1}$ being the reflection coefficient vector of the RIS, where $|\phi_n| = 1$ and $\arg(\phi_n) \in [-\pi, \pi)$ represent the reflection amplitude and phase shift for $n \in \{1, \ldots, N_{\text{RIS}}\}$. Moreover, $\mathbf{n} \sim \mathcal{CN}(\mathbf{0}, \sigma^2 \mathbf{I}_{N_{\text{BS}}})$ is the noise vector, the transmitted signal $\mathbf{x}$ is given by

$$\mathbf{x} = \mathbf{P}^{\frac{1}{2}} \mathbf{s}, \tag{4.11}$$

in which $\mathbf{s}$ includes the transmit symbols from the K users, such that $\mathbb{E}[|[\mathbf{s}]_k|^2] = 1, \forall k \in \{1, \ldots, K\}$, $\mathbf{P} = \text{diag}([p_1, p_2, \ldots, p_K])$ is the power allocated to the UTs, and $p_k \leq P_{k,\max}, \forall k \in \mathcal{K} = \{1, \ldots, K\}$, with $P_{k,\max}$ being the maximum available power (power budget) for each user, and $\mathcal{K}$ is the set of IoT devices.

4.3.2 Problem formulation: instantaneous CSI knowledge

The cascaded channel between the IoT device k, the RIS, and the BS in (4.9) can be rewritten as

$$\begin{aligned} \mathbf{h}_k &= \mathbf{d}_k + \mathbf{F}\mathbf{\Phi}\hat{\mathbf{h}}_k, & (4.12) \\ &= \mathbf{d}_k + \mathbf{F}\text{diag}(\hat{\mathbf{h}}_k)\boldsymbol{\phi}, & (4.13) \\ &= \mathbf{d}_k + \mathbf{F}\hat{\mathbf{H}}_k\boldsymbol{\phi}, & (4.14) \end{aligned}$$

where $\hat{\mathbf{H}}_k = \text{diag}(\hat{\mathbf{h}}_k)$.

By considering known (or accurately estimated) the instantaneous CSI, the BS performs uplink power allocation and controls the RIS phase shift based on the acquired channel information. Subsequently, the BS transmits the uplink transmit power indicator (p_k) and the RIS phase shift vector ($\boldsymbol{\phi}$) to the IoT device and RIS corresponding to the k-th device. Ultimately, each IoT device transmits data to the BS through the uplink channel.

Let $x_k = \sqrt{p_k} s_k$ denote the data signal of the k-th IoT device, where s_k represents the normalized data symbol, and $p_k \geq 0$ is the transmit power of the k-th IoT device.

Based on the combining operation given by 7.13, the spectral efficiency of the k-th user results in

$$\text{SE}_k = \log_2 \left(1 + \frac{p_k |\mathbf{c}_k^H (\mathbf{d}_k + \mathbf{F}\hat{\mathbf{H}}_k\boldsymbol{\phi})|^2}{\sum_{j \neq k}^{K} p_j |\mathbf{c}_k^H (\mathbf{d}_j + \mathbf{F}\hat{\mathbf{H}}_j\boldsymbol{\phi})|^2 + \sigma^2} \right) \tag{4.15}$$

The uplink power minimization problem to optimize the RIS phase shift vector $\boldsymbol{\phi}$, the BS beamforming matrix $\mathbf{C} = [\mathbf{c}_1 \ldots \mathbf{c}_K]$, and the device power vector $\mathbf{p} = [p_1 \ldots p_K]$ is

formulated as

$$\min_{\boldsymbol{\phi},\mathbf{C},\mathbf{p}} \quad \sum_{k=1}^{K} p_k \tag{4.16a}$$

$$\text{s.t.} \quad \frac{p_k|\mathbf{c}_k^H(\mathbf{d}_k + \mathbf{F}\hat{\mathbf{H}}_k\boldsymbol{\phi})|^2}{\sum_{j\neq k}^{K} p_j|\mathbf{c}_k^H(\mathbf{d}_j + \mathbf{F}\hat{\mathbf{H}}_j\boldsymbol{\phi})|^2 + \sigma^2} \geq 2^{\bar{\text{SE}}_k} - 1, \quad \forall k \in \mathcal{K}, \tag{4.16b}$$

$$|\phi_n| = 1 \quad \forall\, n \in \{1, \ldots, N\}, \tag{4.16c}$$

$$\|\mathbf{c}_k\| = 1 \quad \forall k \in \mathcal{K}, \tag{4.16d}$$

$$0 \leq p_k \leq P_{\max,k}, \quad \forall k \in \mathcal{K}, \tag{4.16e}$$

where $\bar{\text{SE}}_k$ is quality of service (QoS) requirement, and $P_{\max,k}$ is the maximum transmit power of the k-th IoT device. In order to solve this problem, an alternating optimization (AO) approach is considered. When the power allocation for the IoT devices is fixed, the linear minimum mean-square error (MMSE) receiver can be considered as the solution for the BS combining vectors. Therefore, the normalized MMSE combining matrix is:

$$\mathbf{C}^{\text{MMSE}} = \frac{(\mathbf{H}\mathbf{H}^H + \sigma^2\mathbf{I}_M)^{-1}\mathbf{H}}{\|(\mathbf{H}\mathbf{H}^H + \sigma^2\mathbf{I}_M)^{-1}\mathbf{H}\|^2}. \tag{4.17}$$

Note that the unit-modulus constraint in the optimization problem is non-convex because it restricts each variable ϕ_n to lie on the complex unit circle, which is a non-convex set, as can be seen in Appendix B. To overcome this problem, the RIS phase shift values can be obtained via manifold-based solution by applying a Riemannian manifold algorithm (BOUMAL, 2023) solving the following optimization problem:

$$\text{Find} \quad (\boldsymbol{\phi}) \tag{4.18a}$$

$$\text{s.t.} \quad \frac{p_k A_{k,k}(\boldsymbol{\phi}, \mathbf{C})}{\sum_{j\neq k}^{K} p_j A_{j,k}(\boldsymbol{\phi}, \mathbf{C}) + \sigma^2} \geq 2^{\bar{\text{SE}}_k} - 1, \quad \forall k \in \mathcal{K}, \tag{4.18b}$$

$$|\phi_n| = 1 \quad \forall\, n \in \{1, \ldots, N\}, \tag{4.18c}$$

$$0 \leq p_k \leq P_{\max,k}, \quad \forall k \in \mathcal{K}, \tag{4.18d}$$

where $A_{j,k}(\boldsymbol{\phi}, \mathbf{C}) = |\mathbf{c}_k^H(\mathbf{d}_j + \mathbf{F}\hat{\mathbf{H}}_j\boldsymbol{\phi})|^2 \;\forall\; j, k \in \mathcal{K}$.

Note that the Lagrangian relaxation can be employed to deal with the complicated rate constraint (WU et al., 2022). Then, the modified objective function is

$$L(\boldsymbol{\phi}, \boldsymbol{\lambda}) = \sum_{k=1}^{K} \lambda_k \left(-\frac{p_k}{2^{\bar{\text{SE}}_k} - 1} A_{k,k}(\boldsymbol{\phi}, \mathbf{C}) + \sum_{k\neq 1}^{K} p_j A_{j,k}(\boldsymbol{\phi}, \mathbf{C}) + \sigma^2 \right) \tag{4.19}$$

where $\boldsymbol{\lambda} = [\lambda_1, \ldots, \lambda_K]^T$ is the Lagrangian multiplier vector obtained by solving the corresponding dual problem. Using the Lagrangian function, the optimization problem is

relaxed into

$$\min_{\boldsymbol{\phi},\boldsymbol{\lambda}} \quad \sum_{k=1}^{K}\lambda_k\left(-\frac{p_k}{2^{\bar{\mathrm{SE}}_k}-1}A_{k,k}(\boldsymbol{\phi},\mathbf{C})+\sum_{k\neq 1}^{K}p_jA_{j,k}(\boldsymbol{\phi},\mathbf{C})+\sigma^2\right) \tag{4.20a}$$

$$\text{s.t.} \quad |\phi_n|=1 \quad \forall\, n\in\{1,\ldots,N\}, \tag{4.20b}$$

$$\lambda_k\geq 0 \quad \forall k\in\mathcal{K}, \tag{4.20c}$$

Observe that the constraint in (4.20b) represents the unit-modulus of the RIS phase shift. Due to the non-convexity of the unit-modulus constraint, problem (4.20) is still a non-convex problem.

To deal with the issues mentioned above, we can sequentially and alternately solve the joint coupled $[\boldsymbol{\phi},\mathbf{C},\mathbf{p}]$ optimization problem. A constraint manifold approach formulates the optimization variable as $\mathscr{P}$, where $\mathscr{P}$ is the *Complex circle manifold*, given by

$$\mathscr{P}=\{\boldsymbol{\phi}\in\mathbb{C}^{N_{\mathrm{RIS}}\times 1}:|\phi_n|=1,\ \forall\, n\in\{1,\ldots,N_{\mathrm{RIS}}\}\}. \tag{4.21}$$

With the Riemannian manifold constraints and its smooth structure, we can address the constraints (4.20b) and (4.20c) of the EE power control problem (4.20). We can do this by applying an AO technique to $\mathbf{p}$ and $(\boldsymbol{\phi},\mathbf{C})$ to minimize the modified objective function on the Riemannian manifold. To do this, in the AO approach, we first fix the uplink transmit power of the IoT devices ($\mathbf{p}$), and then sequentially optimize the phase shift vector $\boldsymbol{\phi}$ by using one of the Riemannian manifold methods, and after that we update the BS combining matrix $\mathbf{C}$ as given (4.17). Next, we use the obtained optimal values for $(\boldsymbol{\phi},\mathbf{C})$ as fixed input and update the Lagrangian multiplier $\boldsymbol{\lambda}$. In the second step, we keep the previous variables fixed to optimize the IoT devices transmit power vector $\mathbf{p}$.

Step I: For a fixed uplink transmit power $\mathbf{p}$ and under Riemannian manifold constraint, the optimization problem can be simplified as:

$$\min_{\boldsymbol{\phi}\in\mathscr{P}} \quad L(\boldsymbol{\phi}). \tag{4.22}$$

Note that $\boldsymbol{\phi}$ in problem (4.22) can be obtained by optimize in relation to $\boldsymbol{\phi}$ maintaining $\mathbf{C}$ fixed. After updating the RIS phase shift vector, the MMSE combining matrix ($\mathbf{C}$) is updated as in eq. (4.17). Then, the Lagrangian multiplier $\boldsymbol{\lambda}$ is updated as in (WU et al., 2022).

Step II: After attaining convergence for $\boldsymbol{\phi}$ and $\mathbf{C}$ in (4.22), the optimization problem of variable $\mathbf{p}$ is formulated simply as a linear programming (LP) problem, which can be easily solved using the convex optimization techniques, e.g., `cvx` optimizer (SHEN et al., 2016). If $\boldsymbol{\phi}$ and $\mathbf{C}$ are given (fixed), the optimization problem becomes a power allocation

problem as follows:

$$\min_{\mathbf{p}\in\Re_+} \quad \sum_{k=1}^{K} p_k \tag{4.23a}$$

$$\text{s.t.} \quad \frac{p_k}{2^{\bar{\text{SE}}_k}-1} A_{k,k}(\boldsymbol{\phi},\mathbf{C}) - \sum_{j\neq k}^{K} p_j A_{j,k}(\boldsymbol{\phi},\mathbf{C}) \geq \sigma^2, \quad \forall k \in \mathcal{K}, \tag{4.23b}$$

$$0 \leq p_k \leq P_{\max,k}, \quad \forall k \in \mathcal{K}, \tag{4.23c}$$

which is a convex optimization problem and then can be solved by the `cvx` solver (GRANT; BOYD, 2014). Alternatively, to solve the given power allocation problem it is also possible to employ an iterative algorithm such as the Water-Filling Algorithm or an AO method.

We repeat Steps I and II (AO procedure) until the tuple $\{\boldsymbol{\phi}, \mathbf{C}, \mathbf{p}\}$ solution converges to fixed values or the difference between consecutive alternate steps achieves a specific threshold ε value, as shown in Fig. 4.2.

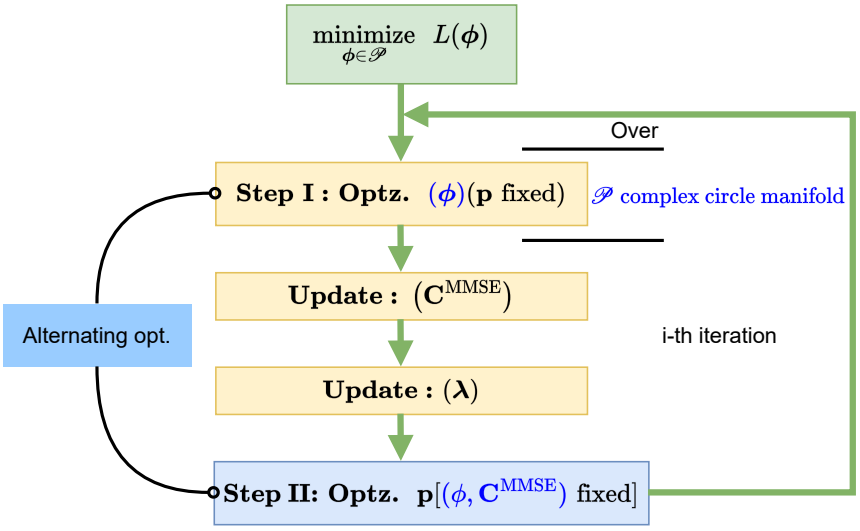

Figure 4.2 – Iterative-alternating optimization (i-AO) steps for the proposed algorithm attains convergence based on AO technique regarding variables $(\boldsymbol{\phi}, \mathbf{C})$ and $\mathbf{p}$.

4.3.3 Problem formulation: statistical CSI knowledge

Here, we consider that, in each channel coherence time, the instantaneous CSI of the aggregated channel $\mathbf{H}$ is known (or accurately estimated) at the BS, which is an upper bound for practical systems. From this, the ZF combiner at the BS is designed as $\mathbf{C} = \mathbf{H}(\mathbf{H}^H\mathbf{H})^{-1}$. Consequently, the detected symbol vector is given by

$$\mathbf{r} = \mathbf{C}^H\mathbf{y} = \mathbf{x} + (\mathbf{H}^H\mathbf{H})^{-1}\mathbf{H}^H\mathbf{n}. \tag{4.24}$$

For ZF, there is no multi-user interference, leading to the SINR reducing to the ratio of transmit power and noise. Based on (4.24), the SINR of user k is given by

$$\begin{aligned} \mathrm{SINR}_k &= \frac{p_k \mathbb{E}[\mathbf{x}\mathbf{x}^H]_{kk}}{\mathbb{E}\left[(\mathbf{H}^H\mathbf{H})^{-1}\mathbf{H}^H\mathbf{n}\mathbf{n}^H\mathbf{H}(\mathbf{H}^H\mathbf{H})^{-1}\right]_{kk}} && (4.25) \\ &= \frac{p_k}{\sigma^2[(\mathbf{H}^H\mathbf{H})^{-1}]_{kk}}. && (4.26) \end{aligned}$$

Then, the k-th user's ergodic SE is lower bounded by

$$\begin{aligned} \mathrm{SE}_k &= \mathbb{E}\left\{\log_2\left(1+\mathrm{SINR}_k\right)\right\} && (4.27) \\ &\geq \log_2\left(1+\frac{p_k}{\sigma^2\mathbb{E}\left\{[(\mathbf{H}^H\mathbf{H})^{-1}]_{kk}\right\}}\right). && (4.28) \end{aligned}$$

As our focus lies in long-term perspective optimization, it becomes valuable to acquire insights into the statistical behavior of the SE of the studied system. In (ZHI et al., 2022c; ZHI et al., 2022b), a rigorous lower bound for the ER employing ZF precoding in the context of the uplink RIS-aided M-MIMO system is derived, as demonstrated in Appendix E, which can be computed for the k-th UT as

$$\mathrm{SE}_k \geq \tilde{\mathrm{SE}}_k = \log_2\left(1+\frac{p_k(N_{\mathrm{BS}}-K)\boldsymbol{\phi}^H\mathbf{B}\boldsymbol{\phi}}{\sigma^2(\kappa+1)\boldsymbol{\phi}^H\mathbf{A}_k\boldsymbol{\phi}}\right), \tag{4.29}$$

where $\mathbf{A}_k$ and $\mathbf{B}$ are constants related to the RIS deployment (RIS-array gain) given as

$$\mathbf{B} = \frac{1}{N_{\mathrm{RIS}}}\mathbf{I}_K + \beta\kappa\mathrm{diag}(\mathbf{a}_N^H)\hat{\mathbf{H}}\boldsymbol{\Lambda}^{-1}\hat{\mathbf{H}}^H\mathrm{diag}(\mathbf{a}_N), \tag{4.30}$$

$$\mathbf{A}_k = \left[\boldsymbol{\Lambda}^{-1}\right]_{k,k}\mathbf{B} - \kappa\beta\mathbf{q}_k\mathbf{q}_k^H, \tag{4.31}$$

$$\mathbf{q}_k^H = \left[\boldsymbol{\Lambda}^{-1}\hat{\mathbf{H}}^H\mathrm{diag}(\mathbf{a}_{\mathrm{N}})\right]_{(k,:)}, \tag{4.32}$$

$$\boldsymbol{\Lambda} = \beta\hat{\mathbf{H}}^H\hat{\mathbf{H}} + (\kappa+1)\boldsymbol{\Omega}_d, \tag{4.33}$$

where $\mathbf{a}_N$ is the steering vector, defined as in eq. (4.8) for ULA arrangement.

Now, the uplink power minimization problem combining the RIS phase shift vector $\boldsymbol{\phi}$ and the device power vector $\mathbf{p} = [p_1 \dots p_K]$ optimization is reformulated as

$$\min_{\boldsymbol{\phi},\mathbf{p}} \quad \sum_{k=1}^{K} p_k \tag{4.34a}$$

$$\text{s.t.} \quad \frac{p_k(N_{\mathrm{BS}}-K)\boldsymbol{\phi}^H\mathbf{B}\boldsymbol{\phi}}{\sigma^2(\kappa+1)\boldsymbol{\phi}^H\mathbf{A}_k\boldsymbol{\phi}} \geq 2^{\tilde{\mathrm{SE}}_k} - 1, \quad \forall k \in \mathcal{K}, \tag{4.34b}$$

$$|\phi_n| = 1 \quad \forall\, n \in \{1,\dots,N\}, \tag{4.34c}$$

$$0 \leq p_k \leq P_{\max,k}, \quad \forall k \in \mathcal{K}, \tag{4.34d}$$

where $\mathcal{K}$ is the set of active IoT devices.

Note that we can obtain the RIS phase shift values ($\boldsymbol{\phi}$) and the power allocation vector ($\mathbf{p}$) employing an AO approach. First, we need to solve problem in relation to $\boldsymbol{\phi}$ maintaining $\mathbf{p}$ fixed, as follows:

$$\begin{aligned} \text{Find} \quad & (\boldsymbol{\phi}) && \text{(4.35a)} \\ \text{s.t.} \quad & \frac{p_k(N_{\text{BS}}-K)\boldsymbol{\phi}^H\mathbf{B}\boldsymbol{\phi}}{\sigma^2(\kappa+1)\boldsymbol{\phi}^H\mathbf{A}_k\boldsymbol{\phi}} \geq 2^{\bar{\text{SE}}_k}-1, \\ & \quad \forall k \in \mathcal{K}, && \text{(4.35b)} \\ & |\phi_n| = 1 \quad \forall\, n \in \{1,\ldots,N\}. && \text{(4.35c)} \end{aligned}$$

Note that the Lagrangian relaxation can be employed to deal with the SE constraint as we have done before. Then, the modified objective function is

$$L(\boldsymbol{\phi},\boldsymbol{\lambda}) = \sum_{k=1}^{K}\lambda_k\left(-\frac{p_k(N_{\text{BS}}-K)}{2^{\bar{\text{SE}}_k}-1}\boldsymbol{\phi}^H\mathbf{B}\boldsymbol{\phi} + \sigma^2(\kappa+1)\boldsymbol{\phi}^H\mathbf{A}_k\boldsymbol{\phi}\right) \tag{4.36}$$

where $\boldsymbol{\lambda} = [\lambda_1,\ldots,\lambda_K]^T$ is the Lagrangian multiplier vector obtained by solving the corresponding dual problem. Using the Lagrangian function, the optimization problem is relaxed into

$$\begin{aligned} \min_{\boldsymbol{\phi},\boldsymbol{\lambda}} \quad & \sum_{k=1}^{K}\lambda_k\left[-\frac{p_k(N_{\text{BS}}-K)}{2^{\bar{\text{SE}}_k}-1}\boldsymbol{\phi}^H\mathbf{B}\boldsymbol{\phi} + \sigma^2(\kappa+1)\boldsymbol{\phi}^H\mathbf{A}_k\boldsymbol{\phi}\right] && \text{(4.37a)} \\ \text{s.t.} \quad & |\phi_n| = 1 \quad \forall\, n \in \{1,\ldots,N\}, && \text{(4.37b)} \\ & \lambda_k \geq 0 \quad \forall k \in \mathcal{K}, && \text{(4.37c)} \end{aligned}$$

Observe that the constraint in (4.37b) represents the unit-modulus of the RIS phase shift. Due to the non-convexity of the unit-modulus constraint, problem (4.37) is still a non-convex problem.

Step I: For a fixed uplink transmit power $\mathbf{p}$ and under Riemannian manifold constraint, the optimization problem can be simplified as:

$$\min_{\boldsymbol{\phi}\in\mathscr{P}} \quad L(\boldsymbol{\phi}). \tag{4.38}$$

Note that $\boldsymbol{\phi}$ in problem (4.38) can be obtained by optimizing in relation to $\boldsymbol{\phi}$ maintaining $\mathbf{p}$ fixed. After updating the RIS phase shift vector, the Lagrangian multiplier vector $\boldsymbol{\lambda}$ is updated. To update the Lagrange multipliers $\boldsymbol{\lambda}$ iteratively in an optimization method such as the Lagrange multipliers method[1], we typically use update rules based on heuristics or specific optimization methods. However, we do not directly rely on the derivative of the Lagrangian function for this purpose; instead, we deploy a gradient-type update rule.

[1]Alternatively, the Penalty method or Interior Point method.

A common approach for updating the Lagrange multipliers consists in deploying a gradient-type update rule. A simple line-search update rule is:

$$\lambda_k^{(t+1)} = \max\left\{0, \lambda_k^{(t)} + \alpha_{\text{lr}} \cdot g_k(\lambda_k^{(t)})\right\}, \tag{4.39}$$

where $\lambda_k^{(t)}$ is the value of the Lagrange multiplier at iteration t, α_{lr} is a step size (or learning rate), and $g_k(\lambda_k^{(t)})$ is a function representing the direction of the gradient at iteration t.

A common choice for $g_k(\lambda_k^{(t)})$ is the constraint violation function, which is positive if the constraint is violated and zero otherwise. For example, for the constraint $\lambda_k \geq 0$, we can have:

$$g_k(\lambda_k^{(t)}) = \begin{cases} -1, & \text{if } \lambda_k^{(t)} > 0 \\ 0, & \text{otherwise} \end{cases}. \tag{4.40}$$

However, the choice of the step size α_{lr} is crucial to ensure the convergence of the method. In general, α_{lr} can be adapted over the iterations to improve convergence.

It is important to note that the choice of update rules for the Lagrange multipliers depends on the specific problem and may require empirical tuning to achieve good performance. Additionally, in complex optimization problems, it may be necessary to use advanced optimization methods such as stochastic gradient algorithms, Newton's algorithms, or second-order optimization algorithms.

Step II: After attaining convergence for $\boldsymbol{\phi}$, the optimization problem of variable $\mathbf{p}$ is formulated simply as a linear programming (LP) problem, which can be easily solved using the convex optimization techniques, *e.g.*, `cvx` optimizer (SHEN et al., 2016). If $\boldsymbol{\phi}$ is given (fixed), the optimization problem becomes a power allocation problem as follows:

$$\min_{\mathbf{p}\in\Re_+} \quad \sum_{k=1}^{K} p_k \tag{4.41a}$$

$$\text{s.t.} \quad \frac{p_k(N_{\text{BS}} - K)}{2^{\bar{\text{SE}}_k} - 1} \frac{\boldsymbol{\phi}^H \mathbf{B} \boldsymbol{\phi}}{(\kappa+1)\boldsymbol{\phi}^H \mathbf{A}_k \boldsymbol{\phi}} \geq \sigma^2, \quad \forall k \in \mathcal{K}, \tag{4.41b}$$

$$0 \leq p_k \leq P_{\max,k}, \quad \forall k \in \mathcal{K}, \tag{4.41c}$$

which is a convex optimization problem and then can be solved by the `cvx` solver (GRANT; BOYD, 2014).

Now, with statistical CSI, the optimization problem is simplified, then we repeat Steps I and II (AO procedure) until the tuple $\{\boldsymbol{\phi}, \mathbf{p}\}$ solution converges to fixed values or the difference between consecutive alternate steps achieves a specific threshold ε value, as illustrated below (Fig. 4.3).

4.3.4 Design of the RIS phase shifts with imperfect CSI

To evaluate the effectiveness of the proposed RIS-aided mmWave CE technique, in Chapter 3, we calculate the UL transmit power to ensure a minimum SE requirement ($\bar{\text{SE}}_k$)

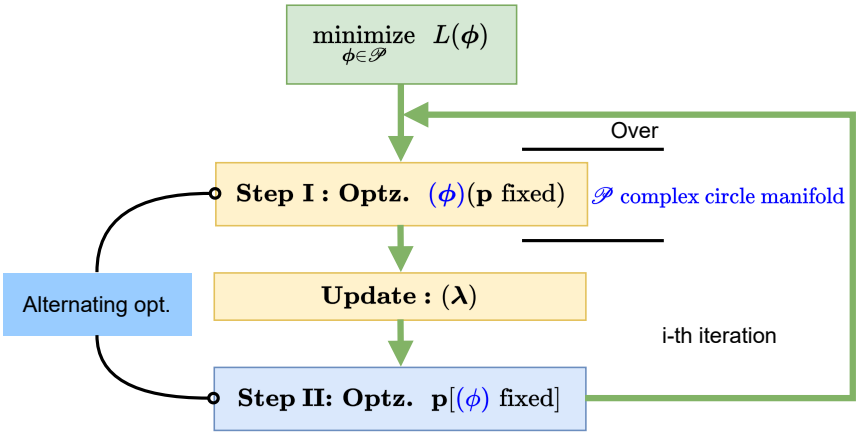

Figure 4.3 – Iterative-alternating optimization (i-AO) steps for the proposed algorithm with statistical CSI, which attains convergence based on AO technique regarding variables ($\boldsymbol{\phi}$) and $\mathbf{p}$.

in a multiuser RIS-aided MISO setup as in (WU et al., 2022). To achieve this objective, we need to optimize the RIS phase shift values and the device power vector, while $\mathbf{w}_{\mathrm{BB},k}$ is adopted to be the MMSE combiner for all UEs, and $\mathbf{W}_{\mathrm{RF}}$ is obtained via beam sweeping in the CE phase.

In the UL RIS-aided MISO, and following the terminology of subsection 3.2.1, the lower bound on the UL effective SE for the k-th user in [bits/s/Hz] can be defined as (ZHU; YANG, 2017; BJöRNSON et al., 2017):

$$\mathrm{SE}_k = \left(1 - \frac{\tau_p}{T_{\mathrm{C}}}\right) \log_2\left(1 + \mathrm{SINR}_k\right), \tag{4.42}$$

where T_{C} is the channel coherence time, τ_p is the period dedicated to training and CE tasks, and SINR_k is the received SINR for user k, given by:

$$\mathrm{SINR}_k = \frac{p_k |\mathbf{w}_{\mathrm{BB},k}^H \mathbf{W}_{\mathrm{RF}}^H (\mathbf{h}_{\mathrm{D},k} + \mathbf{H}_{\mathrm{G}} \boldsymbol{\Theta} \mathbf{h}_{\mathrm{R},k})|^2}{\sum_{j \neq k}^{K} p_j |\mathbf{w}_{\mathrm{BB},k}^H \mathbf{W}_{\mathrm{RF}}^H (\mathbf{h}_{\mathrm{D},j} + \mathbf{H}_{\mathrm{G}} \boldsymbol{\Theta} \mathbf{h}_{\mathrm{R},j})|^2 + \sigma^2}. \tag{4.43}$$

The phase-shift optimization problem can be formulated as:

$$\min_{\boldsymbol{\theta},\mathbf{p}} \quad \sum_{k=1}^{K} p_k \tag{4.44a}$$

$$\text{s.t.} \quad \frac{p_k A_{k,k}(\boldsymbol{\theta})}{\sum_{j \neq k}^{K} p_j A_{j,k}(\boldsymbol{\theta}) + \sigma^2} \geq 2^{\bar{\mathrm{SE}}_k} - 1, \quad \forall k \in \mathcal{K}, \tag{4.44b}$$

$$|\theta_{n_r}| = 1 \quad \forall\, n_r \in \{1, \ldots, N_{\mathrm{RIS}}\}, \tag{4.44c}$$

$$0 \leq p_k \leq P_{\max,k}, \quad \forall k \in \mathcal{K}, \tag{4.44d}$$

where $A_{j,k}(\boldsymbol{\theta}, \mathbf{w}_{\mathrm{BB},k}) = |\mathbf{w}_{\mathrm{BB},k}^H \mathbf{W}_{\mathrm{RF}}^H (\mathbf{h}_{\mathrm{D},j} + \mathbf{H}_{\mathrm{G}} \mathbf{H}_{\mathrm{R},j} \boldsymbol{\theta})|^2 \ \forall\ j,k \in \mathcal{K}$ with $\mathbf{H}_{\mathrm{R},j} = \mathrm{diag}(\mathbf{h}_{\mathrm{R},j})$, $\mathcal{K}$ is the set of UEs, and $P_{\max,k}$ is the maximum transmit power of the k-th UE. To solve problem 4.44, the Lagrangian relaxation can be employed to deal with the complicated

QoS constraint (WU et al., 2022). Also, an alternating optimization (AO) approach is considered. When the UE power allocation is fixed, the RIS phase shift values can be obtained via manifold-based solution by applying a steepest-descent (SD) algorithm for Riemannian manifolds (BOUMAL, 2023) solving the following optimization problem:

$$\min_{\boldsymbol{\theta}\in\mathscr{P}} \sum_{k=1}^{K} l_k \left(-\frac{p_k}{2^{\overline{\mathrm{SE}}_k}-1} A_{k,k}(\boldsymbol{\theta}) + \sum_{k\neq 1}^{K} p_j A_{j,k}(\boldsymbol{\theta}) + \sigma^2 \right) \tag{4.45}$$

where $\mathscr{P}$ is the *Complex circle manifold*, and $\mathbf{l} = [l_1, \ldots, l_K]^T$ is the Lagrangian multiplier vector. After updating the RIS phase shift vector, the Lagrangian multiplier $\mathbf{l}$ is updated as in (WU et al., 2022).

Given $\boldsymbol{\theta}$, the power minimization problem can be obtained by solving

$$\min_{\mathbf{p}} \quad \sum_{k=1}^{K} p_k \tag{4.46a}$$

$$\text{s.t.} \quad \frac{p_k}{2^{\overline{\mathrm{SE}}_k}-1} A_{k,k}(\boldsymbol{\theta}) - \sum_{j\neq k}^{K} p_j A_{j,k}(\boldsymbol{\theta}) \geq \sigma^2, \quad \forall k \in \mathcal{K}, \tag{4.46b}$$

$$0 \leq p_k \leq P_{\max,k}, \quad \forall k \in \mathcal{K}, \tag{4.46c}$$

which is a convex optimization problem and then can be solved by the `cvx` solver (GRANT; BOYD, 2014). The following methods are used for benchmarking the proposed approach for optimizing the RIS phase shifts: MISO system without RIS and perfect CSI estimation, joint conjugate gradient (JCG) and perfect CSI estimation (WU et al., 2022), JCG and NNM CE (WU et al., 2022), SD and hybrid ANM CE (SCHROEDER et al., 2022), and SD and MP-PR ($\gamma = 2$). Unless otherwise stated, the system and channel deployed parameter values are given in Table 3.3.

4.4 Performance Evaluation

The effectiveness of the proposed EE uplink power control in RIS-aided M-MIMO systems is corroborated by the numerical results, where the multiuser combining ($\mathbf{C}$), and the RIS phase-shifts vector ($\boldsymbol{\phi}$) were optimized under RM methods, while the IoT device power allocation vector ($\mathbf{p}$) is obtained via convex optimization with `cvx` solver. Table 4.1 outlines the main system and channel parameter values used in this section based on (YOU et al., 2021; ZENG et al., 2021; WU et al., 2022). Moreover, the path-loss (PL) is modelled as: $\mathrm{PL} = C_0(\frac{d}{D_0})^{-\alpha}$, with d being the distance, α the path-loss exponent, and $C_0 = -30$ dB is the path-loss value at the reference distance $D_0 = 1$ m.

Table 4.1 – Simulation system parameter values, metrics, and optimization variables.

Parameter	**Value**
κ	1
PL factor (IoT device-BS link)	3.8
PL factor factor (IoT device-RIS link)	2.2
PL factor (RIS-BS link)	2.0
IoT device-BS distance	[57-65] [m]
RIS-BS distance	65 [m]
IoT device-RIS distance	[7-11] [m]
PL at the reference distance	$C_0 = -30$ [dB]
Reference distance	$D_0 = 1$ [m]
Number of antennas per IoT device	1
Number of antennas at BS	64
Number of RIS elements	$N = 64$
Number of IoT devices	$K = 8$; $[3:9]$
Carrier frequency	$f = 2.5$ [GHz]
Max power per IoT device	$P_{k,\max} = 1$ [W], $\forall k$
Number of maximum iterations	$\mathcal{I}_{\max} = 5$
Monte-Carlo simulations (MCs)	$\mathcal{T} = 1000$ trials
Optimization Variables	**Method** | **Tools**
Multiuser Combining matrix (BS), $\mathbf{C}$	R. Manifold Optz. | `Manopt` & MMSE
RIS phase-shifts vector, $\boldsymbol{\phi}$	R. Manifold Optz. | `Manopt`
UTs' power transmitting vector, $\mathbf{p}$	Convex Optz. | `cvx`
Metrics	**Range**
Minimum SE requirement ($\bar{\text{SE}}_k$)	$[0.1:0.1:0.7]$; 0.3; $\left[\frac{\text{bps}}{\text{Hz}}\right]$
Background noise variance @BS	$\sigma^2 = -80$; $[-100:5:-70]$ [dBm]

4.4.1 Total UL Power Transmission

In the next, we explore the total uplink average power transmission metric (P_{UT}), which is given by:

$$P_{\text{UT}} = \sum_{k=1}^{K} p_k, \qquad \text{averaged over } \mathcal{T} = 1000 \text{ MCS trials} \tag{4.47}$$

varying the minimum SE requirement ($\bar{\text{SE}}_k$) and the noise variance at the BS (σ^2).

In the UL total average power transmission analysis, eq. (4.47), we have considered different optimization setups to evaluate the achievable performance of the manifold-based algorithms. Figs. 4.4 and 4.5 reveal the performance results for the following schemes:

i) UL M-MIMO system under MMSE combiner ($\mathbf{C}_{\text{MMSE}}$) but without RIS.

Also, we have adopted different RM-based optimization solutions for both optimization variables $\boldsymbol{\phi}$ and $\mathbf{C}$, precisely:

ii) particle swarm optimization (PSO) manifold,

iii) trust-region (TR) manifold,

iv) steepest descent (SD) manifold,

v) conjugate gradient (CG) manifold joint-optimization of (WU et al., 2022) (RCJ-JO).

vi) conjugate gradient (CG) manifold for $\boldsymbol{\phi}$ and MMSE combiner ($\mathbf{C}_{\text{MMSE}}$).

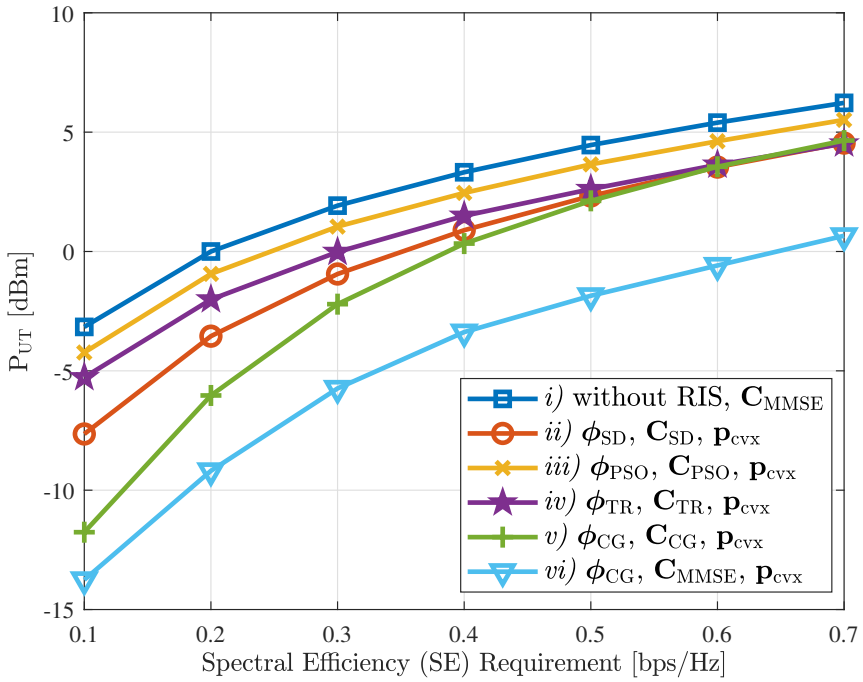

Figure 4.4 – Uplink transmit power (P_{UT}) vs. minimum spectral efficiency requirement ($\bar{\text{SE}}_k$)

In contrast, `cvx` solver (GRANT; BOYD, 2014) is deployed to allocate the optimal power vector $\mathbf{p}$ to the IoT devices.

In Fig. 4.4 we analyze the required uplink transmit power of the IoT devices to achieve the minimum QoS criterion for all of them ($\bar{\text{SE}}_k$), which was varied from 0.1 to 0.7 [bps/Hz]; in this case, we set the noise power as $\sigma^2 = -80$ dBm. Furthermore, in Fig. 4.5 we have set $\bar{\text{SE}}_m = 0.3$ [bps/Hz], while noise power at the BS is varied in the range $\sigma^2 \in [-100; -70]$ dBm.

In both scenarios analyzed in Figs. 4.4 and 4.5, it is evident that the system configuration without RIS represents the worst-case UT transmit power scenario, requiring the highest amount of P_{UT}. Furthermore, as depicted in Fig. 4.4, even with the heuristic PSO-based solution, a noteworthy enhancement is achieved compared to the M-MIMO without RIS, resulting in a power reduction of $\approx 22\%$ in this comparison. Notably, the manifold CG-based solution with the MMSE combining consistently proves to be the choice that achieves the minimum UL power transmission across the entire $\bar{\text{SE}}_k$ range. For instance, when $\bar{\text{SE}}_k = 0.1$ bps/Hz, the CG approach + MMSE combiner yields an impressive power saving of 89% compared to the conventional M-MIMO system. In the RIS-aided configuration, the CG solutions (AO and JO approaches) and also the manifold

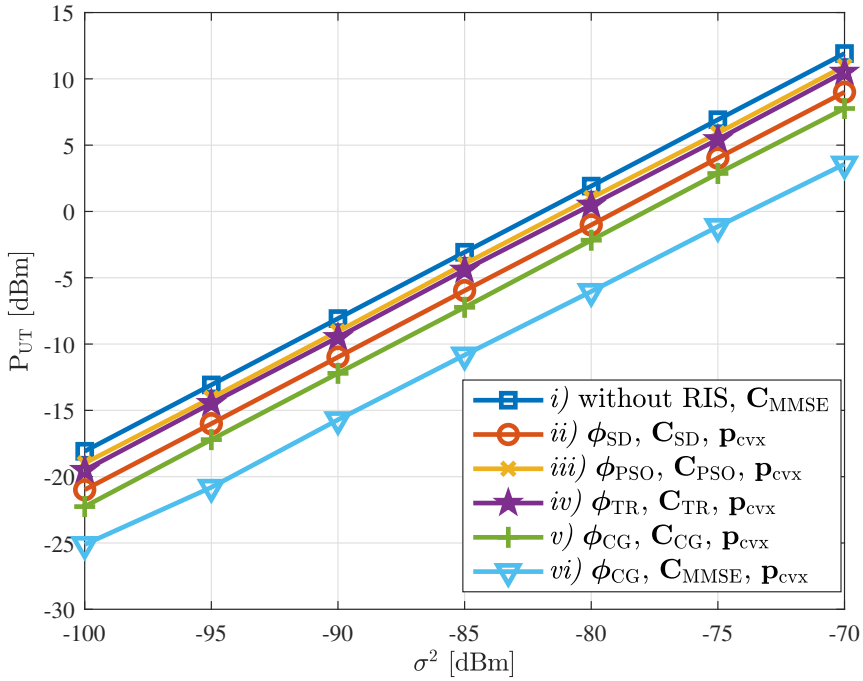

Figure 4.5 – Uplink transmit power (P_{UT}) vs. noise power (σ^2) with $\bar{\text{SE}}_k = 0.3$ [bits/s/Hz].

steepest-descent (SD) scheme for both $\boldsymbol{\phi}$ and $\mathbf{C}$ optimization exhibits power reductions of 82%, 77%, and 61% against the PSO, and TR, respectively, but the approach *vi*) still present a power saving of around 82% compared with approaches *iv*), and *v*). Additionally, it is observed that for $\bar{\text{SE}}_k \geq 0.5$ bps/Hz, the TR, SD, and both CG schemes tend to exhibit similar performance, achieving a power saving of around 35% over the conventional M-MIMO system, *i.e.*, without RIS-aided. At the same point, solution *vi*) shows a transmit power reduction of $\approx 52\%$ against the manifold approaches for both $\boldsymbol{\phi}$ and $\mathbf{C}$ optimization. This can be explained by the fact that with MMSE combiner and perfect CSI, there is no MuI; hence, the SINR of the UTs is significantly improved, resulting in power reduction to guarantee the same QoS requirement. This behavior is not observed with the other approaches that are not capable to completely eliminating the MuI after optimizing the combining matrix $\mathbf{C}$.

In Fig. 4.5, the manifold CG-based approach with the MMSE combining once again emerges as the best solution in terms of UTs' transmission power saving, showcasing superior performance compared to other methods. For instance, when we compare the solution *vi*) against solution *i*), there is a power saving of around 83%; while comparing approach *vi*) in relation to approaches *iv*), and *v*), there is still a power saving of around 55% across all over the analyzed range of σ^2.

4.4.2 Complexity-Performance Trade-off

Optimizing on a manifold ($\mathscr{P}$) is not essentially different from optimizing in $\mathbb{R}^n$ (BOUMAL et al., 2018). Herein, we compare the computation complexity of running time

(seconds) per iteration of the different design approaches. Also, for this analysis, we set $K = 8$, $\bar{\text{SE}}_k = 0.3$ [bits/s/Hz], while $\sigma^2 = -80$ dBm. As a result, the algorithmic complexity is compared via *running time* in Table 4.2. All simulation outcomes were obtained using Matlab (MATLAB R2021a environment) on hardware equipped with an AMD Ryzen 5 5600 CPU @ 3.6 GHz, 32 GB RAM, and an AMD RX 6600 GPU.

Table 4.2 – Running time per iteration, in seconds.

Algorithm	**Running time [s]**
i) MIMO + $\mathbf{C}_{\text{MMSE}}$ w/o RIS	0.0082
ii) PSO-RM	0.0498
iii) TR-RM	0.3096
iv) SD-RM	0.2066
v) RCG-JO (WU et al., 2022)	0.2341
vi) CG-RM ($\boldsymbol{\phi}$) + $\mathbf{C}_{\text{MMSE}}$	0.0947

From Table 4.2, it is possible to notice that the TR-based optimization method exhibits the highest computational complexity among the presented approaches. The increased running time may indicate the additional computational load introduced by certain features or processes specific to the TR algorithm. Furthermore, it is evident that both CG-based solutions (JO and AO) exhibit nearly identical computational complexity. This similarity arises from the fact that, despite RCG-JO utilizing the product of manifolds to jointly optimize $\boldsymbol{\phi}$ and $\mathbf{C}$, all the update operations for these variables must be performed independently (involving Riemannian gradients and retraction operations). Consequently, the computational complexity, in terms of running time, remains almost the same for these approaches. Additionally, it is evident that the SD-based technique exhibits slightly lower complexity compared to the CG counterparts, a fact supported by a direct comparison of Algorithms 7 and 9. A straightforward analysis of these algorithms reveals that the SD solution involves fewer operations than the CG approach. Finally, we have illustrated that approach *vi*) employing the MMSE combiner and the CG-RM algorithm, demands less computational time while delivering substantial performance gains. This efficiency is attributed to the fact that in this solution, the MMSE combiner is computed only once, and only the RIS phase-shift power allocation needs to be recalculated in each iteration. In contrast, the Riemannian manifold-based approaches necessitate updating the combining matrix in every iteration, contributing to a higher computational load.

4.4.3 Instantaneous CSI vs. Statistical CSI

In this section, we aim to validate the accuracy of our proposed solutions and offer insights. Unless specified otherwise, as referenced in (ZHI et al., 2022c), we define $N_{\text{BS}} = N_{\text{RIS}} = 64$. The maximum transmit power per user is set to $P_{k,\max} = 30$ dBm, while

the noise power is $\sigma^2 = -104$ dBm. The BS and the RIS are positioned at coordinates (0, 0) and (0, 700 m) respectively. The number of users is $K = 4$, and they are randomly distributed within a circle centered at (10 m, 700 m) with a radius of 10 m. Differently from table 4.1, path-loss coefficients are 2 (UT-RIS), 2.5 (RIS-BS), and 3 (UT-BS).

In this analysis we have considered the instantaneous CSI approach and the statistical one to optimize the RIS phase shifts and perform the power allocation for the users. In addition, the following benchmarks have been implemented for comparison purposes.

Random case: The phase shift of each RIS element is set randomly in $[0, 2\pi)$.
Case 1: The phase shifts are aligned to the nearest user (user k) so that $\mathbf{a}_N^H \boldsymbol{\Phi} \bar{\mathbf{h}}_k = N_{\text{BS}}$.
Case 2: The phase shifts are aligned to the furthest user (user k) so that $\mathbf{a}_N^H \boldsymbol{\Phi} \bar{\mathbf{h}}_k = N_{\text{BS}}$.
Case 3: The phase shifts are obtained via beam selection algorithm from a codebook based on a DFT matrix.

Fig. 4.6 illustrates the minimum transmit power required to meet specific QoS requirements in terms of SE. It can be observed that, in the absence of an RIS, the system consistently consumes more power to achieve the specified requirements, as anticipated. Additionally, an interesting observation is that the power required for the random approach is nearly the same as in Case 1, where the RIS phase shifts are aligned with the nearest user. This is because, generally, the nearest user already has a favorable channel condition, so the other users do not gain significantly from the RIS and consequently require more power to meet the requirements. Nonetheless, it is noteworthy that even in this scenario, there is a power reduction of approximately 70% compared to the conventional M-MIMO system without RIS. Moreover, it can be notice that for Case 2, where the RIS phase shifts are aligned with the nearest user, we already achieve a power saving of around 20% compared to Case 1. The best solution in this scenario is the phase optimization approach using the Manifold method, which leverages instantaneous channel knowledge. In this case, the reduction in transmit power is approximately 83% compared to the scenario without an RIS. Finally, another interesting behavior is observed with the phase optimization using the Manifold method with statistical channel knowledge. In this configuration, the power consumption increases by approximately 25% compared to the approach using instantaneous channel knowledge, yet it remains at a highly satisfactory level.

Fig. 4.7 illustrates the transmit power required by the UTs to maintain a QoS of $\bar{\text{SE}}k = 1$ bit/s/Hz for varying numbers of RIS elements. In the scenario without RIS, the required power remains constant across the considered range (approximately 28 dBm). As previously explained, Case 1 exhibits almost the same performance as the random solution, which is expected. Additionally, the use of instantaneous CSI results in a significant power reduction; for instance, when $N\text{RIS} = 200$, the power saving is approximately 95% compared to the conventional M-MIMO system. In this scenario, the statistical approach leads to a power increase of approximately 40% ($N_{\text{RIS}} = 200$) compared to the instantaneous

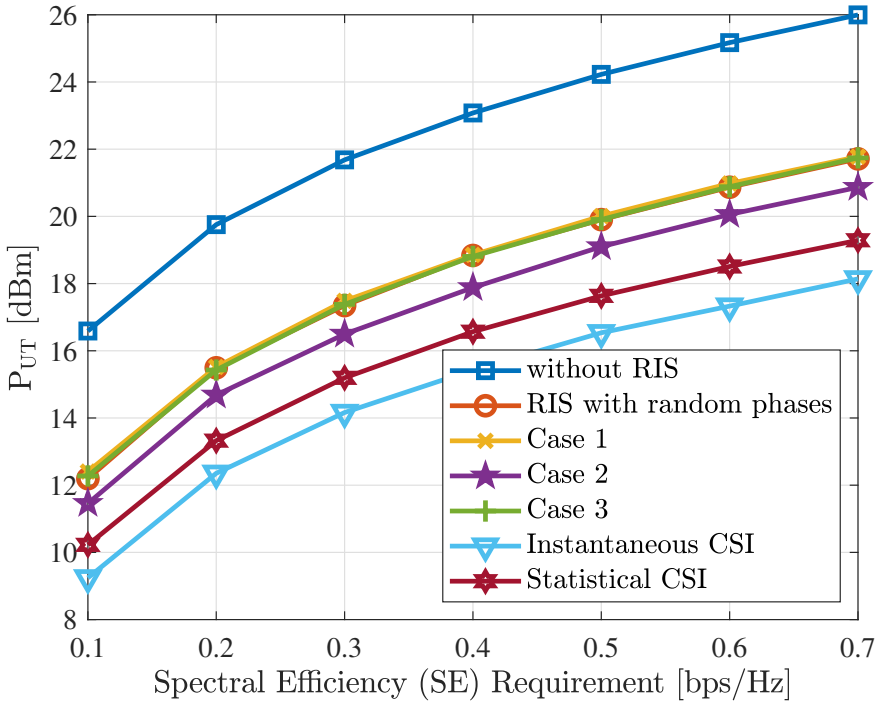

Figure 4.6 – Uplink transmit power (P_{UT}) vs. minimum spectral efficiency requirement ($\overline{\mathrm{SE}}_k$) with ZF combining, $K = 4$, and different RIS design schemes.

CSI case, yet it still achieves a power reduction of 93% compared to the system without RIS.

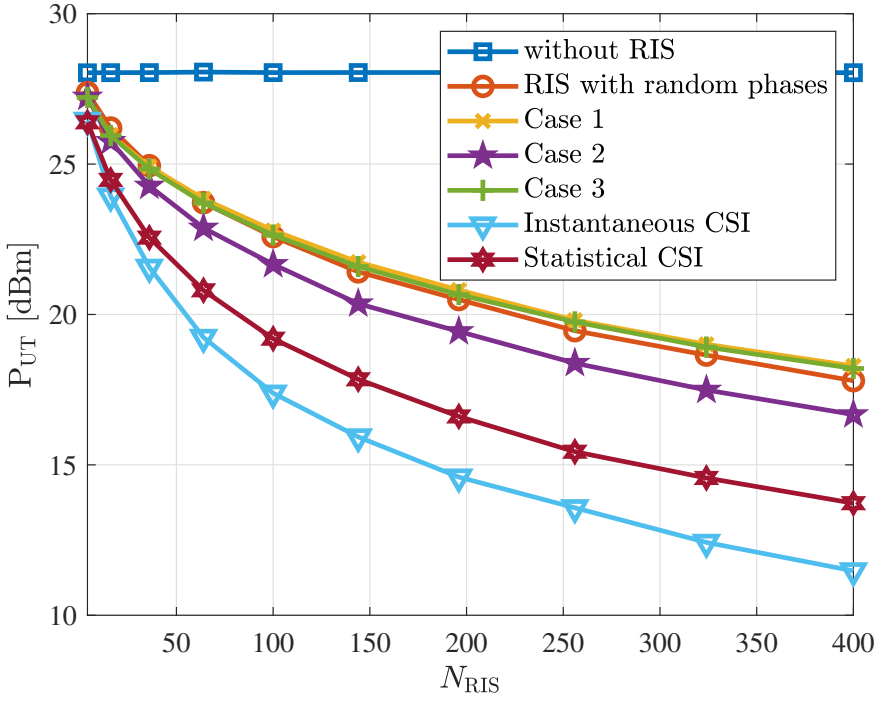

Figure 4.7 – Uplink transmit power (P_{UT}) vs. number of RIS elements (N_{RIS}) with ZF combining, $K = 4$, $\overline{\mathrm{SE}}_k = 1$ bit/s/Hz, and different RIS design schemes.

In Fig. 4.8, the superiority of manifold optimization techniques using both instantaneous and statistical CSI is once again evident. Additionally, it can be observed that

cases 1, 2, and 3 exhibited almost the same performance for all values of K, except for $K = 4$, where the approach aiming to minimize the transmission power of the furthest user proved to be slightly better. Furthermore, for $K = 63$, the manifold optimization approach with instantaneous CSI showed a reduction in transmission power of approximately 96% compared to the scenario without RIS, while the manifold optimization with statistical CSI achieved a 90% reduction in the same comparison. Thus, it is confirmed that the statistical approach yields good results even under high load conditions ($N_{\text{BS}} \approx K^2$).

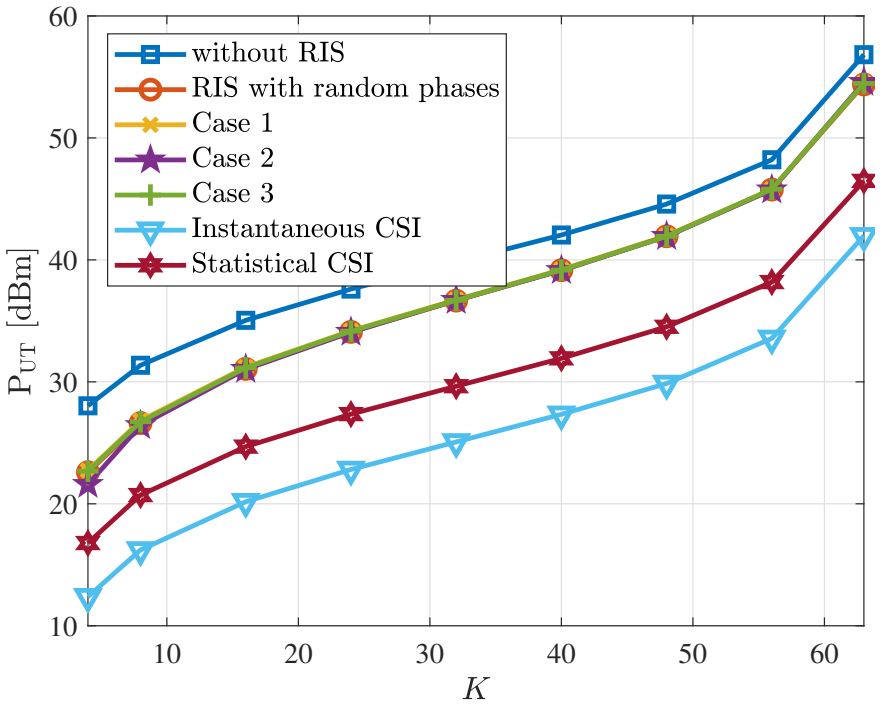

Figure 4.8 – Uplink transmit power (P_{UT}) vs. number of IoT devices (K) with ZF combining, $\bar{\text{SE}}_k = 1$ bit/s/Hz, and $N_{\text{RIS}} = 100$.

4.4.4 Design of the RIS phase shifts with imperfect CSI

Differently from Table 3.3, in Fig. 4.9 we consider $N_{\text{BS}} = 8$ and $P_{\max,k} = 1$ W, $\forall k \in \mathcal{K}$. In Fig. 4.9(a), we analyze the required UL transmit power of the users to achieve the minimum QoS criterion for all users ($\bar{\text{SE}}_k$), which was varied from 0.1 to 0.7 [bits/s/Hz]; in this case, we set the noise power as $\sigma^2 = -80$ dBm. Furthermore, in Fig. 4.9(b) we have set $\bar{R}_m = 0.3$ [bits/s/Hz], while noise power is varied in range $\sigma^2 \in [-100; -70]$ dBm.

For both scenarios analyzed in Fig. 4.9, it can be noticed that the setup without RIS is the worst case, while both scenarios with perfect CSI provide the best ones, being very close to each other. From Fig. 4.9(a), it can be observed that SD with our proposed MP-PR CE technique attains $\approx 70\%$ of power reduction compared with the JCG and

[2] If $N_{\text{BS}} \leq K$, user scheduling techniques can be employed. In each time slot, $\tilde{K} = N_{\text{BS}} - 1$ users can be chosen to be served. Consequently, the condition $N_{\text{BS}} \geq \tilde{K}$ is satisfied, and all the results derived in the Chapter remain valid by substituting K with $\tilde{K}$.

NNM CE (WU et al., 2022), and the SD with the MOMP (BAYRAKTAR et al., 2022). Further, compared with SD and hybrid ANM CE (SCHROEDER et al., 2022), SD and MP-PR ($\gamma = 2$) are significantly superior until $\bar{R}_m < 0.2$ [bits/s/Hz], showing a similar performance from this. In Fig. 4.9(b), it is possible to infer that our MP-PR ($\gamma = 2$) reveals significant gains over the JCG and NNM CE (WU et al., 2022), where the QoS criterion is reached with $\approx 60\%$ less transmitting power for all the considered noise power range. Moreover, the gain of the SD and MP-PR ($\gamma = 2$) over the SD and hybrid ANM CE (SCHROEDER et al., 2022) are in order of 25%. This superiority also applies when we examine these methods' attainable performance-complexity trade-offs.

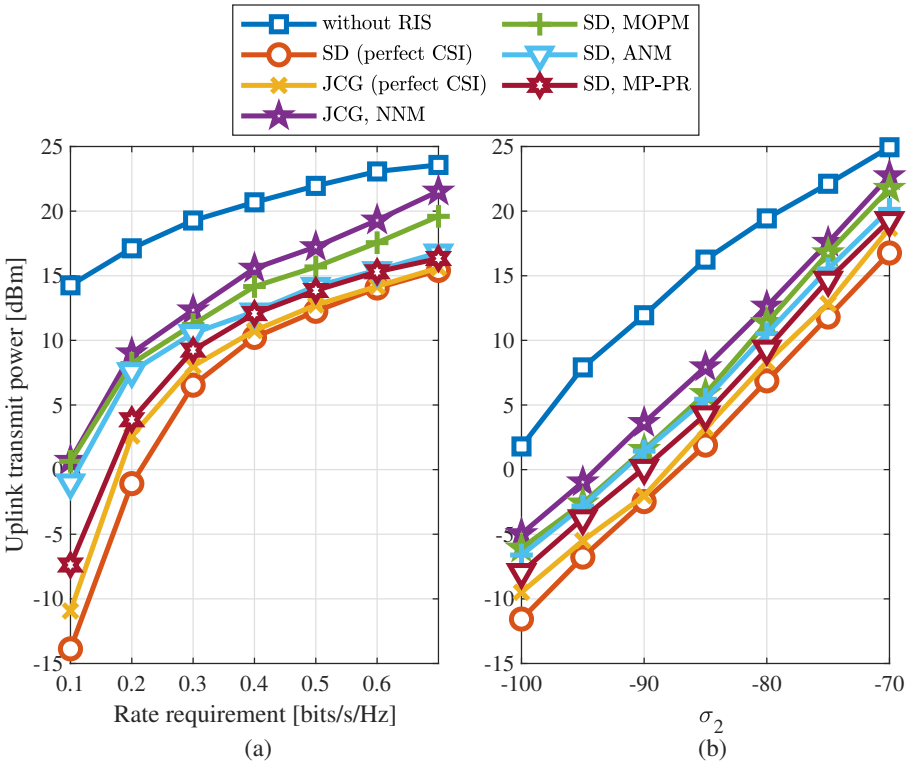

Figure 4.9 – (a) UL transmit power vs. minimum SE requirement ($\bar{\text{SE}}_k$); (b) UL transmit power vs. noise power (σ_2) with $\bar{\text{SE}}_k = 0.3$ [bits/s/Hz].

4.5 Conclusion

We have introduced the RM technique for optimizing the RIS phase-shift and the power allocated to each UT, aiming to reduce the transmit power in the UL of an RIS-assisted M-MIMO IoT network. The fundamental concept behind the proposed RIS phase shift and BS combining optimization algorithms is to employ RM methods for optimizing such $\boldsymbol{\phi}$ vector and $\mathbf{C}$ matrix variables alternately and separately. Additionally, the MMSE and ZF combining methods was taken into consideration. Subsequently, the phase shifts of the RIS were optimized based on the instantaneous or statistical CSI approaches using the CG algorithm. The simulation results indicate that this mixed approach is promising to

minimize the required uplink transmission power to meet the minimum QoS requirements for IoT applications, even when only the statistical CSI knowledge is available. Finally, our numerical results show that the proposed CE method in Chapter 3 combined with the manifold optimization techniques can achieve superior energy efficiency compared to other CE approaches available in the literature, including the low-rank matrix completion based on NNM and the hybrid-ANM methods.

As we discussed in this Chapter, improving the EE of RIS-aided M-MIMO IoT networks is a quite appealing problem, and the use of the manifold optimization framework is very promising for this objective.

5 Conclusions and Perspectives

This thesis work is based on two interesting, complementary and appealing themes currently, which are XL-MIMO and RIS-aided wireless communication systems. The first part of the work (Chapter 2) proposes a double scattering (DS) channel model for XL-MIMO systems with UPA and ULA antenna arrangements. Results show that the XL-MIMO with UPA outperforms the ULA counterpart due to an extra spatial degree of freedom. The MMSE combiner presents optimal performance for both types of massive arrays, while the ZF and MRC combiners face significant performance degradation in crowded scenarios. Birth and death Poisson processes were considered to emulate a dynamic system scenario, revealing SINR performance degradation with increasing scatterer and cluster mobility.

In the second part of this work, a low-complexity CS-based CE method has been proposed for semi-passive RIS-aided mmWave MIMO wireless communication systems. The proposed OMP-PR/SOMP-PR method has demonstrated robust NMSE performance with relatively few active RIS elements. Moreover, the proposed method has shown superior complexity and spectral efficiency performance compared to other CE approaches available in the literature, including the full-passive and hybrid-ANM methods. However, due to its reliance on channel sparsity properties, the proposed method is unsuitable for low-order systems with $M \leq 64$ RIS reflecting elements, while for large scale systems it is very attractive.

The third part of the work proposes an energy-efficient uplink power control in an RIS-aided IoT systems. Since IoT devices are battery-limited, it is of importance to come up with approaches that aim to save the devices consumed power. The proposed approach employs Riemannian manifolds with a power allocation task using a CVX solution to improve EE by reducing the IoT transmit power in RIS-aided uplink M-MIMO systems. Numerical results show that the proposed approach significantly improves the SE-EE trade-off in various scenarios compared to other techniques available in the literature. The proposed method optimizes $\mathbf{\Phi}$ and $\mathbf{p}$ separately and sequentially, allowing for the consideration of only the reflected link to optimize $\mathbf{\Phi}$ while the complete channel is used to optimize $\mathbf{p}$. The proposed approach shows significant gains in saving the uplink transmitting power of the IoT devices. Moreover, the proposed approach results in low computational complexity when compared with other algorithms available in the literature.

We have also provided an alternative approach to address the aforementioned problem. Instead of using instantaneous CSI for the optimization tasks related to $\mathbf{\Phi}$ and $\mathbf{p}$, we have considered a framework based on statistical CSI, where a different optimization problem was developed under these assumptions. It was demonstrated that this further less complex approach can achieve performance very close to that of the previous method

using instantaneous CSI.

As observed throughout this work, the demands for higher data rates, low latency, and massive connectivity in 5G and B5G continue to increase. To meet these requirements, efficient and low-complexity techniques, such as those proposed in this thesis, are essential. Additionally, exploring new technologies and techniques is crucial for the next generation of wireless communication systems.

5.1 Future Research Directions

Interesting research topics to further develop the investigated scenario include: First, although we have assumed a far-field propagation channel in our system model, extending the analysis to near-field propagation channels is a very relevant topic for future works. This is justified since the use of higher frequencies, such as mmWave and terahertz communication, in conjunction with the use of large aperture RISs in an attempt to circumvent the multiplicative path-loss effect, increase the Rayleigh distance, which is widely recognized as the threshold under which the near-field propagation is more prevalent. Second, new opportunities arise in the near-field context, for example, the beam-focusing effect, in which not only the direction of the reflected beam can be adjusted, but also the distance of maximum channel gain. Third, by developing strategies to improve the EE of RIS-aided M-MIMO IoT networks leveraging the beam-focusing effect for near-field scenarios is thus of significant relevance. Fourth, another interesting future direction of this work that we can highlight is the potential integration of the two main topics discussed in this thesis: XL-MIMO and RIS. By combining these technologies, we can explore the unique characteristics of XL-MIMO systems along with the benefits of RIS-assisted systems, as demonstrated throughout this study. This integration is expected to yield even more significant performance gains.

Finally, other important research perspective involves the analysis of multiple RISs. In a typical 6G scenario, multiple RISs can be deployed within a cell, and thus, how to coordinate the operation of these devices is another appealing problem. From an EE perspective, it is also important to obtain the optimal number of RISs and the respective number of RIS elements to be deployed in such arrangement since although the throughput performance can be improved when increasing the number of deployed RISs and/or number of RIS elements, the energy consumption also increases for running the controllers of such devices, also for coordination, and for activation (polarization) of each RIS element.

Bibliography

ABSIL, P.-A.; MAHONY, R.; SEPULCHRE, R. *Optimization Algorithms on Matrix Manifolds*. USA: Princeton University Press, 2007. ISBN 0691132984. Cited 5 times on page(s) 110, 157, 159, 162, and 163.

AL-DULAIMI, A.; WANG, X. *5G Networks: Fundamental Requirements, Enabling Technologies, and Operations Management*. Wiley, 2018. ISBN 9781119332732. Available on: ⟨https://books.google.com.br/books?id=QzinDAEACAAJ⟩. Cited on page 41.

ALEXANDROPOULOS, G. C.; SHLEZINGER, N.; HOUGNE, P. del. Reconfigurable intelligent surfaces for rich scattering wireless communications: Recent experiments, challenges, and opportunities. *IEEE Communications Magazine*, v. 59, n. 6, p. 28–34, 2021. Cited on page 75.

ALEXANDROPOULOS, G. C.; VLACHOS, E. A hardware architecture for reconfigurable intelligent surfaces with minimal active elements for explicit channel estimation. In: *ICASSP 2020 - 2020 IEEE International Conference on Acoustics, Speech and Signal Processing (ICASSP)*. [S.l.: s.n.], 2020. p. 9175–9179. Cited 2 times on page(s) 76 and 96.

ALI, A.; CARVALHO, E. D.; HEATH, R. W. Linear Receivers in Non-Stationary Massive MIMO Channels With Visibility Regions. *IEEE Wireless Commun. Lett.*, v. 8, n. 3, p. 885–888, 2019. Cited on page 46.

ALWIS, C. D.; KALLA, A.; PHAM, Q.-V.; KUMAR, P.; DEV, K.; HWANG, W.-J.; LIYANAGE, M. Survey on 6G Frontiers: Trends, Applications, Requirements, Technologies and Future Research. *IEEE Open J. Commun. Soc.*, v. 2, p. 836–886, 2021. Cited on page 46.

AMIRI, A.; REZAIE, S.; MANCHóN, C. N.; CARVALHO, E. D. Distributed Receiver Processing for Extra-Large MIMO Arrays: A Message Passing Approach. *IEEE Trans. Wireless Commun.*, p. 1–1, 2021. Cited 5 times on page(s) 47, 50, 52, 54, and 58.

AN, J.; XU, C.; GAN, L.; HANZO, L. Low-complexity channel estimation and passive beamforming for ris-assisted mimo systems relying on discrete phase shifts. *IEEE Transactions on Communications*, v. 70, n. 2, p. 1245–1260, 2022. Cited 2 times on page(s) 77 and 78.

ANJINAPPA, C. K.; GüRBüZ, A. C.; YAPıCı, Y.; GüVENç, I. Off-grid aware channel and covariance estimation in mmwave networks. *IEEE Transactions on Communications*, v. 68, n. 6, p. 3908–3921, 2020. Cited 2 times on page(s) 78 and 79.

BAYRAKTAR, M.; PALACIOS, J.; GONZáLEZ-PRELCIC, N.; ZHANG, C. J. Multi-dimensional orthogonal matching pursuit-based ris-aided joint localization and channel estimation at mmwave. In: *2022 IEEE 23rd International Workshop on Signal Processing Advances in Wireless Communication (SPAWC)*. [S.l.: s.n.], 2022. p. 1–5. Cited 5 times on page(s) 79, 97, 103, 104, and 134.

BJÖRNSON, E.; HOYDIS, J.; SANGUINETTI, L. Massive MIMO Has Unlimited Capacity. *IEEE Trans. Wireless Commun.*, v. 17, n. 1, p. 574–590, 2018. Cited on page 67.

BJÖRNSON, E.; SANGUINETTI, L.; WYMEERSCH, H.; HOYDIS, J.; MARZETTA, T. L. Massive MIMO is a reality-What is next? Five promising research directions for antenna arrays. *Digital signal processing (Print)*, v. 94, 2019. Cited on page 46.

BJöRNSON, E.; HOYDIS, J.; SANGUINETTI, L. Massive MIMO networks: Spectral, energy, and hardware efficiency. *Foundations and Trends® in Signal Processing*, Boston - Delft, v. 11, n. 3-4, p. 154–655, 2017. ISSN 1932-8346. Available on: ⟨http://dx.doi.org/10.1561/2000000093⟩. Cited 4 times on page(s) 46, 61, 62, and 125.

BJöRNSON, E.; OZDOGAN, O.; LARSSON, E. G. Reconfigurable Intelligent Surfaces: Three Myths and Two Critical Questions. *IEEE Communications Magazine*, v. 58, n. 12, p. 90–96, 2020. Cited on page 108.

BOUMAL, N. *An introduction to optimization on smooth manifolds*. Cambridge University Press, 2023. Available on: ⟨https://www.nicolasboumal.net/book⟩. Cited 2 times on page(s) 119 and 126.

BOUMAL, N.; ABSIL, P.-A.; CARTIS, C. Global rates of convergence for nonconvex optimization on manifolds. *IMA Jour. of Num. Anal.*, v. 39, n. 1, p. 1–33, 02 2018. ISSN 0272-4979. Available on: ⟨https://doi.org/10.1093/imanum/drx080⟩. Cited on page 129.

BOUMAL, N.; MISHRA, B.; ABSIL, P.-A.; SEPULCHRE, R. Manopt, a Matlab toolbox for optimization on manifolds. *Journal of Machine Learning Research*, v. 15, n. 42, p. 1455–1459, 2014. Available on: ⟨https://www.manopt.org⟩. Cited on page 161.

BRUNTON, S.; KUTZ, J. *Data-Driven Science and Engineering: Machine Learning, Dynamical Systems, and Control*. [S.l.]: Cambridge University Press, 2019. ISBN 9781108422093. Cited on page 97.

CAI, T. T.; WANG, L. Orthogonal matching pursuit for sparse signal recovery with noise. *IEEE Transactions on Information Theory*, v. 57, n. 7, p. 4680–4688, 2011. Cited on page 152.

CARVALHO, E. D.; ALI, A.; AMIRI, A.; ANGJELICHINOSKI, M.; HEATH, R. W. Non-Stationarities in Extra-Large-Scale Massive MIMO. *IEEE Wireless Commun.*, v. 27, n. 4, p. 74–80, 2020. Cited 2 times on page(s) 47 and 48.

CARVALHO, E. de; ALI, A.; AMIRI, A.; ANGJELICHINOSKI, M.; JR., R. W. H. Non-Stationarities in Extra-Large Scale Massive MIMO. *CoRR*, abs/1903.03085, 2019. Available on: ⟨http://arxiv.org/abs/1903.03085⟩. Cited on page 46.

CHEN, J.-q.; ZHANG, Z.; TANG, T.; HUANG, Y.-z. A Non-Stationary Channel Model for 5G Massive MIMO Systems. *Front. Inf. Technol. Electron. Eng.*, v. 18, n. 12, p. 2101–2110, 2017. Cited 4 times on page(s) 47, 48, 58, and 59.

CHEN, S.; SUN, S.; XU, G.; SU, X.; CAI, Y. Beam-Space Multiplexing: Practice, Theory, and Trends, From 4G TD-LTE, 5G, to 6G and Beyond. *IEEE Wireless Commun.*, v. 27, n. 2, p. 162–172, 2020. Cited on page 46.

CHEN, X.; NG, D. W. K.; YU, W.; LARSSON, E. G.; AL-DHAHIR, N.; SCHOBER, R. Massive Access for 5G and Beyond. *IEEE Journal on Selected Areas in Communications*, v. 39, n. 3, p. 615–637, 2021. Cited on page 107.

CHEN, X.; SHI, J.; YANG, Z.; WU, L. Low-complexity channel estimation for intelligent reflecting surface-enhanced massive mimo. *IEEE Wireless Communications Letters*, v. 10, n. 5, p. 996–1000, 2021. Cited on page 77.

CHIEN, T. V.; NGO, H. Q.; CHATZINOTAS, S.; OTTERSTEN, B. Reconfigurable Intelligent Surface-Assisted Massive MIMO: Favorable propagation, channel hardening, and rank deficiency [Lecture Notes]. *IEEE Signal Processing Magazine*, v. 39, n. 3, p. 97–104, 2022. Cited on page 108.

DAHLMAN, E.; PARKVALL, S.; SKOLD, J. *5G NR: The Next Generation Wireless Access Technology*. 1st. ed. USA: Academic Press, Inc., 2018. ISBN 0128143231. Cited on page 41.

DAI, Y.-H. Nonlinear conjugate gradient methods. In: _____. *Wiley Encyclopedia of Operations Research and Management Science*. John Wiley & Sons, Ltd, 2011. ISBN 9780470400531. Available on: ⟨https://onlinelibrary.wiley.com/doi/abs/10.1002/9780470400531.eorms0183⟩. Cited 2 times on page(s) 160 and 161.

DETERME, J.-F.; LOUVEAUX, J.; JACQUES, L.; HORLIN, F. On the noise robustness of simultaneous orthogonal matching pursuit. *IEEE Transactions on Signal Processing*, v. 65, n. 4, p. 864–875, 2017. Cited on page 151.

ERICSSON. *Ericsson mobility report*. [S.l.], 2022. 40 p. Available on: ⟨https://www.ericsson.com/4ae28d/assets/local/reports-papers/mobility-report/documents/2022/ericsson-mobility-report-november-2022.pdf⟩. Cited on page 108.

FUKUDA, R. M.; GUERRA, D. W. M.; KOBAYASHI, R. T.; ABRãO, T. De/pso-aided hybrid linear detectors for mimo-ofdm systems under correlated arrays. *Transactions on Emerging Telecommunications Technologies*, v. 29, n. 12, p. e3495, 2018. E3495 ett.3495. Available on: ⟨https://onlinelibrary.wiley.com/doi/abs/10.1002/ett.3495⟩. Cited on page 160.

GAO, X.; TUFVESSON, F.; EDFORS, O. Massive MIMO Channels – Measurements and Models. In: *2013 Asilomar Conf. Signals Syst. Comput.* [S.l.: s.n.], 2013. p. 280–284. Cited on page 52.

GAO, X.; TUFVESSON, F.; EDFORS, O.; RUSEK, F. Measured Propagation Characteristics for Very-Large MIMO at 2.6 GHz. In: *2012 Conf. Rec. Asilomar Conf. Signals Syst. Comput.* [S.l.: s.n.], 2012. p. 295–299. Cited on page 70.

GERSCHGORIN, S. Uber die abgrenzung der eigenwerte einer matrix. *Izvestija Akademii Nauk SSSR, Serija Matematika*, v. 7, n. 3, p. 749–754, 1931. Cited on page 153.

Gesbert, D.; Bolcskei, H.; Gore, D. A.; Paulraj, A. J. Outdoor mimo wireless channels: models and performance prediction. *IEEE Trans. Commun.*, v. 50, n. 12, p. 1926–1934, 2002. Cited 2 times on page(s) 52 and 53.

GOLUB, G. H.; LOAN, C. F. V. *Matrix Computations*. 4. ed. [S.l.]: Johns Hopkins University Press, 2013. ISBN 9781421408590. Cited on page 95.

GOUDA, B.; ATZENI, I.; TOLLI, A. Distributed precoding design for cell-free massive mimo systems. In: *2020 IEEE 21st International Workshop on Signal Processing Advances in Wireless Communications (SPAWC)*. [S.l.: s.n.], 2020. p. 1–5. Cited on page 113.

GRANT, M.; BOYD, S. *CVX: Matlab Software for Disciplined Convex Programming, version 2.1*. 2014. ⟨http://cvxr.com/cvx⟩. Cited 4 times on page(s) 121, 124, 126, and 128.

GUERRA, D. W. M.; ABRãO, T. Clustered double-scattering channel modeling for xl-mimo with uniform arrays. *IEEE Access*, v. 10, p. 20173–20186, 2022. Cited on page 75.

GUERRA, D. W. M.; FUKUDA, R. M.; KOBAYASHI, R. T.; ABRãO, T. Efficient detectors for mimo-ofdm systems under spatial correlation antenna arrays. *ETRI Journal*, v. 40, n. 5, p. 570–581, 2018. Available on: ⟨https://onlinelibrary.wiley.com/doi/abs/10.4218/etrij.2018-0005⟩. Cited 2 times on page(s) 56 and 159.

GUNNARSSON, S.; FLORDELIS, J.; PERRE, L. V. D.; TUFVESSON, F. Channel Hardening in Massive MIMO: Model Parameters and Experimental Assessment. *IEEE Open J. Commun. Soc.*, v. 1, p. 501–512, 2020. Cited on page 46.

HAN, W.; CHEN, P.; CAO, Z. *Deep Neural Network-Based Quantized Signal Reconstruction for DOA Estimation*. 2020. Cited on page 49.

HAN, Y.; JIN, S.; WEN, C.; MA, X. Channel Estimation for Extremely Large-Scale Massive MIMO Systems. *IEEE Wireless Commun. Lett.*, v. 9, n. 5, p. 633–637, 2020. Cited on page 46.

HE, J.; WYMEERSCH, H.; JUNTTI, M. Channel estimation for ris-aided mmwave mimo systems via atomic norm minimization. *IEEE Transactions on Wireless Communications*, v. 20, n. 9, p. 5786–5797, 2021. Cited on page 77.

HONG, E.-K.; LEE, I.; SHIM, B.; KO, Y.-C.; KIM, S.-H.; PACK, S.; LEE, K.; KIM, S.; KIM, J.-H.; SHIN, Y.; KIM, Y.; JUNG, H. 6g r&d vision: Requirements and candidate technologies. *Journal of Communications and Networks*, v. 24, n. 2, p. 232–245, 2022. Available on: ⟨http://doi.org/10.23919/JCN.2022.000015⟩. Cited on page 42.

HU, J.; LIU, X.; WEN, Z.-W.; YUAN, Y.-X. A Brief Introduction to Manifold Optimization. *Journal of the Operations Research Society of China*, Operations Research Society of China, v. 8, n. 2, p. 199–248, jun 2020. ISSN 2194-668X. Available on: ⟨https://doi.org/10.1007/s40305-020-00295-9http://link.springer.com/10.1007/s40305-020-00295-9⟩. Cited on page 111.

HU, J.; YIN, H.; BJöRNSON, E. Mmwave mimo communication with semi-passive ris: A low-complexity channel estimation scheme. In: *IEEE GLOBECOM*. [S.l.: s.n.], 2021. p. 01–06. Cited on page 76.

HU, X.; ZHANG, R.; ZHONG, C. Semi-passive elements assisted channel estimation for intelligent reflecting surface-aided communications. *IEEE Transactions on Wireless Communications*, v. 21, n. 2, p. 1132–1142, 2022. Cited 2 times on page(s) 76 and 77.

HUANG, C.; MO, R.; YUEN, C. Reconfigurable intelligent surface assisted multiuser miso systems exploiting deep reinforcement learning. *IEEE Journal on Selected Areas in Communications*, v. 38, n. 8, p. 1839–1850, 2020. Cited on page 76.

HUANG, T.; YANG, W.; WU, J.; MA, J.; ZHANG, X.; ZHANG, D. A Survey on Green 6G Network: Architecture and Technologies. *IEEE Access*, v. 7, p. 175758–175768, 2019. Cited on page 108.

HUANG2019, C.; ZAPPONE, A.; ALEXANDROPOULOS, G. C.; DEBBAH, M.; YUEN, C. Reconfigurable intelligent surfaces for energy efficiency in wireless communication. *IEEE Transactions on Wireless Communications*, v. 18, n. 8, p. 4157–4170, 2019. Cited on page 114.

HUO, Y.; DONG, X.; FERDINAND, N. Distributed reconfigurable intelligent surfaces for energy-efficient indoor terahertz wireless communications. *IEEE Internet of Things Journal*, v. 10, n. 3, p. 2728–2742, 2023. Cited on page 116.

JEVREMOVIC, V. Metamaterials and reconfigurable intelligent surfaces. 2023. IBwave, White Paper. Cited on page 109.

JIANG, H.; ZHANG, Z.; WU, L.; DANG, J.; GUI, G. A 3-D Non-Stationary Wideband Geometry-Based Channel Model for MIMO Vehicle-to-Vehicle Communications in Tunnel Environments. *IEEE Trans. Veh. Technol.*, v. 68, n. 7, p. 6257–6271, 2019. Cited on page 47.

JIN, S.; GAO, X.; YOU, X. On the ergodic capacity of rank-1 ricean-fading mimo channels. *IEEE Transactions on Information Theory*, v. 53, n. 2, p. 502–517, 2007. Cited on page 166.

JIN, Y.; ZHANG, J.; ZHANG, X.; XIAO, H.; AI, B.; NG, D. W. K. Channel estimation for semi-passive reconfigurable intelligent surfaces with enhanced deep residual networks. *IEEE Transactions on Vehicular Technology*, v. 70, n. 10, p. 11083–11088, 2021. Cited on page 76.

LI, Z.; ZHANG, J.; ZHU, J.; DAI, L. Ris energy efficiency optimization with practical power models. In: *2023 International Wireless Communications and Mobile Computing (IWCMC)*. [S.l.: s.n.], 2023. p. 1172–1177. Cited on page 115.

LIU, G.; JIANG, D. 5g: Vision and requirements for mobile communication system towards year 2020. *Chinese Journal of Engineering*, v. 2016, n. ID 5974586, 2016. Available on: ⟨http://dx.doi.org/10.1155/2016/5974586⟩. Cited on page 39.

LIU, H.; ZHANG, J.; WU, Q.; XIAO, H.; AI, B. Admm based channel estimation for riss aided millimeter wave communications. *IEEE Communications Letters*, v. 25, n. 9, p. 2894–2898, 2021. Cited on page 76.

LIU, S.; GAO, Z.; ZHANG, J.; RENZO, M. D.; ALOUINI, M.-S. Deep denoising neural network assisted compressive channel estimation for mmwave intelligent reflecting surfaces. *IEEE Transactions on Vehicular Technology*, v. 69, n. 8, p. 9223–9228, 2020. Cited 8 times on page(s) 76, 80, 81, 83, 96, 102, 103, and 104.

LIU, Y.; LIU, X.; MU, X.; HOU, T.; XU, J.; RENZO, M. D.; AL-DHAHIR, N. Reconfigurable Intelligent Surfaces: Principles and Opportunities. *IEEE Communications Surveys & Tutorials*, v. 23, n. 3, p. 1546–1577, 2021. Cited on page 108.

LóPEZ, C. F.; WANG, C.-X. A Study of 2D Non-Stationary Massive MIMO Channels by Transformation of Delay and Angular Power Spectral Densities. *IEEE Trans. Veh. Technol.*, v. 69, n. 12, p. 14212–14224, 2020. Cited 2 times on page(s) 47 and 48.

LóPEZ, C. F.; WANG, C.-X.; ZHENG, Y. A 3D Non-Stationary Wideband Massive MIMO Channel Model Based on Ray-Level Evolution. *IEEE Trans. Commun.*, p. 1–1, 2021. Cited 2 times on page(s) 47 and 48.

LU, H.; ZENG, Y. How Does Performance Scale with Antenna Number for Extremely Large-Scale MIMO? In: *ICC 2021 - IEEE Int. Conf. Commun.* [S.l.: s.n.], 2021. p. 1–6. Cited on page 46.

LU, H.; ZENG, Y. Near-Field Modelling and Performance Analysis for Multi-User Extremely Large-Scale MIMO Communication. *IEEE Commun. Lett.*, p. 1–1, 2021. Cited on page 46.

MA, X.; FANG, Y.; ZHANG, H.; GUO, S.; YUAN, D. Cooperative beamforming design for multiple ris-assisted communication systems. *IEEE Transactions on Wireless Communications*, v. 21, n. 12, p. 10949–10963, 2022. Cited on page 115.

MA, Z.; AI, B.; HE, R.; ZHONG, Z.; YANG, M. A Non-Stationary Geometry-Based MIMO Channel Model for Millimeter-Wave UAV Networks. *IEEE J. Sel. Areas Commun.*, v. 39, n. 10, p. 2960–2974, 2021. Cited 2 times on page(s) 47 and 48.

MARSCH, P.; BULAKCI, O.; QUESETH, O.; BOLDI, M. *5G System Design: Architectural and Functional Considerations and Long Term Research*. 1st. ed. [S.l.]: Wiley Publishing, 2018. ISBN 1119425123. Cited 2 times on page(s) 39 and 41.

MILLER, C. L.; DMOCHOWSKI, P. A.; SMITH, P. J. Efficient channel estimation for ris. In: *ICC 2021 - IEEE International Conference on Communications*. [S.l.: s.n.], 2021. p. 1–6. Cited 2 times on page(s) 77 and 78.

MUIRHEAD, R. J. *Aspects of Multivariate Statistical Theory*. [S.l.]: Wiley-Interscience, 2005. Cited 2 times on page(s) 165 and 166.

MUZAVAZI, R.; OYERINDE, O. O. Channel estimation and data detection schemes for orthogonal time frequency space massive mimo systems. *Computers and Electrical Engineering*, v. 102, p. 108215, 2022. ISSN 0045-7906. Cited on page 97.

NADEEM, Q.-U.-A.; KAMMOUN, A.; DEBBAH, M.; ALOUINI, M.-S. Asymptotic Analysis of RZF Over Double Scattering Channels With MMSE Estimation. *IEEE Trans. Wireless Commun.*, v. 18, n. 5, p. 2509–2526, 2019. Cited on page 62.

NGO, H. Q. Massive mimo: Fundamentals and system designs. *5G and Beyond*, 2015. Available on: ⟨https://api.semanticscholar.org/CorpusID:20926911⟩. Cited on page 50.

NGO, H. Q.; LARSSON, E. G.; MARZETTA, T. L. Energy and spectral efficiency of very large multiuser mimo systems. *IEEE Trans. Commun.*, v. 61, n. 4, p. 1436–1449, 2013. Cited on page 61.

OSSEIRAN, A.; MONSERRAT, J. F.; MARSCH, P. *5G Mobile and Wireless Communications Technology*. 1st. ed. USA: Cambridge University Press, 2016. ISBN 1107130093. Cited 2 times on page(s) 39 and 41.

PAN, C.; REN, H.; WANG, K.; XU, W.; ELKASHLAN, M.; NALLANATHAN, A.; HANZO, L. Multicell mimo communications relying on intelligent reflecting surfaces. *IEEE Transactions on Wireless Communications*, v. 19, n. 8, p. 5218–5233, 2020. Cited on page 114.

PAN, C.; REN, H.; WANG, K.; KOLB, J. F.; ELKASHLAN, M.; CHEN, M.; RENZO, M. D.; HAO, Y.; WANG, J.; SWINDLEHURST, A. L.; YOU, X.; HANZO, L. Reconfigurable intelligent surfaces for 6g systems: Principles, applications, and research directions. *IEEE Communications Magazine*, v. 59, n. 6, p. 14–20, 2021. Cited on page 75.

PAYAMI, S.; TUFVESSON, F. Channel Measurements and Analysis for Very Large Array Systems at 2.6 GHz. In: *2012 6th Eur. Conf. Antennas Propag. EUCAP*. [S.l.: s.n.], 2012. p. 433–437. Cited on page 70.

RAPPAPORT, T. S.; XING, Y.; MACCARTNEY, G. R.; MOLISCH, A. F.; MELLIOS, E.; ZHANG, J. Overview of millimeter wave communications for fifth-generation (5g) wireless networks—with a focus on propagation models. *IEEE Transactions on Antennas and Propagation*, v. 65, n. 12, p. 6213–6230, 2017. Cited on page 97.

REHMAN, H. U.; BELLILI, F.; MEZGHANI, A.; HOSSAIN, E. Joint active and passive beamforming design for irs-assisted multi-user mimo systems: A vamp-based approach. *IEEE Transactions on Communications*, IEEE, v. 69, n. 10, p. 6734–6749, 2021. Cited on page 113.

REN, H.; ZHANG, Z.; PENG, Z.; LI, L.; PAN, C. Energy minimization in ris-assisted uav-enabled wireless power transfer systems. *IEEE Internet of Things Journal*, v. 10, n. 7, p. 5794–5809, 2023. Cited on page 115.

RODRIGUES, V. C.; AMIRI, A.; AO, T. A.; CARVALHO, E. de; POPOVSKI, P. Low-Complexity Distributed XL-MIMO for Multiuser Detection. In: *2020 IEEE Int. Conf. Commun. Workshops (ICC Workshops)*. [S.l.: s.n.], 2020. p. 1–6. Cited on page 46.

RODRíGUEZ-FERNáNDEZ, J.; GONZáLEZ-PRELCIC, N.; HEATH, R. W. A compressive sensing-maximum likelihood approach for off-grid wideband channel estimation at mmwave. In: *2017 IEEE 7th International Workshop on Computational Advances in Multi-Sensor Adaptive Processing (CAMSAP)*. [S.l.: s.n.], 2017. p. 1–5. Cited 2 times on page(s) 78 and 79.

SCHROEDER, R.; HE, J.; BRANTE, G.; JUNTTI, M. Two-stage channel estimation for hybrid ris assisted mimo systems. *IEEE Transactions on Communications*, v. 70, n. 7, p. 4793–4806, 2022. Cited 5 times on page(s) 77, 79, 80, 126, and 134.

SHEN, X.; DIAMOND, S.; GU, Y.; BOYD, S. Disciplined convex-concave programming. In: *2016 IEEE 55th Conference on Decision and Control (CDC)*. [S.l.: s.n.], 2016. p. 1009–1014. Cited 2 times on page(s) 120 and 124.

SIRITEANU, C.; MIYANAGA, Y.; BLOSTEIN, S. D.; KURIKI, S.; SHI, X. Mimo zero-forcing detection analysis for correlated and estimated rician fading. *IEEE Transactions on Vehicular Technology*, v. 61, n. 7, p. 3087–3099, 2012. Cited on page 166.

SIRITEANU, C.; TAKEMURA, A.; KURIKI, S.; RICHARDS, D. S. P.; SHIN, H. Schur complement based analysis of mimo zero-forcing for rician fading. *IEEE Transactions on Wireless Communications*, v. 14, n. 4, p. 1757–1771, 2015. Cited 2 times on page(s) 166 and 167.

TAGUE, J. A.; CALDWELL, C. I. Expectations of useful complex wishart forms. *Multidimensional Syst. Signal Process.*, Kluwer Academic Publishers, USA, v. 5, n. 3, p. 263–279,

jul 1994. ISSN 0923-6082. Available on: ⟨https://doi.org/10.1007/BF00980709⟩. Cited on page 167.

TAHA, A.; ALRABEIAH, M.; ALKHATEEB, A. Deep learning for large intelligent surfaces in millimeter wave and massive mimo systems. In: *IEEE (GLOBECOM)*. [S.l.: s.n.], 2019. p. 1–6. Cited 2 times on page(s) 76 and 96.

TAHA, A.; ALRABEIAH, M.; ALKHATEEB, A. Enabling large intelligent surfaces with compressive sensing and deep learning. *IEEE Access*, v. 9, p. 44304–44321, 2021. Cited 2 times on page(s) 76 and 88.

TAHA, A.; ZHANG, Y.; MISMAR, F. B.; ALKHATEEB, A. Deep reinforcement learning for intelligent reflecting surfaces: Towards standalone operation. In: *2020 IEEE 21st International Workshop on Signal Processing Advances in Wireless Communications (SPAWC)*. [S.l.: s.n.], 2020. p. 1–5. Cited on page 76.

TANIGUCHI, L. M.; ABRãO, T. Stochastic Channel Models for Massive and Extreme Large Multiple-Input Multiple-Output Systems. *Trans. Emerg. Telecommun. Technol.*, v. 31, n. 9, p. e4099, 2020. Available on: ⟨https://onlinelibrary.wiley.com/doi/abs/10.1002/ett.4099⟩. Cited on page 47.

TANIGUCHI, L. M.; SOUZA, J. H. I. de; GUERRA, D. W. M.; ABRãO, T. Resource efficiency and pilot decontamination in xl-mimo double-scattering correlated channels. *Transactions on Emerging Telecommunications Technologies*, v. 32, n. 12, p. e4365, 2021. Available on: ⟨https://onlinelibrary.wiley.com/doi/abs/10.1002/ett.4365⟩. Cited on page 57.

TARIQ, F.; KHANDAKER, M. R. A.; WONG, K.-K.; IMRAN, M. A.; BENNIS, M.; DEBBAH, M. A speculative study on 6g. *IEEE Wireless Communications*, v. 27, n. 4, p. 118–125, 2020. Cited on page 75.

TREES, H. L. V. *Optimum Array Processing, Part IV of Detection, Estimation, and Modulation Theory*. New York, NY, USA: Wiley, 2002. Cited 2 times on page(s) 76 and 77.

TRENDAFILOV, N.; GALLO, M. *Multivariate Data Analysis on Matrix Manifolds (with Manopt)*. 1. ed. Cham: Springer Series, 2021. 450 p. ISBN 9783030769734. Cited on page 159.

TROPP, J. Greed is good: algorithmic results for sparse approximation. *IEEE Transactions on Information Theory*, v. 50, n. 10, p. 2231–2242, 2004. Cited on page 152.

VANELLI-CORALLI, A.; GUIDOTTI, A.; FOGGI, T.; COLAVOLPE, G.; MONTORSI, G. 5g and beyond 5g non-terrestrial networks: trends and research challenges. In: *2020 IEEE 3rd 5G World Forum (5GWF)*. [S.l.: s.n.], 2020. p. 163–169. Cited on page 41.

VANNITHAMBY, R.; TALWAR, S. *Towards 5G Applications: Requirements and Candidate Technologies*. John Wiley & Sons, 2017. ISBN 978-1-118-97984-6. Available on: ⟨https://doi.org/10.1002/978-1-118-97984-6⟩. Cited on page 39.

WANG, P.; FANG, J.; DUAN, H.; LI, H. Compressed channel estimation for intelligent reflecting surface-assisted millimeter wave systems. *IEEE Signal Processing Letters*, v. 27, p. 905–909, 2020. Cited on page 77.

WANG, Z.; LIU, L.; CUI, S. Channel estimation for intelligent reflecting surface assisted multiuser communications: Framework, algorithms, and analysis. *IEEE Transactions on Wireless Communications*, v. 19, n. 10, p. 6607–6620, 2020. Cited 2 times on page(s) 77 and 78.

WANG, Z.; LIU, L.; ZHANG, S.; CUI, S. Massive MIMO Communication With Intelligent Reflecting Surface. *IEEE Transactions on Wireless Communications*, v. 22, n. 4, p. 2566–2582, 2023. Cited on page 108.

WEI, L.; HUANG, C.; ALEXANDROPOULOS, G. C.; SHA, W. E. I.; ZHANG, Z.; DEBBAH, M.; YUEN, C. Multi-user holographic mimo surfaces: Channel modeling and spectral efficiency analysis. *IEEE Journal of Selected Topics in Signal Processing*, v. 16, n. 5, p. 1112–1124, 2022. Cited on page 76.

WEI, X.; SHEN, D.; DAI, L. Channel estimation for ris assisted wireless communications—part ii: An improved solution based on double-structured sparsity. *IEEE Communications Letters*, v. 25, n. 5, p. 1403–1407, 2021. Cited on page 78.

WU, J.; KIM, S.; SHIM, B. Energy-efficient power control and beamforming for reconfigurable intelligent surface-aided uplink iot networks. *IEEE Transactions on Wireless Communications*, v. 21, n. 12, p. 10162–10176, 2022. Cited 17 times on page(s) 76, 79, 80, 81, 83, 88, 97, 99, 115, 116, 119, 120, 125, 126, 128, 130, and 134.

WU, Q.; ZHANG, R. Beamforming optimization for intelligent reflecting surface with discrete phase shifts. In: IEEE. *ICASSP 2019-2019 IEEE International Conference on Acoustics, Speech and Signal Processing (ICASSP)*. [S.l.], 2019. p. 7830–7833. Cited on page 113.

WU, Q.; ZHANG, R. Intelligent reflecting surface enhanced wireless network via joint active and passive beamforming. *IEEE Transactions on Wireless Communications*, v. 18, n. 11, p. 5394–5409, 2019. Cited on page 114.

WU, Q.; ZHANG, S.; ZHENG, B.; YOU, C.; ZHANG, R. Intelligent Reflecting Surface-Aided Wireless Communications: A Tutorial. *IEEE Transactions on Communications*, v. 69, n. 5, p. 3313–3351, 2021. Cited on page 108.

WU, S.; WANG, C.-X.; AGGOUNE, e.-H. M.; ALWAKEEL, M. M.; YOU, X. A General 3-D Non-Stationary 5G Wireless Channel Model. *IEEE Trans. Commun.*, v. 66, n. 7, p. 3065–3078, 2018. Cited 3 times on page(s) 47, 48, and 58.

XIE, H.; XU, J.; LIU, Y.-F. Max-min fairness in irs-aided multi-cell miso systems with joint transmit and reflective beamforming. *IEEE Transactions on Wireless Communications*, IEEE, v. 20, n. 2, p. 1379–1393, 2020. Cited on page 113.

YANG, X.; CAO, F.; MATTHAIOU, M.; JIN, S. On the Uplink Transmission of Extra-Large Scale Massive MIMO Systems. *IEEE Trans. Veh. Technol.*, v. 69, n. 12, p. 15229–15243, 2020. Cited on page 46.

YOU, L.; XIONG, J.; NG, D. W. K.; YUEN, C.; WANG, W.; GAO, X. Energy Efficiency and Spectral Efficiency Tradeoff in RIS-Aided Multiuser MIMO Uplink Transmission. *IEEE Trans. on Signal Proc.*, v. 69, p. 1407–1421, 2021. ISSN 1053-587X. Available on: ⟨https://ieeexplore.ieee.org/document/9309152/⟩. Cited 2 times on page(s) 114 and 126.

ZAIDI, A.; ATHLEY, F.; MEDBO, J.; GUSTAVSSON, U.; DURISI, G.; CHEN, X. *5G Physical Layer: Principles, Models and Technology Components*. 1st. ed. USA: Academic Press, Inc., 2018. ISBN 0128145781. Cited on page 40.

ZENG, M.; BEDEER, E.; DOBRE, O. A.; FORTIER, P.; PHAM, Q.-V.; HAO, W. Energy-Efficient Resource Allocation for IRS-Assisted Multi-Antenna Uplink Systems. *IEEE Wireless Communications Letters*, v. 2337, n. 1, p. 1–1, 2021. ISSN 2162-2337. Available on: ⟨https://ieeexplore.ieee.org/document/9369326/⟩. Cited 2 times on page(s) 114 and 126.

ZHANG, J.; QI, C.; LI, P.; LU, P. Channel estimation for reconfigurable intelligent surface aided massive mimo system. In: *2020 IEEE 21st International Workshop on Signal Processing Advances in Wireless Communications (SPAWC)*. [S.l.: s.n.], 2020. p. 1–5. Cited on page 77.

ZHANG, Q.; LU, Z.; JIN, S.; WONG, K.-K.; ZHU, H.; MATTHAIOU, M. Power scaling of massive mimo systems with arbitrary-rank channel means and imperfect csi. In: *2013 IEEE Global Communications Conference (GLOBECOM)*. [S.l.: s.n.], 2013. p. 4157–4162. Cited on page 166.

ZHANG, W.; KIM, T. Successful recovery performance guarantees of somp under the ℓ_2-norm of noise. *IEEE Transactions on Vehicular Technology*, v. 73, n. 2, p. 2156–2170, 2024. Cited on page 151.

ZHI, K.; PAN, C.; REN, H.; CHAI, K. K.; ELKASHLAN, M. Active ris versus passive ris: Which is superior with the same power budget? *IEEE Communications Letters*, v. 26, n. 5, p. 1150–1154, 2022. Cited on page 75.

ZHI, K.; PAN, C.; REN, H.; WANG, K. Ergodic rate analysis of reconfigurable intelligent surface-aided massive mimo systems with zf detectors. *IEEE Communications Letters*, v. 26, n. 2, p. 264–268, 2022. Cited 2 times on page(s) 122 and 167.

ZHI, K.; PAN, C.; ZHOU, G.; REN, H.; ELKASHLAN, M.; SCHOBER, R. Is ris-aided massive mimo promising with zf detectors and imperfect csi? *IEEE Journal on Selected Areas in Communications*, v. 40, n. 10, p. 3010–3026, 2022. Cited 3 times on page(s) 122, 130, and 167.

ZHOU, G.; PAN, C.; REN, H.; WANG, K.; NALLANATHAN, A. A framework of robust transmission design for irs-aided miso communications with imperfect cascaded channels. *IEEE Transactions on Signal Processing*, IEEE, v. 68, p. 5092–5106, 2020. Cited on page 113.

ZHOU, G.; PAN, C.; REN, H.; POPOVSKI, P.; SWINDLEHURST, A. L. Channel estimation for ris-aided multiuser millimeter-wave systems. *IEEE Transactions on Signal Processing*, v. 70, p. 1478–1492, 2022. Cited on page 89.

ZHU, Y.; YANG, T. Low complexity hybrid beamforming for uplink multiuser mmwave mimo systems. In: *2017 IEEE Wireless Communications and Networking Conference (WCNC)*. [S.l.: s.n.], 2017. p. 1–6. Cited on page 125.

Appendix

APPENDIX A – Proof of Convergence for the SMP-PR Algorithm

For simplicity of analysis, we have considered a bounded noisy scenario; then, we provided the performance of support recovery and convergence of SOMP-PR/SMP-PR based on proofs presented in (ZHANG; KIM, 2024; DETERME et al., 2017). Notice that the convergence analysis for the OMP-PR/MP-PR can use the same procedure. Basically, we have the problem of sparse signal recovery for channel estimation, in which a conventional linear observation model is assumed as follows:

$$\mathbf{Y}_k = \boldsymbol{\Upsilon}_k \mathbf{H}_{\mathrm{R},k} + \mathbf{N}, \tag{A.1}$$

where $\mathbf{Y}_k \in \mathbb{C}^{M \times N_{\mathrm{SC}}}$ is the observation matrix, $\boldsymbol{\Upsilon}_k \in \mathbb{C}^{M \times \gamma^2 N_{\mathrm{RIS}} N_{\mathrm{UE}}}$ with $M \ll \gamma^2 N_{\mathrm{RIS}} N_{\mathrm{UE}}$ is the measurement matrix, $\mathbf{H}_{\mathrm{R},k} \in \mathbb{C}^{\gamma^2 N_{\mathrm{RIS}} N_{\mathrm{UE}} \times N_{\mathrm{SC}}}$ is the row-sparse matrix with only $L \ll \gamma^2 N_{\mathrm{RIS}} N_{\mathrm{UE}}$ rows being non-zero, and $\mathbf{N} \in \mathbb{C}^{M \times N_{\mathrm{SC}}}$ is the measurement noise matrix.

First, we consider two important characteristics of measurement matrix that are widely adopted in this analysis: *(i)* restricted isometry property (RIP) and *(ii)* mutual incoherence property (MIP). Specifically, the measurement matrix for the k-th user ($\boldsymbol{\Upsilon}_k$) satisfies the RIP of order L with the restricted isometry constant (RIC) δ_L if δ_L is the smallest constant such that

$$(1 - \delta_L)\|\mathbf{x}\|_2^2 \leq \|\boldsymbol{\Upsilon}_k \mathbf{x}\|_2^2 \leq (1 + \delta_L)\|\mathbf{x}\|_2^2 \tag{A.2}$$

holds for all L-sparse signal $\mathbf{x} \in \mathbb{C}^{\gamma^2 N_{\mathrm{RIS}} N_{\mathrm{UE}} \times 1}$. Meanwhile, the mutual coherence of a matrix $\boldsymbol{\Upsilon}_k$ is defined as

$$\mu = \max_{i \neq j} |\langle [\boldsymbol{\Upsilon}_k]_{:,i}, [\boldsymbol{\Upsilon}_k]_{:,j} \rangle|, \tag{A.3}$$

where $[\boldsymbol{\Upsilon}_k]_{:,i}$ denotes the ith column of $\boldsymbol{\Upsilon}_{\boldsymbol{k}}$, and $\langle \cdot, \cdot \rangle$ denotes the inner product.

Denoting $\mathbf{P}^{[i]} = [\boldsymbol{\Upsilon}_k]_{:,\hat{\mathcal{T}}^{(i)}} [\boldsymbol{\Upsilon}_k]^{\dagger}_{:,\hat{\mathcal{T}}^{(i)}} \in \mathbb{C}^{M \times M}$ and $\mathbf{P}_{\perp}^{[i]} = \mathbf{I} - \mathbf{P}^{[i]}$, the residual of ith iteration is expressed as

$$\mathbf{R}^{[i]} = \mathbf{P}_{\perp}^{[i]} \mathbf{Y}_k = \mathbf{P}_{\perp}^{[i]} (\boldsymbol{\Upsilon}_k \mathbf{H}_{\mathrm{R},k} + \mathbf{N}), \tag{A.4}$$

where the columns of residue $\mathbf{R}^{[i]}$ belong to the column subspace of $\mathbf{P}_{\perp}^{[i]}$.

Before delving into assessing the convergence guarantee provided by our proposed algorithm, we compile key findings and establish practical conditions that will serve as our foundation.

Lemma 1 (Property of matrix $\boldsymbol{\Upsilon}_k$) (TROPP, 2004): For the model outlined in eq. (A.1), let us define the constant

$$G = \max_{\mathbf{a}\in[\boldsymbol{\Upsilon}_k]_{:,\mathcal{T}^c}} \|([\boldsymbol{\Upsilon}_k]_{:,\mathcal{T}}^H[\boldsymbol{\Upsilon}_k]_{:,\mathcal{T}})^{-1}[\boldsymbol{\Upsilon}_k]_{:,\mathcal{T}}^H\mathbf{a}\|_1 \tag{A.5}$$

where $\mathcal{T} \subset 1,\ldots,N$ with $|\mathcal{T}| = L$, and $\mathcal{T}^c \subset \{1,\ldots,N\}$ with $|\mathcal{T}^c| = N - L$ denotes the complement of the set $\mathcal{T}$. Then, the value of G is upper bounded by $G \leq \frac{L\mu}{1-(L-1)\mu}$, where the constant μ is the mutual coherence of matrix $\boldsymbol{\Upsilon}_k$.

Lemma 2 (Minimal eigenvalue inequality) (CAI; WANG, 2011). The minimum eigenvalue of $[\boldsymbol{\Upsilon}_k]_{:,\mathcal{T}}^H[\boldsymbol{\Upsilon}_k]_{:,\mathcal{T}}$ is less than or equal to the minimum eigenvalue of $[\boldsymbol{\Upsilon}_k]_{:,\hat{\mathcal{T}}_c^{(i)}}^H\mathbf{P}_\perp^{[i]}[\boldsymbol{\Upsilon}_k]_{:,\hat{\mathcal{T}}_c^{(i)}}$, where $\hat{\mathcal{T}}_c^{(i)}$ denotes the complement of the selected support set $\hat{\mathcal{T}}^{(i)}$ over the universe $\mathcal{T}$ with $|\hat{\mathcal{T}}_c^{(i)}| = L - i$.

Given the signal model in (A.1), for the proposed two-stage algorithm (sensing support columns recovery and the optimization of the phase rotation angles) we also have

$$\|\boldsymbol{\Upsilon}_k\mathbf{x}\|_2^2 \leq \|(\boldsymbol{\Upsilon}_k \odot \mathbf{R}_{\text{eq}})\mathbf{x}\|_2^2 \tag{A.6}$$

where $\mathbf{R}_{\text{eq}}$ refers to the phase rotation matrix. Therefore, it becomes evident that if the first stage of the SOMP-PR/SMP-PR converges, the two-stage algorithms will also converge. From this, a sufficient condition for the successful support recovery in the first stage of SOMP-PR/SMP-PR is provided in the following theorem.

Theorem 1. Considering the signal model in equation (A.1), assuming the mutual coherence μ of the measurement matrix $\boldsymbol{\Upsilon}_k$ satisfying $\mu < 1/(2L-1)$, with noise bounded by $\|\mathbf{N}\|_2 \leq \epsilon$. Then, if the following condition holds,

$$C_{\min} = \min_{i\in\mathcal{T}} \|[\mathbf{H}_{\text{R},k}]_{i,:}\|_2 > \frac{2\epsilon}{1-(2L-1)\mu}, \tag{A.7}$$

Algorithm 5 successfully recovers the support set $\mathcal{T}$.

Proof: By applying Theorem 1, we only need to prove that Algorithm 2 terminates correctly, *i.e.*, $i = L$. In other words, it is sufficient to show that when $i < L$, we have $\|\mathbf{R}^{[i]}\|_2 > \epsilon$, and when $i = L$ we have $\|\mathbf{R}^{[i]}\|_2 \leq \epsilon$. First of all, when $i = L$, the following condition holds,

$$\begin{aligned} \|\mathbf{R}^{[L]}\|_2 &= \|\mathbf{P}_\perp^{[L]}\boldsymbol{\Upsilon}_k\mathbf{H}_{\text{R},k} + \mathbf{P}_\perp^{[L]}\mathbf{N}\|_2 \\ &= \|\mathbf{P}_\perp^{[L]}\mathbf{N}\|_2 \\ &\leq \|\mathbf{N}\|_2 \leq \epsilon. \end{aligned} \tag{A.8}$$

When $i < L$, one can have the following,

$$\begin{aligned}
\|\mathbf{R}^{[i]}\|_2 &= \|\mathbf{P}_{\perp}^{[i]}\boldsymbol{\Upsilon}_k\mathbf{H}_{\mathrm{R},k} + \mathbf{P}_{\perp}^{[i]}\mathbf{N}\|_2 \\
&\geq \|\mathbf{P}_{\perp}^{[i]}\boldsymbol{\Upsilon}_k\mathbf{H}_{\mathrm{R},k}\|_2 - \|\mathbf{P}_{\perp}^{[i]}\mathbf{N}\|_2 \\
&\overset{(a)}{=} \|\mathbf{P}_{\perp}^{[i]}[\boldsymbol{\Upsilon}_k]_{:,\hat{\mathcal{T}}_c^{(i)}}[\mathbf{H}_{\mathrm{R},k}]_{\hat{\mathcal{T}}_c^{(i)},:}\|_2 - \epsilon \\
&\overset{(b)}{\geq} \sqrt{\lambda_{\min}\left([\boldsymbol{\Upsilon}_k]_{:,\hat{\mathcal{T}}_c^{(i)}}^H\mathbf{P}_{\perp}^{[i]}[\boldsymbol{\Upsilon}_k]_{:,\hat{\mathcal{T}}_c^{(i)}}\right)}\|[\mathbf{H}_{\mathrm{R},k}]_{\hat{\mathcal{T}}_c^{(i)},:}\|_2 - \epsilon \\
&\overset{(c)}{\geq} \sqrt{\lambda_{\min}\left([\boldsymbol{\Upsilon}_k]_{:,\mathcal{T}}^H\boldsymbol{\Upsilon}_k]_{:,\mathcal{T}}\right)}\|[\mathbf{H}_{\mathrm{R},k}]_{\hat{\mathcal{T}}_c^{(i)},:}\|_2 - \epsilon \\
&\overset{(d)}{\geq} \sqrt{1-(L-1)\mu}\|[\mathbf{H}_{\mathrm{R},k}]_{\hat{\mathcal{T}}_c^{(i)},:}\|_2 - \epsilon
\end{aligned} \tag{A.9}$$

where $\lambda_{\min}(\mathbf{A})$ returns the minimal eigenvalue of $\mathbf{A}$; equality (a) is due to the definition of projection matrix $\mathbf{P}_{\perp}^{[i]}$, *i.e.*, $\mathbf{P}_{\perp}^{[i]} = \mathbf{I} - [\boldsymbol{\Upsilon}_k]_{:,\hat{\mathcal{T}}^{(i)}}[\boldsymbol{\Upsilon}_k]_{:,\hat{\mathcal{T}}^{(i)}}^{\dagger}$, (b) follows from the idempotency and symmetry properties of orthogonal projection matrices, (c) is due to Lemma 2, and (d) is due to the Gershgorin disk theorem (GERSCHGORIN, 1931).

Given the condition in (A.7), the first term on the right hand side of (A.9) can be further lower bounded by

$$\begin{aligned}
\sqrt{1-(L-1)\mu}\|[\mathbf{H}_{\mathrm{R},k}]_{\hat{\mathcal{T}}_c^{(i)},:}\|_2 &\geq \sqrt{1-(L-1)\mu}\min_{i\in\mathcal{T}}\|[\mathbf{H}_{\mathrm{R},k}]_{i,:}\|_2 \\
&\overset{(a)}{\geq} \frac{2\sqrt{1-(L-1)\mu}\epsilon}{1-(2L-1)\mu} \\
&\overset{(b)}{\geq} 2\epsilon,
\end{aligned} \tag{A.10}$$

where (a) in eq. (A.10) is due to (A.7) and (b) follows from the fact that $\sqrt{1-(L-1)\mu} \geq 1-(2L-1)\mu$. Combining (A.9) with (A.10) leads to $\|\mathbf{R}^{[i]}\|_2 > \epsilon$, $\forall i < L$. This concludes the proof.

Then the first stage of Algorithm 5 successfully recovers the support set $\mathcal{T}$. Therefore, Algorithm 5 converges with exactly L iterations.

APPENDIX B – Non-convexity of the Unit-Modulus Constraint

The unit-modulus constraint in the problem 4.16 is non-convex because it restricts each variable ϕ_n to lie on the complex unit circle, which is a non-convex set.

To elaborate, a set $\mathcal{S}$ is convex if, for any two points $x, y \in \mathcal{S}$, the line segment connecting x and y lies entirely within $\mathcal{S}$. Mathematically, this means that for any $x, y \in \mathcal{S}$ and any $\alpha \in [0, 1]$, the point $\alpha x + (1 - \alpha)y$ also lies in $\mathcal{S}$.

Now, let us consider the unit-modulus constraint $|\phi_n| = 1$ for all $n \in \{1, \ldots, N\}$. This constraint means that each ϕ_n must lie on the unit circle in the complex plane, i.e., $\phi_n = e^{j\theta_n}$ for some real angle θ_n. The set of all such ϕ_n is the unit circle, denoted by:

$$\mathcal{S} = \{\phi \in \mathbb{C} \mid |\phi| = 1\}. \tag{B.1}$$

To determine if $\mathcal{S}$ is convex, consider two points ϕ_1 and ϕ_2 on the unit circle. These points can be written as $\phi_1 = e^{j\theta_1}$ and $\phi_2 = e^{j\theta_2}$ for some real angles θ_1 and θ_2. For any $\alpha \in [0, 1]$, the point $\alpha\phi_1 + (1 - \alpha)\phi_2$ is given by:

$$\alpha\phi_1 + (1 - \alpha)\phi_2 = \alpha e^{j\theta_1} + (1 - \alpha)e^{j\theta_2}. \tag{B.2}$$

However, this new point $\alpha\phi_1 + (1 - \alpha)\phi_2$ does not generally lie on the unit circle. In fact, its modulus is given by:

$$|\alpha\phi_1 + (1 - \alpha)\phi_2| = |\alpha e^{j\theta_1} + (1 - \alpha)e^{j\theta_2}|. \tag{B.3}$$

Since $|e^{j\theta_1}| = 1$ and $|e^{j\theta_2}| = 1$, the modulus of $\alpha\phi_1 + (1 - \alpha)\phi_2$ will generally be less than 1 unless $\phi_1 = \phi_2$, which means that $\alpha\phi_1 + (1 - \alpha)\phi_2$ does not lie on the unit circle. Therefore, the unit circle is not a convex set.

This non-convexity of the unit-modulus constraint $|\phi_n| = 1$ makes the optimization problem non-convex because the feasible set defined by this constraint is non-convex. As a result, standard convex optimization techniques cannot be directly applied to solve the problem.

APPENDIX C – Definitions on Riemannian Manifolds

A Riemannian manifold is a space that locally looks like a Euclidean space, but the distances and angles between points are defined by a Riemannian metric tensor. This tensor assigns a positive definite inner product to each tangent space of the manifold, which allows us to define concepts such as length, angle, and curvature. Basically, the tangent space $\mathcal{T}_p\mathcal{M}$ at a point p of a Riemannian manifold $\mathcal{M}$ is the set of all tangent vectors at point p. Intuitively, $\mathcal{T}_p\mathcal{M}$ is the space of all directions in which one can move away from p on $\mathcal{M}$, where the curve μ of $\mathcal{M}$ is a mapping from $\mathbb{C}$ to $\mathcal{M}$.

A key concept in Riemannian geometry is the *Riemannian gradient* $\nabla_{\mathcal{M}} f(p)$ of a smooth function $f : \mathcal{M} \to \mathbb{C}$ at a point $p \in \mathcal{M}$. This gradient is a vector in $\mathcal{T}_p\mathcal{M}$ that points in the direction of the steepest-descent of f at p, taking into account the curvature of $\mathcal{M}$. The Riemannian gradient can be obtained by projecting the Euclidean gradient of f onto $\mathcal{T}_p\mathcal{M}$. Therefore, the Riemannian gradient can be expressed as:

$$\nabla_{\mathcal{M}} f(p) = \text{Proj}\{\mathcal{T}_p\mathcal{M}(\nabla f(p))\} \tag{C.1}$$

where $\nabla f(p)$ is the Euclidean gradient of f at p, and $\text{Proj}\{\mathcal{T}_p\mathcal{M}\}$ is the projection operator onto the tangent space $\mathcal{T}_p\mathcal{M}$. A Riemannian gradient is an important tool in the optimization on Riemannian manifolds. In particular, it is used in gradient-based algorithms that require the computation of a descent direction at each iteration.

Another key operator in many optimization algorithms on manifolds is the *retraction operation*. The retraction operation is a way of moving from a point on a manifold to a nearby point while staying on the manifold. Mathematically, retraction is a smooth map that takes a point on the tangent space at a certain point on the manifold and returns a point on the manifold. The retraction map $\text{Ret}_p : \mathcal{T}_p\mathcal{M} \to \mathcal{M}$ is a smooth map that satisfies the following properties (ABSIL et al., 2007):

1. $\text{Retr}_p(0_p) = p$, where 0_p denotes the zero element in $\mathcal{T}_p\mathcal{M}$.
2. The *directional derivative* of the retraction map at 0_p is the identity map, *i.e.*, $D\,\text{Ret}\,p(0_p) = \text{id}_{\mathcal{T}_p\mathcal{M}}$, where $\text{id}_{\mathcal{T}_p\mathcal{M}}$ is the identity mapping on $\mathcal{T}_p\mathcal{M}$.
3. $\text{Ret}_p(v)$ is a point on the manifold for all $v \in \mathcal{T}_p\mathcal{M}$.

For example, in the case of the *complex circle manifold*, a common choice for the retraction map is the exponential map, denoted by Exp_p for a point p on the manifold. The exponential map takes a point v in the tangent space at p and returns a nearby point on the manifold.

Therefore, the retraction operator via an exponential map for the *complex circle manifold* is given by:

$$\text{Retr}_p(v) = \text{Exp}_p(v) = p \cdot e^{iv}, \tag{C.2}$$

where p is a complex number with magnitude 1 (*i.e.*, $|p| = 1$), v is a real number, and i is the imaginary unit. Hence, we have the complex multiplication operation to rotate p by an angle v. This operation returns a point on the complex circle manifold with magnitude 1, so it stays on the manifold. Another option to perform the retraction operation for the complex circle manifold is given by:

$$\text{Retr}_p(v) = (p + v) \odot \frac{1}{|p + v|}. \tag{C.3}$$

It is important to note that there are several ways to construct a retraction map, depending on the manifold.

APPENDIX D – Manifold-Based Solution Methods

Riemannian manifolds are mathematical objects that generalize the notion of Euclidean space to more complex and curved geometries. They are widely used in optimization (ABSIL et al., 2007). A Riemannian manifold is a space that locally looks like a Euclidean space, but the distances and angles between points are defined by a Riemannian metric tensor. This tensor assigns a positive definite inner product to each tangent space of the manifold, which allows us to define concepts such as length, angle, and curvature. A couple of key definitions and concepts in Riemannian geometry, including *Riemannian gradient* $\nabla_{\mathcal{M}} f(p)$ and *retraction operation* $\text{Retr}_p(v)$ are provided in Appendix C.

D.1 Manifold PSO-Based Solution Method

The manifold particle swarm optimization (PSO)-based algorithm relies on an iterative optimization process that combines the heuristic PSO algorithm with the Riemannian manifold (TRENDAFILOV; GALLO, 2021). PSO is a population-based heuristic evolutionary optimization algorithm that uses a set of particles to explore the solution space, searching for a global or a local solution. In the case of manifold PSO-based, the manifold is used to restrict the search of the particles to a specific Riemannian manifold subspace. This is useful in optimization problems where the solutions have a geometric structure, *e.g.*, when the problem is subject to constraints or when the optimal solution lies in a specific manifold. By limiting the search of particles to a Riemannian manifold, the PSO-based algorithm can perform a more efficient and precise search in the solutions space, considering the constraints imposed by the manifold.

The manifold PSO-based algorithm is very similar to the standard PSO algorithm with modifications to account for optimization on Riemannian manifolds. The algorithm's objective is to minimize a function $f(\boldsymbol{\zeta})$ on a Riemannian manifold $\mathscr{M}$, where $\boldsymbol{\zeta}$ is a particle in $\mathscr{M}$. The PSO algorithm updates the velocity and position of each particle using respectively (GUERRA et al., 2018):

$$\mathbf{V} = w\mathbf{V} + c_1\mathbf{R}_1 \odot (\mathbf{M}_{\text{PB}} - \boldsymbol{\Psi}) + c_2\mathbf{R}_2 \odot (\mathbf{M}_{\text{GB}} - \boldsymbol{\Psi}), \tag{D.1}$$

$$\boldsymbol{\Psi} = \boldsymbol{\Psi} + \mathbf{V}, \tag{D.2}$$

where N_{dim} represents the dimensionality of the problem, w represents the inertia factor, and matrices $\mathbf{R}_1$ and $\mathbf{R}_2$ are composed by elements drawn from the uniform distribution $\mathcal{U}[0, 1]$. Matrices $\boldsymbol{\Psi} \in \mathbb{R}^{N_{\text{dim}} \times N_{\text{pop}}}$ and $\mathbf{V} \in \mathbb{R}^{N_{\text{dim}} \times N_{\text{pop}}}$ store the position and velocity of N_{pop}

particles of the swarm in each column, such that $\mathbf{\Psi} = [\boldsymbol{\psi}_1 \dots \boldsymbol{\psi}_{N_{\text{pop}}}]$ and $\mathbf{V} = [\mathbf{v}_1 \dots \mathbf{v}_{N_{\text{pop}}}]$. The matrix $\mathbf{M}_{\text{PB}}$ is constructed with the personal best position of each particle, while the best position matrix is given by $\mathbf{M}_{\text{GB}} = [\boldsymbol{\psi}_{\text{GB}} \dots \boldsymbol{\psi}_{\text{GB}}] \in \mathbb{R}^{N_{\text{dim}} \times N_{\text{pop}}}$, where vector $\boldsymbol{\psi}_{\text{GB}} \in \mathbb{R}^{N\text{dim} \times 1}$ denotes the best position in the swarm, *i.e.*, the global best position that minimizes the fitness function.

In the initialization of the implemented manifold PSO-based algorithm, the positions of the particles $\mathbf{\Psi}$ are generated randomly following a uniform distribution inside the search space. Those positions are set as the personal best position of the particle in the matrix $\mathbf{M}_{\text{PB}}$. The fitness function is evaluated ($\boldsymbol{\zeta}_k = \mathbf{\Psi}_k, k = 1, \dots, N_{\text{iter}}$) and the position of the particle that produces the lowest value (since we are dealing with a minimization problem) is set as the global best position $\mathbf{\Psi}_{\text{GB}}$, and the matrix $\mathbf{M}_{\text{GB}}$ is formed (FUKUDA et al., 2018). After evaluation of eq.(D.1) and eq.(D.2), matrices $\mathbf{M}_{\text{PB}}$ and $\mathbf{M}_{\text{GB}}$ are updated and the process is repeated till the stop criterion is met; herein, the criterion of maximum number of evaluations N_{iter} is deployed. The output of the algorithm is the vector of the best position $\boldsymbol{\psi}_{\text{GB}}$. A pseudocode summarizing the procedure described for the evolutionary heuristic PSO algorithm is presented in **Algorithm 6**.

Algorithm 6 Manifold PSO-based

Input: $c_1, c_2, w, N_{\text{pop}}, N_{\text{iter}}$
Generate initial positions $\mathbf{P}$
for $k = 1$ until N_{iter} **do**
  Fitness function evaluation and initialization of $\mathbf{M}_{\text{PB}}$, $\mathbf{M}_{\text{GB}}$
  Calculate velocity, eq. (D.1)
  Calculate position, eq. (D.2)
  Update each particle's position by applying the retraction operation
  Evaluate fitness function for all particles $\mathbf{p}_k$
  Update personal best matrix $\mathbf{M}_{\text{PB}}$
  Update global best matrix $\mathbf{M}_{\text{GB}}$
end for
Output: $\mathbf{p}_{\text{GB}}$

D.2 Manifold CG-Based Algorithm

In order to solve an optimization, we also can apply a modified version of the classical *conjugate gradient* (CG) *method* (DAI, 2011) by using the Riemannian manifold concepts, namely Riemannian conjugate gradient (RCG). To achieve this goal, we update the conjugate direction $\mathbf{D}$ and the point $\mathbf{X}$ as follows:

$$\mathbf{D}_k = -\nabla_{\mathcal{M}} f(\mathbf{X}_k) + \beta_k \, \text{Proj}\{\mathcal{T}_{\mathbf{X}_k}\mathcal{M}(\mathbf{D}_{k-1})\}, \tag{D.3}$$

$$\mathbf{X}_{k+1} = \text{Retr}_{\mathbf{X}_k}(\alpha_k^{\text{ss}} \mathbf{D}_k), \tag{D.4}$$

where $\text{Proj}\{\mathcal{T}_{\mathbf{X}_k}\mathcal{M}(\mathbf{D}_{k-1})\}$ is the projection operator onto the tangent space $\mathcal{T}_{\mathbf{X}_k}\mathcal{M}$, $\nabla_{\mathcal{M}} f(\mathbf{X}_k)$ denotes the Riemannian gradient of the objective function at $\mathbf{X}_k$, with $\mathbf{X}_k$

being, *e.g.*, the phase shift matrix $\mathbf{\Phi}$, $\text{Retr}_p(v)$ is the *retraction operator*, which can be an exponential map in v for the case of the complex circle manifold as defined, *e.g.*, in eq. (C.2), β_k is the Fletcher-Reeves conjugate gradient parameter, and α_k^{ss} is the step size at the k-th iteration of the RCG algorithm (DAI, 2011). In addition, the conjugate gradient parameter β_k is calculated as:

$$\beta_k = \frac{||\nabla_{\mathcal{M}} f(\mathbf{X}_k)||^2}{||\nabla_{\mathcal{M}} f(\mathbf{X}_{k-1})||^2}. \tag{D.5}$$

Besides, the step size α_k^{ss} at the k-th iteration is calculated using a line search algorithm, aiming to find a step size α_k^{ss} that reduces the objective function sufficiently while satisfying the Armijo rule[1], a sufficient condition for the step size to be accepted, given by (DAI, 2011):

$$f(\text{Retr}_{\mathbf{X}_k}(\alpha_k^{\text{ss}} \mathbf{D}_k)) \leq f(\mathbf{X}_k) + c_1 \alpha_k^{\text{ss}} \langle \nabla_{\mathcal{M}} f(\mathbf{X}_k), \mathbf{D}_k \rangle, \tag{D.6}$$

where $\langle X, Y \rangle$ is the inner product between X and Y, and c_1 is a constant chosen to be a small positive number, *e.g.*, $c_1 = 10^{-4}$.

The line search algorithm starts with an initial step size α_0^{ss} (e.g., $\alpha_0^{\text{ss}} = 1$) and iteratively adjusts the step size until the Armijo rule is satisfied. Then, the *backtracking line search* algorithm is used as follows (BOUMAL et al., 2014):

1. Set $\alpha_k^{\text{ss}} = \alpha_0^{\text{ss}}$, and $\mathbf{X}_{\text{new}} = \mathbf{X}_k + \alpha_k^{\text{ss}} \mathbf{D}_k$.
2. If the Armijo rule is satisfied, then return α_k^{ss}.
3. Otherwise, decrease the step size by a factor $\rho \in (0, 1)$, *i.e.*, $\alpha_k^{\text{ss}} \leftarrow \rho \alpha_k^{\text{ss}}$, and set $\mathbf{X}_{\text{new}} = \mathbf{X}_k + \alpha_k^{\text{ss}} \mathbf{D}_k$.
4. Repeat steps 2-3 until the Armijo rule is satisfied or the step size becomes too small.

If the step size becomes too small, the line search algorithm terminates with the current iterate $\mathbf{X}_k$. Otherwise, the line search algorithm returns the step size α_k^{ss} that satisfies the Armijo rule.

The step-by-step procedure for the manifold CG-based algorithm is provided in **Algorithm 7**.

D.3 Manifold RTR-Based Scheme

The Riemannian trust-region (RTR) solution is an optimization procedure that iteratively solves a trust-region subproblem to obtain a search direction for updating the

[1]Armijo Rule is a an alternative approach to optimal line search; also known as backtracking line search, the Armijo rule ensures that the OF f decreases sufficiently at every iteration. In return, it reduces complexity as compared to optimal line search. The Armijo rule corresponds to a fast time scale procedure implemented at every iteration of the gradient descent algorithm (slow time scale).

Algorithm 7 Manifold CG-based

Input: Input parameters: c_1, ϵ, $\mathcal{M}$, N_{iter}
$k = 0$
$\beta_0 = 0$
Initialize $\mathbf{X}_0$ randomly from the manifold $\mathcal{M}$
$\mathbf{D}_0 = -\nabla_{\mathcal{M}} f(\mathbf{X}_0)$
while $k \leq N_{\text{iter}}$ and $||\mathbf{X}_k - \mathbf{X}_{k-1}||^2 \leq \epsilon$ **do**
    $k = k + 1$
    $\nabla_{\mathcal{M}} f(\mathbf{X}_k) = \text{Proj}\{\mathcal{T}_{\mathbf{X}_k}\mathcal{M}(\nabla f(\mathbf{X}_k))\}$
    Update β_k according to eq. (D.5)
    Update $\mathbf{D}_k$ according to eq. (D.3)
    Find the step size $\alpha_k^{\text{ss}} > 0$ via backtracking line search algorithm
    Update $\mathbf{X}_k$ according to eq. (D.4)
end while
Output: $\mathbf{X}_k$

current iteration. The trust-region subproblem involves minimizing a quadratic objective function within a trust region defined by a radius parameter. The solver seeks to find a point that improves the objective function within the trust region. The radius parameter is adjusted based on the quality of the updated values at each iteration (ABSIL et al., 2007).

The trust region starts with an initial point $\mathbf{X}_0$ and a radius parameter $\Delta_0 > 0$. At each iteration k, the algorithm solves the trust-region subproblem:

$$\begin{aligned} \underset{\boldsymbol{\eta} \in \mathcal{T}_{\mathbf{X}_k}\mathcal{M}}{\text{minimize}} \quad & m_k(\boldsymbol{\eta}) = f(\mathbf{X}_k) + \langle \nabla_{\mathcal{M}} f(\mathbf{X}_k), \boldsymbol{\eta} \rangle + \tfrac{1}{2}\langle \boldsymbol{\eta}, \mathcal{H}_k \boldsymbol{\eta} \rangle, \\ \text{s.t.} \quad & ||\boldsymbol{\eta}||^2 \leq \Delta_k^2, \end{aligned} \tag{D.7}$$

where $\mathcal{H}_k$ is the Hessian of the objective function at $\mathbf{X}_k$. Then, the new candidate is obtained as $\mathbf{X}_{k+1} = \text{Retr}_{\mathbf{X}_k}(\boldsymbol{\eta}_k)$, where $\boldsymbol{\eta}_k$ is the solution of the trust-region subproblem at the k-th iteration. The trust-region radius Δ_k is updated based on the ratio of the actual to the predicted reduction in the objective function as:

$$\rho_k = \frac{f(\mathbf{X}_k) - f(\mathbf{X}_{k+1})}{m_k(\mathbf{0}_{\mathbf{X}_k}) - m_k(\boldsymbol{\eta})}. \tag{D.8}$$

If ρ_k is small, the update is rejected, and the trust-region radius Δ_k is reduced. If ρ_k is large, the update is accepted, and the trust-region radius is increased. If ρ_k is in a middle range, the update is accepted without changing the trust-region radius. Therefore, the trust-region solver finishes when a stopping criterion is met, such as reaching a maximum number of iterations N_{iter} or achieving a small gradient norm. A pseudocode for the manifold RTR-based solution is presented in **Algorithm 8**.

D.4 Manifold SD-Based Solution

The steepest-descent (SD) algorithm for Riemannian manifolds (RSD) uses a first-order gradient method to solve an optimization problem. Given a smooth objective function

Algorithm 8 Manifold RTR-based Solver

Input: Input parameters: $\overline{\rho} \in [0, \frac{1}{4})$, Δ_0, $\Delta_{\max} > 0$, $\mathcal{M}$, N_{iter}
Output: $\mathbf{X}_k$
$k = 0$
Initialize $\mathbf{X}_0$ randomly from the manifold $\mathcal{M}$
while $k < N_{\text{iter}}$ **do**
    Obtain $\boldsymbol{\eta}_k$ by solving the subproblem in (D.7) (*e.g.*, applying the CG method)
    Evaluate ρ_k according to eq. (D.8)
    if $\rho_k > 1/4$ **then**
        $\Delta_{k+1} = \frac{1}{4}\Delta_k$
    else if $\rho_k > 3/4$ and $||\boldsymbol{\eta}_k|| = \Delta_k$ **then**
        $\Delta_{k+1} = \min(2\Delta_k, \Delta_{\max})$
    else
        $\Delta_{k+1} = \Delta_k$
    end if
    if $\rho_k > \overline{\rho}$ **then**
        $\mathbf{X}_{k+1} = \text{Retr}_{\mathbf{X}_k}(\boldsymbol{\eta}_k)$
    else
        $\mathbf{X}_{k+1} = \mathbf{X}_k$
    end if
    $k = k + 1$
end while

f on a Riemannian manifold $\mathcal{M}$, the algorithm finds a point $\mathbf{X} \in \mathcal{M}$ that minimizes f. The SD method works by taking steps toward the negative gradient of f at the current point (ABSIL et al., 2007). The SD algorithm begins with an initial guess $\mathbf{X}_0$ on the manifold $\mathcal{M}$. At each iteration, it calculates the gradient of f at the current point $\mathbf{X}_k$ by using the Riemannian gradient operator. Then, it takes a step in the direction of the negative gradient scaled by a step size α_k^{ss}, *i.e.*, $-\alpha_k^{\text{ss}} \nabla_{\mathcal{M}} f(\mathbf{X}_k)$. The step size is selected by a line search algorithm satisfying the Armijo rule, such as backtracking line search, similarly as occurs in the RCG algorithm. The algorithm then updates the point on the manifold to

$$\mathbf{X}_{k+1} = \text{Retr}_{\mathbf{X}_k}(-\alpha_k^{\text{ss}} \nabla_{\mathcal{M}} f(\mathbf{X}_k)). \tag{D.9}$$

This procedure repeats until convergence or the maximum number of iterations is achieved. A pseudocode for the RSD solution is given in **Algorithm 9**.

Algorithm 9 Manifold SD-based

Input: Input parameters: $\mathcal{M}$, N_{iter}
Output: $\mathbf{X}_k$
$k = 0$
Initialize $\mathbf{X}_0$ randomly from the manifold $\mathcal{M}$
while $k \leq N_{\text{iter}}$ **do**
    $\nabla_{\mathcal{M}} f_3(\mathbf{X}_k) = \text{Proj}\{\mathcal{T}_{\mathbf{X}_k}\mathcal{M}(\nabla f(\mathbf{X}_k))\}$
    Find the step size $\alpha_k^{\text{ss}} > 0$ via backtracking line search algorithm
    Update $\mathbf{X}_{k+1}$ according to eq. (D.9)
    $k = k + 1$
end while

APPENDIX E – Lower Bound of the Ergodic Spectral Efficiency with ZF Combiner

In this section, we will proof the derivation of the explicit formula for the rate SE_k, which is utilized in Chapter 4 to propose a statistical CSI-based RIS design to minimize the total transmit power. Recalling that the k-th user's ergodic SE with ZF combining is lower bounded by

$$\begin{aligned} \mathrm{SE}_k &= \mathbb{E}\left\{\log_2\left(1+\mathrm{SINR}_k\right)\right\} && \text{(E.1)} \\ &\geq \log_2\left(1+\frac{p_k}{\sigma^2\mathbb{E}\left\{\left[(\mathbf{H}^H\mathbf{H})^{-1}\right]_{kk}\right\}}\right), && \text{(E.2)} \end{aligned}$$

we need to calculate $\mathbb{E}\left[(\mathbf{H}^H\mathbf{H})^{-1}\right]_{kk}$ to derive SE_k. For this purpose, we express matrix $\mathbf{H}^H$ as

$$\mathbf{H}^H = \sqrt{\frac{\beta\kappa}{\kappa+1}}\hat{\mathbf{H}}^H\boldsymbol{\Phi}^H\overline{\mathbf{F}}^H + \sqrt{\frac{\beta}{\kappa+1}}\hat{\mathbf{H}}^H\boldsymbol{\Phi}^H\tilde{\mathbf{F}}^H + \boldsymbol{\Omega}_d^{1/2}\overline{\mathbf{D}}^H. \tag{E.3}$$

For simplicity, we define $\mathbf{H}^H \triangleq [\mathbf{h}_1,\ldots,\mathbf{h}_{N_{\mathrm{BS}}}]$, $\overline{\mathbf{F}}^H \triangleq [\overline{\mathbf{f}}_1,\ldots,\overline{\mathbf{f}}_{N_{\mathrm{BS}}}]$, $\tilde{\mathbf{F}}^H \triangleq [\tilde{\mathbf{f}},\ldots,\tilde{\mathbf{f}}_{N_{\mathrm{BS}}}]$, and $\overline{\mathbf{D}}^H \triangleq [\overline{\mathbf{d}}_1,\ldots,\overline{\mathbf{d}}_{N_{\mathrm{BS}}}]$. Noting that $\tilde{\mathbf{F}}$ and $\overline{\mathbf{D}}$ are composed of i.i.d. complex Gaussian variables, and are mutually independent, we have

$$\tilde{\mathbf{f}}_m \sim \mathcal{CN}(\mathbf{0},\mathbf{I}_{N_{\mathrm{RIS}}}), \quad 1\leq m\leq N_{\mathrm{BS}}, \tag{E.4}$$

$$\overline{\mathbf{d}}_m \sim \mathcal{CN}(\mathbf{0},\mathbf{I}_K), \quad 1\leq m\leq N_{\mathrm{BS}}, \tag{E.5}$$

where $\tilde{\mathbf{f}}_i$ and $\tilde{\mathbf{f}}_j$ are mutually independent for $i\neq j$; $\overline{\mathbf{d}}_i$ and $\overline{\mathbf{d}}_j$ are mutually independent for $i\neq j$; $\tilde{\mathbf{f}}_i$ and $\overline{\mathbf{d}}_j$ are mutually independent for all i and j. Given that a linear transformation of a standard Gaussian random vector remains Gaussian (MUIRHEAD, 2005), we find

$$\begin{aligned} &\sqrt{\frac{\beta\kappa}{\kappa+1}}\hat{\mathbf{H}}^H\boldsymbol{\Phi}^H\overline{\mathbf{f}}_m+\sqrt{\frac{\beta}{\kappa+1}}\hat{\mathbf{H}}^H\boldsymbol{\Phi}^H\tilde{\mathbf{f}} \\ &\qquad\sim\mathcal{CN}\left(\sqrt{\frac{\beta\kappa}{\kappa+1}}\hat{\mathbf{H}}^H\boldsymbol{\Phi}^H\overline{\mathbf{f}}_m,\frac{\beta}{\kappa+1}\hat{\mathbf{H}}^H\hat{\mathbf{H}}\right), \quad \forall m \end{aligned} \tag{E.6}$$

and

$$\boldsymbol{\Omega}_d^{1/2}\overline{\mathbf{d}}_m \sim \mathcal{CN}(\mathbf{0},\boldsymbol{\Omega}_d), \quad \forall m, \tag{E.7}$$

where we have $\boldsymbol{\Phi}^H\boldsymbol{\Phi}=I_N$ and $\boldsymbol{\Omega}_d=\boldsymbol{\Omega}_d^H$.

Next, considering that the sum of independent Gaussian vectors is still Gaussian distributed (MUIRHEAD, 2005), we derive the statistics of the m-th column of the aggregated channel $\mathbf{H}^H$ as

$$\mathbf{h}_m \sim \mathcal{CN}\left(\sqrt{\frac{\beta\kappa}{\kappa+1}}\hat{\mathbf{H}}^H\mathbf{\Phi}^H\overline{\mathbf{f}}_m, \frac{\beta}{\kappa+1}\hat{\mathbf{H}}^H\hat{\mathbf{H}}+\mathbf{\Omega}_d\right), \quad 1\le m\le N_{\text{BS}}, \tag{E.8}$$

where $\mathbf{h}_m$, $1\le m\le N_{\text{BS}}$, are mutually independent. Therefore, $\text{vec}(\mathbf{H}^H)$ is a complex Gaussian vector with the following mean and covariance matrices

$$\mathbb{E}\left\{\text{vec}(\mathbf{H}^H)\right\} = \text{vec}\left(\sqrt{\frac{\beta\kappa}{\kappa+1}}\hat{\mathbf{H}}^H\mathbf{\Phi}^H\overline{\mathbf{F}}^H\right), \tag{E.9}$$

$$\text{Cov}\left\{\text{vec}(\mathbf{H}^H)\right\} = \mathbf{I}_{N_{\text{BS}}}\otimes\left(\frac{\beta}{\kappa+1}\hat{\mathbf{H}}^H\hat{\mathbf{H}}+\mathbf{\Omega}_d\right), \tag{E.10}$$

where $\text{vec}\{\cdot\}$ and $\otimes$ denote the vectorization by column stacking and the Kronecker product, respectively.

Using the distribution of $\text{vec}(\mathbf{H}^H)$ and following the notations in (JIN et al., 2007), matrix $\mathbf{H}$ is a complex Gaussian distributed matrix, described as

$$\mathbf{H}\sim\mathcal{CN}\left(\sqrt{\frac{\beta\kappa}{\kappa+1}}\overline{\mathbf{F}}\mathbf{\Phi}\hat{\mathbf{H}}, \mathbf{I}_{N_{\text{BS}}}\otimes\left(\frac{\beta}{\kappa+1}\hat{\mathbf{H}}^H\hat{\mathbf{H}}+\mathbf{\Omega}_d\right)\right). \tag{E.11}$$

Therefore, the product $\mathbf{H}^H\mathbf{H}$ follows a complex non-central Wishart distribution (MUIRHEAD, 2005), expressed as

$$\begin{aligned}\mathbf{H}^H\mathbf{H}\sim\mathcal{W}_K\Bigg(&N_{\text{BS}}, \frac{\beta}{\kappa+1}\hat{\mathbf{H}}^H\hat{\mathbf{H}}+\mathbf{\Omega}_d,\\ &\left(\frac{\beta}{\kappa+1}\hat{\mathbf{H}}^H\hat{\mathbf{H}}+\mathbf{\Omega}_d\right)^{-1}\frac{\beta\kappa}{\kappa+1}\hat{\mathbf{H}}^H\mathbf{\Phi}^H\overline{\mathbf{F}}^H\overline{\mathbf{F}}\mathbf{\Phi}\hat{\mathbf{H}}^H\Bigg).\end{aligned} \tag{E.12}$$

Although the non-central Wishart distribution (E.12) is precise, its statistics are very complex, making it difficult to obtain a tractable expression for insightful analysis. To simplify the analysis, as in (SIRITEANU et al., 2012; SIRITEANU et al., 2015; ZHANG et al., 2013), we approximate the non-central Wishart distribution (E.12) as a central Wishart distribution with the same first-order moment.

Firstly, the first-order moment for the non-central Wishart distribution under consideration is (SIRITEANU et al., 2015)

$$\begin{aligned}\mathbb{E}\left[\mathbf{H}^H\mathbf{H}\right] &= N_{\text{BS}}\left(\frac{\beta}{\kappa+1}\hat{\mathbf{H}}^H\hat{\mathbf{H}}+\mathbf{\Omega}_d\right)+\frac{\beta\kappa}{\kappa+1}\hat{\mathbf{H}}^H\mathbf{\Phi}^H\overline{\mathbf{F}}^H\overline{\mathbf{F}}\mathbf{\Phi}\hat{\mathbf{H}}\\ &= N_{\text{BS}}\left(\frac{\beta}{\kappa+1}\hat{\mathbf{H}}^H\hat{\mathbf{H}}+\mathbf{\Omega}_d\right)+N_{\text{BS}}\frac{\beta\kappa}{\kappa+1}\hat{\mathbf{H}}^H\mathbf{\Phi}^H\mathbf{a}_N\mathbf{a}_N^H\mathbf{\Phi}\hat{\mathbf{H}},\end{aligned} \tag{E.13}$$

where the last equality is obtained using the fact that $\overline{\mathbf{F}}=\mathbf{a}_M\mathbf{a}_N^H$ and $\mathbf{a}_M^H\mathbf{a}_M=N_{\text{BS}}$.

Therefore, a virtual central Wishart distribution with this moment is given by (SIRITEANU et al., 2015)

$$\mathbf{H}^H\mathbf{H} \sim \mathcal{W}_K\left(N_{\text{BS}}, \frac{\beta}{\kappa+1}\hat{\mathbf{H}}^H\hat{\mathbf{H}} + \boldsymbol{\Omega}_d + \frac{\beta\kappa}{\kappa+1}\hat{\mathbf{H}}^H\boldsymbol{\Phi}\mathbf{a}_N\mathbf{a}_N^H\boldsymbol{\Phi}\hat{\mathbf{H}}\right). \tag{E.14}$$

Based on the obtained complex central Wishart distribution (E.14), and utilizing (TAGUE; CALDWELL, 1994), we can find the expectation of the matrix inverse as follows

$$\mathbb{E}\left[(\mathbf{H}^H\mathbf{H})^{-1}\right] = \frac{1}{N_{\text{BS}}-K}\left(\frac{\beta}{\kappa+1}\hat{\mathbf{H}}^H\hat{\mathbf{H}} + \boldsymbol{\Omega}_d + \frac{\beta\kappa}{\kappa+1}\hat{\mathbf{H}}^H\boldsymbol{\Phi}^H\mathbf{a}_N\mathbf{a}_N^H\boldsymbol{\Phi}\hat{\mathbf{H}}\right)^{-1}. \tag{E.15}$$

By substituting (E.15) into (E.2), we obtain the lower bound of the ergodic SE for user k as follows

$$\text{SE}_k \geq \log_2\left(1 + \frac{p_k(N_{\text{BS}}-K)}{\sigma^2(\kappa+1)\left[\left(\boldsymbol{\Lambda} + \beta\kappa\hat{\mathbf{H}}^H\boldsymbol{\Phi}^H\mathbf{a}_N\mathbf{a}_N^H\boldsymbol{\Phi}\hat{\mathbf{H}}\right)^{-1}\right]_{kk}}\right), \tag{E.16}$$

where $\boldsymbol{\Lambda} = \beta\hat{\mathbf{H}}^H\hat{\mathbf{H}} + (\kappa+1)\boldsymbol{\Omega}_d$.

By defining the following constants $\mathbf{A}_k$, $\mathbf{B}$, and $\mathbf{q}_k^H$, which are related to the RIS-array gain, as

$$\mathbf{B} = \frac{1}{N_{\text{RIS}}}\mathbf{I}_K + \beta\kappa\text{diag}(\mathbf{a}_N^H)\hat{\mathbf{H}}\boldsymbol{\Lambda}^{-1}\hat{\mathbf{H}}^H\text{diag}(\mathbf{a}_N), \tag{E.17}$$

$$\mathbf{A}_k = \left[\boldsymbol{\Lambda}^{-1}\right]_{k,k}\mathbf{B} - \kappa\beta\mathbf{q}_k\mathbf{q}_k^H, \tag{E.18}$$

$$\mathbf{q}_k^H = \left[\boldsymbol{\Lambda}^{-1}\hat{\mathbf{H}}^H\text{diag}(\mathbf{a}_{\text{N}})\right]_{(k,:)}, \tag{E.19}$$

and after some manipulations, we obtain (ZHI et al., 2022b; ZHI et al., 2022c)

$$\text{SE}_k \geq \tilde{\text{SE}}_k = \log_2\left(1 + \frac{p_k(N_{\text{BS}}-K)\boldsymbol{\phi}^H\mathbf{B}\boldsymbol{\phi}}{\sigma^2(\kappa+1)\boldsymbol{\phi}^H\mathbf{A}_k\boldsymbol{\phi}}\right). \tag{E.20}$$